TOR VERGATA
UNIVERSITÀ DEGLI STUDI DI ROMA

SAPIENZA
UNIVERSITÀ DI ROMA

University of Tor Vergata
University of Sapienza

Astronomy Astrophysics and Space Science (AASS)
PhD in Astrophysics

The hunt for short-period exo-Neptunes and their characterization

via radial-velocity follow-up of *TESS* planetary candidates

Thesis Advisor
Prof. Luigi Mancini

Co-advisors
Dr. Aldo S. Bonomo
Dr. Alessandro Sozzetti

Name
Luca Naponiello
1931745

Academic Year MMXX-MMXXIII (XXXVI cycle)

Not all those who wander are lost

Abstract

Despite the discovery of thousands of planets beyond our Solar System, many questions still remain, primarily about the mechanisms of formation and evolution that give rise to the extraordinary diversity of exoplanets in terms of their physical parameters, planetary architecture and atmospheric composition. The pursuit to unveil planetary demographics and statistics has in part been constrained by inherent observational biases, which resulted in an overrepresentation of large, massive planets and small planets with relatively short orbital periods ($P_{orb} \lesssim 20$ days). A poorly researched class of planets is in particular that of Neptunians, also due to their relative rarity. The objective of this PhD program is to bridge this gap by conducting a comprehensive exploration of Neptune-sized exoplanets, a category that remains underrepresented especially in the close proximity of their host stars (the so-called hot-Neptune desert), while delving into their intriguing variety. Several open questions concern the main mechanisms of formation and evolution of Neptunian planets, such as the origin of the desert, their atmospheric composition, and the diversity of their physical parameters. As a matter of fact, within the class of Neptune-type planets, objects of similar radius can have very different bulk densities and compositions, as they can vary from relatively low-density planets with thick hydrogen-helium atmospheres, up to high-density planets with thinner atmospheres and large rocky cores.

During this research we selected a dozen Neptune-sized transit candidates orbiting around bright FGK dwarfs, first identified by the Transiting Exoplanet Survey Satellite (*TESS*), in order to cover as much *parameter space* as possible, particularly in terms of planetary radii and orbital periods (or temperatures). As part of the broader framework of the Italian Global Architecture of Planetary Systems (GAPS) project, these selected candidate hosts have been subjects of radial velocity (RV) follow-up for the purpose of validating the transiting planets and performing an in-depth characterization of their physical and orbital characteristics, through Bayesian combined analyses of both RVs and *TESS* photometry. The task has been carried out utilizing the High Accuracy Radial Velocity Planet Searcher for the Northern Hemisphere (HARPS-N), a cross-dispersed high-resolution ($R = 115\,000$) échelle spectrograph, operating in the wavelength range of 3830-6930 Å, and installed at the Telescopio Nazionale Galileo (TNG) in La Palma, Spain. Over the course of a three-year endeavor, the study has yielded up to now the validation and characterization of two sub-Neptunes (TOI-2443 b, TOI-5076 b), two super-Neptunes (TOI-1694 b, TOI-1710 b), and three Neptune-sized planets (TOI-1272 b, TOI-1422 b, TOI-1853 b), along with the discovery of three non-transiting Neptune-mass planets (TOI-1272 c, TOI-1272 d, TOI-1422 c) and one Jovian (TOI-1694 c) on outer orbits. In particular, we focused on the analysis and characterization of the systems TOI-1710 (König, Damasso, Hébrard, Naponiello, et al. (2022)), TOI-1422 (Naponiello et al., 2022) and TOI-1853 b (Naponiello et al. 2023, Nature). The warm super-Neptune TOI-1710 b ($T_{eq} = 687 \pm 50$ K, $R_p = 5.34 \pm 0.11\,R_\oplus$, $M_p = 28.3 \pm 4.7\,M_\oplus$) is found to have a thicker gaseous envelope compared to Neptune (amounting to $20 - 30\%$ of its mass fraction) due to its low density of $\rho_p = 0.94 \pm 0.22$ g cm^{-3}. In light of its relatively long orbital period and eccentricity compatible with zero ($P_{orb} = 24.283429 \pm 0.000043$ days, $e_p = 0.16 \pm 0.08$), we suggest that TOI-1710 b may have migrated to its current position during the disc phase. Similarly, the warm Neptune-sized TOI-1422 b ($T_{eq} = 867 \pm 17$ K, $R_p = 3.96^{+0.13}_{-0.11}\,R_\oplus$) is one among the most inflated Neptunian plan-

ets ($M_p = 9.0^{+2.3}_{-2.0}\,M_\oplus$, $\rho_p = 0.79^{+0.29}_{-0.23}$ g cm^{-3}), and we expect it to also have an extensive gaseous envelope (amounting to $10 - 25\%$ of its mass fraction). Its candidate companion, TOI-1422 c, is a non-transiting Neptune-mass planet ($M_p = 11.1^{+2.6}_{-2.3}\,M_\oplus$) on a outer orbit ($P_{orb} = 29.29^{+0.21}_{-0.20}$ days). The fact that TOI-1422 c has not been scattered away suggests that TOI-1422 b has not undergone high-eccentricity migration, and that it may have migrated through the disc, analogously to TOI-1710 b. Finally, one especially noteworthy discovery is TOI-1853 b, a newfound Neptune-sized planet in the hot-Neptune desert ($R_p = 3.46 \pm 0.08\,R_\oplus$, $P_{orb} = 1.2436258 \pm 0.0000015$ days, $T_{eq} = 1479 \pm 25$ K) on a circular orbit, which stands out as the most massive and densest *Neptunian* planet ever documented ($M_p = 73.2 \pm 2.7\,M_\oplus$, $\rho_p = 9.74^{+0.82}_{-0.76}$ g cm^{-3}). The physical properties of TOI-1853 b cannot be explained by the core accretion formation model alone, as the assembly of its exceptionally heavy core necessitates the exploration of alternative evolution-migration models (i.e. a catastrophic origin which may result from either multiple planetary impacts or high-eccentricity migration followed by severe tidal dissipation).

In conclusion, this research effort resulted in novel findings which have particularly contributed to enlarging the population of well-characterized exo-Neptunes, paving the way for future statistical studies. Furthermore, as new instruments and satellites aid scientists in probing the depths of space (such as *JWST*, or the coming *Ariel* mission), the mass measurements provided in this thesis will be critical especially for the study of atmospheres. In turn, the atmospheric characterization of Neptunian planets (e.g. through either transmission or emission spectroscopy) will provide additional constraints on their formation and migration scenarios, shedding light on the complexities of exoplanetary systems in general.

Keywords: Exoplanetary systems – Techniques: radial velocities, photometry – Stars: TOI-1272, TOI-1422, TOI-1694, TOI-1710, TOI-1853, TOI-2443, TOI-5076

Acknowledgements

First and foremost, I would like to thank my supervisor, Prof. Luigi Mancini, for his knowledgeable guidance, constant encouragement, and wisdom in steering my research. His dedication to scientific excellence and passion for exoplanets have been a constant source of inspiration throughout this journey. I extend my gratitude especially to dr. Aldo Bonomo, dr. Alessandro Sozzetti, dr. Mario Damasso and Prof. Emanuele Pace for their time, patience, lessons and valuable insights. I am also grateful to the institutions that have enabled this research, in particular the University of Florence, which funding and support has been instrumental in the continuation of this research, and I am thankful for their trust in my abilities.

A heartfelt thank you goes to the whole exoplanet research community and to all those who, directly or indirectly, have contributed to my research journey. Every discussion, every suggestion, and every shared moment have contributed to shaping this thesis and my development as a researcher. The completion of this doctoral thesis has been made possible through the collaboration, support, and inspiration of all these extraordinary individuals. I am truly fortunate to have had their presence along this path.

Lastly, a special thanks to my family and friends for their unwavering support, love, and patience throughout my academic path. Their words of encouragement have consistently fueled my determination and kept me going.

Contents

List of Figures

List of Tables

Acronyms

AIC Akaike information criterion

AO Adaptive Optics

APF Automated Planet Finder

Ariel Atmospheric Remote-sensing infrared Exoplanet Large-survey

au astronomical unit

BIC Bayesian information criterion

BIS Bisector Inverse Slope

BLS Box Least Squares

C/O Carbon-to-Oxygen

CARMENES Calar Alto high-Resolution search for M dwarfs with Exoearths with Nearinfrared and optical Echelle Spectrographs

CBV Cotrending Basis Vector

CCD Charged-Coupled Device

CCF cross-correlation function

CHEOPS Characterizing Exoplanet Satellite

COROT Convection, Rotation, and Planetary Transits

DRS Data Reduction Software

DV Data Validation

EB Eclipsing Binary

ESPRESSO Echelle SPectrograph for Rocky Exoplanet and Stable Spectroscopic Observations

EXPRES EXtreme PREcision Spectrograph

FAP False Alarm Probability

FEROS Fiber-fed Extended Range Optical Spectrograph

FFI Full Frame Image

FOV Field of View

FWHM Full Width at Half-Maximum

GAPS Global Architecture of Planetary Systems

GLS Generalized Lomb-Scargle

GP Gaussian Process

H-R Hertzsprung–Russell

HARPS-N High Accuracy Radial velocity Planet Searcher for the Northern hemisphere

HEM high-eccentricity migration

HIRES High Resolution Echelle Spectrometer

HJ Hot Jupiter

HN Hot Neptune

IAU International Astronomical Union

JWST James Webb Space Telescope

LDC Limb Darkening Coefficient

LoS Line-of-Sight

MCMC Markov Chain Monte Carlo

NEID NN-explore Exoplanet Investigations with Doppler spectroscopy

PDC-SAP Pre-search Data Conditioning SAP

PLATO PLAnetary Transits and Oscillations of stars

ppm parts-per-million

ppt parts-per-thousand

QLP Quick-Look Pipeline

RMS root-mean-square

RV Radial Velocity

SAP Simple Aperture Photometry

SDE Signal Detection Efficiency

SED Spectral Energy Distribution

SNR Signal-to-noise ratio

SOPHIE Spectrographe pour l'Observation des Phénomènes des Intérieurs stellaires et des Exoplanètes

SPIRou SPectropolarimètre InfraROUge

SPOC Science Processing Operations Center

TCE Threshold Crossing Event

TERRA Template Enhanced Radial velocity Re-analysis Application

TESS Transiting Exoplanet Survey Satellite

TIC TESS Input Catalog

TLS Transit Least Squares

TNG Telescopio Nazionale Galileo

TOI TESS Object of Interest

TTV Transit timing variation

WN Warm Neptune

Chapter 1

Introduction

After almost 30 years of exploration, exoplanetary science has now entered a mature phase in which the determination of the physical properties of planets and the origin of their observed, astonishing diversity is no longer a pipedream. Thanks to a surge of discoveries with transit and Radial Velocity (RV) surveys (Section 1.5), extrasolar planets are starting to fill the full range of parameter space in terms of orbital arrangements and multiplicity properties (Winn and Fabrycky, 2015). This growing data set is allowing astronomers, for the first time, to estimate the frequency of planets with different properties like mass, size, orbital characteristics, host-star properties, and to probe the diverse outcomes of planet formation and evolution (see Section 1.6). In particular, taking into account the effect of observational biases, small (low-mass) planets between the size (mass) of Earth and Neptune substantially outnumber Jupiter-type planets (see Figure 1.1), and the occurrence rates of terrestrial and giant exoplanets appear to depend non-trivially on the properties (e.g. mass, metallicity) of the parent stars (Howard et al., 2013). However, the category of intermediate radius/mass planets, or Neptune-type planets, currently underrepresented at *short* orbital periods ($P_{orb} < 100$ days), has shown that objects of comparable radius can have very diverse average densities, and therefore different inferred internal structures (see Section 1.3.2). Figure 1.2 shows that well-characterized exoplanets are much closer to their host stars compared to Solar System planets (left panel), due to the current observation biases, while they often share similar densities (right panel), although exo-Neptunes in general exhibit a plethora of densities that can extend from very low up to the ones of rocky-type planets. As a case in point, the short-period super Neptune TOI-532 b (Kanodia et al., 2021) has a radius of $5.8^{+0.2}_{-0.2}\,R_\oplus$, a mass of $61^{+10}_{-9}\,M_\oplus$ and, therefore, is as dense as Neptune ($1.7^{+0.3}_{-0.3}$ g cm^{-3}), while the Neptune-sized TOI-2196 b (Persson et al., 2022) has a radius of $3.5^{+0.2}_{-0.2}\,R_\oplus$, a mass of $26^{+1.3}_{-1.3}\,M_\oplus$ and is almost twice as dense ($3.3^{+0.5}_{-0.4}$ g cm^{-3}). Even more dense is the ultra-short-period planet TOI-849 b (Armstrong et al., 2020), which has a radius of $3.4^{+0.2}_{-0.1}\,R_\oplus$, a mass of $39^{+3}_{-3}\,M_\oplus$ and thus a bulk density similar to that of Earth ($5.2^{+0.7}_{-0.8}$ g cm^{-3}). The paradigm that large planets are always gaseous while small ones are rocky in nature is wearing out.

Moreover, the atmospheric properties of otherwise similar planets (in mass and radius) can also be very different, and the zoo of atmospheric realizations is even more impressive considering the still relatively small sample of planets with detected atmospheres (Sing et al., 2015). The diversity of exoplanetary characteristics clearly demonstrates that most of the gross features of the Solar

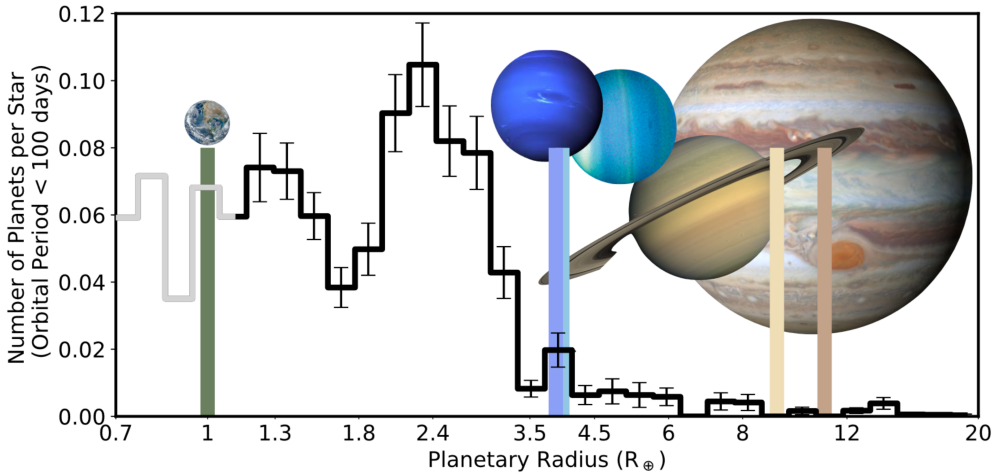

Figure 1.1: Histogram of the average number of planets per star (with orbital period below 100 days), as a function of planet radii. The real number of exoplanets detected (before 2017) has been multiplied by a correction factor, which takes into account the observational biases, for completeness (however the gray region at small radii suffers from low completeness and should be considered with caution). Figure courtesy of Wakeford and Dalba 2020.

System are but one outcome in a continuum of possibilities. The answer to the question of what is the origin of the observed diversity of planetary systems is one of the most important challenges in modern astronomy. The observed planetary properties (including internal structure, atmospheric composition and orbital architecture – refer to Section 1.3) are the result of the complex interplay between a variety of physical and dynamical processes operating on different timescales during formation and subsequent orbital evolution; these in turn depend on environmental conditions, such as disc properties, planet multiplicity, and stellar radiation fields. However, a statistical study of

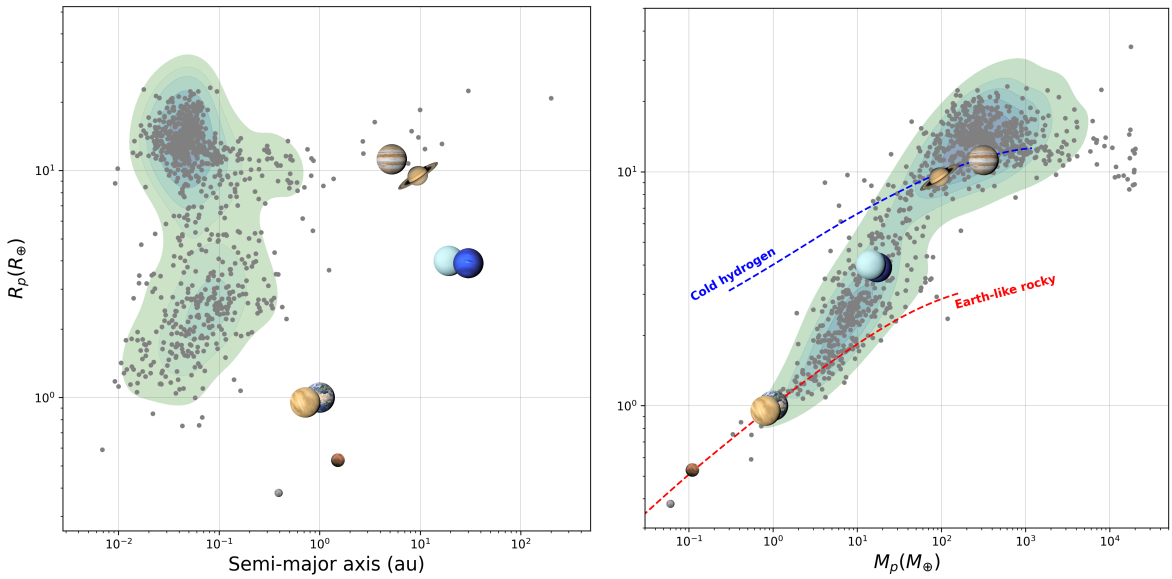

Figure 1.2: Distribution of transiting exoplanets with mass and radius uncertainty levels of at least 2σ (as extracted from `exoplanets.eu`), compared to the planets of the Solar System, displayed with radius as a function of semi-major axis (left panel) and mass (right panel). Density model lines are shown for a Earth-like rocky composition, or 32.5% Fe + 67.5% $MgSiO_3$ (red dashed line), and cold hydrogen (Becker et al. 2014) (blue dashed line).

planet properties requires a well-considered research approach, involving the identification of clear and robust diagnostics, and a significant investment of observing time with cutting-edge instrumentation, which is the reason why several dedicated projects (both from the ground and in space) are now planned to tackle different aspects of this question. Space-based missions like Kepler-K2 (now concluded), Transiting Exoplanet Survey Satellite (*TESS*), the Characterizing Exoplanet Satellite (CHEOPS) (on-going) (Broeg et al., 2013), and the PLAnetary Transits and Oscillations of stars (*PLATO*) (to be launched in 2026) (Rauer et al., 2014) focus on the systematic study of orbital architectures and structural properties of planetary systems, while other space and ground-based large and extremely-large facilities, such as the James Webb Space Telescope (*JWST*) (on-going) (McElwain et al., 2023) or the incoming Extremely Large Telescope (*ELT*) (to be operative in 2028) (Chornock et al., 2019), have atmospheric characterization as one of the main science drivers.

The Italian long-term, multi-program Global Architecture of Planetary Systems (GAPS) (Covino et al., 2013, Poretti et al., 2016) exploits high-precision Doppler measurements with the High Accuracy Radial velocity Planet Searcher for the Northern hemisphere (HARPS-N) (Cosentino et al., 2012) instrument at Telescopio Nazionale Galileo (TNG), in La Palma (Spain), renowned as one of the most accurate spectrographs in the northern hemisphere (see Section 1.5.2). One of the aims of the GAPS consortium is to obtain an accurate mass determination of *low-mass* (or non-Jovian) planets. In this context, the observations of both Warm Neptunes (WNs) and Hot Neptunes (HNs) is crucial to understanding the evolution of planetary systems as they are thought to be planets in transition; i.e. they are believed to form far from the parent stars (see Section 1.1), and then somehow migrate closer where they get heavily irradiated and cannot sustain their atmosphere anymore, perhaps eventually exposing only their core. This might explain why the proximity of stars is marked by a significant scarcity of Neptune-like exoplanets, often referred to as the *hot-Neptune desert* (Mazeh et al., 2016). In general, Neptune-type planets are a rare discovery, especially those with very short orbital periods (potentially owing to the influence of photo-evaporation), thus the intricate details of their formation and potential migration, along with their typical composition, remain elusive.

This PhD project has been carried out within the GAPS project framework, and aims at furthering our understanding of key aspects of planet formation and evolution processes focusing on the characterization of hot, warm, and temperate transiting Neptunes to determine their orbital (period, semi-major axis, eccentricity) and physical (radius, mass, density) parameters, and thus investigate their internal structure, formation, and evolution via a combination of high-sensitivity photometric and spectroscopic measurements. The thesis is organized as follows: the subsequent introductory sections lay out the basics of exoplanet research, Chapter 2 delves into the primary data analysis tools utilized in this study, Chapters 3, 4 and 5 encompass the examination of all observed systems, including two first-authored papers (Chapters 4 and 5, presented separately for clarity), while the concluding Chapter 6 offers a summary of the research findings, along with a general overview of the current state of exo-Neptunes research. All figures presented in this thesis were created by the author unless otherwise indicated in the captions.

1.1 Exoplanet definition and demographics

According to the International Astronomical Union (IAU), the official definition of *exoplanet* is expected to evolve as our overall knowledge improves, but at present time is the following:

- Objects with true masses below the limiting mass for thermonuclear fusion of deuterium (currently calculated to be 13 Jupiter masses for objects of solar metallicity) that orbit stars, brown dwarfs or stellar remnants and that have a mass ratio with the central object below the L4/L5 instability ($\frac{M}{M_{central}} < \frac{2}{25+\sqrt{621}}$) are "planets" (no matter how they formed);
- The minimum mass/size required for an extrasolar object to be considered a planet should be the same as that used in our Solar System.

However, no particular feature has been observed around the 13 Jupiter mass-limit (Schneider et al., 2011) (a value that is in any case unjustified for planets with rocky cores), and the composition of a planet does influence deuterium fusion (Spiegel et al., 2011). One alternative is to link the definition of an exoplanet to their formation, since the direct gravitational collapse of clouds of gas, responsible for the birth of stars, can also form star-like objects below 13 Jupiter masses. In this context, objects formed through gravitational instability should not count as planets (Schlaufman, 2018). The difficulty here lies in the simple fact that most of the time it's impossible to tell the formation history of an exoplanet, which is even more problematic for non-transiting objects with unknown orbital inclination, and therefore with only a lower limit on the mass. As a consequence, most exoplanet databases include objects with mass (or minimum mass) up to 30 Jupiter masses or even more.

After centuries of speculations, thanks to a general improvement in science and technology, the 20th century saw a rise of tentative, erroneous, detections which finally lead up to the first confirmation of an exoplanet detection in 1992 around the pulsar PSR B1257+12 (Wolszczan and Frail, 1992). A couple of years later, in 1995, 51 Pegasi b was recognized as the first exoplanet orbiting a Sun-like star (Mayor and Queloz, 1995), a discovery awarded with the Nobel prize in 2019. Since then, more than 5500 exoplanets have been found with a plethora of unique characteristics. Based on their orbital period (P) and equivalent temperatures, exoplanets are described as Hot ($P \lesssim 10$ days), Warm ($10 \lesssim P \lesssim 100$ days) and Cold ($P > 100$ days), and are generally distributed among the following categories (refer also to Figure 1.3):

- **Jovian planets** - They have dimensions similar to Jupiter and Saturn, with $8R_\oplus$ (Earth-radii) $\lesssim R_\mathrm{p} \lesssim 15R_\oplus$, and $80M_\oplus$ (Earth-masses) $\lesssim M_\mathrm{p} \lesssim 4000M_\oplus$ (though, as stated above, establishing a definitive upper mass limit is not straightforward). These planets possess thick, gaseous atmospheres with a variety of gases, predominantly hydrogen and helium. Initially, it was theorized that Jovian planets would form at a considerable distance from their parent stars, analogous to the positions of Jupiter and Saturn in our own Solar System. However, many exoplanets classified as Hot Jupiters (HJs) have been found orbiting in close proximity to their host stars, some even at ultra-short orbital periods. This observation challenges the traditional formation theory and suggests that planetary migration plays a significant role in shaping the orbits of exoplanets (see Section 1.6.2);

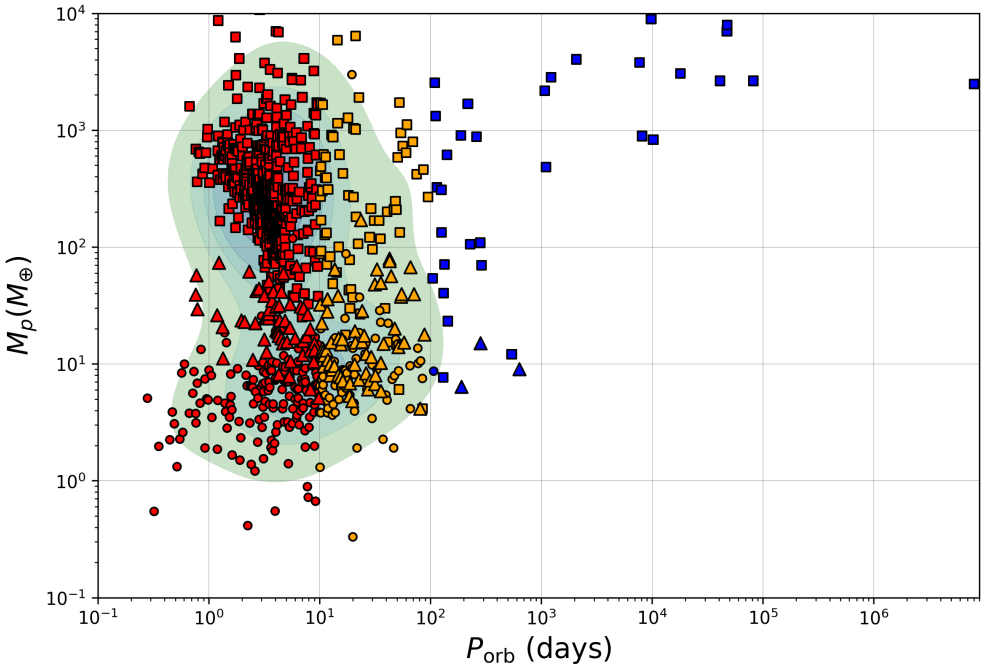

Figure 1.3: Current population of exoplanets, as extracted from `exoplanets.eu`, with mass uncertainty levels of at least 2σ. The Hot (red), Warm (orange) and Cold (blue) exoplanets have been further marked with circles, triangles and squares to indicate, respectively, Earth-type and small planets, Neptunian planets and Jovians (as defined in Section 1.1).

- **Neptunian planets** - They have dimensions similar to Neptune and Uranus, typically with radii ranging from $3.5R_\oplus \lesssim R_\text{p} \lesssim 6R_\oplus$, and masses within the range of $10M_\oplus < M_\text{p} \lesssim 50M_\oplus$. Like their Solar System counterparts, these planets are supposed to have substantial atmospheres, composed of hydrogen, helium and mixture of other elements (such as water, methane and ammonia). Neptune-sized planets can have a variety of orbital periods, but they generally don't occupy positions close to the stars (i.e. the hot-Neptune desert). They are believed to form outside the so-called *snow line*[1], so that they can accumulate a great amount of volatile elements, however it is likely that planet migration plays a significant role for them as well. Intriguingly, Neptunian planets exhibit a wide range of densities, reflecting their varying compositions, and as a result, they present a captivating field of study for astronomers and planetary scientists (see Section 1.3.2);

- **Small planets** - They are planets with $1R_\oplus \lesssim R_\text{p} \lesssim 3.5R_\oplus$ and $1M_\oplus \lesssim M_\text{p} \lesssim 20M_\oplus$, unseen in the Solar System. When they present a significant amount of rocks, suggesting a composition akin to our home planet, they are classified as super-Earths ($R_\text{p} \lesssim 1.7R_\oplus$), otherwise they are simply sub-Neptunes ($1.7R_\oplus \lesssim R_\text{p} \lesssim 3.5R_\oplus$) as they generally present a significant amount of volatile elements, similarly to Neptunian planets. The corrected distribution of exoplanets (as of 2017), plotted in Figure 1.1, proves how small planets outnumber the others, but it also highlights an observed scarcity of planets with $1.5R_\oplus \lesssim R_\text{p} \lesssim 2R_\oplus$, the so-called *radius gap*, which may be attributed to photoevaporation-driven mass loss (Fulton et al., 2017);

[1]The snow line is a boundary in a planetary system beyond which temperatures are low enough for volatile substances such as water, methane, and ammonia to condense into solid ices.

- **Earth-type planets** - They have radii and masses comparable to Earth's ($R_\mathrm{p} \lesssim 1R_\oplus$, $0.5M_\oplus \lesssim M_\mathrm{p} \lesssim 2M_\oplus$), and are primarily composed of dense, rocky materials, featuring solid surfaces and very thin atmospheres. Earth-type exoplanets are of particular interest for their potential to host life as we know it, beyond our Solar System.

1.2 Detection and characterization techniques

Many techniques have been employed to successfully discover exoplanets over the course of the last three decades, which are here listed in order of efficiency (i.e. the percentage of exoplanets discovered, as evaluated on the NASA exoplanet archive):

- Pulsar timing ($\ll 1\%$) - Supernovae often leave behind ultra-dense remnants known as pulsars, which are neutron stars that emit radio waves at precisely regular intervals, depending on their rotation speed. If a pulsar hosts one or more planets, the gravitational pulls alter the timing of these signals, making it possible to indirectly infer their presence. Similarly, planets can be inferred by measuring deviations from periodic activities of other variable stars;

- Astrometry ($\ll 1\%$) - Observing the position of a star in the sky, over the course of time, can reveal motion changes due to the gravitational influence of one or more planets. This method has not been very successful so far, but things have started to change with the beginning of the Gaia space mission (Gaia Collaboration, 2022);

- Direct imaging ($\approx 1\%$) - Exoplanets can be directly seen by capturing the light they either reflect from their host stars or emit as thermal radiation. Resolving planets close to their star is very difficult, however, the reflection and emissions of planets on extended orbits can be unveiled by blocking the overwhelming starlight (for instance by using the equivalent of a coronagraph). The planet radiation can span from being approximately a thousand times fainter than the host star itself for a HJ observed in the infrared, to more than a billion times fainter for Earth-like planets observed in the visible spectrum;

- Gravitational microlensing ($\lesssim 4\%$) - A star can act as gravitational lens for another, distant star in the background, because the gravitational field of the former bends the light coming from behind (relatively to our line of view) and magnifies it, when the foreground and background stars are nearly perfectly aligned to the observer[2]. This alignment typically lasts for a few weeks or months, and a planet orbiting the lensing star may cause magnification anomalies (depending mostly on its mass and position), which can be measured to infer the planet's properties;

- Doppler method ($\lesssim 20\%$) - Since a star is also orbiting around the overall center of mass of its system, periodical variations in its RV (calculated from the Doppler effect in stellar spectral lines – refer to Section 2.1), or the speed at which it moves towards or away from us, can outline the presence of planets (see Section 1.2.1);

[2]Deforming the background light into a so-called *Einstein ring* shape (Pinochet and Jan, 2018), in case of perfect alignment (usually on cosmological scales, when a massive galaxy cluster acts as a gravitational lens).

- Transit method ($\approx 75\%$) - The probability that the planet's orbit intersects our Line-of-Sight (LoS) is small, but when that happens the planet passes in front of its host star disk and temporarily causes a drop in luminosity that is proportional to the planet size (see Section 1.2.2);
- Transit timing variations (TTVs) ($\lesssim 1\%$) - Planets in the same system perturb each other's orbits, leading to small variations in the times of transit and thus allowing for the indirect detection of other companions.

Every method has its own observation biases and can reveal only a specific set of the planet's properties, so they are often complementary. In the following subsections, only the Doppler and transit methods are going to be covered in depth, because they are the most successful methods by far and they are central to the work done in this PhD thesis.

1.2.1 Doppler method

Stars move on their own orbits in response to the gravitational pull of any planetary (or stellar) companions, leading to displacements that are difficult to detect on the celestial plane (unless the companion is massive; either a star or a gas giant, see Gaia Collaboration 2022). On the radial axis, however, such tiny movements induce a convenient change in the star's spectral line position due to the Doppler effect. In fact, even if the speed of the star around the system's center of mass might be relatively small, the periodical shift of the lines towards red and blue light is potentially measurable and can reveal such companions. For instance, Jupiter is forcing the Sun to move around its center of mass by about 12 m/s, while Earth is contributing only by 9 cm/s, and the best modern spectrometers can reveal signals down to ≈ 0.3 m/s (see Section 1.5.2), so they are definitively precise enough to spot Jupiter-like planets around Sun-like stars, but not Earths on a 1 year-long orbit. In this context, the inclination of the orbital plane of the companion relative to our LoS (i), is of fundamental importance because when i is perpendicular to our LoS, the movement of the star is confined to the celestial plane only, and viceversa when i is parallel to our LoS the full displacement is projected on the radial axis. For this reason, the Doppler method presents a degeneracy between the mass of the companion and the inclination of its orbital plane, in the sense that we can only measure their combination $[M_{\rm p}\sin(i)]$.

For a planet orbiting around its host star, the equation of motion is given by simply substituting the force of gravitational attraction, between the two bodies, into Newton's second law of motion. The bounded solutions of the differential equation are ellipses, and their orbit is given, in planar polar coordinates, by the function (see e.g., Bozza et al. 2016):

$$r(\nu) = \frac{a(1-e^2)}{1+e\cos(\nu)} \tag{1.1}$$

where the polar angle $\nu(t)$ is the so-called true anomaly (refer to Figure 1.4), and is a function of time (note that *anomalies* are just the historic names of the angles used to describe the motion of planets). Two other anomalies are the eccentric one, $E(t)$, and the mean one, $M(t)$. While the eccentric anomaly can be seen as the angle traced by the planet in the case of a circular orbit,

the mean anomaly is more difficult to physically interpret as it increases linearly with time and measures the percentage of the area of the ellipse that is spanned by the position vector:

$$M(t) \equiv \frac{2\pi}{P}(t - T_0) \tag{1.2}$$

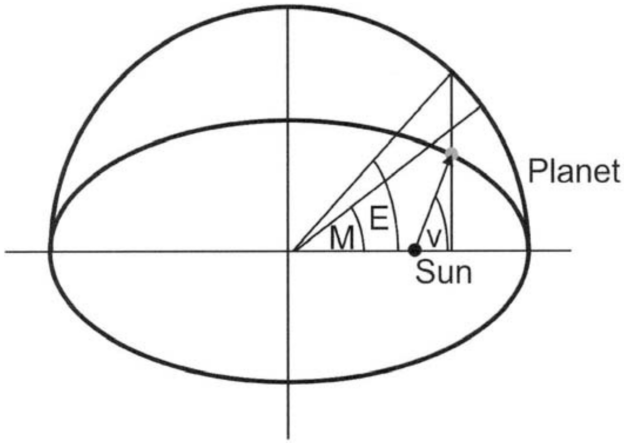

Figure 1.4: Schematic of an eccentric planet orbiting around its parent star, located in one of the focal points. The larger semi-circle represents the orbit as if it was circular with radius equal to the semi-major axis, while ν, E and M are the so-called true, eccentric and mean anomalies respectively. Figure courtesy of Varvoglis 2006.

where T_0 is the time of periastron passage. Finding the relations between the anomalies requires a bit of algebra (see Murray and Dermott 1999), but doing so allows us to find the velocity of the star:

$$V = r\frac{d\nu}{dt} = \frac{2\pi a^2\sqrt{1-e^2}}{rP}\frac{M_{\rm p}^2}{(M_s + M_{\rm p})^2} \tag{1.3}$$

which projected onto the radial axis becomes:

$$V_r = \frac{M_{\rm p}}{M_s + M_{\rm p}} \cdot \frac{2\pi a \sin(i)}{P\sqrt{1-e^2}}[\cos(\nu(t) + \omega) + e\cos(\omega)] = K \cdot [\cos(\nu(t) + \omega) + e\cos(\omega)] \tag{1.4}$$

where the systemic velocity μ_0, the overall radial velocity of the barycenter, has been removed as it is irrelevant for the planetary mass determination. K is the semi-amplitude of V_r, that we can express using Kepler's third law:

$$K = \frac{M_{\rm p}\sin(i)}{(M_s + M_{\rm p})^{2/3}} \cdot \frac{(2\pi G/P)^{1/3}}{\sqrt{1-e^2}} \propto M_{\rm p}\, P^{-1/3} M_s^{-2/3} \tag{1.5}$$

and it depends on the inclination, periodicity, eccentricity of the orbit and the mass of both the planet and its host star. From Eq. (1.5) it is straightforward to understand why the Doppler method is more sensitive to massive and/or short-period exoplanets. Note that V_r is always periodic but it can differ from a sinusoidal function when the orbit is not circular (see Figure 1.5). In short, the RVs allow us to derive the "minimum mass" of the planet, $M_{\rm p}\sin(i)$, the orbital period P, its eccentricity e and the argument of periastron ω, the time of periastron T_0 and the bulk velocity of the system μ_0 (sometimes also referred to as V_0 or γ). The Doppler method can produce false signals, mostly due to star magnetic fields or various types of stellar activity that cause periodic RVs. In such cases, it is important to estimate the star rotation period, for example through many different activity indexes

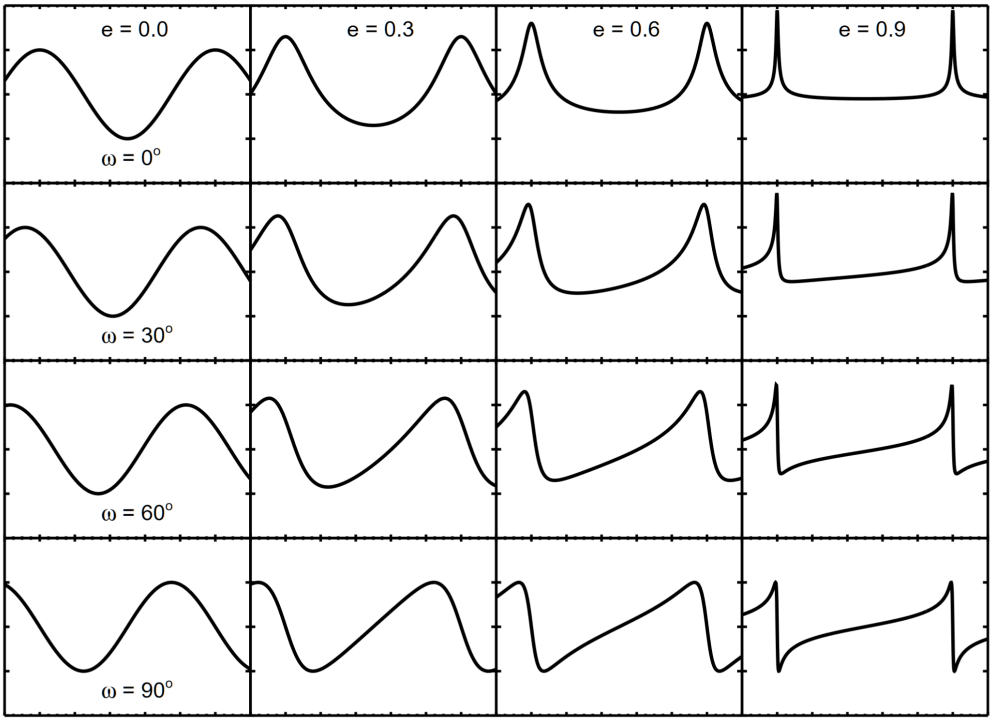

Figure 1.5: RVs as a function of time, estimated in the case of orbiting companions with the same mass, orbital period and time of conjunction, but different eccentricity and argument of periastron. The eccentricity (argument of periastron) is the same for every column (row). Figure courtesy of Wright and Gaudi 2013.

(refer to Section 1.4.3), in order to infer whether the RV signals are truly coming from planets or not.

Despite the high precisions that dedicated spectrographs can reach today, the Doppler method is less efficient compared to the transit method, whereby many stars can be observed at once and consequently the probability of finding exoplanets is higher. Furthermore, high Signal-to-noise ratio (SNR) spectra are often required to measure K-signals with high precision, so this method is mainly used for bright (or relatively nearby) stars. For these reasons, nowadays RVs are mostly used to confirm and characterize exoplanet candidates detected through other methods, rather than find them through dedicated surveys, as was done in the early years of discoveries (though many RV surveys are still happening).

1.2.2 Transit method

For any exoplanet, assuming that the inclination of its orbital plane compared to our LoS, i, is unknown, the probability that in our viewpoint it partially eclipses its own star is given by the fraction of celestial sphere swept by the penumbra of the planet itself (refer to Figure 1.6). The apparent separation between the center of the planet and the star (i.e. the impact parameter, b – refer to Figure 1.7) can be approximated by (Winn, 2010):

$$b = \frac{a\cos(i)}{R_s}\left(\frac{1-e^2}{1+e\sin(w)}\right) \xrightarrow[e\to 0]{} \frac{a\cos(i)}{R_s}\,, \tag{1.6}$$

where e, w are the eccentricity and the argument of periastron, while R_s and a are the radius of the star and the planet's orbital semi-major axis. The opening angle of the cone that sweeps out the

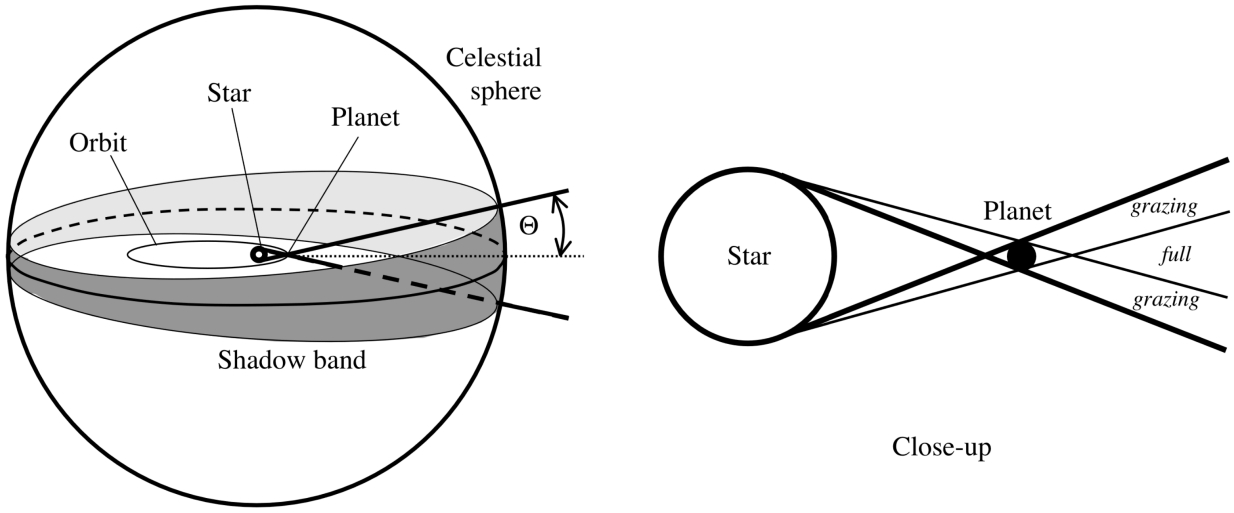

Figure 1.6: The planet projects a penumbra on the celestial sphere within a cone of opening angle Θ (left panel). A close-up of the transit geometry (right panel), shows how the transit might be seen by a random observer located far away on the right, i.e. either as a full transit or grazing one according to the actual position of the observer on the celestial sphere. Figure courtesy of Winn 2014.

shadow band on the celestial sphere (i.e. the region of visibility), Θ, can instead be defined as:

$$\sin(\Theta) = (R_s \pm R_\mathrm{p})/a\,, \tag{1.7}$$

where R_p is the planet's radius and the plus or minus sign indicate whether the transit is grazing or full. Since $\cos(i)$ is uniformly distributed for a randomly-placed observer, the probability of, at least, a grazing eclipse is the fraction of celestial sphere swept by the cone:

$$P\left(|b| < 1 + R_\mathrm{p}/R_s\right) = \frac{\int_{-(R_s+R_\mathrm{p})/a}^{(R_s+R_\mathrm{p})/a} d\cos(i)}{\int_{-1}^{+1} d\cos(i)} = \frac{R_s + R_\mathrm{p}}{a} \xrightarrow[R_s \gg R_\mathrm{p}]{} 0.5\% \left(\frac{R_s}{R_\odot}\right)\left(\frac{a}{1\,AU}\right)^{-1}, \tag{1.8}$$

or roughly half a per cent for exoplanets orbiting around Sun-like stars at a distance of 1 astronomical unit (au). This chance does increase for close-in planets, which together with the fact that it takes less observing time to find a short-period planet, clearly explains why the transit method is strongly biased towards finding them. When the planet is eclipsing the star (refer to Figure 1.7), if the SNR is high enough, depending especially on the observing instrument setup, a drop in brightness flux (Δf) can be appreciated. At astronomical distances, the overall depth of transit (δ) is only dependent on the object radii:

$$\delta = \frac{\Delta f}{f} \approx \left(\frac{R_\mathrm{p}}{R_s}\right)^2, \tag{1.9}$$

which means that the sensitivity of a transit survey is overall biased towards large-radii planets with short orbital periods. As a point of reference, an Earth-size planet transiting a Sun-like star would present a transit depth of only 0.08%, so it would require an extremely precise instrumental setup on top of 1-2 years of continuous observing time to discover and confirm if $P_{orb} \approx 1$ year. In reality, the shape of a transit is rounded (see the difference between the right side and the left side of Figure 1.7), because the limb-darkening effect makes the central part of the star disk appear brighter than the edge (limb) due to an increase in effective optical depth. More precisely, if the

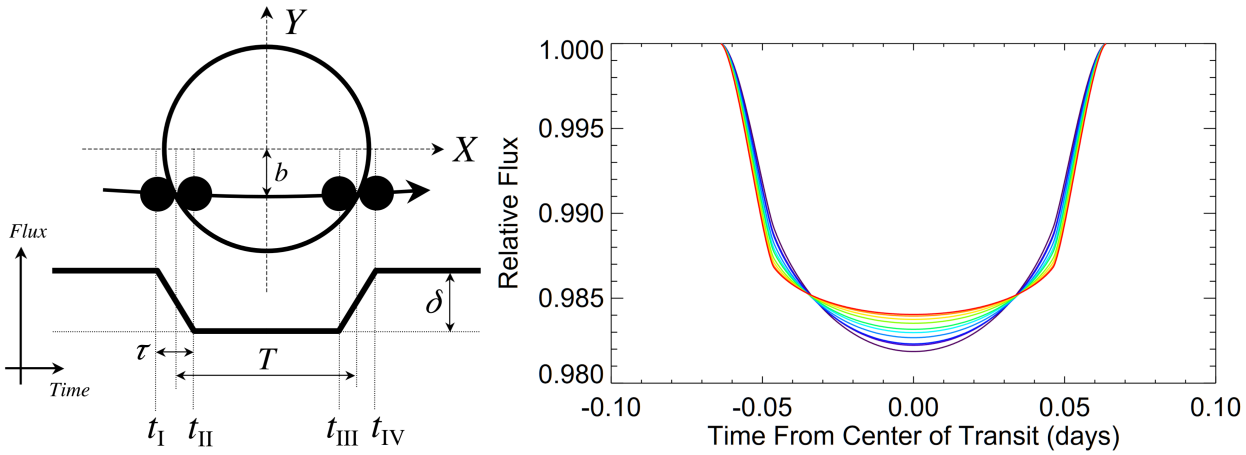

Figure 1.7: On the left, a transit is illustrated as seen from the observer, together with its simplified light curve, showing several useful quantities used in this work (figure courtesy of Winn 2014). On the right, the actual light curve shapes for ten different bandpasses, including the limb-darkening effect (figure courtesy of Knutson et al. 2007).

intensity seen from the center of the star is I_0 then the intensity seen in the direction ϕ can be expressed, for instance, with a quadratic law:

$$I_\phi / I_0 = 1 - u_1 \left[1 - \cos(\phi)\right] - u_2 [1 - \cos(\phi)]^2 \ , \tag{1.10}$$

where (u_1, u_2) are the Limb Darkening Coefficients (LDCs) that depend on the host star properties (effective temperature, metallicity, surface gravity) and the photometric band selected for observing the transit. In order to minimize the correlation between u_1 and u_2 and only sample realistic physical values, in this work the LDCs are fitted with the Kipping parametrization (q_1, q_2), which also allows for a more efficient sampling scheme (see the full details in Kipping 2013):

$$\begin{aligned} q_1 &\equiv (u_1 + u_2)^2 \\ q_2 &\equiv \frac{u_1}{2(u_1 + u_2)} \, . \end{aligned} \tag{1.11}$$

Thus, using the mean intensity $I_m = \frac{\int I_\phi d\omega}{\int d\omega}$, i.e. the sum of the intensities over the disk divided by the solid angle subtended by the disk itself, the depth of the transit can more realistically be described by:

$$\delta \approx \left(\frac{R_\mathrm{p}}{R_s} \right)^2 \frac{I_\phi}{I_m} \, . \tag{1.12}$$

Besides the transit depth (i.e. the radius of the planet, if we can evaluate the size of the star, see Section 1.3), and the orbital period, the transit light curve also provides the ingress/egress duration τ and transit duration T ($t_{IV} - t_I$, or $t_{IV} - t_I - \tau$ according to different definitions), which can be used to find the impact parameter b, the orbital inclination i and the scaled semi-major axis a/R_s (for a full set of calculations, refer to Perryman 2018).

False alarms and false positives

However, the transit method is not without its challenges. Whether conducting ground-based or space-based surveys, researchers must assess the likelihood that the observed transits are genuinely

planetary in origin. Two common issues that we must grapple with to ensure the reliability of our findings are false alarms and false positives; the former happen when transit-detection software generates a signal that surpasses the detection threshold, yet no actual transits are present, while the latter are authentic transit-like events, but of different astrophysical origin. The transit validation usually involves comparing the probability that the transits result from planets against the likelihood of transit-like events originating from other sources. Astrophysical false positives come in various forms, each requiring distinct validation strategies, the most common of which are (Brown, 2003):

- A low-mass stellar companion: In close stellar binaries with significant size disparities, low-mass stellar companions (e.g. white or brown dwarfs) can produce flat-bottomed transits similar to planetary transits. The presence of deep secondary eclipses and the self-luminosity of the smaller star may distinguish them;
- A Grazing Eclipsing Binary (EB): These systems involve two stars with similar mass and radius, inclined in a way that they exhibit grazing stellar eclipses that can be mistaken for planetary transits. Differences in effective temperatures and color indices can be indicators of grazing binaries, along with V-shaped transit model fits which often yield high values for the impact parameters;
- A Blended EB: Chance alignments of a bright, isolated star with a fainter, background EB can lead to diluted eclipses that mimic planetary transits. Detailed modeling, along with factors like inconsistent effective temperatures and wavelength-dependent eclipse depths, can reveal such impostors;
- A hierarchical triple: These systems resemble blended EBs, but the faint EB and the brighter diluting star are part of a physically associated triple system. Detecting shifts in the light centroid during eclipse events is very challenging but could in principle reveal hierarchical triples, along with spectroscopic follow-up.

High angular-resolution imaging (see Section 1.5.3) is often necessary to validate transits and distinguish between genuine planetary transits and the various types of astrophysical false positives, offering a cost-effective solution due to its minimal observing time requirements. On the contrary, a more resource-intensive and expensive approach involves directly determining the mass of the companion through the measurement of RVs and TTVs.

1.3 Host star and exoplanet characterization

A precise study and characterization of exoplanets cannot be dissociated from an investigation of their host stars. As we have seen, transit and RV measurements only provide the planet's radius and mass relative to the stellar ones. Consequently, the accuracy of the planets' properties (mass, radius, density, age) critically depends on the achieved accuracy of the hosts' properties. This is the reason why *TESS* was designed to observe bright and close stars (see Section 1.5.1), so that they could be better characterized compared to the dimmer stars observed by the Kepler mission (which greatly contributed to the exoplanetary field nonetheless).

1.3.1 Stellar parameters

High-resolution spectroscopy involves a detailed analysis of the shape, intensity and position of the spectral lines in a star's spectrum. By comparing these features to theoretical models and established classification systems, we can derive the stellar effective temperature, T_{eff}, surface gravity, $\log g$, metallicity (e.g. the iron abundance [Fe/H]) and spectral type. Conversely, both stellar masses and radii in principle can be estimated by exploiting empirical relations with luminosity or parameters such as T_{eff}, $\log g$ and [Fe/H] (Torres et al., 2010). However, empirical relations often lack accuracy mostly due to limited and noisy data, age variability, and limitations in generalization. A more direct and precise estimation of the radii can for instance be achieved by measuring the apparent angular size of stars in the sky using interferometry, provided that their distance (or parallax) is known with great accuracy. For distant stars a direct angular diameter measurement is very challenging, and interferometry is often not available, therefore the stellar radii can more consistently be estimated by fitting the stellar Spectral Energy Distribution (SED) (i.e. the energy emitted by the star as a function of wavelength). Provided that magnitudes (fluxes) of different bandwidths are available for a specific star, the SED can be reconstructed (right panel of Figure 1.8) by imposing Gaussian priors on the already derived T_{eff} and [Fe/H], and comparing the fluxes with theoretical values, accounting both for the interstellar extinction rate and the distance of the star, optimally retrieved again from accurate parallaxes. Fortunately, thanks to the *Gaia* mission we now have very precise distances for many stars, compared to just a few years ago (see Section 1.5.4).

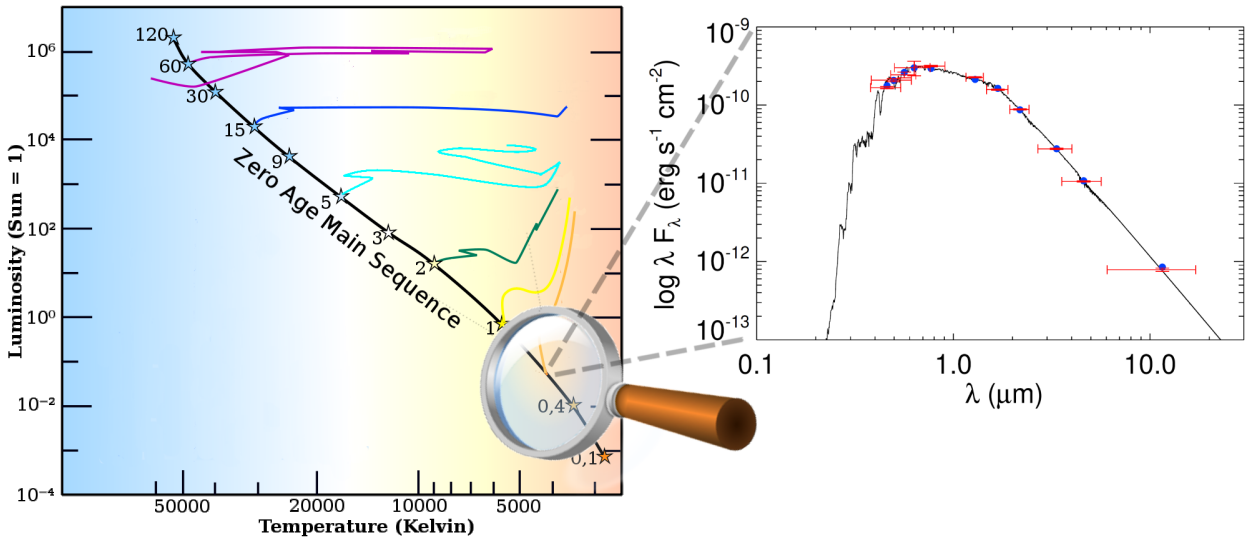

Figure 1.8: On the left, the evolutionary tracks of stars with different starting masses are plotted on top of the Hertzsprung–Russell (H-R) diagram, starting from their main-sequence phase (figure adapted from D'Antona and Mazzitelli 1994). The sun in yellow, for instance, will become a Red Giant (RG) before expanding further into the Asymptotic Giant Branch (AGB). On the right, an example of fitted SED (for TOI-1853, a K2-V star, see Chapter 5).

Unlike binary systems, where very precise dynamical masses can be derived either with astrometry or spectroscopy, the mass of single stars can be accurately estimated by comparing the stellar observed properties (i.e. T_{eff}, [Fe/H] from spectroscopy and the stellar luminosity from the SED fit and *Gaia*

parallax) with expected stellar evolution tracks and isochrones (H-R diagram[3] curves of stars of the same age). The stellar evolutionary tracks are a set of mathematical models based on our current understanding of stellar physics, which provide a comprehensive picture of how the star changes throughout its lifetime. Therefore, by fitting stellar models such as Y2 (Demarque et al., 2004) (but also PARSEC, Dartmouth, MIST, etc), we can infer the stellar physical properties, i.e. radius, mass and age. The estimation of stellar ages are very valuable, since they are pivotal in evaluating the timescales of star-planet interactions and the evolution of planetary physical and orbital parameters.

The procedure described above has been used in Naponiello et al. 2022 and Naponiello et al. 2023, where the values of the stellar radius (R_s), mass (M_s) and age (τ_s) have been determined by first extracting the atmospheric parameters of the star from the HARPS-N spectra and then incorporating them as Gaussian priors in the fitting process of both the SED and evolutionary tracks. Finally, it is important to note that different evolutionary tracks usually yield very consistent values (though low-mass stars are always more difficult to reproduce), and that the realistic uncertainties of SED + evolutionary tracks fitting, derived by taking into account the differences among stellar models, typically are $\delta R_s/R_s \approx 1-3\%$, $\delta M_s/M_s \approx 3-6\%$ and $\delta \tau_s/\tau_s \approx 20-100\%$ (Tayar et al., 2022) for solar-type stars, or larger for M stars (especially τ_s).

Asteroseismology

It is a relatively recent insight that the star interior is a stage for the propagation of sound waves that can be mostly detectable photometrically (see e.g., Handler 2013). The study of such oscillations is called asteroseismology and is of fundamental importance for understanding stellar structures because their individual frequency and amplitude correlate with the physical state (temperature, chemical composition) of the various layers that these waves pass through. Non-radial oscillation modes are classified into "p modes" (located in the envelopes) when the pressure force is dominant in restoring the equilibrium of the perturbed star, "g modes" (located in the deep interiors) when the buoyancy force of Archimedes is the restoring agent, and mixed modes, usually present in evolved stars only. In analogy to the vibration modes of a 1D string, the modes of a star can be characterized by their frequency, amplitude and number of nodes (i.e. points where the *string* does not move during the vibration cycle), with the only difference being that three integer numbers are needed to indicate the positions of the nodes in a star, instead of one. Thus, for each mode, the nodes are indicated by three labels (l, m, n), where $l = m = 0$ indicates that the fluid elements in the star are displaced in the radial direction only. The highest frequency of the acoustic nodes defines the upper boundaries of the p-mode resonant cavities and can be expressed as (García and Ballot, 2019):

$$\nu_{max} \propto \frac{M_s}{R_s^2 \sqrt{T_{eff}}}\,, \tag{1.13}$$

[3]Stars have varying evolutions and lifetimes depending on their initial mass; for instance they start as protostars and eventually become main-sequence stars through nuclear fusion. Stellar evolution is studied by observing stars at different stages on the H-R diagram. This diagram displays stars' luminosity against their surface temperature, and helps astronomers categorize stars into various stages of their evolution, providing insights into their life cycles and characteristics.

while the large-frequency separation (refer to Figure 1.9) is:

$$\Delta\nu_l = \nu_{n+1,l} - \nu_{n,l} \approx \Delta\nu \propto \sqrt{\frac{M_s}{R_s^3}}\,, \tag{1.14}$$

which highlights the link between the oscillations and the stellar physical properties.

Non-radial oscillations make parts of the star move up while others move down with a mode-dependent periodicity (and a timescale of a few minutes only), provoking changes in the temperature and radius of the stellar gas. Stellar surfaces, with the exception of the Sun, cannot be resolved enough to study these oscillations, so their signature is hidden in the stellar quantities integrated over the stellar disk, such as the brightness flux (or RV variations responsible for noise in the doppler shift). However, the symmetry axis of the oscillations may be inclined with respect to the LoS of the observer, which may cause partial or complete cancellation of the photometric variability (note that this does not happen spectroscopically because the integrated velocity is not very sensitive to limb darkening). Measuring such small flux variations during an oscillation cycle has become possible thanks to the low noise, low cadence, and long-uninterrupted time series data provided by exoplanet space mission surveys such as Kepler (e.g. Yu et al. 2018) and *TESS* (e.g. Handberg et al. 2021), for stars up to magnitude ≈ 15. In particular, asteroseismology will play a central role for the *PLATO* space telescope, which is supposed to launch in 2026 and will search for planetary transits while also detecting host star oscillations (refer to Chapter 6) and thus measuring stellar physical properties with increased precision in order to better characterize the found exoplanets.

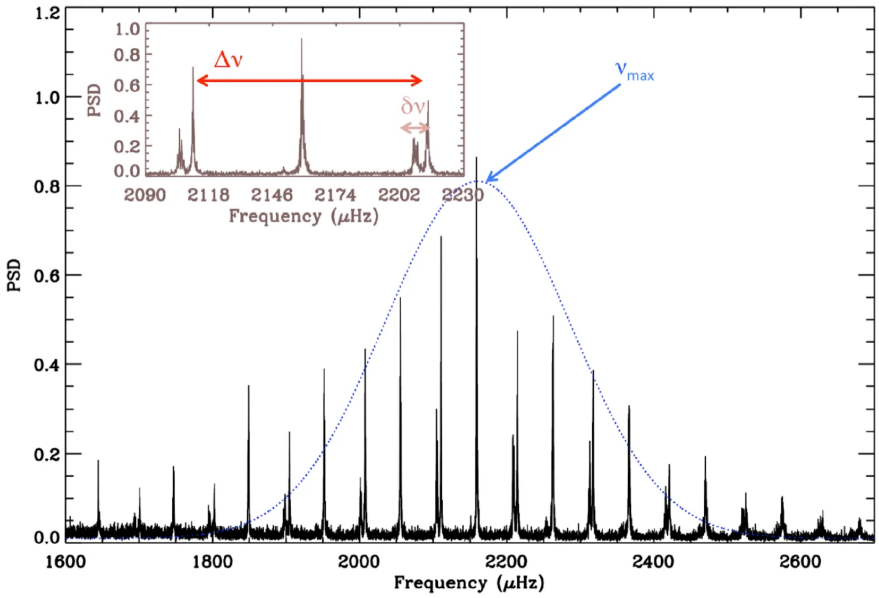

Figure 1.9: Power spectrum density as a function of frequency for a Kepler target. A blue dotted line shows the Gaussian fit employed to obtain the frequency at maximum power, while the inset on the top-left is a zoomed version that shows the large frequency separation between two consecutive modes (at angular degree $l = 0$) along with the small frequency separation $\delta\nu$. Figure courtesy of García and Ballot 2019.

1.3.2 Exoplanet bulk densities and compositions

While the distributions of mass and size, extracted mainly from transit and Doppler surveys, provide valuable insights into the relative occurrence of planets of different types (granted that precise evaluations of both host stellar masses and radii have also been performed, as discussed above), connecting these two properties remains a challenge because planets of similar size can exhibit significant variations in mass. In order to comprehensively understand exoplanets, we must estimate their bulk density, as this information is essential for inferring potential compositions and internal structures. Fortunately, for planets that transit relatively bright stars, the mass-radius degeneracy can be resolved by combining the transit and Doppler methods (see Section 2.6 for a description of the joint analysis), or the same can be done for multiple transiting systems exhibiting extensive TTVs. Several studies have harnessed these well-characterized planets to investigate the Mass-Radius (M-R) relation empirically, as recently done by Otegi et al. 2020 (refer to Figure 1.10). By being able to place an exoplanet on an M-R diagram, researchers gain the means to infer compositions consistent with the observed data, considering a wide range of possible configurations, including variations in the proportion of ice, rock, gas, or other constituents. The inferred compositions are the result of a comparison between the exoplanet's observed radius and mass and theoretical models of planetary structure, which consider factors such as the planet's equilibrium temperature, surface gravity and the presence of atmospheres. For example, a low-density exoplanet positioned on the diagram may suggest a composition rich in volatiles, such as water or hydrogen-helium (H/He), while a high-density placement could indicate a rocky composition, although often very different compositions are compatible with the same object (see the case of TOI-1853 b in Chapter 5). The M-R relation is then a crucial tool for statistically exploring exoplanet demographics, offering valuable insights into the internal structure and, consequently, the physical and chemical processes governing planet formation and evolution, such as planetary migration, atmospheric loss, and inflation mechanisms.

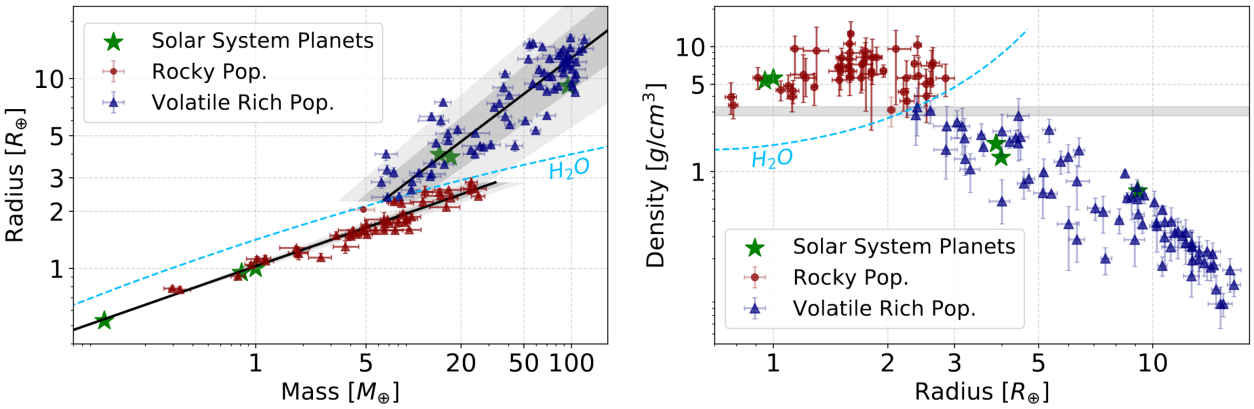

Figure 1.10: On the left, two different M-R relations are derived by fitting rocky (in red) and volatile-rich (in blue) populations of well-characterized exoplanes under 120 $M_\oplus$, along with the solar system planets in green. The grey and light-grey envelopes represent the $\pm 1\sigma$ and $\pm 2\sigma$ regions of the fit. On the right, the bulk density of these planets is plotted over their radius. In both plots, the dotted cyan line corresponds to the composition line of pure water (at 300 K and 1 bar). Figure courtesy of Otegi et al. 2020.

As a matter of fact, Fig. 1.10 visually illustrates the two distinct exoplanet populations identified in Otegi et al. 2020. The *rocky* population closely mirrors an Earth-like composition for planets up to approximately 25 $M_\oplus$ (super-Earths). However, between 10 and 25 $M_\oplus$, these worlds seem to

be slightly less dense, suggesting the possibility of ice-rich cores (yet not fully volatile-rich). This observation supports the notion that this upper mass limit corresponds to the maximum core mass attainable during giant planet formation, as theoretically predicted (see Section 1.6.1), although it's worth noting that new, challenging dense exoplanets have been discovered since this study (see Chapter 5). The second population, characterized by less dense planets with a more volatile-rich composition (Neptunes), exhibits a significantly larger dispersion in mass and radius. This dispersion suggests various core masses accumulating gas or potential influences from other parameters (like insolation, which could lead to atmospheric loss). However, despite the existence of the radius gap (Fulton et al., 2017), which implies a distinct transition between super-Earths and sub-Neptunes between 1.5 $R_\oplus$ and 2 $R_\oplus$, these two exoplanet populations display considerable overlap in mass and radius. Notably, the composition line of pure water at a temperature of 300 K and a pressure of one bar (i.e. a water world without an atmosphere, see Otegi et al. 2020 for the full details about the equation of state) can serve as a demarcation between the populations. Additionally, there appears to be a density cutoff around ≈ 3 g cm^{-3}.

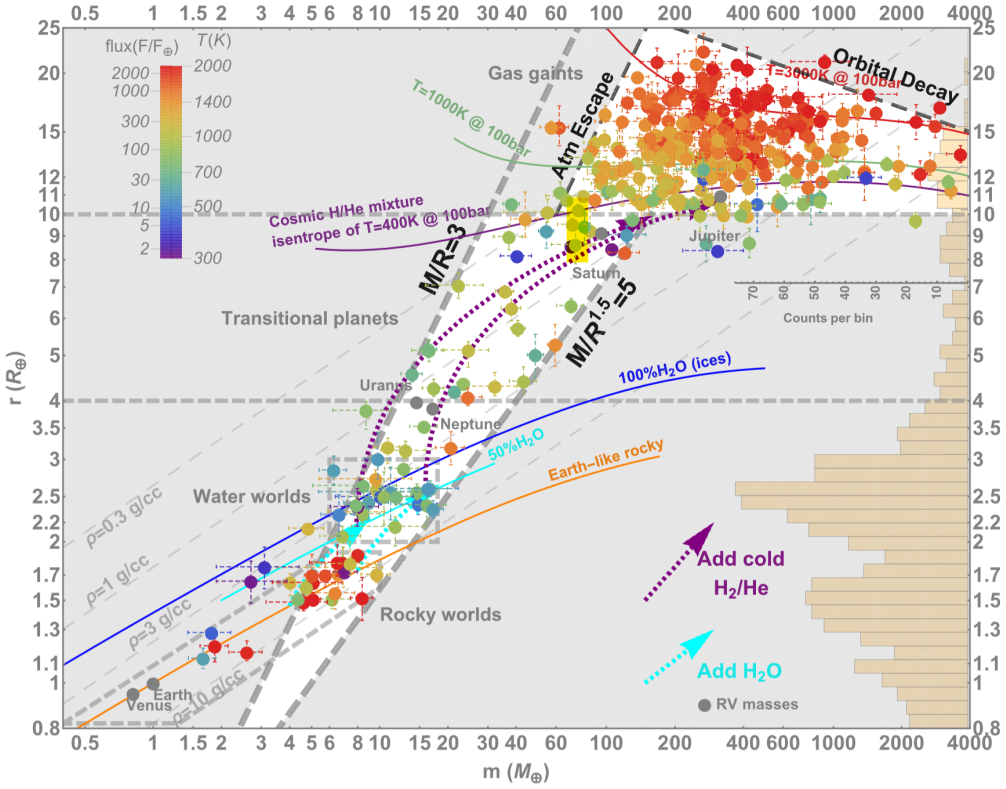

Figure 1.11: Radius-mass diagram for exoplanets with densities constrained to better than ±50% (as of 2019). The color of the points is a measure of equilibrium temperature, as indicated by the legend on the top left. The labeled lines are isodensity curves. The log-binned radius distribution is shown as a histogram on the right y-axis and the dotted cyan and purple arrows show the growth trajectories of planets formed by the addition of either H_2O ices or H_2/He gas to a planetary core. Figure courtesy of Zeng et al. 2019.

Nevertheless, estimating the density alone may not suffice to deduce the internal structure of an exoplanet, particularly for intermediate planets. Different structural configurations can yield the same bulk density (refer to Figure 1.11 for a general overview). Moreover, density estimation often carries substantial uncertainties. To break this degeneracy and avoid ambiguous conclusions about

compositions, studying atmospheric composition through transmission or emission spectroscopy (as discussed in Section 1.3.3) can be invaluable. Analyzing the composition of exoplanets and their atmospheres draws upon our understanding of the most abundant dusty and molecular constituents in protoplanetary disks and our solar system. Iron and silicates are the primary refractory constituents, while water is the dominant volatile expected to exist in either a solid or liquid state. Planets with sufficiently high escape velocities and low temperatures should be capable of retaining atmospheres of essentially primordial gaseous composition. In contrast, smaller planets, if they retain atmospheres at all, are likely to possess atmospheres with a relatively high mean molecular weight.

1.3.3 Exoplanetary atmospheres

Atmospheres are the keys to unlocking exoplanets' formation and evolution history. Fortunately, during a transit event, some of the light from the star passes through the planet's atmosphere before reaching us, while when the planet itself is eclipsed, there is a small change in brightness due to the lack of both planet thermal emission and reflection (see Figure 1.12). In the first case, we can exploit transmission spectroscopy to infer the chemical composition of an exoplanet's atmosphere, by measuring how transit depth, which is wavelength-dependent, changes through the observed spectrum. In order to do so, the light curve is binned into different spectrophotometric channels and fit separately. Any variation in transit depth as a function of wavelength arises from the transmission of starlight through the planet's atmosphere, and the amplitude of these spectral features is related to the atmospheric scale height H (i.e. the altitude over which density and pressure fall by a factor of e^{-1}). Using eq. 1.9 we can approximate such amplitudes as (see e.g., Kreidberg 2018):

$$\delta_\lambda = \frac{(R_\mathrm{p} + n_\lambda H)^2}{R_s^2} - \left(\frac{R_\mathrm{p}}{R_s}\right)^2 \approx 2 n_\lambda R_\mathrm{p} H / R_s^2 \,, \tag{1.15}$$

where n_λ is the number of scale heights crossed at wavelength λ. From the ideal gas law, assuming hydro-static equilibrium, the scale height is $H \propto T_{eq}/(\mu g)$, so we can assume that targets with low surface gravity (g), low atmospheric mean molecular weight (μ), high equilibrium temperatures (T_{eq}) and relatively large radii (R_p/R_s), are the best targets to observe, with spectral features that can reach amplitudes of $\delta_\lambda \approx 0.1\%$.

On the other hand, the thermal structure of the atmosphere can be appreciated by exploiting emission spectroscopy. When the planet passes behind the host star, the measured photometric flux is due only to the star (f_s) and can be used as a baseline, so that any increase in flux (f_p) when the planet comes back into view, is traced back to the planet's thermal emission and reflection. Hence if $B(\lambda, T)$ is the black-body spectral radiance at temperature T, as a first-order approximation the relative thermal emission is:

$$\frac{f_p}{f_s} = \frac{B(\lambda, T_p)}{B(\lambda, T_s)} \left(\frac{R_\mathrm{p}}{R_s}\right)^2 . \tag{1.16}$$

This ratio is much larger at longer wavelengths because stars are hotter than planets. At the same time, T_p is dependent on the wavelength because the planet-emitted light comes from higher altitudes at more opaque wavelengths and viceversa. Therefore, the temperature-pressure profile can be inferred from the amplitudes, positions and shapes of the spectral features. Instead, reflected

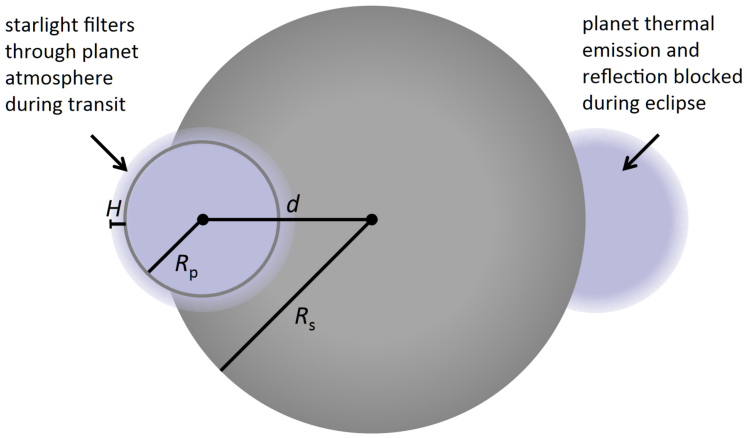

Figure 1.12: Geometry of transit and secondary eclipse during transmission and emission spectroscopy measurements. The planetary height scale H is shown to highlight the fact that the starlight is also partially passing through the planet's atmosphere. Figure courtesy of Kreidberg 2018.

light is more easily detected at optical (or short) wavelengths, but in general it has a lower amplitude compared to thermal emission. If $\Phi(\alpha)$ is the reflected light intensity at phase angle α, and A_g is the geometric albedo (i.e. the ratio of planet reflection relative to that of an ideal mirror), the total reflected light flux is (see e.g., Kreidberg 2018):

$$f_{ref} = A_g(R_\mathrm{p}/a)^2\Phi(\alpha). \tag{1.17}$$

A special subset of planets are the short-period ones, because in a relatively short time span they get tidally locked to their host stars (i.e. their rotation period tends to be equal to their orbital period), and so one half of the planet is always illuminated, all-while reaching higher temperatures and emitting more thermal radiation. For them, it is also feasible to take continuous photometric and/or spectroscopic measurements over the entire orbit, in order to observe all the longitudes of the planet in succession (obtaining a so-called *emission phase curve*). Furthermore, their emission spectra can be disentangled from the total spectrum thanks to a rapid orbital speed that causes a measurable Doppler shift during the full orbit (see e.g., Pino et al. 2020).

However, clouds and hazes influence the chemistry, radiation transport, total energy budget and advection (i.e. the transport of a substance by bulk motion of a fluid) of a planet's atmosphere. Their existence, and our ability to model them, are two major limitations in interpreting exoplanetary spectra and retrieving accurate molecular abundances, since condensates can either weaken or entirely mask spectral features, depending on the clouds' height (Fortney, 2005), even though the scattering opacity is greatly reduced in the infrared. The atmospheric temperatures of hot exoplanets allow for the condensation of many components, including silicates, while sulphur-bearing compounds are expected in cooler atmospheres. Given that clouds are widespread in the Solar System, it was reasonable to assume the same for exoplanets, and in fact almost all exoplanets, or at least the hot ones currently amenable to transit characterization, exhibit some level of cloud cover (Sing et al., 2015). A compelling example is the completely flat transmission spectra of the super-Earth GJ 1214 b (Kreidberg et al., 2014). As a final note of caution, transmission spectroscopy might be influenced in a non-trivial way by wavelength-dependent starspots (the starspot

contrast for example is higher at shorter wavelengths) and stellar activity regions in general (see, e.g., Fournier-Tondreau et al. 2023). For a brief description of stellar activity refer to Section 1.4.

Nevertheless, the use of transmission and emission spectroscopy is expected to increase dramatically with the launch, in 2029, of the Atmospheric Remote-sensing infrared Exoplanet Large-survey (*Ariel*) space telescope (Tinetti et al., 2021), whose principal mission will be to observe the primary and secondary eclipses of at least a thousand known exoplanets, in order to characterize their chemical composition and thermal structure at high precision. Compared to the *JWST*, which became operative last year (in 2022) and is already doing these kinds of observations occasionally (Lustig-Yaeger et al., 2023), *Ariel* will have much more observing time, albeit with a much smaller mirror.

1.3.4 Architecture of exoplanetary systems

The structure of our Solar System is characterized by eight nearly circular, coplanar orbits with low mutual inclinations, a quasi-geometric progression in orbital spacings, and a hierarchical mass distribution. Its architectural organization has long served as a foundational framework for theorizing and comprehending planetary formation and evolution. Similarly, comprehending the intricate dynamics of exoplanetary systems and gaining insights into their formation and evolution demand a comprehensive exploration of their architectural properties. For starters, multi-planetary systems are expected to feature dynamical resonances, much like the Solar System. Mean-motion resonances occur when planetary orbital periods are related by simple integer ratios (e.g., 2:1 or 3:2), while secular resonances involve long-term interactions leading to variations in orbital parameters (see e.g., Veras and Ford 2010), including orbital spacings. These resonances are primarily driven by various forms of apsidal motion (libration, circulation, or transitional states) and can result in complex interactions that significantly influence the long-term stability and evolution of planetary systems, altering in particular the values of eccentricity and mutual inclinations over extensive timescales.

Determining the number of planets per star is a challenging task due to sensitivity limitations and selection biases. Moreover, the concept of *Kepler dichotomy* emerged as soon as researchers sought to decipher the connection between the multiplicity of Kepler planetary systems and their mutual inclination distribution (Zhu and Dong, 2021). Two distinct populations of systems were revealed, a smaller one with low mutual inclinations and compact configurations (similar to the Solar System), and a larger one with single transiting planets, which was significantly underpredicted by early modeling efforts (by nearly 50%). It's still unclear wether the majority of the single transits are due to high mutual inclinations or really one-planet systems, even if the fraction of systems showing TTVs has been proved to be relatively consistent between the two (Zhu and Dong, 2021). Collectively, different exoplanet statistical analyses together indicate that systems with small planets (with orbital periods $\lesssim$ 1 year) are generally as coplanar as the Solar System (Winn and Fabrycky, 2015), though overall it still remains unclear whether the architecture of the Solar System is a common archetype or an exception. Nevertheless, geometric progressions and mean-motion resonances have been identified in multi-planetary systems. Notably, for planet pairs with a combined mass exceeding 1 Jupiter mass, there is an observed clustering within the 2:1 resonance that appears unlikely to result from mere statistical fluctuations (Wright et al., 2011). For lower-mass planets,

the situation becomes more intricate, with a tendency to avoid exact resonances (see Figure 1.13). Instead, these systems often exhibit period ratios slightly larger than the resonant values (Fabrycky et al., 2014). This phenomenon may be related to tidal dissipation within the inner planet, driving the orbits to expand. Additionally, the presence of many low-density planets in compact systems ($\lesssim 1$ g cm^{-3}, see e.g., Lissauer et al. 2013) offers hints about their formation and/or stability, since closely packed systems are more prone to dynamical instability, and massive planets are more likely to eject one another, while smaller planets are more likely to collide until the system stabilizes (Ford and Rasio, 2008).

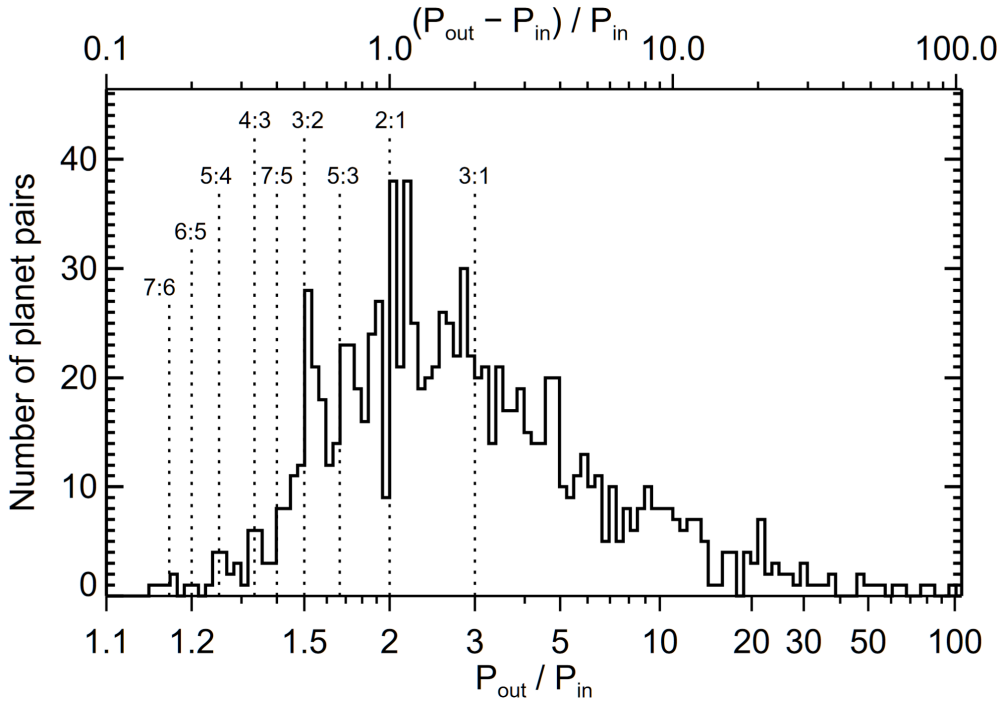

Figure 1.13: Period ratios of Kepler planet pairs. Figure courtesy of Winn and Fabrycky 2015.

In this context, orbital eccentricities further serve as valuable clues for understanding the evolutionary history of exoplanetary systems. The Solar System's remarkable coplanarity is considered compelling evidence that planets originated within a flat, rotating disk, as there are today no apparent mechanisms for damping inclinations. However, highly inclined exoplanetary systems might exist on shorter timescales, with large mutual inclinations leading to the excitation of eccentricities and eventual orbital crossings, culminating in system destruction (due to the Kozai-Lidov instability, see Lubow and Ogilvie 2017). Therefore, examining eccentricity as a function of other orbital parameters can offer valuable insights into the statistical properties of the exoplanet population. For example, two studies by Van Eylen et al. (2019) and Mills et al. (2019) both confirmed that single transiting planets have a higher mean eccentricity, and the latter also suggested that planets with higher eccentricities tend to orbit stars with high metallicity. This tentative relationship could be attributed to the fact that high metallicity environments favor the formation of giant planets, and interactions between giant planets and inner systems can excite eccentricities while simultaneously reducing the apparent multiplicity of close-in planets, because they are subject to mutual inclination excitation (Mustill et al., 2017).

Any mechanism influencing the eccentricity of planets, whether small or giant, may also alter their orbital orientations in space. Therefore, determining the angle between a planet's orbital axis and its host star's spin, referred to as spin-orbit obliquity, becomes a pivotal parameter for analysis. Determining the obliquity is a challenging task, as direct observation of the star's rotation and the planet's orbit is not feasible, however it can be indirectly estimated (see the following subsection). This measurement holds for instance the potential to elucidate the relative roles of the two main mechanisms that act to shrink the orbits of giant planets (see Section 1.6.2): planet-planet scattering and disk-planet interactions.

Rossiter–McLaughlin effect

The light coming from the side of a star that is rotating towards our LoS is blue-shifted and, conversely, the light coming from the side that is rotating away is red-shifted. During a primary eclipse, a transiting planet covers different portions of its host star, thus the measured RVs can be offset depending on how long the transiting planet spends on one side over the other. The shape of this so-called Rossiter-McLaughlin effect (McLaughlin, 1924, Rossiter, 1924) then contains information about the sky-projected spin-orbit angle λ (refer to Figure 1.14), other than the rotational speed of the star, the relative size of both star and planet, and the impact parameter. Over the years, this technique has proven to be crucial for the orbital characterization of planetary systems, as the angle λ, or rather the true spin-orbit angle Ψ, can be used to study for instance the interaction, via tidal forces, between a star and its planets. The angle Ψ is related to λ by the relation (see e.g., Triaud 2018):

$$\cos(\Psi) = \cos(i_s)\cos(i) + \sin(i_s)\sin(i)\cos(\lambda)\,, \tag{1.18}$$

so it requires knowledge of i_s, the inclination of the stellar rotation axis in the sky. In theory, i_s can be determined knowing the rotation period of the star and using $\nu \sin(i_s)$, the projected star rotational velocity on the equator (obtained for example through the spectral-synthesis technique, see Biazzo et al. 2022), but this estimation carries on the, usually high, uncertainty of the stellar rotation period. As a first-order approximation, the semi-amplitude of the Rossiter-McLaughlin effect is:

$$A_{RM} \approx \frac{2}{3}\left(\frac{R_\mathrm{p}}{R_s}\right)^2 \nu \sin(i_s)\sqrt{1-b^2}\,. \tag{1.19}$$

From Eq. (1.19) we can deduce that this effect is hard to detect on relatively small transiting exoplanets revolving around stars with low $\nu \sin(i_s)$ (i.e. either non-active stars or stars that we see pole-on, with $i_s \approx 0$). The observation sampling is especially important, because if it's too low, relatively to the duration of the transit, the number of measurements may not be sufficient to reveal an event that could last only ≈ 30 minutes in the worst case (for very short-period planets). On the other hand, the Rossiter-McLaughlin effect is hard to detect on long transits (long-period planets) which can outlast the duration of any observing night. If we define two distances, x_1 and x_2, as shown in Figure 1.14:

$$\begin{aligned} x_1 &= \sqrt{1-b^2}\cos(\lambda) - b\sin(\lambda) \\ x_2 &= \sqrt{1-b^2}\cos(\lambda) + b\sin(\lambda)\,, \end{aligned} \tag{1.20}$$

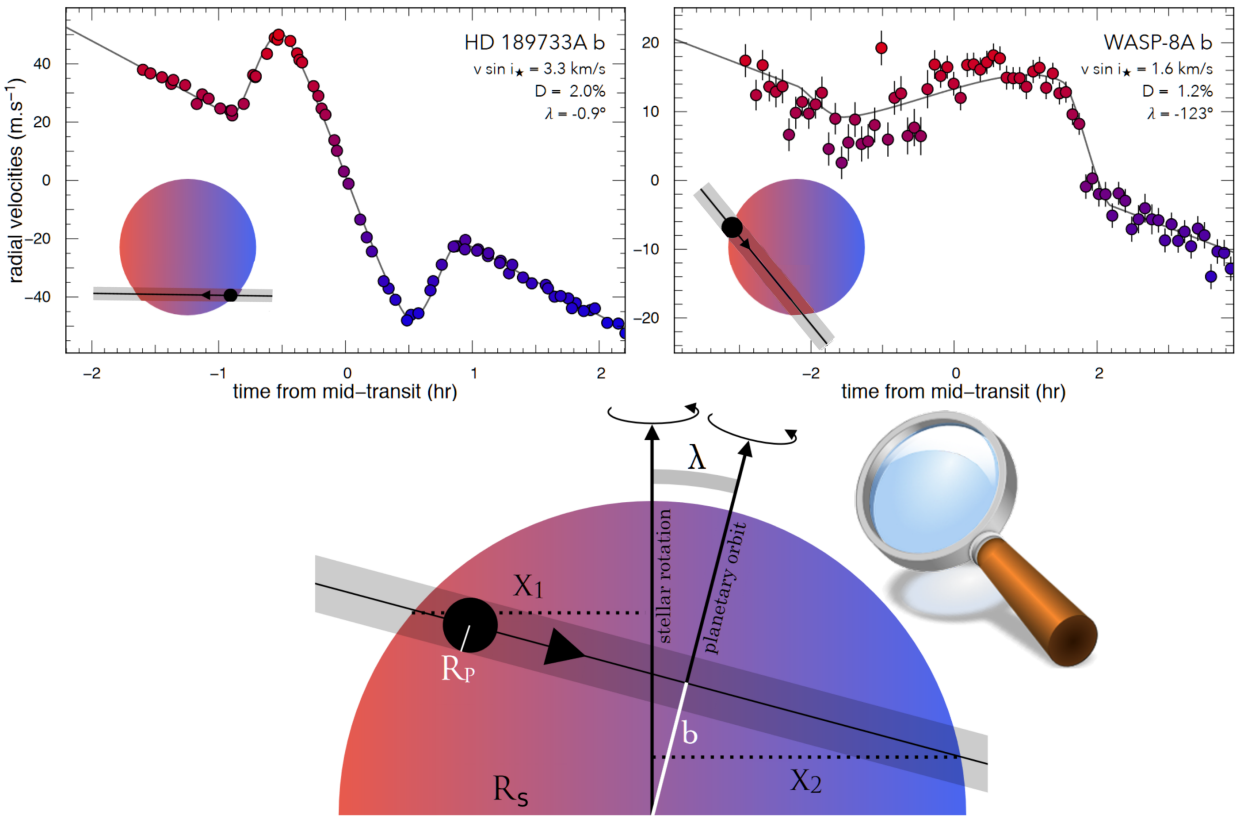

Figure 1.14: The top-left and top-right panels show the Rossiter-McLaughlin effect obtained for HD 189733 b and WASP-8 b, two transiting HJs, with the HARPS spectrograph. The RV points are colored based on the absolute red/blueshift. A visual representation of the derived orbits is shown in each panel, while a larger generic version is pictured on the bottom to highlight various important parameters. Figure adapted from Triaud 2018.

then we can measure the semi-amplitude of the Rossiter-McLaughlin effect and the asymmetry between both extrema by using:

$$\begin{aligned} \frac{1}{2}\nu\sin(i_s)(x_1+x_2) &= \sqrt{1-b^2}\nu\sin(i_s)\cos(\lambda) \\ \frac{1}{2}\nu\sin(i_s)(x_1-x_2) &= b\nu\sin(i_s)\sin(\lambda)\,, \end{aligned} \tag{1.21}$$

where the dependence on λ is finally explicit. However, from these equations, a degeneracy is clearly evident between $\nu\sin(i_s)$ and λ when the impact parameter, b, is very small because the planet always covers both sides of the star in the same amount of time regardless of how large λ is.

1.4 The impact of stellar noise

Of fundamental importance for both host star and exoplanet characterization is a thorough understanding of the various sources of stellar noise that can pollute RV or photometric measurements.

1.4.1 RV noise

The main sources of noise for RV measurements are p-mode oscillations (discussed already in Sect. 1.3.1), granulation and stellar magnetic activity (Chaplin et al., 2019). To begin with, the RV

amplitude of p-mode oscillations can be a few centimeters or a few meters per second (for solar-like stars it is typically $1-2$ m/s, see e.g. Bozza et al. 2016) and their timescale is $5-15$ minutes, thus an optimal mitigation strategy for RVs is just to use exposure times of ≈ 15 minutes or averages of shorter exposures for bright stars which would otherwise saturate the CCD detector. Secondly, granules are convection cells omnipresent in the photosphere of stars, the deepest regions transparent to photons of a certain wavelength (i.e. the region we actually can see). They are caused by convection currents of plasma directly below the photosphere, in the so-called convective zone (the grainy appearance of stars is in fact produced by the tops of these convective cells and takes the name of *granulation*). At the center of the granules, the plasma is hotter (brighter) because the plasma is rising, while on the outer edge it is cooler (darker) as it is descending after being cooled at the surface, leading to a net convective blueshift. Below the photosphere, there is a layer of *supergranules* which are larger, longer-lived, and carry magnetic field bundles to the edges of the cells (presenting a great challenge to the detection of small planets, see, e.g., Meunier and Lagrange 2019). Overall, the correlated granulation noise can last between 15 minutes to 24 hours and can have RV amplitudes in the range $1-3$ m/s, depending on the spectral type of the star (Dumusque et al., 2010). Supergranulation excluded, the best observational strategy would be to obtain multiple (at least 2) RV measurements per night for each star, separated by one to two hours.

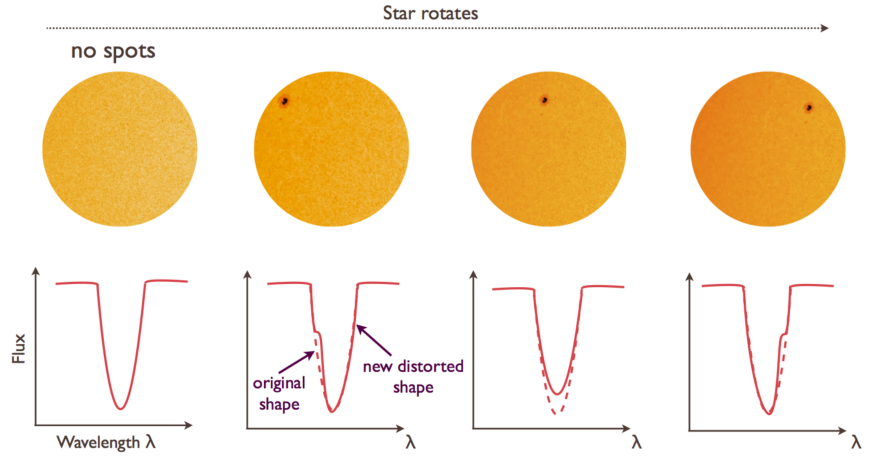

Figure 1.15: Diagram of a starspot crossing the stellar disc and its influence on the spectral lines symmetry, leading to variations in the RVs due to the blocked flux. Figure courtesy of R. Haywood (PhD Thesis, 2014).

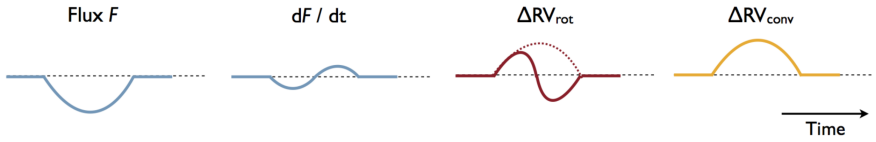

Figure 1.16: The effect of the passage of a starspot on the photometric flux (F) and its first time derivative (dF/dt). ΔRV_{rot} and ΔRV_{conv} are respectively the RV perturbation incurred by the simple presence of a spot on the rotating photosphere, and the additional effect of the suppression of the convective blueshift. Figure courtesy of R. Haywood (PhD Thesis, 2014).

Above all, the largest source of noise are stellar active regions, such as dark spots, dark filaments and bright faculae, which are areas of intense stellar magnetic activity. Due to their temperature contrast, these regions affect the shape of spectral lines (refer to Figure 1.15) and deform the cross-

correlation function (CCF) profile, which produces an offset in the RV extraction (done by fitting a Gaussian function to the CCF). The quenching of convective blueshifts in stellar active regions[4] also leads to extra RV variations (refer to Figure 1.16). In this context, stellar activity indicators (see Section 1.4.3) are valuable tools to identify periodicities associated with stellar activity or significant correlations with RV measurements (e.g. using the Pearson coefficient, see e.g. Freedman et al. 2007). However, stellar active regions vary spatially and temporally over one rotation period (short-term activity) or several rotation periods and activity cycles (long-term activity), therefore these variations are not strictly periodic and have prompted, in the last decade, the use of Gaussian Processs (GPs) for RV data analysis (refer to Section 2.5).

1.4.2 Photometric noise

For photometric measurements, the amplitude of p-mode oscillation noise lies in the range $0.1 - 0.3$ parts-per-thousand (ppt), and is typically negligible compared to photon noise. Similarly, the photometric granulation noise is also negligible as it amounts to $\approx 50 - 500$ parts-per-million (ppm). In contrast, the photometric noise due to stellar active regions can in some cases reach the high level of $\approx 1\%$. One way to treat this noise is to fit many transits together (assuming the out-of-transit flux constant), because planets might sometimes pass in front of an active region and cause a short drop or bump in the transit shape, respectively for bright and dark spots (refer to Figure 1.17 for a comparison between transits and RVs), and this distortion can be averaged out by using multiple events. Another way is to employ GPs in the analysis, similarly to what is done for RVs (refer to Section 2.5). Otherwise, the photometric impact of these regions can also be simulated and removed (using, for instance, specific spot models); however, there exists a strong degeneracy in determining the properties of the stellar active regions, making this task exceptionally challenging and computationally expensive. Lastly, for very active stars the situation is more complicated, as long transit durations might be comparable to the rotation period of the star (i.e. the stellar active regions move significantly during the course of a single transit) and even the out-of-transit flux can change considerably.

1.4.3 Stellar activity indicators

For the purpose of analyzing photometric or RV data contaminated by stellar noise, it's crucial to be able to estimate the level of activity of the star, which is inevitably linked to the stellar rotation period. For stars with efficient dynamo action, or deep enough sub-photospheric convective envelopes ($T_{eff} < 6500$ K), the most sensitive activity diagnostics of chromosphere magnetic activity are the cores of the Hα[5], Ca I (calcium) and Ca II H (396.85 nm) and K (393.37 nm) lines (for M-dwarfs, other valuable chromospheric spectroscopic indicators are Na I and He I). The flux ratio between the two bandpasses centered on the H and K emission cores and the two continuum region on either side, i.e. the so-called S-index, also has a practical value as it includes contributions from both the photosphere and the chromosphere. When we correct for the photospheric contribution

[4]Convective blueshifts are the shifts in the wavelengths of spectral lines of stars caused by convective motions in their atmospheres (involving the rising of hotter material to the surface). These blueshifts can be disrupted (*quenched*) by strong magnetic fields on the surface of the star.

[5]The Hα is a visible spectral line of the hydrogen atom (the first of the Balmer series) with a wavelength of 656.28 nm (deep-red).

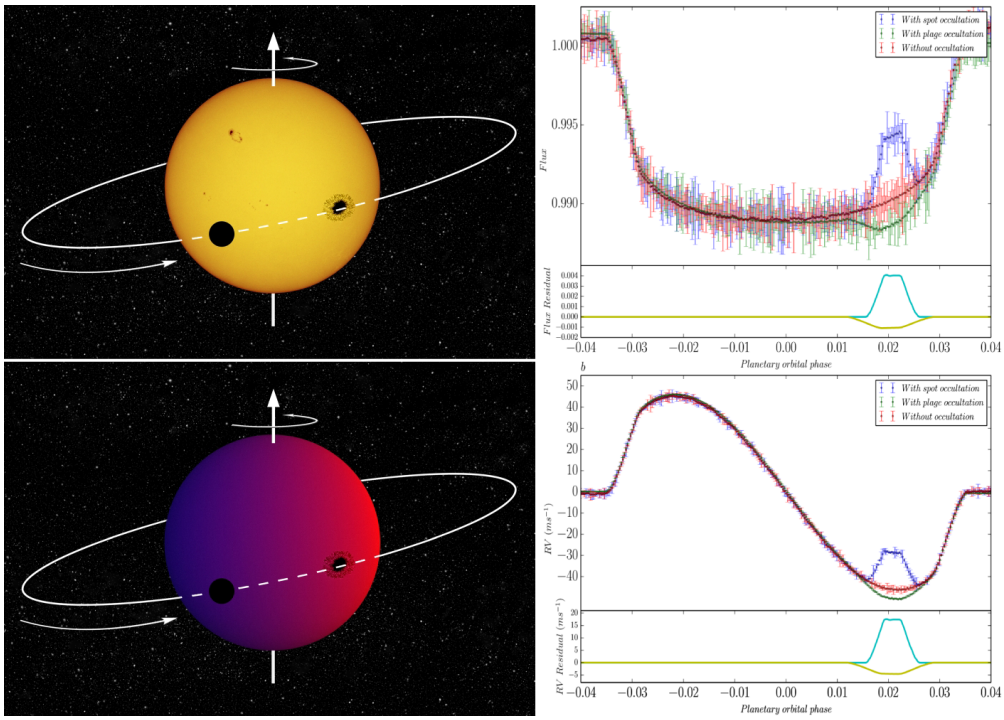

Figure 1.17: On the left, this figure showcases a photometric (top) and spectroscopic (bottom) observation of a transiting exoplanet, following a trajectory which eventually overlaps with a stellar spot. On the right, a simulated light curve (top) and RV variation (bottom) of a planetary transit (red) are shown along the anomaly curves due to the occultation of, respectively, a stellar spot (blue) and a plage (green; note however that the color is not linked to the observed band, as plages should only be seen in the blue one, see the emblematic case of Mohler-Fischer et al. 2013). Figure courtesy of Oshagh et al. 2016.

to the H and K lines, and normalize the chromospheric flux to the total (bolometric) luminosity of the star, we can further derive the so-called $\log R'_{\mathrm{HK}}$ activity index, which allows for a comparison of activity levels for different stars (see e.g. Oshagh et al. 2017).

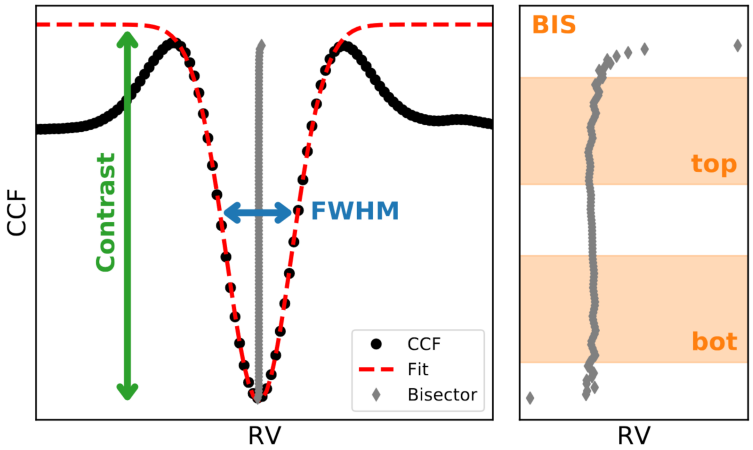

Figure 1.18: Visual representation of CCF activity parameters. A typical CCF for a star is shown by black dots, along with its best Gaussian fit in the red dashed line. The Contrast and Full Width at Half-Maximum (FWHM) are labeled in green and blue, while the Bisector is represented by gray diamonds. On the right, the central region of the CCF is zoomed in to show the bisector shape and the regions used to compute the Bisector Inverse Slope (BIS), by subtracting the average of bottom RV to the top ones. Figure courtesy of Lafarga et al. 2020.

For the photospheric magnetic activity the most commonly used line-profile (asymmetry) indicators are the FWHM, the Contrast and the BIS of the CCF (refer to Figure 1.18). The FWHM is used to represent the width of the star spectral lines (i.e. width of the line distribution at half the maximum intensity) and can be considered an indicator of starspots for solar-type stars. This is because the presence of spots leads to a reduction of the normalized line profile (refer to Figure 1.15), and consequently to an increase in the line-width to compensate and preserve the area (approximately, see Costes et al. 2021). The Contrast of the CCF refers to the ratio of the amplitude of the peak of the CCF to the surrounding noise level, and it is sensitive to star variability, line asymmetries, distortions and broadening due to stellar activity, as it quantifies the strength of the correlation signal in relation to the background noise. Conversely, the bisectors are the differences between the midpoints of the two halves of the Gaussian spectral line profile, and the BIS is obtained by fitting a linear regression to the bisectors and calculating the slope of the fitted line. Increase in stellar activity broadens the bisector span since the BIS is sensitive to velocity suppression and traces inhibition of convection in active regions (Costes et al., 2021).

1.5 Instruments

This dissertation would not have been possible without the use of state-of-the-art instrumentation, which will be briefly described in this section.

1.5.1 Space and ground-based photometers

TESS is the space telescope of NASA's Explorer program launched in April 2018 and it is designed to carry out the first all-sky transiting exoplanet survey in space (Ricker et al., 2014). Its primary mission objective was to survey the brightest stars (magnitude $5 \lesssim V \lesssim 12$ for spectral classes G, K, M) near the solar system (less than 200 pc away, or 30 pc for M stars) over a two-year period, but it has now entered its 5^{th} year and is on a second extended mission which will run at least for two more years. *TESS* is on a highly elliptical orbit ($e = 0.55$) around the Earth, with its further point being close to the distance of the Moon, and in a 2:1 resonance with the Moon itself in order to minimize the satellite destabilizing gravitational effect. This orbit is believed to be stable for at least one decade and allows *TESS* to downlink the data collected to Earth every 13.70 days, as it passes its

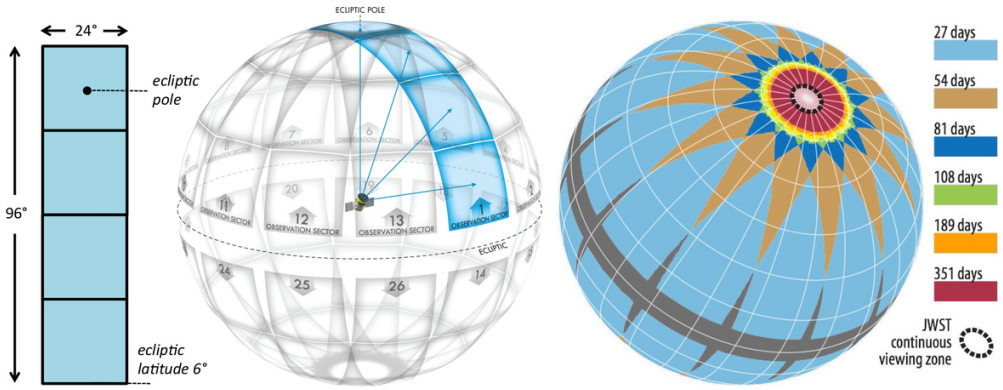

Figure 1.19: Diagram of the 26 sectors covered by *TESS* along with the overall coverage of the sky for the first two years of the mission (figure from the *TESS* instrument handbook).

perigee at a distance of 108 000 km. The survey was designed to observe many different sectors at a time, each one being $24° \times 96°$ thanks to four wide-angle telescopes each associated with an identical 16.8 megapixel Charged-Coupled Device (CCD) detector (of bandpass range 600-1000 nanometers or nm) at temperature -75° C, with an overlap at the ecliptic poles that allows for more sensitivity toward longer-period exoplanets in that region. This means that every two years (one for each hemisphere) *TESS* surveys more than 85% of the sky continuously almost for 27 days, or more where there are overlaps (refer to Figure 1.19). During this time the cameras take images every 2 seconds, but to deal with the limited store and downlink capabilities, cutouts around 15'000 selected stars per orbit (20 000 from the first extended mission) are coadded over a 2-minute period, while Full Frame Images (FFIs) are coadded over 30-minutes (10-minutes and 200-seconds respectively from the first and second extended mission). Starting from the first extended mission, up to a thousand selected stars per sector have also been monitored at a 20-second cadence (read more in Section 2.2).

TESS was built to reach a photometric precision of around 100 ppm for its full-frame images and around 60 ppm for the 2-minute cadence data. This level of precision is suitable for detecting Earth-sized and larger exoplanets around a wide range of host stars. However, it's important to note that the actual precision achieved in observations can vary from one target to another depending on several factors, including the target star's brightness, the instrument's stability, and the density of stars in the observed field. So far, *TESS* has discovered more than 7000 transiting exoplanet candidates (however only ≈ 400 of those have been confirmed to date), following a legacy of space-based exoplanetary transit surveys, each contributing significantly to our understanding of exoplanets. The earliest one, the Convection, Rotation, and Planetary Transits (COROT), was launched in 2006, designed to detect exoplanets and study stellar interiors. COROT discovered more than 30 worlds during its mission. Then, in 2009, Kepler was launched and provided exceptionally high-precision photometry, leading to the first burst of exoplanet discoveries, with thousands of statistically validated worlds. The mission continued as K2 in 2014, after the telescope encountered technical issues but continued to discover new worlds and conduct a variety of astronomical observations. Finally, CHEOPS launched in 2019, and it serves as a dedicated mission for characterizing known exoplanets, with a particular focus on determining their sizes with high photometric precision, complementing the work of other transit surveys like *TESS*.

The importance of observing transits from the ground is not to be undervalued. Once a space photometer, like *TESS*, finds an exoplanet candidate, ground-based telescopes can be used to follow-up the candidate as long as needed with higher resolution and different wavelengths. This allows us to check and optimize ephemerides, look for TTVs, rule out nearby EB-blend scenarios (see Section 1.2.2) and compare transit depths across multiple bands, which in the case of planets should be mostly comparable (as transit depths are achromatic, aside from minor changes due to a possible atmosphere). In this PhD work I have used light curves taken with the MuSCAT2 imager installed at the 1.52 m Telescopio Carlos Sanchez in the Teide Observatory (in g, r, i and z_s bands), the 0.61 m University of Louisville Manner Telescope (ULMT) located at Steward Observatory (through a Sloan-r' filter) and with the Las Cumbres Observatory Global Telescope (LCOGT) 1.0 m network note at Siding Spring Observatory (through a Sloan-g' band filter) as described in Chapter 5.

1.5.2 High-resolution échelle spectrographs

HARPS-N is an échelle spectrograph installed at the TNG, a 3.58-metre telescope located at the Roque de los Muchachos Observatory on the island of La Palma, Canary Islands (Spain) (Cosentino et al., 2012). HARPS-N is the northern hemisphere twin of the similar HARPS instrument installed on the ESO 3.6-metre telescope at La Silla Observatory in Chile, and it observes in the optical band (383-690 nm). In a standard grating, light of a single wavelength is diffracted to specific angles corresponding to higher orders, exploiting a number of slits with widths close to the wavelength of diffracted light, and the angular spacing between higher orders decreases. Instead, an échelle grating is a specialized type of diffraction grating with a lower groove density, optimized for high incidence angles and high diffraction orders which allow for increased dispersion of spectral features at the detector, leading overall to a better differentiation of these features. Échelle gratings intentionally exploit the overlapping of multiple higher orders, using a second dispersive element like a grating or prism, inserted perpendicularly as "cross disperser" (order separator), to separate the overlapping orders (see Figure 1.20). This configuration produces a spectrum consisting of oblique stripes with slightly overlapping wavelength ranges across the imaging plane.

In order to reach RV accuracies of $\approx$ 1 m/s (for stars with magnitude $V \approx 10$), HARPS-N has both high resolving power ($R = 115\,000$) and high-stability, which in Europe is matched only by Calar Alto high-Resolution search for M dwarfs with Exoearths with Nearinfrared and optical Echelle Spectrographs (CARMENES) (Quirrenbach, 2018). This is achieved by observing the target star and a reference spectrum (for example a thorium lamp) simultaneously using two identical optic fibre feeds, providing a Field of View (FOV) of 1 *arcsecond* ($1''$), while mechanically, the stability is assured by keeping the spectrographs in a vacuum vessel which is temperature-controlled to within 0.01 K. Reaching very low levels of RV scatter, i.e. below $\approx$ 1 m/s, however, is not only

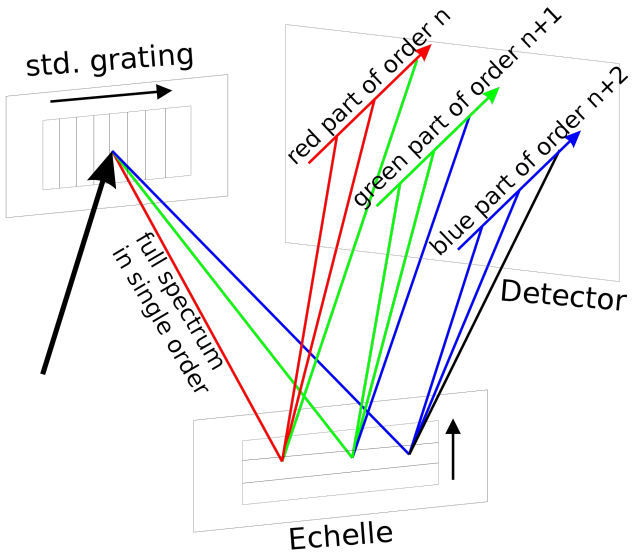

Figure 1.20: Illustration of an échelle spectrograph. The first, standard grating is optimized for a single lower order, while the échelle enhances the output intensity using multiple higher orders. The diffractive elements are mounted orthogonally, allowing for transversal separation of the highly illuminated échelle orders. This configuration ensures that only partial spectra of each individual order lie within the illuminated region, resulting in spectral overlap limited to specific sections (as shown by the green line in the red portion, and the blue line in the green portion). Figure courtesy of Heidt 2022.

a technological challenge because seismic pulsations (see Section 1.3.1) and star activity in general (see Section 1.4) can physically contaminate the data by producing comparable signals. As a result, so far only Echelle SPectrograph for Rocky Exoplanet and Stable Spectroscopic Observations (ESPRESSO) (Pepe et al., 2021), in the southern hemisphere, and EXtreme PREcision Spectrograph (EXPRES) (Jurgenson et al., 2016), in the northern hemisphere, managed to achieve a RV scatter of ≈ 25 cm/s on quiet stars for short periods of time, despite them being designed to consistently reach accuracies of 10 cm/s (thus making it potentially capable of measuring Earth-like RV signals). Other excellent échelle spectrographs used for exoplanet research include the one installed at the Automated Planet Finder (APF) (Vogt et al., 2014), a robotic telescope facility located at the Lick Observatory on Mount Hamilton in California, the NN-explore Exoplanet Investigations with Doppler spectroscopy (NEID) (Schwab et al., 2016), located at the Kitt Peak National Observatory in Arizona, the High Resolution Echelle Spectrometer (HIRES), which operates at the W. M. Keck Observatory in Hawaii (Vogt et al., 1994), the Spectrographe pour l'Observation des Phénomènes des Intérieurs stellaires et des Exoplanètes (SOPHIE) (Bouchy, F. et al., 2013, Perruchot et al., 2008), located at the Haute-Provence Observatory in France, and the Fiber-fed Extended Range Optical Spectrograph (FEROS) (Kaufer et al., 1999), installed at the MPG/ESO 2.2-meter telescope situated at ESO's La Silla Observatory. For the infrared, GIANO (Oliva et al., 2006) is also installed at the TNG on the island of La Palma in the Canary Islands, and the SPectropolarimètre InfraROUge (SPIRou) (Donati et al., 2018) is installed at the Canada-France-Hawaii Telescope on Maunakea in Hawaii.

1.5.3 High-contrast and high-resolution imagers

Survey telescopes, like *TESS*, usually have a large FOV because they are designed to observe as many stars as possible on the sky at the same time, and this usually involves having large pixels (the resolution for *TESS* is 20 arcsec/pixel). Since these pixels can gather light from many stars at once, it's not straightforward to realize which star is actually responsible for the detection of a transit-like event in specific *aperture* pixels. This means that until some form of validation is carried out, the exoplanet remains unconfirmed. Sometimes, there are background stars dim enough to go unnoticed but bright enough to *significantly* dilute the transit depth, so even if an exoplanet is confirmed (for example via RV), its radius (and density) may not be well-constrained. The same happens for binary/ternary systems where it is not known in front of which star the planet is transiting. In these cases, follow-up high-resolution imaging is fundamental to either confirm or characterize exoplanets, and this can be done from the ground with cutting edge Adaptive Optics (AO) systems, accomplished for instance by the NIRC2 instrument on the Keck-II telescope, and optical speckle imaging, accomplished by the 'Alopeke camera at Gemini North and the Southern Astrophysical Research (SOAR) telescope (see Chapter 5).

When the starlight is captured by a telescope, the consequent diffraction pattern is known to form a bright central spot, the Airy disk, inside which no multiple sources can be distinguished. Any group of objects whose images are closer together than the diffraction limit, appear as a single light source. While the angular resolution of a telescope can be enhanced by employing a larger main mirror (assuming the observed wavelength remains constant), which not only gathers more light but also enables the resolution of objects that are closer together when compared to a smaller

mirror, this improvement diminishes for mirrors larger than approximately 20 cm. This reduction in performance is due to practical constraints imposed by atmospheric conditions, as the random and turbulent nature of the atmosphere distorts the Airy disk, transforming it into a pattern of spots spread across a larger area. AO is an active technique that aims to compensate for light distortion with a deformable secondary mirror. In its simplest form, a wavefront sensor takes some astronomical light, then a computer measures the distortions due to the atmosphere and on a timescale of milliseconds (ms) the mirror is reshaped according to the corrections sent by the computer.

On the other hand, speckle imaging is based on the idea that the atmosphere is effectively *frozen* during a so-called *coherence time*, a value that is wavelength-dependent (10 or 100 ms respectively for visible and infrared light). This implies that for exposure times shorter than the coherence time, the movement of the atmosphere almost has no effect and the captured image is a snapshot of the atmospheric seeing at that instant. The obvious downside is that telescopes have to be large enough (or the stars bright enough) to capture sufficient starlight in a very short amount of time. Then, the final image can be reconstructed by putting together all the short-exposure images by a process of alignment (when only the best short-exposures are used, this process is called *lucky imaging*). Both AO and speckle imaging can produce images with angular resolutions of ≈ 30 milliarcseconds (mas) for stars of magnitude $V \approx 10$.

1.5.4 Space-based astrometer

Gaia, the queen of astrometry (Gaia Collaboration, 2022), is a space observatory that succeeded the Hipparcos mission (ESA, 1997) and was launched by the European Space Agency (ESA) in 2013 with the primary goal of measuring the positions, distances, and motions of stars with unparalleled precision. Gaia aims to construct the largest and most precise 3D space catalog, including approximately 1 billion astronomical objects (mostly stars) in the Milky Way, by continuously monitoring its target objects (i.e. observing each of them around 70 times over the course of its mission). Originally planned to operate for five years, Gaia's mission has been extended and will operate until the second quarter of 2025.

The spacecraft's spectrophotometric measurements yield detailed physical properties of observed stars (brighter than magnitude 20), including luminosity, temperature, gravity, and elemental composition. In particular, it is equipped with three main instruments: the astrometry instrument (Astro), the photometric instrument (BP/RP), and the Radial-Velocity Spectrometer (RVS). The astrometry instrument measures the angular position of stars, enabling the determination of parallax, distance, and proper motion. The photometric instrument acquires luminosity measurements of stars in a wide spectral band, while the RVS measures the velocity of celestial objects along the line of sight and provides information on temperature, mass, age, and elemental composition by analyzing high-resolution spectra. The precise parallax of Gaia allows for far better distance estimations (therefore better radius estimations for both parent stars and exoplanets), and its astrometric measurements can provide additional clues on the possibility that one or more host star inner companions may have gone undetected by high-resolution imaging. Astrometry also stands as an independent exoplanet detection technique (see Section 1.2), and Gaia is expected to find hundreds to thousands of giant exoplanets on wide orbits during its lifetime.

1.6 Planetary formation and migration in a nutshell

The study of planet formation has a long history, kicked off by Immanuel Kant (1755) and Pierre-Simon de Laplace (1796) through the formulation of the nebular hypothesis (i.e. the idea that the contraption of a gas nebula caused a higher concentration of materials in the center, and lead to the formation of the Sun and similarly then the planets in the debris disk). The initial models aimed to explain the properties of our own solar system, assuming that other planetary systems would have similar structures, but today the solar system still remains a benchmark for testing planet formation models due to the obvious wealth of information available. However, the discovery of exoplanets revolutionized our understanding of planetary systems. Types of planets that do not exist in the solar system have been found, such as super-Earths, sub-Neptunes and HJs (Section 1.1), which challenge the assumptions of previous models. This proves that exoplanetary systems can be dramatically different from our own, and modern planet formation models need to account for this diversity (see Section 1.6.1). Nowadays, the formation of planets is inferred also through the observations of other stellar systems and the combination of various pieces of information. Proto-planetary disks around young stars, for instance, play a crucial role in planet formation theory, as they provide the initial conditions and a case study for how planets interact with the disk. Understanding the physical and chemical properties of these disks is also important for determining the availability of solid materials and the timescale for giant planet formation.

In order of distance from the Sun, the solar system has four terrestrial planets, two gas giants and two ice giants, all spinning in the same direction as they orbit the Sun (with the exception of Venus and Uranus). The plane orthogonal to the total angular momentum of the system is almost aligned with the Sun's equator and all of the planets' orbits, which are almost circular. Despite this well-organized nature, the orbital structures of small bodies in the outer solar system indicate that there has been a period of dynamical instability involving the giant planets (Nesvorný , 2018) before they entered into mean motion resonance with each other. After the dissipation of gas from the proto-planetary disk, this instability might have increased the mutual separations, eccentricities and inclinations of the planets' orbits. Furthermore, to explain the relatively small mass of Mars and the depletion of the asteroid belt, it has also been proposed that Jupiter migrated inward to $\approx 1.5 - 2$ au, during the gas disk phase, before moving outward due to the influence of Saturn (Walsh et al., 2011), while outward migration of Neptune is believed to be responsible for the resonant capture of Pluto (and other asteroids) into a 3:2 resonance with the ice giant. Planetary migration can in fact lead to planets being captured in (chains of) orbital resonances, which however can be disrupted by turbulence in the disk, instabilities once the gas disk dissipates, interactions with leftover planetesimals or tidal interactions with the star. This theory contradicts a longstanding belief that the planets in our solar system formed in their current observed position.

However, the discovery of HJs and several smaller exoplanets with short orbital periods proves that orbital migration does occur, most likely when the gaseous disk is still present (see Section 1.6.2). Other scenarios can in principle explain HJs, such as mutual scattering of giant planets or in situ formation (see e.g., Poon et al. 2021), but the heavy-element enrichment observed in warm Jupiters and the existence of systems with medium-mass planets in resonance with each other (such

as the notorious case of TRAPPIST-1; see Grimm et al. 2018) strongly support the concept of migration. Furthermore, during the process of migration the star's radiation output undergoes significant variations, thereby exerting a substantial influence on the planet's evolutionary path. These variations can lead to phenomena such as atmospheric evaporation, dramatically impacting the planet's physical characteristics and overall fate within its planetary system.

1.6.1 Core accretion vs disk instability

The standard model for planet formation today is known as *core accretion* (Alibert et al., 2005) and it involves the build-up of a planetary core made of heavy elements, followed by the accretion of gas from the disk if present. According to this model, the formation begins in proto-planetary disks with the collision and aggregation of dust grains which stick to each other by electrostatic forces. Dust can form clumps due to various hydrodynamical effects (such as the *streaming instability*, e.g. Youdin and Goodman 2005), and gradually grows into larger pebbles ranging from centimeters to meters in size (see Figure 1.21). When such clumps become dense enough the dust can remain bound by self-gravity against the diffusion generated by turbulence, and eventually grow large enough to exert gravitational attraction on the surrounding material, which accelerates the growth until they reach the size of ≈ 100 kilometers (km). The question of whether the formation of a core is dominated by the accretion of planetesimals (large objects) or pebbles (small objects), remains unanswered (Helled and Morbidelli, 2021), but a combination of the two can likely explain the growth history of Jupiter (estimating its total heavy-element mass in $\approx 30 M_{\oplus}$). Within the proto-planetary disk, and beyond the snow line ($\approx 2-3$ au for Sun-like stars), where the tempera-

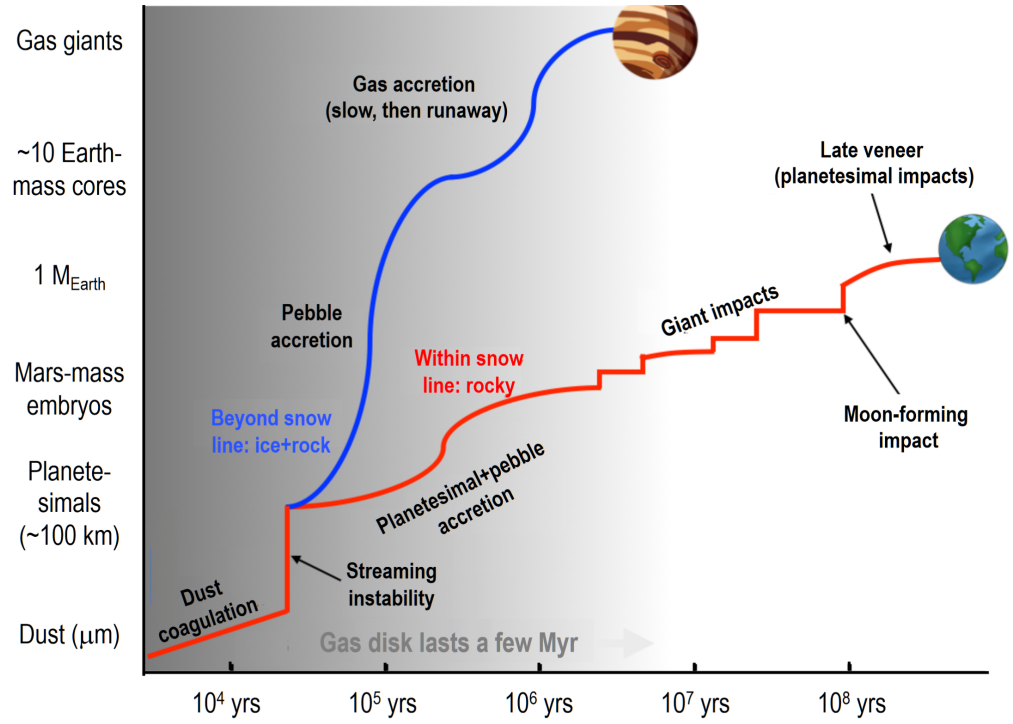

Figure 1.21: Schematic view of the different processes involved in the formation of gas giants and terrestrial planets. In our current understanding, the growth tracks of these planets diverge during the pebble accretion process, which is not very effective within the snow line. A number of important effects are not shown, such as the large-scale migration. Figure courtesy of Meech and Raymond 2005.

ture is low enough for water to condense into ice grains, any proto-planet can capture ice grains and grow faster. When the proto-planetary mass exceeds $\approx 2\,M_\oplus$, this process can lead to the formation of sub-Neptunes and Neptune-like planets with bound envelopes of H-He gas. Once the mass of the gaseous envelope becomes comparable to the heavy-element mass (both $\approx 10 M_\oplus$) the proto-planet starts accumulating gas rapidly through a process called *runaway accretion* (Pollack et al., 1996) that rapidly transforms it into a gas giant like Saturn and Jupiter.

However, the formation of intermediate-mass/size planets like super-Earths and sub-Neptunes, which appear to be extremely common (see Figure 1.1), remains challenging. If they are all born as Neptunes, they are expected to form at large distances, beyond the snow line, via pebble/-planetesimal accretion followed by inward migration (see Section 1.6.2). In this case, they should contain a large amount of volatile elements (like water), but many super-Earths and a couple of sub-Neptunes appear to have almost no atmosphere and be made of refractory elements, suggesting that they might have formed *in situ* instead, from the accumulation of refractory dust in the inner edge of the proto-planetary disk. In contrast, the formation of terrestrial planets requires collisions between proto-planets and has a longer timescale. Some exoplanets appear to have heavy-element mass fractions much higher than the ones predicted from standard formation models, therefore this enrichment can hardly be explained unless the stellar nebula was extremely metal-rich or giant impacts are invoked (see the case of TOI-1853 b in Chapter 5). For *giant* exoplanets, one explanation could be planetesimal accretion during inward migration (Kessler and Alibert, 2023).

An alternative paradigm for the formation of very massive planets is the *disk instability* model (see e.g., Lasota and Hameury 1998), which suggests that gaseous planets, similarly to stars, can emerge through local gravitational instabilities within distant, massive and cold regions of the proto-planetary disk, even if its effectiveness is still being investigated. In particular, when the local density and temperature conditions reach a critical threshold, the gravitational forces within the disk become dominant, causing the region to fragment into clumps or spiral arms (of several Jupiter masses). This threshold is usually expressed by the Safronov-Toomre criterion (Mayer et al., 2004):

$$Q = \frac{c_s\, k}{\pi G \Sigma} \tag{1.22}$$

where $Q < 1$ implies instability. Note that c_s is the speed of sound and is proportional to $T^{1/2}$ (where T is the temperature), G is the gravitational constant, Σ is the surface density of the disk and k is the epicyclic frequency, or the frequency at which a radially displaced fluid parcel oscillates. These clumps then continue to evolve as they accrete material and grow in size, but they also undergo further collapse and contraction until they become giant planets. If one or more clumps reach a point where their materials become dense and hot enough to trigger nuclear fusion, they become stars instead. The disk instability model is necessary to explain the occurrence of giant planets around M stars, the formation of planets a few times more massive than Jupiter, the presence of giant planets at large distances and the formation of planets in very short timescales. A correlation between the occurrence rate of giant planets and stellar metallicity has been widely observed (Johnson et al., 2010), and it aligns with the predictions of the core accretion model (though it may be explained with disk instability as well, see, e.g., Nayakshin 2015), but no such correlation has been proven

for very massive giant planets, which might imply that these are truly formed by disk instability instead.

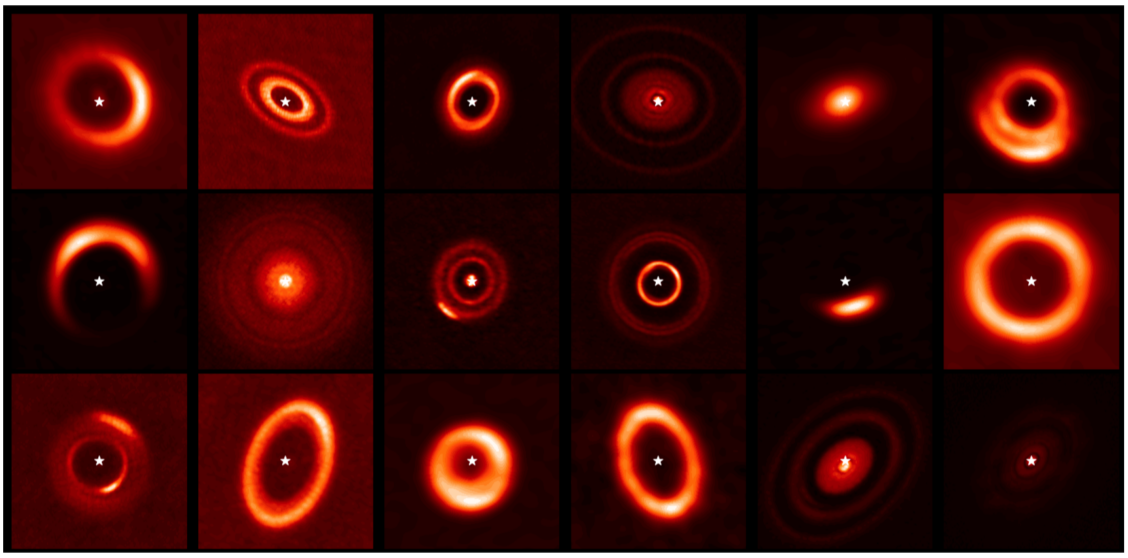

Figure 1.22: Proto-planetary disks observed with the Atacama Large Millimeter/submillimeter Array (ALMA) (Wootten and Thompson, 2009). Many different structures can be appreciated, such as gaps, rings, asymmetries and clumps. Figure courtesy of van der Marel et al. 2019.

1.6.2 Disk vs disk-free migration

Observations suggest that gas in proto-planetary disks can last a few to several million years (Ercolano and Pascucci, 2017). Disk migration is a phenomenon that occurs due to the gravitational force exerted by a massive body within such disk of gas (which in turn expresses a torque, or an equal and opposite force on the body), causing disturbances in its density distribution. This disturbance leads to changes in the planet's orbit, affecting its angular momentum and orbital elements. When the semi-major axis increases, the migration is called *outward*, whereas a decrease of the semi-major axis leads to *inward migration*. The disk migration can be split into three edge cases:

- **Type I disk migration** primarily affects small planets ($M_{\rm p} \approx M_{\oplus}$) and is driven by torques generated by *Lindblad* and co-rotation resonances (Binney and Tremaine, 2008), that induce spiral density waves in the gas disk around the planet. Compared to the inner spiral wave, the outer one exerts a stronger torque that causes a loss of angular momentum and forces the planet to migrate inward rather quickly (in $\lesssim 10^5\, yr$), but additional co-rotation torques and the density variations caused by the horseshoe paths followed by the gas (in the planet's reference frame, since the gas reverses direction when it approaches the planet) can also affect the angular momentum.

- When the planet is massive enough ($M_{\rm p} \approx 100\, M_{\oplus}$), it creates a gap in the gas disk (see Figure 1.22) and the planet undergoes **Type II disk migration**, which is physically driven by the same type of torques of type I (see e.g., Edgar 2008). In case II, the planet's tidal torque takes away angular momentum from the gas in smaller orbits while also transferring angular momentum to the gas exterior of the planet's orbit, thereby creating a gap with an extension that depends on the planetary mass, temperature and viscosity of the gas. If no

gas crosses this gap, the planet follows the viscous evolution of the gas, so it can either spiral inward in the inner disk, or it can spiral outward in the outer disk, with a longer timescale ($\approx 10^6$ yr) compared to type I.

- **Type III disk migration** has very short timescales ($\approx 10^3$ yr) and applies only to extreme cases, such as massive disks where the planet can only open partial gaps (see e.g., Lin and Papaloizou 2010). It is characterized by co-orbital torques exerted by gas trapped in the planet's Lagrange points (locations where small-mass objects are in equilibrium under the gravitational influence of both the star and the planet) and the planet's initial rapid radial motion. The planet's radial motion displaces gas within its co-orbital region, creating an asymmetry between the density of the gas in the leading and trailing sides. In some cases, fast outward type III migration may permanently deliver giant planets to distant orbits, if type II migration fails to bring them back afterwards.

A minor contribution to migration can further be provided, after the disappearence of the disk, by leftover planetesimals (Walsh and Morbidelli, 2011), as during these encounters planets exchange angular momentum. If the average angular momentum of the planetesimals is higher relative to the planet, it can lead to outward migration, whereas the opposite can cause inward migration. In a single-planet system, the planetesimals can only be lost through ejection, leading to inward migration. In a multiple-planet system, other planets can either expedite the removal of planetesimals or act as sources to deliver more planetesimals to the first planet. In general, *planetesimal-driven migration* is dampened when the planetesimals are lost more rapidly than new ones are encountered.

However, planetary migration does not end with the disappearance of the gas disk and the planetesimals. In fact, even the ice giants of the solar system may have been scattered onto their current, large orbits by close encounters with Jupiter and Saturn (Gomes et al., 2005). For starters, following the dissipation of the disk, a system of proto-planets can become dynamically unstable and undergo gravitational mutual interactions (planet-planet scattering), which can push planets into highly eccentric orbits and trigger high-eccentricity migration (HEM) (see e.g., Owen and Lai 2018). A close interaction between a planet and its host star at periapsis can induce a tidal bulge on the star, which lags behind when the stellar rotation period is longer than the planet's orbital period. This lag creates a torque that removes angular momentum from the planet, causing its semi-major axis to decrease. In particular, the planet experiences the most significant deceleration near periapsis, resulting in a slower reduction in its periapsis compared to its apoapsis, hence reducing its eccentricity as a consequence. This process can last for billions of years, typically reducing by half the initial semi-major axis (or more, depending on the eccentricity) of the involved planets once they become *circularized*. HEM can also be triggered by secular interaction dynamics in multi-planet systems (Wu and Lithwick, 2011), or in a binary star system where an exoplanet orbits a single star. Specifically, if the planet's orbit is inclined with respect to the plane of the binary stars, interactions with the more distant star (or a planetary companion on a highly inclined orbit) can lead to changes in the planet's inclination and eccentricity due to the *Kozai mechanism* (Shevchenko, 2017), and lower the planet's semi-major axis, forcing it to close star encounters. Kozai cycles cease when the orbit contracts to a degree where the planet is no longer significantly influenced by the third object. Finally, HEM can happen as a combination of all these processes (see e.g., Nagasawa et al. 2008).

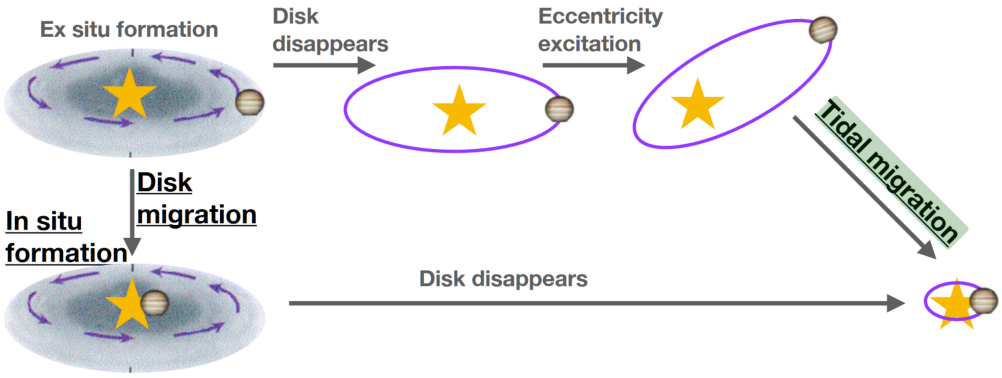

Figure 1.23: This illustrations shows three origins hypotheses for HJs: in situ formation, disk migration and HEM. Figure courtesy of Dawson and Johnson 2018.

The architectural characteristics of planetary systems can provide insights into their migration history, as systems that underwent disk migration might exhibit more compact and resonant planetary configurations due to the tidal forces and angular momentum exchange within the disk. In contrast, disk-free migration may lead to a broader range of planetary architectures, with less disposition toward compact, resonant configurations. In the case of disk migration, one might also expect that the distribution of eccentricities would be influenced by the damping effects of the disk, resulting in lower average values. Conversely, in the case of disk-free migration, the values may exhibit a wider range, as interactions and scattering events tend to drive eccentricity growth. As a matter of fact, both mechanisms are presumably at play according to the eccentricity distribution of known giant planets, though the HEM scenario seems favored (for a detailed overview see e.g., Bonomo et al. 2017). This is because significant eccentricities are more often found at wider separations from the parent stars (where tidal interactions are negligible), while circular orbits are found at small distances, at a separation that is greater than or equal to twice the Roche limit (Faber et al., 2005):

$$a_R = 2.16\, R_p\, (M_s/M_p)^{1/3} \tag{1.23}$$

that is the distance at which a planet (or any object) is no longer able to hold itself together due to the gravitational forces exerted by the host star (or any massive nearby celestial body). Nevertheless, planetary migration is a highly intricate phenomenon, and after decades of extensive observational and theoretical research, no consensus has been reached even for the primary mechanism responsible for the formation of HJs (Dawson and Johnson, 2018). Despite thousands of studies conducted over the past two decades, even the predominant channel for the origin of the most easily observable exoplanets remains a subject of ongoing debate (of which the three main hypotheses are summarized in Figure 1.23).

1.6.3 Planetary evolution

Lastly, for the purpose of connecting the formation models and the current-state observed parameters (mass, radius and period) it is important to model the long-term planetary evolution, which encompasses various processes (each related to planetary migration in its own way), such as:

- **Photo-evaporation** (see e.g. Owen and Lai 2018) - It occurs when the intense X-UV radi-

ation from a star interacts with the gas molecules in a planet's atmosphere, resulting in the gradual ejection and loss of atmospheric mass over time, depending on the absolute intensity of the stellar radiation, the planet orbital distance and its mass (the atmospheric loss is more substantial for less massive planets due to their weaker gravitational pull);

- **Core-powered mass loss** (see e.g. Ginzburg et al. 2018) - It refers to a critical phase in the evolution of exoplanets that occurs following the dissipation of the protoplanetary disk, typically over a timescale of a few million years. During this phase, the inner layers of the planet's atmosphere begin to cool, and this process, over time, can induce the loss of the loosely bound outer layers of the atmosphere. As a result, the planet's radius shrinks, typically converging to a size approximately twice that of its underlying core. The fate of the gas envelope surrounding the core is determined by the relative heat capacities of these two components. When the core dominates, its cooling luminosity can initiate a process of stripping off the overlying atmosphere, leading to the complete removal of the planet's atmosphere. Conversely, if the heat capacity of the gas envelope is larger (due to a massive atmosphere), the envelope cools down while remainining relatively intact, and resulting in a significant increase in the planet's radius;

- **Giant impacts** (see e.g. Liu et al. 2015) - Collisions play a crucial role in planetary evolution, especially in shaping the composition and fate of planetary atmospheres. These high-energy events can have the effect of essentially erasing the primordial atmospheres, because the energy influx severely heats the envelope, causing the gas to reach escape velocities and resulting in hydrodynamic escape of the envelope. The shockwave produced by a giant impact also has a role, as it can eject a fraction of the outer layers, though the thermal effect tends to be more significant (Biersteker and Schlichting, 2019). Importantly, once these atmospheres are lost, they cannot be easily replenished if the gas disk has already dissipated;

- **Out-gassing** (see e.g. Dorn et al. 2018) - It involves the release of volatile substances from the planet's interior due to geological activity, contributing to the replenishment of the planet's atmosphere and influencing the composition of its surface materials.

While significant progress have been made, there are still fundamental questions that remain unanswered due to the complex nature of the process. For instance, to explain the radius gap, or the size bimodality at observed at $1.5R_\oplus \lesssim R_\mathrm{p} \lesssim 2R_\oplus$, one theory proposes that super-Earths were originally similar to sub-Neptunes but eventually lost their primordial H/He dominated atmospheres (due to giant impacts, photo-evaporation, or core-powered mass loss, see, e.g., Owen and Wu 2017), while another theory suggests that it may simply be a manifestation of different core compositions (with sub-Neptunes having a water-ice rich core and super-Earths having a rocky core, see, e.g., Lopez and Fortney 2013).

Chapter 2

Data analysis

The detection and characterization of exoplanets present significant challenges. Given their distance from us and their faint signatures against those of their host stars, the quest to unveil and characterize these objects demands sophisticated data reduction and analysis techniques, including statistical tools and computational simulations. A wide range of approaches, from *traditional* methods to state-of-the-art procedures, are presented throughout this section for both ground-based and space-based observations, in order to explain how the results of this PhD thesis have been achieved.

2.1 RV data reduction

In Section 1.5.2 we gave an overview of HARPS-N, the spectrograph used to obtain the RVs exploited in this work. Once an observation has been executed by HARPS-N, the corresponding raw image is registered and reduced by the appropriate data reduction recipe. The standard one for high-precision Doppler measurements is the automatic Data Reduction Software (DRS) (Dumusque, 2021), that is designed to reduce observations obtained from two fibers. The role of the DRS is to transform the raw data into reduced data of scientific quality, and it is composed by a set of programs that perform different calibration and science tasks online, taking as inputs the data produced by the instrument along with calibration exposures. In particular, the target star is observed through the first spectrograph fiber (A), while the second one (fiber B) can be pointed at the background sky or to a spectral source for simultaneous wavelength reference, such as a Thorium-Argon (ThAr) lamp, a gas absorption cell, or a Fabry-Pérot interferometer (i.e. an optical cavity made from two parallel reflecting surfaces that can be used to control and measure light wavelenghts). The thorium mode is often preferred because it is stable on longer timescales compared to the Fabry-Pérot source. The purpose of the second channel is also to measure any instrumental drift occurred between calibration (done usually at the beginning of any observing night) and observation, which can then be converted and subtracted from the measured stellar RV in the last step of the DRS. In most of the observations performed during this work, the use of a lamp wouldn't have improved the precision on the relative RVs measurements, due to the photonic noise level of the stars involved ($V_{mag} \approx 10 - 12$), so fiber B was actually pointed on the sky in order to correct for any increase in background luminosity due to the Moon. Overall, the main steps of the scientific data reduction are:

- **Bias and dark subtraction.** A dark frame is an image captured in complete darkness that represents only the unwanted signal (noise) from charge accumulation on the sensor in a give

amount of time, while the bias frame is taken with virtually no exposure time and it shows the noise due to the sensor and the electronics that elaborate the sensor data.

- **Background subtraction.** The background emission is due to the overall (diffused) flux level of the image and the (local) inter-order scattering, that is proportional to the flux of the adjacent orders.

- **Order extraction with cosmic-ray rejection.** High-energy particles coming from space sometimes hit the detector and can produce bright spots that mimic genuine spectral features. Before tracing the exact center of each spectral order (the dispersed wavelength components) on the detector, it is essential to remove cosmic ray events with techniques like median filtering (i.e. replacing each value by the median of its neighbours) or sigma-clipping (i.e. removing data more distant than the desired amount of sigma from the median value).

- **Flat-fielding.** In order to reduce pixel-to-pixel sensitivity variations or distortions in the optical path, the images are first divided by the flat-field image (acquired by imaging a uniformly-illuminated source) which correct the relative pixel sensitivity along the spatial profile, when the stability is not good enough, and then each order of the star spectrum is divided by the *flat-field spectrum*, which is built by measuring the localization exposure (Baranne et al., 1996) and reduced in the same way as any astronomical image.

- **Bad pixels correction.** Some pixels exhibit higher or lower sensitivity to light (hot and cold pixels), or they do not respond to light at all (dead pixels). Some may be stuck at some value until the sensor is reset, others may have serious manufacturing imperfections to start with. To correct these, their values are often replaced by interpolation or masking (if they have not been corrected with bias/dark frame subtraction and flat-fielding).

- **Wavelength calibration.** This can be carried out for instance with the known emission lines of a ThAr source. An algorithm filters unblended and relatively strong spectral lines from a ThAr spectrum extracted from a lamp exposure, which are then fitted by a Gaussian for a precise estimation of their location, and a two-dimensional (2D) polynomial is used to constrain the global wavelength solution (effectively converting pixels to wavelengths).

- **Merging and rebinning of the spectral orders**. This step involves combining the individual spectral orders obtained into a final, continuous spectrum and adjusting the spectral sampling (binning) as needed.

- **Instrumental drift correction (if applicable).** The recorded wavelengths can be affected by factors like temperature changes, mechanical instabilities or variations in the instrument's optical properties. Over time, these factors can cause a drift that needs to be corrected.

- **Flux normalization.** The flux is time dependent and it changes between observations due to both observational and instrumental effects (such as atmospheric differential refraction, differential adsorption or telescope tracking errors).

- **RV computation.** This is usually done either via cross correlation or least-squares matching, taking into account that the measured velocity from the observer's frame (geocentric frame)

has to be transformed to the frame centered on the solar system barycenter. The *barycentric correction* ensures that the RV measurement reflects the motion of the star relative to the center of mass of the solar system, rather than the observer's motion on Earth. Furthermore, to minimize the effect of Earth's atmosphere, the spectral orders most contaminated by telluric lines are often neglected in this computation (but also refer the following subsection).

2.1.1 RV extraction through cross correlation

Let A_0 be the reduced spectrum obtained at the epoch of reference, then for a given pixel i, we can call the photoelectric intensity $A_0(i)$ and the wavelength $\lambda(i)$. At a different epoch, if we ignore the detector noise, the spectrum A should have the same intensity level, however due to a relative RV it could be stretched by a Doppler shift:

$$\frac{\delta V}{c} = \frac{\delta \lambda}{\lambda}. \tag{2.1}$$

When this shift is negligible compared to the line width, the change of intensity at a given pixel can be expressed by:

$$A(i) - A_o(i) = \frac{\partial A_0 i}{\partial \lambda(i)} \delta\lambda(i) = \frac{\partial A_0(i)}{\partial \lambda(i)} \frac{\delta V(i)}{c} \lambda(i) \tag{2.2}$$

therefore the Doppler shift is:

$$\frac{\delta V(i)}{c} = \frac{A(i) - A_0(i)}{\lambda(i)(\partial A_0(i)/\partial \lambda(i))}. \tag{2.3}$$

Hence, a change of velocity can be measured through a change in the spectrum intensity (see Bouchy et al. 2001 for a complete description). With the standard DRS, the extraction of RVs is performed by cross-correlating the stellar reduced spectra with a suitable mask (i.e. a template spectrum of the closest possible spectral type) chosen from a template library. The mask consists in a list of wavelength ranges and weights used to identify and define the contribution of each single spectral line to the cross-correlation. The wavelength shift is then measured by fitting a Gaussian function to the cross correlation of the stellar spectrum with the chosen mask, which is composed of a multitude of lines that span the entire HARPS-N spectral range. Therefore, the contribution of all pixels has to be summed considering a weight $W(i)$, which can be linked to the dispersion, or root-mean-square (RMS), $\delta V_{RMS}(i)$, and can be also used to eliminate unwanted lines (like telluric absorption lines):

$$\frac{\delta V}{c} = \frac{\sum \frac{\delta V(i)}{c} W(i)}{\sum W(i)}. \tag{2.4}$$

The commonly employed weights are usually the expected depths of the spectral lines. The resulting CCF is a representation of the average shape of the absorption profiles across this range (see Figure 2.1), and can additionally be employed to build stellar activity indicators, such as the BIS, the Contrast and the FWHM (refer to Section 1.4.3 and Figure 1.18).

The final precision on the RVs of a given star depends on multiple factors, the most important of which are usually the stellar apparent magnitude (linked to photon noise[1]), spectral type and

[1]For a 8th magnitude K0-dwarf, an exposure of 60 seconds is equivalent to a photon-noise error of 1.3 m/s

age. For stars later (colder) than about spectral type F6 ($\approx$6500 K), the RV error is below the nominal 10 m s^{-1} threshold needed to detect a Jovian planet at 5 au from a sun-like star. The number of spectral lines decreases with increasing effective temperature, so much that a G-type star has approximately ten times more spectral lines than an A-type star, hence for earlier spectral types (hotter stars) the error increases dramatically (also due to an increase in mean rotation rate; note that the same applies for young, active stars in general). All things considered, we can use the following expression (Bozza et al., 2016) to predict the RV measurement error for spectral data:

$$\sigma[m/s] \propto (SNR)^{-1} R^{-3/2} B^{-1/2} (v \sin i/2)\, f(SpT) \tag{2.5}$$

where R is the resolving power of the spectrograph ($\lambda/\delta\lambda$), B is the wavelength coverage in Å, $v \sin i$ is the rotational velocity of the star in km s^{-1} (only when $v \sin i > 2$ km s^{-1}) and $f(SpT)$ is a function of the spectral type. Finally, the accuracy can also be affected by the instrumental setup, due to telescope focus fluctuations, centering errors and calibration errors (for the ThAr lamp this is expected to be ≈ 0.5 m/s mostly due to the zero-point error).

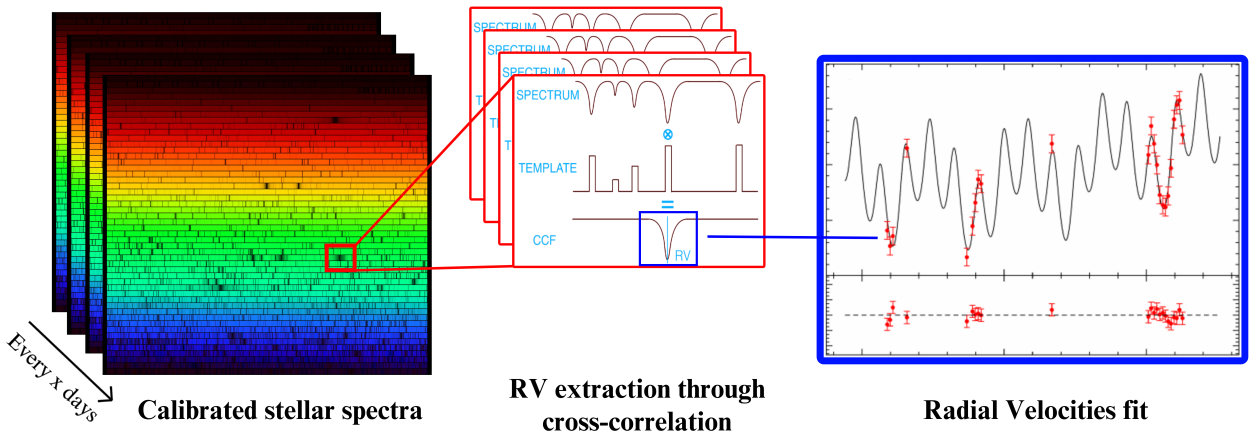

Figure 2.1: A visualization of RV extraction through cross-correlation (note that the spectra have been colored for visual purposes only). The spectra are obtained at a typical cadence of days or weeks, and after they have been reduced the RV is estimated by cross-correlating all, or a selection of, the wavelengths (the red box represents only a smaller portion of the spectra). The RV fit on the right is from Lovis et al. 2006.

2.1.2 RV extraction through least-square matching

The Template Enhanced Radial velocity Re-analysis Application (TERRA) software is an alternative, different algorithm for computing RVs based on the least-squares minimization of the differences between the observed spectrum and a parameterized template derived from the same observations (Anglada-Escudé and Butler, 2012). In particular, in order to obtain maximal precision with the highest possible SNR, TERRA constructs a template by carefully co-adding all the available spectra. At first, the RV and flux normalization coefficients are evaluated with respect to the higher SNR observation (used as preliminary template). Then, taking into account the heliocentric motion of the observer and the fact that each observed spectra is taken at different epochs, the barycentric wavelengths of the spectra at each epoch are calculated from the preliminary RVs by interpolation

(SNR=50), though only when the seeing is better than 1″, since the fiber has a 1″ aperture on the sky.

(read the full details on Anglada-Escudé and Butler 2012). Finally, the higher SNR template is built by co-adding all the observations. If the target star has been observed throughout a year, in different phases of the Earth motion around the Sun, a telluric free spectrum can be generated on regions with mild contamination, otherwise the telluric features have to be removed from the coadding. It should be noted that long-term instrumental stability is fundamental because the template is already convolved with the instrumental profile.

While the performance on F, G and K stars are similar between the DRS and TERRA, the least-square matching approach makes a better use of the Doppler information hidden in the blended spectra of M dwarfs, by providing a better fit to the lines compared to the CCF approach (which employs a Gaussian function with a constant baseline, see however Perger, M. et al. 2017 for a detailed comparison).

2.2 Photometric data reduction

As described in Sect. 1.5.1, *TESS* acquires time-series photometry with a baseline of $\approx$ 27 days or more, depending on possible sector overlaps, and produces many science products. FFI files cover the whole FOV of the CCDs and are taken with a cadence of 30-minutes (nominal mission), 10-minutes (first extended mission) or 200-seconds (second extended mission). *TESS* cutouts are taken from calibrated FFIs (without background subtraction) around specific stars, while target pixel files are much smaller pixel areas that are downloaded at faster cadence (every 2-minutes or 20-seconds, starting from the extended mission), each containing one target from a pre-defined subset. The luminous sources to be observed at short cadence, included in this subset, are selected from the so-called TESS Input Catalog (TIC) (Stassun et al., 2018), managed by the *TESS* Stellar Properties Working Group. For both *TESS* cutouts and target pixel files, an array of fluxes, or light curve objects, are extracted from the images by using aperture photometry (see Figure 2.2), a procedure by which the measured brightness values of all pixels within a defined region around the target star are summed over time (the choice of this *aperture* size is critical to capturing the entire flux from the star while minimizing contamination from nearby sources). These objects actually contains many time-series, including position vectors (the precise positions of the included stars), quality flags (indicators of data quality and any potential issue or anomaly associated with each cadence), along with the Simple Aperture Photometry (SAP) and Pre-search Data Conditioning SAP (PDC-SAP) light curves. The extraction process includes the correction of various instrumental effects, the subtraction of background light, the de-blending of the flux time series (i.e. the removal of the expected flux from each non-target star in the aperture), and the correction to the Solar System barycentric reference frame.

After being extracted, both SAP and PDC-SAP undergo basic data reduction steps, including bias and dark subtraction, flat-fielding, and correction for bad pixels (the same procedures described in Section 2.1). The PDC-SAP are flux series already corrected for both the common instrumental systematics using the Cotrending Basis Vector (CBV) files (a set of systematic trends present in the ensemble light curve data for each CCD). In the highest level of data processing, the PDC-SAP light curves, true astrophysical signals may be removed by the detrending procedure (or spurious

ones may be introduced by the CBV correction), so the SAP light curves can still be useful to study phenomena like the stellar variability, and especially to estimate the stellar rotation period, which can be falsely interpreted as a planetary signal in the RVs. The light curve of each star observed in short cadence is further detrended and searched for flux decrements compatible with the passage of an exoplanet, known as Threshold Crossing Events (TCEs), with the help of Box Least Squares (BLS), Transit Least Squares (TLS) and similar periodograms (see Section 2.3.2). Once at least one TCE has been identified for a star, the signals are put through a process called Data Validation (DV) (Twicken et al., 2018), in which many diagnostic parameters are evaluated to help determine if the TCEs were truly caused by planetary transits or if instrumental artifacts, blended binaries or other astrophysical phenomena could explain the signals better. For instance, the measured angular distance between the target star position and the location of the transiting source (determined from the in- and out-of-transit flux-weighted centroid shift) helps determine if the signal is due to a blended binary or a background star in the same aperture pixels. All these steps are performed by data processing pipelines, and in this work we exploit the most widely used one: the Science Processing Operations Center (SPOC) pipeline (Jenkins et al., 2016) developed at the NASA Ames Research Center, which is much more reliable than the Quick-Look Pipeline (QLP) (Huang and Vanderburg, 2020), as the name would suggest.

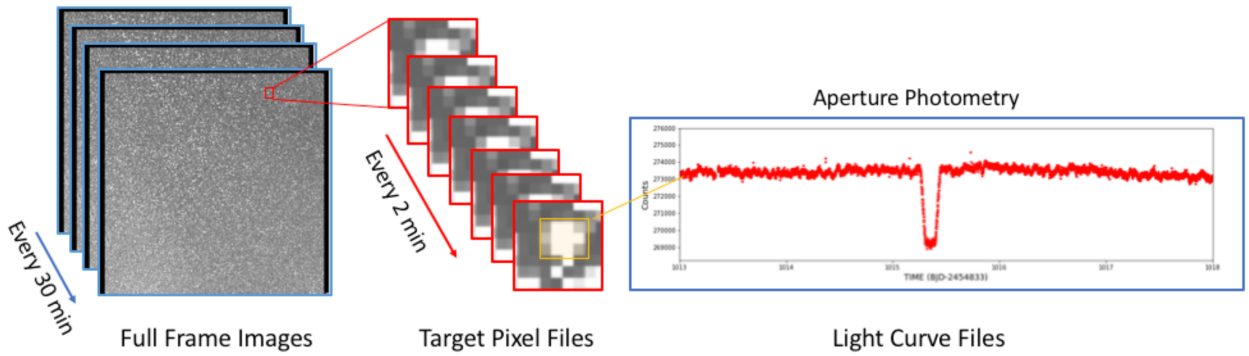

Figure 2.2: A visualization of *TESS* data products; the FFIs, the target pixel files and the resulting light curve from aperture photometry. The cadences can be different from the ones written here, as described in the text of this section (figure from *TESS* instrument handbook).

Finally, when a signal has been determined to be sufficiently consistent with a transit (or eclipse), the target is turned into a TESS Object of Interest (TOI), highlighting the fact that it is worthy of follow-up observations, even if it still might turn up to be a false positive. An exoplanet is considered confirmed either when the mass of the transiting planet has been measured (with RVs or rarely TTVs), or if that's not possible, when all other possible explanations are removed conclusively by other means (mainly high resolution imaging and on-ground photometric follow-up).

2.3 Periodograms

In the context of RV analysis, one of the initial steps involves the search for periodic signals, with tools such as the Generalized Lomb-Scargle (GLS) periodogram (VanderPlas, 2018) (see Section 2.3.1), that can be attributed either to planetary gravitational influences or to stellar phenomena like rotation. Similar analyses are conducted on activity indicators to identify any stellar signals

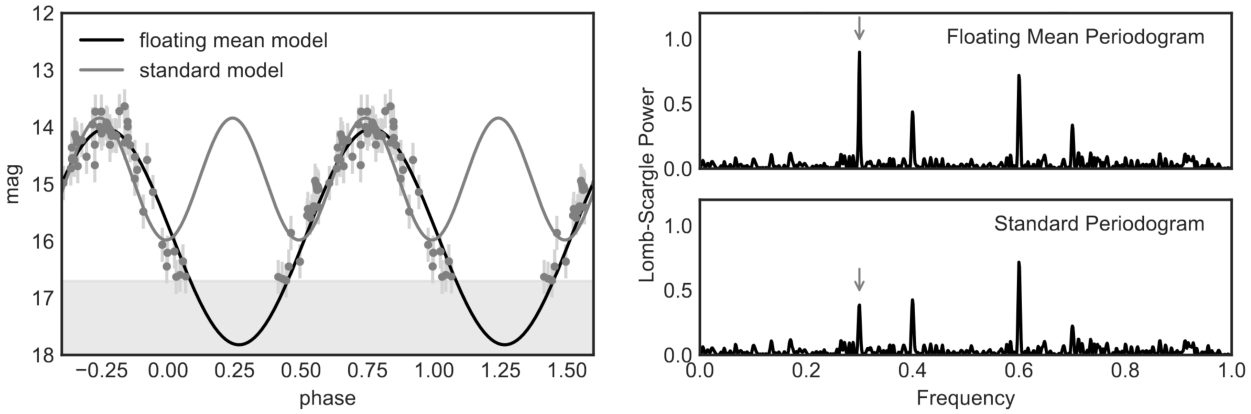

Figure 2.3: An example of partial phase coverage measurements is plotted on the left panel (the pink area is unaccessible because of observational constraints). On the right panel, the standard periodogram fails to recover the true frequency of 0.3 because it assumes that the true mean of the signal is the mean of the observed data, while the periodogram with a floating mean term (such as the Generalized Lomb-Scargle one) catches the true frequency correctly. Figure courtesy of VanderPlas 2018.

within the RV data that may be present in these indicators as well. However, when it comes to searching for transit signals, the GLS periodogram does not perform optimally, because transit signals are non-sinusoidal and have very sharp temporal concentration. To address this, more efficient techniques such as the BLS algorithm (Kovács et al., 2002) have to be employed (see Section 2.3.2).

2.3.1 Generalized Lomb-Scargle periodogram

Based on the idea that any periodic function can be represented by a sum of trigonometric functions (like sine and cosine), the classical Fourier analysis, also known as Fourier transform, is a mathematical technique used to decompose such functions into their constituent sinusoidal components (with different frequencies, amplitudes and phases). Given a K-long time-series data set $y(t)$, the Fourier transform can convert the data from the time domain into the frequency domain, which in the discrete implementation is the equivalent of:

$$F_y(w) = \sum_{k=1}^{K} y(t_k) e^{-i\omega t_k} \tag{2.6}$$

where ω is the frequency times 2π and $e^{-i\omega t_k} = \cos(\omega t_k) - i\sin(\omega t_k)$. Every frequency is associated to an amplitude (power), forming the so-called *power spectrum*:

$$A(\omega) = \sqrt{P_y(\omega)} = \frac{1}{K^{1/2}}|F_y(\omega)| = \frac{1}{K^{1/2}}\sqrt{\left(\sum_{k=1}^{K} y_k \cos(\omega t_k)\right)^2 + \left(\sum_{k=1}^{K} y_k \sin(\omega t_k)\right)^2} \tag{2.7}$$

Significant (high power) peaks in the power spectrum likely indicate that the data set includes periodic signals at those specific frequencies. However, classical Fourier analysis assumes evenly spaced data points, which is never the case for astronomical observations limited by diurnal, lunar, or seasonal cycles and weather conditions.

The Lomb-Scargle periodogram (VanderPlas, 2018) is a technique built to address the limitations of the classical Fourier analysis, as it can accomodate irregularly sampled data by employing weighted least-squares fitting to sinusoidal functions. In order to do so, the amplitude is defined as:

$$A(\omega) = \sqrt{P_y(\omega)} = \frac{1}{2}\sqrt{\frac{[\sum_k y_k \cos(\omega(t_k - \tau))]^2}{\sum_k \cos^2(\omega(t_k - \tau))} + \frac{[\sum_k y_k \sin(\omega(t_k - \tau))]^2}{\sum_k \sin^2(\omega(t_k - \tau))}} \tag{2.8}$$

where $\tan(2\omega\tau) = (\sum_k \sin(2\omega t_k))/(\sum_k \cos(2\omega t_k))$. In its generalized version, it considers both the uncertainties of the data and a constant term in the fit of the wave function, resulting in less susceptibility to aliasing and more accurate frequency determinations. This last step turns out to be very important in many circumstances, especially when a periodic event is observed in partial phase coverage due to observational constraints (refer to Figure 2.3). Similarly to the Fourier transform, the Lomb-Scargle periodogram computes the power spectrum in order to evaluate the strengths of periodic signals at different frequencies. The uncertainties of the derived periods, however, cannot be meaningfully expressed because rather than the imprecision in the location of a particular peak, the concern for periodograms is more about the disjointed inaccuracy associated with false peaks or aliases. In particular, the peak widths do not depend on the number of observations or their SNR, and the data quality and quantity is reflected instead in the height of the peak in relation to the background, which is a measure of significance rather than precision of the associated frequency. The False Alarm Probability (FAP) is a measure of the probability that a data set with no signal would, coincidentally, lead to a peak of similar magnitude to the one of interest. In the GLS periodogram the FAP of the peaks can be assessed by different statistical tests, such as the bootstrap method (a resampling, computational technique which involves the generation of multiple samples obtained by randomly sampling the original data point, see e.g. Sulis et al. 2017), or analytically, as simply as:

$$FAP(\omega) \approx 1 - (1 - e^{-P(\omega)})^M \tag{2.9}$$

if the number of independent frequencies (those that are not correlated), M, can be estimated. A further Lomb-Scargle generalization consists of fitting multiple sinusoidal components rather than a single one (see, e.g., Baluev 2013). This can be useful to fit complicated models but, at the same time, the addition of terms raises the periodogram noise due to the appearance of new aliases and because a better fit to the data means higher power for all the frequencies, not only the one of interest.

The GLS periodogram is now extensively used in astronomy to reveal periodic signals in irreguarly sampled time-series data. It is therefore not difficult to understand why it is the first, most important tool to reveal possible planetary (periodic) signals hidden in the measured RVs of a star. When using the GLS periodogram to confirm or find new planetary signals in the RV data, it is essential not to forget the drawbacks of this approach. In fact, it's not uncommon for the largest peak in the periodogram to arise from an alias of the true frequency, due to actual shape of the signal, noise or the survey window. For instance, the function that represents the sampling pattern of the observations, the so-called *window function*, can have frequency peaks (δf) due to common constraints (e.g. $\delta f = 1$ observation/day). This can lead to spurious peaks in the GLS periodogram located at $f_{true} + n\delta f$, or:

$$P_{alias} = \left(\frac{1}{P_{true}} + n\delta f \right)^{-1} \tag{2.10}$$

where n is a positive or negative integer. When the periodic signals are not strictly sinusoidal, it's possible that harmonics of the true frequency have higher power than the real one. In that case:

$$P_{alias} = \left(\frac{m}{P_{true}} + n\delta f \right)^{-1} \tag{2.11}$$

where m is an integer representing the harmonic. Finally, every peak at frequency f_{true} has a corresponding peak at $-f_{true}$, and aliases that cross into negative frequencies are effectively reflected into the positive-frequency range. Taking this into account, all the possible aliases of the true period P_{true} due to a spurious peak f_s are:

$$P_{alias} = \left| \frac{m}{P_{true}} + nf_s \right|^{-1}. \tag{2.12}$$

2.3.2 Box and Transit Least Squares periodograms

Transit-like events are not modeled well by sinusoidal functions, therefore the GLS periodogram is not an efficient tool to look for planetary transits as much as it is for RV signals, especially at short wavelengths, where stellar limb darkening is more pronounced, and when the duration of the transit is short relative to the orbital period. A better way to find transits in the light curve of a star would be to employ an algorithm that exploits the rectangular, box-like shape of the signal (see Fig. 1.7). The BLS periodogram (Kovács et al., 2002) has been specifically designed to perform least squares fits of step (box) functions to folded light curves corresponding to various test periods. In particular, since the out-of-transit baseline flux can be set to zero (or normalized to 1), the box-shaped transit model is defined by four parameters: the time of the center of the box (T_0 or transit epoch), the

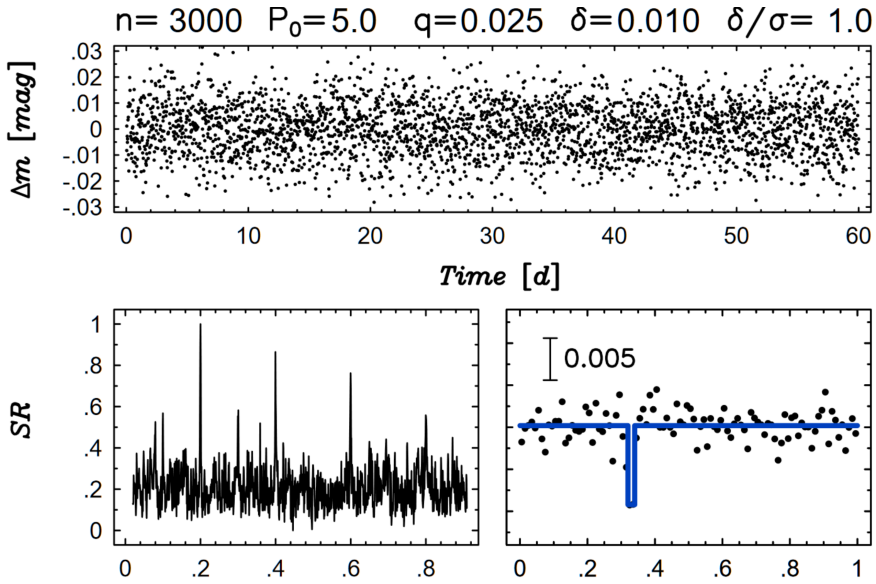

Figure 2.4: Example of BLS periodogram (bottom-left panel) for a photometric time series (top panel), along with the light curve phase-folded at the frequency with highest SR (bottom-right panel). n is the number of data points, σ is the noise level of each observation and q is the ratio between the transit duration and the period (P_0). Figure courtesy of Kovács et al. 2002.

period (P), the duration of the box (T) and the depth of the box (δ). For a given trial period, the light curve is permutated (folded), and the step function is fit with two flux level parameters, one measured between two flux values $[i_1, i_2]$ and one outside. Similarly to the other periodograms, the BLS one also evaluates an equivalent of the *power spectrum* by defining the Signal Residue (SR) of the time series for all the trial periods (see Figure 2.4). Then, the Signal Detection Efficiency (SDE) can simply be defined as:

$$SDE = \frac{SR_{peak} - < SR >}{\sigma(SR)} \tag{2.13}$$

where <SR> is the average of all the signal residues. Given that the condition $\Delta i_{min} < i_2 - i_1 < \Delta i_{max}$ is satisfied, where $\Delta i_{min/max}$ depend on the suspected transit length, for any particular (i_1, i_2), the averaged squared deviation of the fit is minimized, and the overall, absolute minimum corresponds to the best trial period (the one with the highest SR). In practical implementations, the folded time series is divided into bins so that the computation can be more efficient, although the resolution has to be chosen carefully because it affects the efficiency of the signal detection as the SR is strongly dependent on the transit phase only when the bin size is comparable to the actual length of the transit (note that a smaller bin is always favored at cost of efficiency).

Compared to other periodograms, the use of a pre-determined shape to fit the transit features of a light curve makes the BLS periodogram very efficient which is why it has become the standard tool for exoplanet transit searches in large data sets. On the down side, this algorithm assumes only two levels of flux and so it ignores features like the limb darkening (see Sect. 1.2.2) and the ingress/egress shape. Given the growth of computer *power* in the last two decades, the idea of building a better tool at the expense of increased computational demand is no longer far-fetched. The TLS periodogram is an alternative tool, proposed in 2019 (Hippke and Heller, 2019), which has a substantial higher rate detection especially for small planets with few transits, or grazing transits where the shape is highly non-rectangular. The TLS algorithm is simply based on the search for transits with more realistic transit-like functions rather than a basic box (refer to Figure 2.5). As for the BLS, it phase-folds data over a range of trial periods and then it calculates the χ^2 statistic

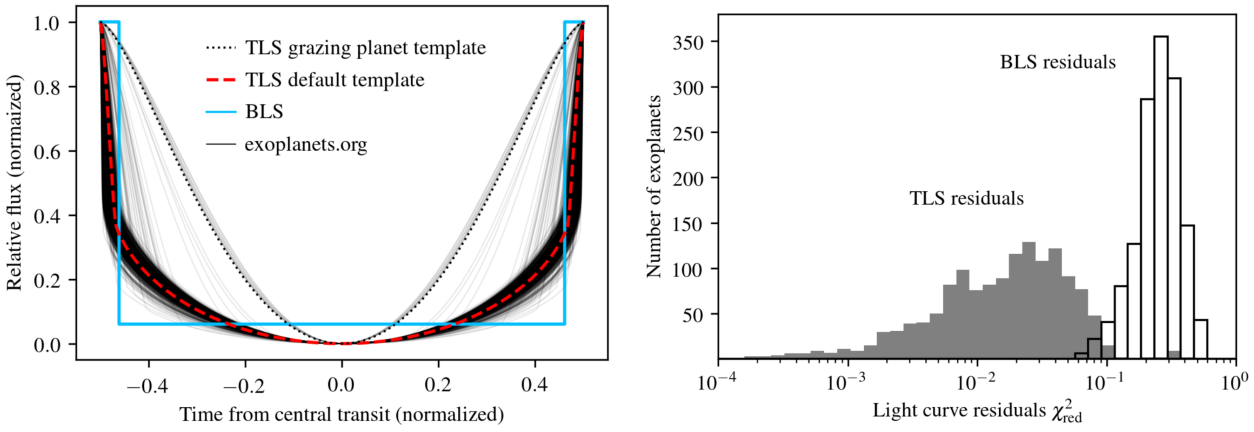

Figure 2.5: On the left, this plot shows the transit shapes of 2346 *Kepler* planets with small radii ($< 5R_\oplus$) as black lines, along with the default TLS templates for normal and grazing planets. The best-fitting box from the BLS algorithm is shown in cyan for comparison. On the right the gray histogram report the reduced χ^2 residuals for both TLS and BLS. Figure courtesy of Hippke and Heller 2019.

between the K data points of the transit model (y^m) and the measured fluxes (y):

$$\chi^2(P, T_0, T) = \sum_{k=1}^{K} \frac{(y_k^m(P, T_0, T) - y_k)^2}{\sigma_k^2} \tag{2.14}$$

where σ_k^2 are the standard deviations of the fluxes. The TLS finds the global minimum by searching for the minimum χ^2 of all the (T_0, T) combinations at a fixed P:

$$\chi^2_{min,glob} = min(\chi^2(P, T_0, T)). \tag{2.15}$$

The test statistic of TLS is a modified version of the BLS SDE, derived from all the data points in the phase-folded light curves, instead of only the binned ones. The SR here is calculated directly from the distribution of minimum χ^2 (which could be done in principle also for the BLS):

$$SR(P) = \frac{\chi^2_{min,glob}}{\chi^2_{min}(P)} \tag{2.16}$$

which means that $SR(P)$ is confined between 0 and 1 ($SR_{peak} = 1$), therefore:

$$SDE(P) = \frac{1 - < SR(P) >}{\sigma(SR(P))}. \tag{2.17}$$

With the advent of *artificial intelligence*, new techniques are being developed to look for transits with even higher accuracy, such as deep learning algorithms trained on a series of real or artificial transit shapes (see, e.g, Schanche et al. 2019). As of today, machine-learning methods appear promising but have not yet become common due to many reasons, one of which is the difficulty in understanding the origin of the results due to many abstraction layers (depending on their implementation).

2.4 Bayesian statistics

Traditionally, the *probability* associated with an event has been interpreted as the limit of the relative frequency of that event after a number of trials that tends towards infinity. Bayesian statistical methods, as opposed to the so-called *frequentist* interpretation, instead exploit the Bayes' theorem to compute and update probabilities, based on prior knowledge such as the results of previous experiments, after obtaining new data. Originally formulated by Thomas Bayes in 1763, Bayesian methods were viewed unfavorably for centuries, mainly due to the substantial amount of computation they demanded. However, the landscape has significantly changed with the rise of modern computers and advanced algorithms, such as Markov Chain Monte Carlo (MCMC) and, as a result, these methods have gained popularity and are finding increasing applications (for exoplanet science, see e.g. Parviainen 2018). In Bayes' interpretation of the probability theory, given a model A_i and a data set B the *posterior probability* that A_i is the best model to describe B, compared to other ones, is the following:

$$P(A_i|B) = \frac{P(B|A_i)P(A_i)}{P(B)}\,, \tag{2.18}$$

where $P(A_i)$ is the *prior probability* of model A before new evidence has been taken into account, $P(B) = \sum_i P(B|A_i)P(A_i)$ is a normalization factor that takes into account all the models consid-

ered, and $P(B|A_i)$ is the probability (i.e. the likelihood, $\mathcal{L}$) that data B is well fit by model A_i. Essentially, in Eq. (2.18) $P(A_i)$ is updated to $P(A_i|B)$ after new measurements (B) have been taken into consideration. Assuming independent and Gaussian distributed parameters, the likelihood for A_i can be expressed as:

$$\mathcal{L}_i = P(B|A_i) = \prod_{k=1}^{K} \left(\frac{1}{\sqrt{2\pi(\sigma_k^2 + \sigma_{jit}^2)}} \right) e^{\sum_{k=1}^{K} -\frac{(B_k - A_{i,k})^2}{2(\sigma_k^2 + \sigma_{jit}^2)}}, \tag{2.19}$$

where K is the total number of measurements, σ_k is the k measurement uncertainty and the free parameter σ_{jit} is an additional white noise term (while this can be from different origins, several noise sources would not be white in the data, such as stellar magnetic activity, granulation, stellar oscillations, and even unexpected planetary signals, for both RV and transit data). In the context of exoplanet characterization, Bayesian statistics can play a crucial role in determining the most likely values and confidence intervals for fitted planetary parameters, by efficiently sampling their posterior distributions. It's important to mention that the same can be done for the stellar parameters, as the derived planetary parameters (e.g. R_p) are determined by combining the posterior distributions of the fitting parameters (the ratio of the radii: R_p/R_s) with those of the stellar parameters (R_s).

2.4.1 Markov Chain Monte Carlo

In a real case scenario, such as a data set of RV measurements, for which we need to find the best model fit, A_i is composed of many parameters. The aforementioned MCMC algorithm allows to evaluate the posterior distributions of all the parameters involved, by sampling the *parameter space* via a succession of random steps (i.e. a random-walk) such that the number of samples in a particular region of this space is proportional to the posterior density for that region (see e.g., Speagle 2019). Multiple *chains* (collections of steps) can be evolved in parallel, sampling all the parameters starting from the prior space. If $\vec{x}_{j,n}$ is the parameter vector of chain j at iteration n, the next step $\vec{x}_{j,n+1}$ is accepted only if it comes with an increase of likelihood ($\mathcal{L}_{j,n+1} > \mathcal{L}_{j,n}$), otherwise the step is rejected (in some variations the rejection is also dependent on the result of a random number, which helps the chain not to get stuck in local maxima). The gist is in how this *next step* is calculated. There are many ways to do it, for instance in the Metropolis-Hastings algorithm (see e.g., Robert 2015) the *proposal distribution*, q, simply starts from the previous step and adds a small random perturbation q:

$$\vec{x}_{j,n+1} = \vec{x}_{j,n} + q(\vec{x}_{j,n+1}|\vec{x}_{j,n}). \tag{2.20}$$

In order to sample the parameter space effectively, the scale and direction of these *jumps* can be better determined using the genetic algorithm known as Differential Evolution (DE). In the DE-MCMC implementation (Ter Braak, 2006a), the proposal distribution depends on the number of free parameters N, on a very small random value e and on two chains ($\vec{x}_{C_1}, \vec{x}_{C_2}$) randomly chosen from all the steps of each chain:

$$\vec{x}_{j,n+1} = \vec{x}_{j,n} + \gamma(\vec{x}_{C_1} - \vec{x}_{C_2}) + e \tag{2.21}$$

where $\gamma = 2.38/\sqrt{2N}$. Instead, in the affine-invariant ensemble sampler for MCMC, or EMCEE

(Foreman-Mackey et al., 2013), the proposal distribution is a random variable, z, drawn from the distribution $g(z)$, which is $1/\sqrt{z}$ if $z \in [\frac{1}{a}, a]$ and zero otherwise, with $a = 2$:

$$\vec{x}_{j,n+1} = \vec{x}_{C_1} + z(\vec{x}_{j,n} - \vec{x}_{C_1}). \tag{2.22}$$

In every case, once the parameter space has been adequately sampled and all the chains have reached a stable state, the computation ends because any further iteration is unlikely to significantly improve the estimations. One example of *convergence criterion* is the Gelman-Rubin diagnostic (Gelman and Rubin, 1992), according to which the convergence can be achieved if the variance between the parallel chains is comparable to the variance within each chain (so that they are well mixed), however every specific implementation employs different ones. Finally, before evaluating the posterior distributions, the starting steps of each chain (*burn-ins*) are usually removed since they should be very distant from the parameter space where the likelihood eventually reaches its maximum. For the purpose of selecting the preferred model among many, two of the most widely used tools are the Bayesian information criterion (BIC) (Schwarz, 1978) and Akaike information criterion (AIC) (Akaike, 1974), formally defined as:

$$\begin{aligned} BIC_i &= -2 \ln \mathcal{L}_i + N \ln K \\ AIC_i &= -2 \ln \mathcal{L}_i + 2N. \end{aligned} \tag{2.23}$$

where better models have lower values. Both tools introduce a penalty term that is higher for an increasing number of free parameters N (i.e. increased model's complexity), because in principle models with fewer parameters should always be favored when the likelihoods are similar, while the BIC also takes into account the total number of measurements K. However, it is important to note that both BIC and AIC assume Gaussian distributions for the posteriors and they only take the maximum of the likelihood into account, instead of the integral of $\mathcal{L}$ over the parameter space.

2.4.2 Nested sampling

An alternative computational method for Bayesian model parameter estimation and model comparison is *nested sampling* (Skilling, 2004), which is the basis of the sampling method used in this dissertation. Unlike MCMC, nested sampling slices the posterior into many simpler distributions, sampling from each of those in turn and re-combining the results afterwards (see Figure 2.6). It employs a set of *active* points that are iteratively updated, and to which a likelihood level is associated. At each iteration the algorithm removes the point with the lowest likelihood and replaces it with a new point from the prior distribution, only if the new associated likelihood is higher. Actually, in a few implementations (e.g. `MultiNest` python package) every point is associated to a weight so no sampled point is ever removed, which sometimes causes a much faster convergence by better exploiting the sampling. Nested sampling turns out to be very effective at handling multimodal distributions, and it can be conceptually simpler to implement because it does not require setting up proposal distributions or dealing with chain tuning. The so-called *bayesian evidence*, $\mathcal{Z}_i$, for model A_i can be written as:

$$\mathcal{Z}_i = \int P(A_i|B) d\vec{x}_i = \int \mathcal{L}_i P(A_i) dx_{i,1} dx_{i,2} ... dx_{i,K} \tag{2.24}$$

though this integral is very challenging to estimate, so in nested sampling it is re-factored as a one-dimensinoal integral taken over the prior volume X of the parameter space:

$$\mathcal{Z}_i = \int_0^1 \mathcal{L}_i(X) dX \tag{2.25}$$

where $\mathcal{L}_i(X)$ is one or multiple iso-likelihood contours that outline the edges of X, defined as the fraction of the prior volume where the likelihood is higher than the threshold λ (note that the prior is normalized so X is null when λ is infinite, and X is 1 when λ is null):

$$X(\lambda) = \int_{\mathcal{L}_i \geq \lambda} P(A_i) d\vec{x}_i. \tag{2.26}$$

During each iteration the bayesian evidence is updated by the difference $\Delta\mathcal{Z}$ (usually written as $\Delta \ln \mathcal{Z}$), and a common stopping criterion is defined by the user through a tolerance Δz below which the algorithm is said to have converged. The final, direct estimation of the evidence is incredibly useful for the model selection. Following the guidelines of Trotta 2008, we consider $\Delta \ln \mathcal{Z} < 2$ (posterior odds of $\approx 7:1$) weak evidence in favor of one model over the other, $\Delta \ln \mathcal{Z} > 5$ (posterior odds of $\approx 150:1$) strong evidence, while everything in between as moderate evidence. It is important to remember, however, that model evidences are heavily impacted by the priors used to estimate them (i.e. the priors between the models have to be compatible for the comparison to make sense).

Since the number of live points is constant, the prior volume *shrinkage rate* is always the same and often many samples are taken in regions which have little effect on calculation accuracy, yet this can be solved with *dynamic* nested sampling, for instance with the Python package `dynesty` (Speagle, 2020). In this implementation, the number of samples taken in different regions of the

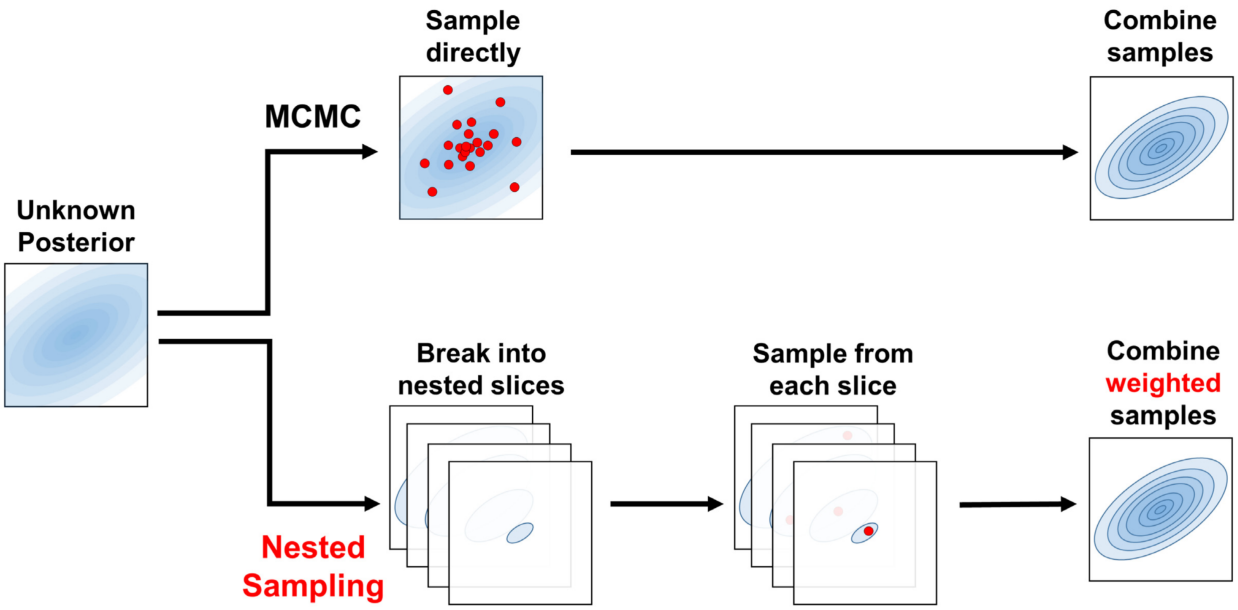

Figure 2.6: A schematic illustration of how MCMC and nested sampling methods approach the problem of sampling from the posterior. MCMC methods do it directly from the posterior, while nested sampling breaks up the posteriors into slices. Figure courtesy of Speagle 2020.

parameter space is dynamically adjusted in order to change the focus of the algorithm during the run. On the other hand, the converge criteria are harder to define because they have to take into account how much of the posterior distribution has been explored (see for example Section 3.4 of ref. Speagle 2020).

2.5 Gaussian Processes

In probability theory, a *stochastic process* is a collection of random variables representing the evolution of a system in the parameter space or in time (e.g. the random movement of particles in a fluid, known as *Brownian motion*). When every finite linear combination of these random variables is normally distributed, the process is called *Gaussian*. In Bayesian inference, a GP can be used as a prior probability distribution for the parameters (or functions) that need to be estimated using a set of measurements, and is fully specified by a mean function and a kernel (covariance) function, which captures our assumptions about the relationships between such parameters (refer to the comprehensive review of Aigrain and Foreman-Mackey 2023). The utility of GPs is that the distributions of the derived quantities (i.e. average value and uncertainty) can be obtained explicitly. In particular, when the data set is correlated (i.e. it's affected by red noise), the probability distribution function is no longer represented by Eq. 2.19, but rather by:

$$\mathcal{L}_i = \left(\frac{1}{2\pi}\right)^{N/2} \frac{1}{\sqrt{det\,\mathcal{K}}}\; e^{-\frac{1}{2}(\underline{B}-\underline{A}_i)^T\,\mathcal{K}^{-1}\,(\underline{B}-\underline{A}_i)} \tag{2.27}$$

where N is the number of measurements, $(\underline{B}, \underline{A}_i)$ are the conjugate transposes of the data and model matrices, and $det\,\mathcal{K}$ is the determinant of the covariance matrix $\mathcal{K}$, whose elements are determined by a covariance function:

$$\mathcal{K}_{i,j} = k(t, t'), \tag{2.28}$$

that is precisely the GP kernel. In case of white noise (independent and identically distributed data) $\mathcal{K} = \sigma^2\mathcal{I}$, where $\mathcal{I}$ is the identity matrix, and the likelihood can be expressed again by Eq. 2.19. There are a number of common GP kernels implemented to disentangle stellar activity in light curves and RV data, and among the most widely used are the squared exponential (Eq. 2.29), the periodic (Eq. 2.30) and the quasi-periodic (Eq. 2.31) kernels (implemented following Espinoza et al. 2019):

$$k(t, t') = h^2\, e^{-\frac{(t-t')^2}{2\lambda_e^2}} \tag{2.29}$$

$$k(t, t') = h^2\, e^{\frac{-\sin[\pi(t-t')/P]}{2\lambda_p^2}} \tag{2.30}$$

$$k(t, t') = h^2\, e^{\frac{-\sin[\pi(t-t')/P]}{2\lambda_p^2} - \frac{(t-t')^2}{2\lambda_e^2}} \tag{2.31}$$

where h represents the total amplitude of the process, λ_e is the decay timescale ($\approx$ active regions decay, in the case of stars), P is the periodic term ($\approx$ the stellar rotation period) and λ_p is the complexity of the observed signals. It is straightforward to see that the quasi-periodic kernel includes both the periodic and the squared exponential components, and as such it better resembles stellar

activity variations (for this reason it is among the most widely used kernels for light curves and RV analysis). These coefficients define the behaviour and the characteristics of the GP and are called *hyper-parameters*. They are usually employed with uniform priors, with the exception of P, which can have a Gaussian prior centered on the stellar rotation period, if it has been estimated with some accuracy through other means (i.e. via photometric variations or clear signals in the activity indexes). The use of uninformative priors for GPs is not advisable, as they are very powerful and should be employed with sensible boundaries (see, e.g., Nicholson and Aigrain 2022).

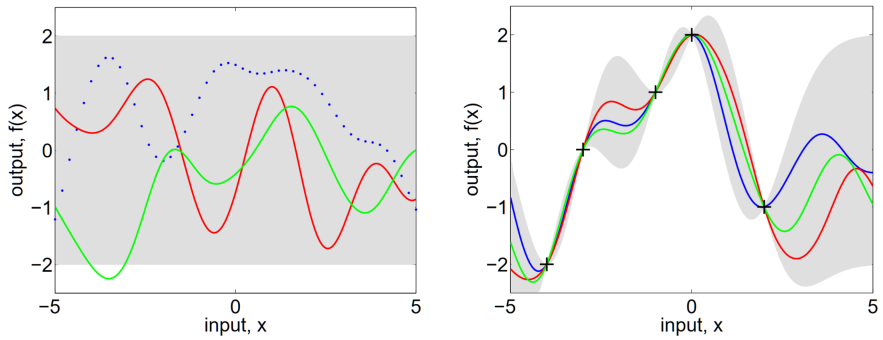

(a), prior (b), posterior

Figure 2.7: In panel (a), three functions are drawn at random from a GP prior (the blue dotted line actually shows the generated values). In panel (b), the three random functions are drawn from the posterior, so they are conditioned by the observations. The pink area represents the 95% confidence region for both priors and posteriors (i.e. the mean plus and minus two standard deviations for each value). Note how the posterior uncertainty collapses on the five observations, due to their assumed noise-free nature. Figure courtesy of Rasmussen and Williams 2006.

Suppose we have a data set consisting of five noise-free observations, and we are only interested in functions that pass through these points exactly (as opposed to passing as close to them as possible, which would be the case for non-ideal, noisy measurements). The kernel would then represent our best *a priori* mathematical interpretation of the physical event that's influencing the observations, and its specification is fundamental because it fixes the properties of the functions considered for inference. The properties of the kernel can be manipulated by adjusting the hyper-parameters priors (e.g. the stellar rotation period has to be reasonable, it cannot result in any possible value!), and the combination of the prior and the actual data eventually leads to the posterior distribution (refer to Figure 2.7).

2.6 Combined transit-RV analysis

As anticipated, confirming transiting candidates, like TOIs, as new exoplanets most of the time requires follow-up RV observations, which are fundamental to constrain the physical parameters of the planet (in particular the mass and density) and its orbit. In the last decade, many tools have been developed to perform analyses of exoplanetary signals given either photometry, RVs or both. In this work, we have employed the Python wrapper `juliet` (Espinoza et al., 2019), a versatile tool that can be used for the combined analysis of photometric and spectroscopic measurements, even from multiple instruments, with all the advantages of nested sampling (described in Section 2.5). Jointly fitting transit and RV data provides multiple advantages, as it improves the accuracy of the

shared parameters (summarized in Table 2.1) and reduces parameter correlations by addressing the degeneracies that can occur when fitting either type of data in isolation.

In `juliet`, the data modelling can exploit GPs, with the added possibility of sharing hyper-parameters between photometry and RVs at the same time, which is often important to disentangle stellar activity from planetary signals. Specifically, `juliet` considers a common model in which each data-point $y(t_{i,l})$, at time $t_{i,l}$ for the data-point l of instrument i, is given by a probabilistic model of the form:

$$y(t_{i,l}) = \mathcal{M}_i(t_{i,l}) + LM_i(t_{i,l}) + \epsilon_i(t_{i,l}) \tag{2.32}$$

where $\mathcal{M}_i(t_{i,l})$ is the photometric or RV model that depends on instrumental parameters and physical parameters of the system, $LM_i(t_{i,l})$ is a linear model for instrument i and $\epsilon_i(t_{i,l})$ is a zero-mean noise term. The latter can be defined as having a universal component for all the instruments (doing the same type of observation), so that:

$$\epsilon_i(t_{i,l}) = \epsilon(t_{i,l}) + \bar{\epsilon}_i(t_{i,l}) \tag{2.33}$$

where $\bar{\epsilon}_i(t_{i,l}) = N(0, \sigma^2_{w,i} + \sigma^2_{t_{i,l}})$ is the white-noise component, with $N(\mu, \sigma^2)$ being a normal distribution with mean μ and variance σ^2. The formal uncertainties for data-point $y(t_{i,l})$ is denoted as $\sigma^2_{t_{i,l}}$ while $\sigma^2_{w,i}$ is an additional jitter term for each instrument. In this case, the covariance matrix is of the form:

$$\mathcal{K}(t_{i,l}, t_{j,m}) = k(x_{i,l}, x_{j,m}) + (\sigma^2_{w,i} + \sigma^2_{t_{i,l}})\delta_{t_{i,l},t_{j,m}} \tag{2.34}$$

with the first term being null in the case of a pure white-noise model (without GPs) and $\delta_{t_{i,l},t_{j,m}}$ being the Kronecker's delta (defined as equal to one when its two variables are identical, and zero otherwise). The photometric model is expressed as:

$$\mathcal{M}_i(t_{i,l}) = [\mathcal{T}_i(t_{i,l})D_i + (1 - D_i)] \left(\frac{1}{1 + D_i M_i} \right) \tag{2.35}$$

where $\mathcal{T}_i(t_{i,l})$ is the full transit model of all the planets that may be present in the light curve for instrument i, generated using `batman` (Kreidberg, 2015), the most common Python package for modelling exoplanetary transits. D_i is the dilution factor used to correct for flux contamination of unwanted sources in the aperture pixels (or miscalculated background flux) and M_i is the offset or the mean out-of-transit flux. Let F_T be the out-of-transit flux of the target star (in the observed passband) and $\sum_n F_n$ be the total flux from the n unwanted sources in the aperture, then the dilution factor is defined as:

$$D = \frac{1}{1 + \sum_n F_n / F_T} \tag{2.36}$$

and it can take the values between 0 (full dilution) and 1 (no dilution at all). The transit parameters that are allowed to vary for each planet are: the period of the orbit P, the reference time of the transit center T_0, the planet-to-star radius ratio $p = R_\mathrm{p}/R_s$, the relative semi-major axis a/R_s, the impact parameter b (from Eq. 1.6), the limb-darkening parameters (u_1, u_2), and (e, ω), respectively

the eccentricity and argument of periastron passage of the orbit. Instead of fitting directly for (p, b), in `juliet` we fit for two parameters (r_1, r_2) defined between 0 and 1, following the proposal of Espinoza 2018. Then (p, b) can be recovered with the following equations:

$$\begin{aligned} b &= [1 + p_l][1 + (r_1 - 1)/(1 - A_r)] \\ p &= (1 - r_2)p_l + r_2 p_u \end{aligned} \tag{2.37}$$

where (p_l, p_u) are respectively the lower and upper limit for p (e.g. 0 and 1 in the unconstrained case) and $A_r = (p_u - p_l)/(2 + p_l + p_u)$. This ensures that the condition $b < 1 + p$ is always satisfied without the need for rejecting any samples. Another parametrization is employed for the eccentricity and argument of periastron passage (e, ω), sampled as $\mathcal{S}_1 = \sqrt{e}\sin(\omega)$, $\mathcal{S}_2 = \sqrt{e}\cos(\omega)$ (defined between -1 and +1), following the suggestion of Eastman et al. 2013. Then the two parameters can be recovered from:

$$\begin{aligned} e &= \mathcal{S}_1^2 + \mathcal{S}_2^2 \\ \omega &= \arctan(\mathcal{S}_1/\mathcal{S}_2). \end{aligned} \tag{2.38}$$

Finally, as anticipated in Sect. 1.2.2, for the LDCs of each instrument (if the observed passbands are different) we employ the parametrization proposed in Kipping 2013, with (q_1, q_2) being defined between 0 and 1, from which we can retrieve the quadratic LDCs using the equations:

$$\begin{aligned} u_1 &= 2q_2\sqrt{q_1} \\ u_2 &= \sqrt{q_1}(1 - 2q_2). \end{aligned} \tag{2.39}$$

In addition, a common stellar density ρ_s is fitted for all the transiting exoplanets in the system, instead of a/R_s for each of them, because the latter can be recovered using Kepler's third law from the period of the respective planet (Sozzetti et al., 2007):

$$a/R_s = [(\rho_s G P^2)/(3\pi)]^{1/3} \tag{2.40}$$

where G is the gravitational constant. Hence, a Gaussian prior for the density can be set if the stellar parameters are well confined, which in turns helps to constrain the eccentricity, because the stellar density and the eccentricity both influence the transit duration. The stellar density retrieved from the combined fit and the one derived from the stellar parameters can in fact be significantly different when an eccentric planet is fitted on a circular orbit (see Van Eylen and Albrecht 2015 for the details). Finally, in order to generate the transit model, the inclination of the orbit is entered in `batman` via the transformation:

$$i_p = \arccos\left[\frac{b}{a/R_s}\left(\frac{1 + e\sin(\omega)}{1 - e^2}\right)\right]. \tag{2.41}$$

Instead, the RV model is given by:

$$\mathcal{M}_i(t_{i,l}) = \mathbb{K}(t_{i,l}) + \mu_i + \mathcal{Q}(t'_{i,l})^2 + A t'_{i,l} + B \tag{2.42}$$

where $\mathbb{K}(t_{i,l})$ should not be confused with the covariance matrix ($\mathcal{K}$), as it represents the full Keplerian signal of all the planets in the system and is computed using the open source Python package `radvel` (Fulton et al., 2018). μ_i is the systemic velocity measured by instrument i, while $\mathcal{Q}$ and A are the optional quadratic and linear terms along with the corresponding intercept B, which can be useful to catch long-period trends in the data (due to distant planetary/stellar companions and long-term activity). The trend should be common to all instruments, so it depends on a universal user-defined time $t'_{i,l}$. The parameters of the keplerian RV model are (for each planet): the period of the orbit P, the reference time of transit center T_0, the eccentricity and argument of periastron passage (e, ω), the systemic RV μ and the semi-amplitude of the RV variation due to the planet, K, which is the only parameter not in common with the transit model (along with μ). Refer to Table 2.1 for a summary of all the parameters involved for both models, excluded any parameter that may be included from GPs (see Section 2.5).

Table 2.1: List of parameters that define either the transit and RV models, or both, for instrument i. Note that (a) the planetary parameters should be defined for each planet in the system, (b) here, *uninformative* priors are uniformly distributed priors that encompass the whole range of physically possible values (e.g. [0,1[for e), while *uniform* priors can be restricted due to previous knowledge (e.g. the orbital period of a transiting TOI candidate). *The limb darkening coefficients may be different between instruments, if they observe different bandwidths; for *TESS*, a Gaussian prior might be sometimes preferred instead of a uninformative one.

Parameter	Unit	Model	Typical prior	Description
Planetary				
P	days	both	Uniform	Orbital period
T_0	days	both	Uniform	Reference time (transit-center)
p	—	transit	Uniform	Planet-to-star radius ratio, via (r_1, r_2)
b	—	transit	Uninformative	Impact parameter, via (r_1, r_2)
ρ_s	$\mathrm{g\,cm^{-3}}$	transit	Gaussian	Stellar mean density
e	—	both	Uninformative	Orbit eccentricity, via (S_1, S_2)
ω	deg	both	Uninformative	Argument of periastron, via (S_1, S_2)
K	$\mathrm{m\,s^{-1}}$	RV	Uniform	Velocity semi-amplitude
Instrumental				
D_i	—	transit	Fixed	Dilution factor
M_i	relative flux	transit	Uniform	Relative flux offset
$(u_{1,i}, u_{2,i})^*$	—	transit	Uninformative	LDCs
μ_i	$\mathrm{m\,s^{-1}}$	RV	Uniform	Systemic RV

Planet derived parameters

We can directly estimate the values and uncertainties of the orbital period P of a planet, along with its eccentricity e and argument of periastron ω (or their parametrizations), by sampling from the posterior distributions of the combined RV+transit analysis. Similarly, if the stellar radius R_s has been constrained (refer to Section 1.3), the planet radius R_p and the semimajor axis a can be derived respectively from $p = R_p/R_s$ and Eq. 2.40 (after P and ρ_s have been extracted from their posterior distributions as well). The orbit inclination can further be derived from Eq. 2.41, using b, ρ_s and P. At this point, the planet mass M_p can be recovered by reversing Eq. 1.5, which in the case of $M_s \gg M_p$ is simply:

$$M_p \approx K \frac{M_s^{2/3}}{\sin(i)} \frac{\sqrt{1-e^2}}{(2\pi G/P)^{1/3}} \tag{2.43}$$

after K has been evaluated from its posterior distribution, and assuming that the stellar mass M_s has also been constrained (Section 1.3). Now we can handily derive both the surface gravity g_p and the bulk density ρ_p of the planet, using their definitions:

$$g_p = \frac{GM_p}{R_p^2}, \tag{2.44}$$

$$\rho_p = \frac{3\,M_p}{4\pi R_p^3}. \tag{2.45}$$

Finally, for the calculation of the planetary equilibrium temperature T_{eq}, it is assumed that both the planet and the star are perfectly spherical black bodies and that the planet has uniform heat redistribution from the day side to the night side. The star emits isotropically according to the Stefan-Boltzmann law, i.e. based on its effective temperature T_{eff}. The incident radiation on the planetary surface is a portion of this radiation (depending on the distance, or semimajor axis) which is also partly reflected into space (depending on the planet surface's albedo A), before being absorbed, and thus heating the planet. Thermal equilibrium is achieved when the power transmitted from the star to the planet equals that lost by the planet into space, and the T_{eq} at which this equilibrium is reached is (see e.g., Pierrehumbert 2010):

$$T_{eq} = T_{eff}\,(1-A)^{1/4}\sqrt{\frac{R_s}{2a}}, \tag{2.46}$$

though the fraction of incoming light reflected back into space (the albedo) is difficult to determine and it's often fixed (e.g. to 0 or 0.5).

Chapter 3

Results

3.1 Target selection

For the purpose of discovering and characterizing new Neptunian exoplanets, I exploited the large and continuously-updated dataset of *TESS* planetary candidates, while the satellite is still finding new exoplanet candidates on its second extended mission (more than 5 years after its launch). At the beginning of this thesis work, *TESS* had found more than 2000 total candidates, of which only ≈ 100 had been confirmed, and at least as many were already discarded as false positives or known planets, while today they are respectively ≈ 7000 and ≈ 400. Half of the candidates are not observable in the northern hemisphere, where the TNG operates, and a lot of those are either smaller or bigger gaseous giant candidates.

In summary, for the purpose of optimizing the amount of observing time reserved within the GAPS group, I selected Neptunian TOIs using the following criteria:

- $2.5R_\oplus \lesssim R_\mathrm{p} \lesssim 6R_\oplus$ – This is the approximate range of Neptunian planets (leaving some margin for large sub-Neptunes);
- Host-star declination $\gtrsim -20$, or in general stars that could be observed for long periods of time at the TNG, at sufficiently low airmass values;
- $V \lesssim 12\,\mathrm{mag}$ – We excluded *dimmer* stars as they required longer exposure times, with the exception of targets with expected high signals such as TOI-1853;
- $N_\mathrm{obs} \lesssim 50 - 100$ – We excluded any target that was expected to require more than 1 or 2 semesters of observation (the equivalent of ≈ 50 or ≈ 100 measurements) in order for it to be confirmed and characterized (or its mass to be evaluated with a 5-10 σ level of significance).

I have estimated the number of expected observations using the available star properties from the TIC (Stassun et al., 2018), while evaluating the planetary mass with the empirical formula from Otegi et al. 2020 for volatile-rich planets:

$$M_\oplus = (1.74 \pm 0.38)\, R_\oplus^{1.58\pm0.10} \tag{3.1}$$

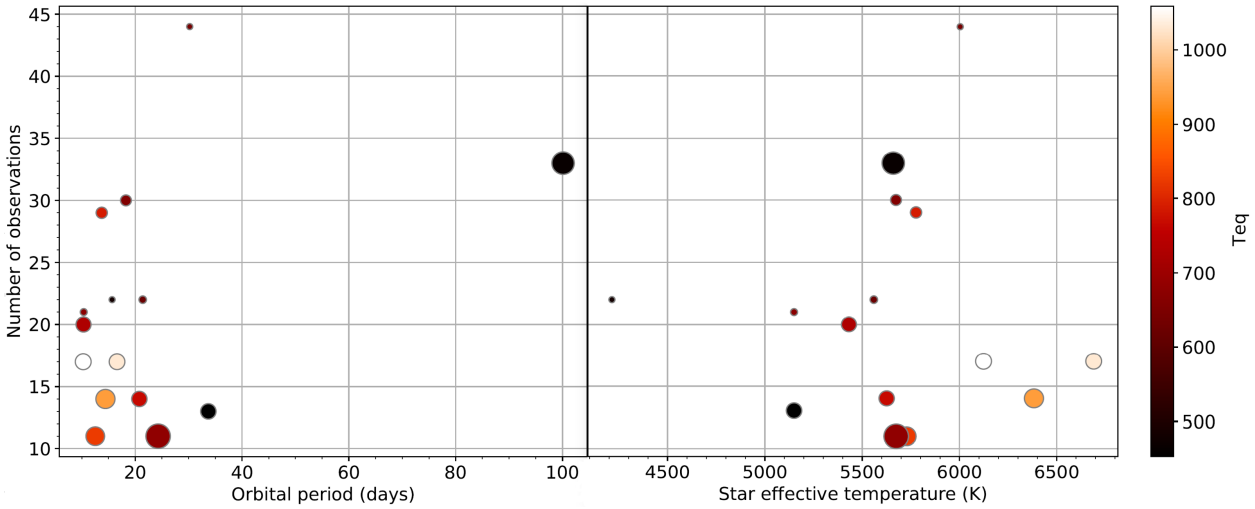

Figure 3.1: A display of optimal *TESS* candidates for RV follow-up at the TNG with HARPS-N, as evaluated in late 2020 for the scope of this PhD thesis. The expected number of observations required to confirm such candidates is plotted over the orbital period estimated with *TESS* light curves on the left, and over the star effective temperature on the right. The size of the circle is proportional to the size of the planet candidate, while their color is an estimation of their equilibrium temperature.

while I have estimated the RV uncertainty using the formula (Bouchy et al., 2001):

$$\delta V_{RMS} = \frac{c}{Q\sqrt{F_{\rm s}\, S_{\rm tel}\, e_{\rm tot}}} \sqrt{\frac{2.512\, V_{\rm mag}}{t_{\rm exp}}}\,, \tag{3.2}$$

where δV_{RMS} represents the uncertainty on the radial velocity change δV, c is the speed of light (in $\mathrm{m\,s^{-1}}$), Q is the star quality factor ($Q \approx 7000$ for mild active G0 stars), $F_{\rm s}$ is the integrated stellar flux (photons $\mathrm{cm^{-2}\ s^{-1}}$), $S_{\rm tel}$ is the telescope area, or $\pi \left(\frac{3.6\,m}{2}\right)^2$ for the TNG, $e_{\rm tot}$ is the total efficiency of the setup (≈ 0.05 for HARPS-N; including atmosphere, telescope, spectrograph and detector), t_{exp} is the exposure time (usually ≈ 15 minutes) and $V_{\rm mag}$ is the magnitude of the star in the V band.

Figure 3.1 shows the few remaining candidates from the very first screening. These candidates still needed to be filtered to minimize any potential time wasted on false positives (possibly signaled by low transit SNR, transit centroid offsets, V-shaped transits, odd-even transit depth differences, flux contaminations, etc.) or targets much more challenging than initially thought, often due to strong stellar variability (seen either in the light curve or in a preliminary spectroscopic follow-up[1]), other than candidate multiplicity in the same system. I have used several tools for this screening process, notably the GLS, BLS and TLS periodograms, as described in Sections 2.3.1 and 2.3.2, which have been of fundamental importance to measure respectively the level of stellar magnetic activity and the true strength of the transit signals (along with the river plot depicted in Figure 3.2). At last, the final targets were chosen to try to cover as much parameter space as possible; in particular, I chose both Warm and Hot Neptunes, mostly corresponding to relatively "long"

[1]The most important value to estimate via spectroscopic follow-up is $v \sin i$, i.e. the rotational velocity of a star as observed from Earth, where i is the unknown inclination angle of the star relative to the line of sight. It is an indication of how active the star is (young stars rotate quicker than old stars because stars lose angular momentum over time, and younger stars are usually more active), and it's also an indication of the RV error (as fast rotators present broader spectral lines).

($P_{\rm orb}$ > 10 days) and "short" orbital periods ($P_{\rm orb}$ < 10 days), at the same time avoiding any possible target conflict with other similar follow-up observing groups. However, the target list was often updated during the past 3 years in order to replace confirmed planets and quickly catch new promising TOIs. The analyses of the TOI-1422 and TOI-1853 systems have been presented in detail in Chapters 4 (Naponiello et al., 2022) and 5 (Naponiello et al. 2023, Nature), while the (full or partial) results for the other targets are detailed in the following sections in chronological order, aside from the latest targets TOI-5544, TOI-5706 and TOI-5817, whose observations started in 2023 and are still on-going (see Table 3.1 for a summary).

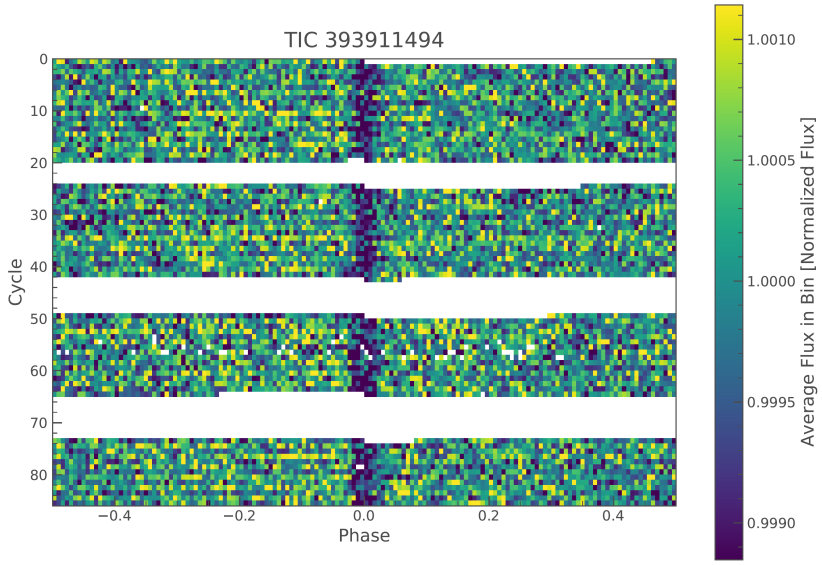

Figure 3.2: Example of river plot for TOI-2106.01, which was part of my screening process. In the river plot, each transit is displayed as a single row, so that all the transit signals should appear as a vertical dark river at the center of the plot. Any variation can be an indication of false positives, incorrect periods estimation or TTVs (due to other stellar or planetary companions).

3.2 The super-Neptune TOI-1710 b

TOI-1710 is a G5V dwarf star which was observed by *TESS* in Sectors 19-20, 26 and 40, and was first identified as the host of an exoplanetary candidate in the *TESS* DV report of early August 2020. The candidate TOI-1710.01 passed all the *TESS* validation tests and had been measured to have a radius of $\approx 5.3\,R_{\oplus}$ and an orbital period of $\approx$ 24.3 days. In the framework of the GAPS project, my collaborators collected 31 high-resolution spectra using the HARPS-N spectrograph between October 2020 and April 2021, with an extracted RV precision ranging from 0.9 to 3.4 m s^{-1} and a median value of 1.4 m s^{-1}, revealing a RMS of 6.1 m s^{-1}. Almost in the same time span, a RV follow-up campaign for TOI-1710 was executed with SOPHIE, a stabilized échelle high-resolution spectrograph installed at the 1.93-meter telescope of the Observatoire de Haute-Provence in France, totalling 30 RVs with precisions ranging from 2.3 to 2.9 m s^{-1}, a median value of 2.4 m s^{-1} and a similar RMS of 7.4 m s^{-1}. The common purpose of the two independent campaigns was to establish the planetary nature of the transiting candidate and to characterize its properties. Our results have been published in König, Damasso, Hébrard, Naponiello, et al. (2022) where the leading author and I jointly analyzed the HARPS-N and SOPHIE data.

Table 3.1: List of chosen *TESS* candidates. The first three (TOI-1272, TOI-1422 and TOI-1694) were selected before the start of the thesis work by the GAPS Neptunian subgroup; however, they have been analyzed and/or published during this PhD thesis work. (*) In the Status column, the letters S, MA and IA stand for, respectively, Selection, Main Analysis and Independent Analysis, and they represent my role in the published or coming paper.

TOI Candidate	Orbital period (days)	Expected radius ($R_\oplus$)	Measured radius ($R_\oplus$)	Expected mass ($M_\oplus$)	Measured mass ($M_\oplus$)	Status (my role*)
TOI-1272 b	3.32	4.59	4.14 ± 0.21	19.15	24.6 ± 2.3	In-prep (IA)
TOI-1272 c	8.69	–	–	–	$> 26.7 \pm 3.1$	In-prep (IA)
TOI-1272 d	13.07	–	–	–	$> 14.0 \pm 2.7$	In-prep (IA)
TOI-1422 b	13.00	3.85	3.96 ± 0.13	14.64	9.0 ± 2.3	Published (MA)
TOI-1422 c	29.3	–	–	–	$> 11.1 \pm 2.6$	Published (MA)
TOI-1694 b	3.77	5.48	5.33 ± 0.10	25.58	29.2 ± 1.5	In-prep (MA)
TOI-1694 c	383	–	–	–	$> 313 \pm 13$	In-prep (MA)
TOI-1710 b	24.28	5.40	5.34 ± 0.11	24.99	28.3 ± 4.7	Published (IA)
TOI-1794 b	8.76	2.97	–	9.12	–	In-prep (S)
TOI-1803 b	6.29	2.99	–	16.56	–	In-prep (S)
TOI-1803 c	12.89	4.22	–	9.21	–	In-prep (S)
TOI-1853 b	1.24	3.78	3.46 ± 0.08	14.22	73.2 ± 2.7	Published (S+MA)
TOI-2443 b	15.67	2.69	2.72 ± 0.27	8.31	6.3 ± 1.3	In-prep (S+MA)
TOI-5076 b	23.44	3.13	3.2 ± 0.1	10.56	15 ± 2	Submitted (S+IA)
TOI-5544 b	4.21	3.32	–	11.59	–	On-going (S)
TOI-5706 b	0.36	3.41	–	12.09	–	On-going (S)
TOI-5817 b	15.61	3.03	–	10.03	–	On-going (S)

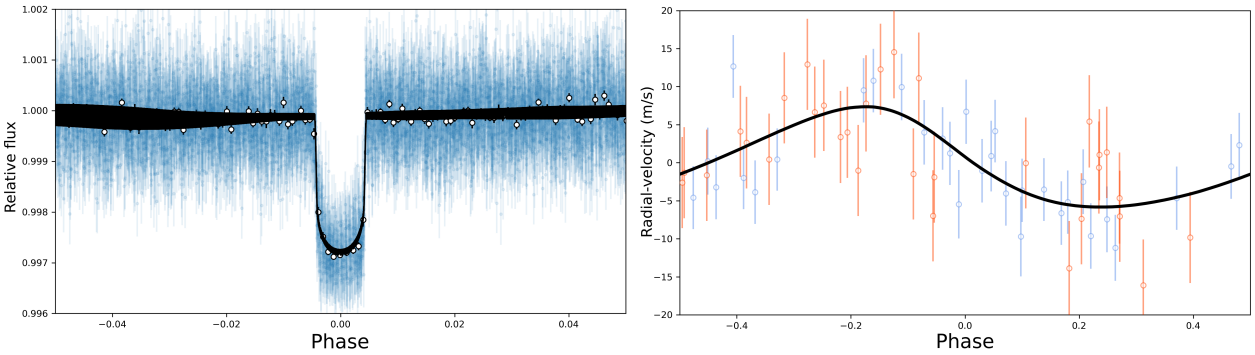

Figure 3.3: On the left, the *TESS* light curve is folded in phase with TOI-1710 b's best-fit model period of my independent analysis. The binned light curve is shown by black circles, while the black line is the best-fit of the entire light curve (taking into account both the transits and some modulation). On the right, both the RVs of HARPS-N (in blue) and SOPHIE (in red) are folded with the same period, while the solid line represents the best orbital solution.

My collaborators derived the host atmospheric parameters ($T_{\rm eff}$, the metallicity [Fe/H], the microturbulence velocity ξ and the surface gravity $\log g$) from the coadded HARPS-N spectra using the equivalent widths of the iron emission lines (i.e. a measurement of the intensity of a line in the spectrum) and a grid of model atmospheres. The physical parameters ($R_{\rm s}$, $M_{\rm s}$ and age) have been estimated fitting the SED and using the isochrones and stellar tracks, while the stellar rotation period has been estimated via three different methods for an average of $<P_{\rm rot}>= 22.5 \pm 2.0$ days (however the accuracy of this estimation is unclear; see König et al. 2022 for the details), which is compatible with the orbital period of the planet candidate. Despite this complication, the planet contribution to the RV signal is quite evident in the SOPHIE + HARPS-N dataset, and therefore

my collaborators and I were able to confirm the planetary nature of TOI-1710.01 (now TOI-1710 b) with a combined analysis of the spectroscopic data along with *TESS* photometry. The detailed analysis revealed a planet larger than Neptune, $R_p = 5.34 \pm 0.11\, R_\oplus$, with a mass $M_p = 28.3 \pm 4.7\, M_\oplus$ and thus a bulk density of $\rho_p = 0.94 \pm 0.22$ g cm^{-3}, revolving on a quasi-circular orbit every 24.283429 ± 0.000043 days (Figure 3.3). Due to its relatively long orbital period and eccentricity compatible with zero ($e_p = 0.16 \pm 0.08$), TOI-1710 b may have migrated to its current position during the disc phase. The dispersion of the RV residuals is higher than expected, probably due to the rotation period of the star; however, the planet parameters have been proven to be consistent with other analyses which included different GP kernels for the modelling of stellar activity.

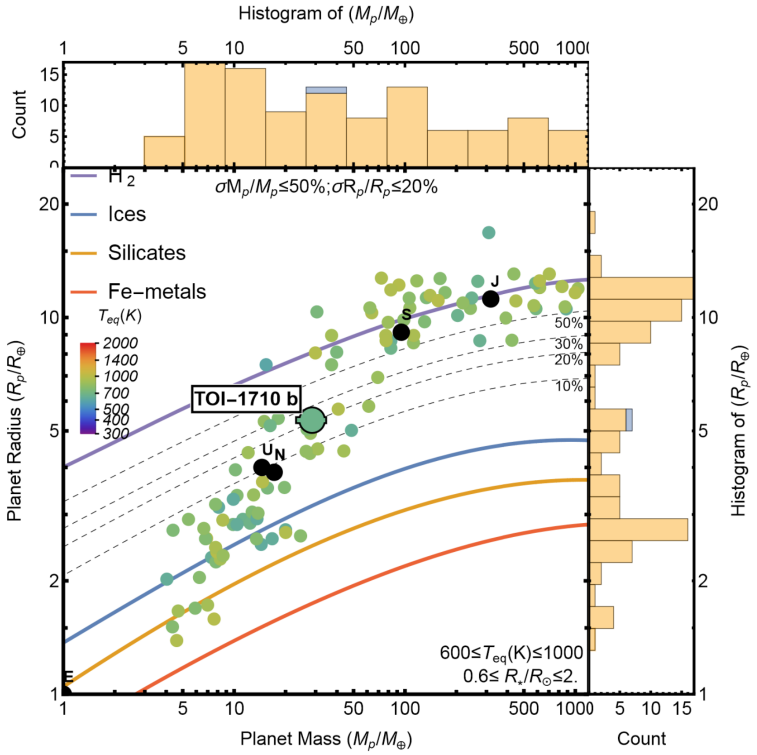

Figure 3.4: Radius-mass diagram of known transiting exoplanets (before the publication date) with equilibrium temperature $T_{\rm eq}$ between 600 and 1000 K and precise radius-mass measurements. The dashed lines show the composition models with a relatively cold hydrogen envelope of mass fractions of 10, 20, 30 and 50%. The solar system planets are shown as black dots. Figure courtesy of König et al. 2022.

TOI-1710 b fits well inside a radius-mass diagram (Figure 3.4), and it is slightly beyond Uranus and Neptune, both in mass and radius, or right below the domain of giant gaseous planets. In terms of composition, due to a bulk density lower than that of Neptune, TOI-1710 b is likely to have a thicker gaseous envelope (amounting to $20 - 30\%$ of its mass fraction) on top of an ice-rich core. With an equilibrium temperature of $T_{\rm eq} = 687 \pm 50$ K, it can potentially be a good candidate for atmospheric characterization by *JWST*, as it falls in its second quartile rank for transmission spectroscopy follow-up efforts, although being one of the candidates with the brightest host stars.

3.3 The multi-planet systems TOI-1272 and TOI-1694

The two systems TOI-1272 and TOI-1694 were unexpectedly chosen as targets also by another group in their RV follow-up campaign. Specifically, within the *TESS*-Keck Survey, TOI-1272 was chosen for an apparent mismatch between the observed transit duration and the expected duration for a circular orbit (see the upper panel of Figure 3.5), which was interpreted as a sign of possible eccentricity (even if this effect may also be caused by a low value of the impact parameter). Conversely, TOI-1694 was chosen as a potential host of a distant gas giant, due to elevated RV variability (unrelated to the Neptune-sized candidate TOI-1694 b). Two research papers (MacDougall et al. 2022 and Van Zandt et al. 2023, respectively) have been published while we were still observing these objects. The HIRES instrument at the Keck Observatory obtained 62 and 20 spectra respectively, which were enough to confirm the planetary nature of candidates TOI-1272.01 (now TOI-1272 b), TOI-1694.01 (now TOI-1694 b) along with a companion for each of them, TOI-1272 c and TOI-1694 c. However, with HARPS-N my collaborators also took 94 and 90 spectra of both stars, and the combined data set holds additional surprises (Pinamonti, Naponiello et al, in preparation).

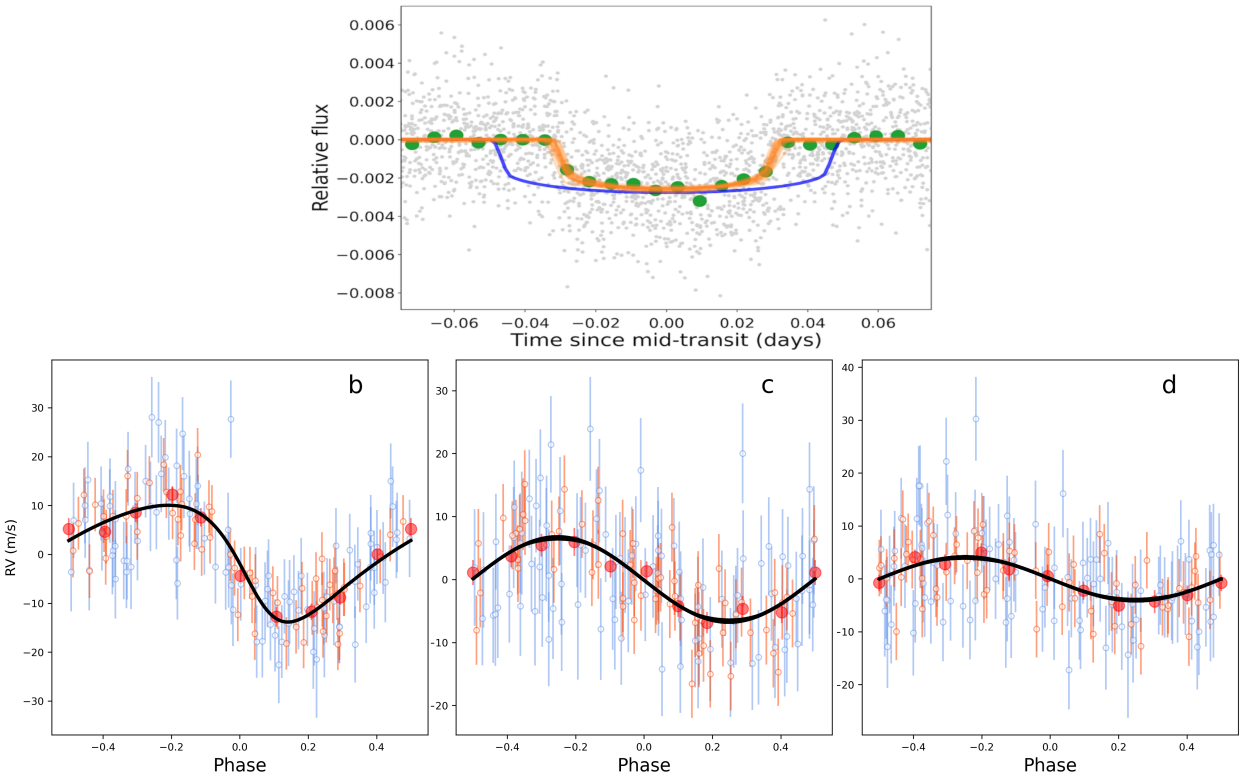

Figure 3.5: On the top, the phase-folded transits of TOI-1272 b are shown along with their transit model fits (in orange), and their expected shape (or duration) for a circular orbit (in blue) – from MacDougall et al. 2022. On the bottom, the best-fit models (black lines) of HIRES (in red) and HARPS-N (in blue) RVs, phase-folded respectively for TOI-1272 b, TOI-1272 c and candidate TOI-1272 d (from my preliminary analysis, but see MacDougall et al. 2022 for a comparison of the first two RV phase plots).

In particular, with HIRES alone, TOI-1272 b was revealed to be a Neptune-like planet with a radius of $4.1 \pm 0.2\, R_\oplus$, a mass of $24.6 \pm 2.3\, M_\oplus$ and thus a bulk density of 1.9 ± 0.3 g cm^{-3}, revolving every 3.31599 ± 0.00002 days around its parent star on an elliptic orbit ($e_\mathrm{b} = 0.34 \pm 0.06$). A strong secondary signal was also detected and attributed to a non-transiting planet, TOI-1272 c, on a close,

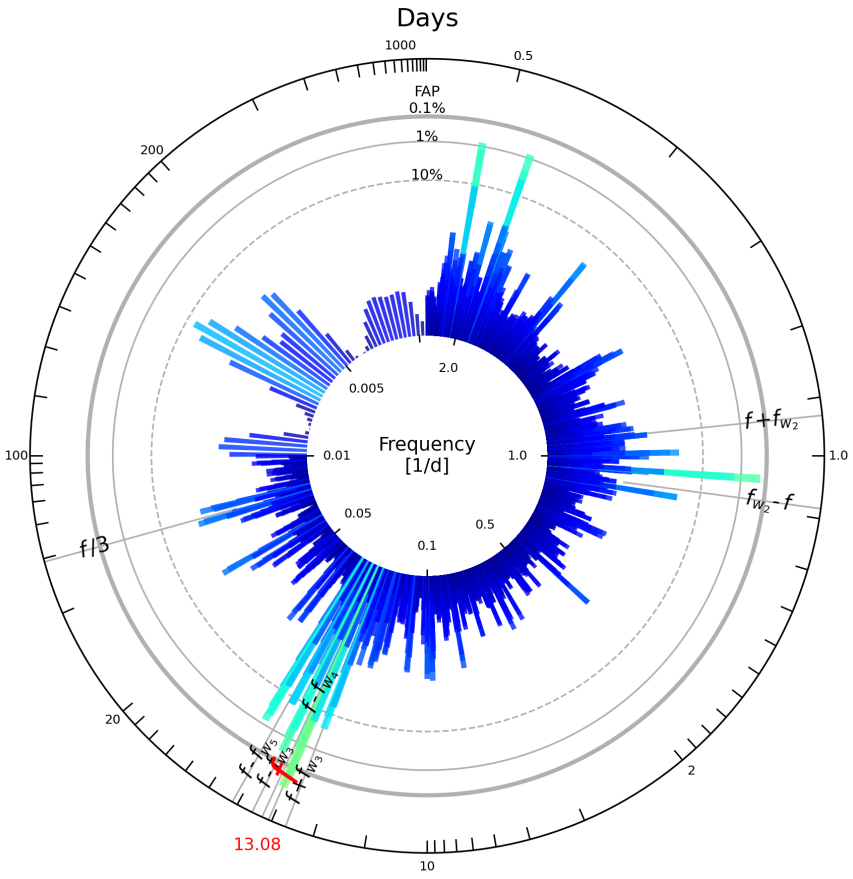

Figure 3.6: The GLS periodogram of the residuals of the eccentric 2-planet best-fit model for the joint HIRES+HARPS-N RV data set of TOI-1272, plotted as a function of both days and frequency (1/days) respectively on the outside and the inside of the circle. The periodogram peaks are represented by columns, resembling the hands of a clock, with a color scale ranging from blue to green depending on their intensity. The three circles (dashed, normal and bold) represent the 0.1%, 1% and 10% FAP levels. The highest peak (f) is identified in red, along with its possible aliases (in black), including those related to the window function peaks (f_w, ordered by intensity). The remaining peaks with a FAP of $\approx$1% are close to the notorious 1-day and 0.5-day window function peaks, with the exclusion of the one at $\approx$14.5 days.

likely circular orbit with $P_c = 8.689 \pm 0.008$ days and $M_c \sin i = 26.7 \pm 3.1\, M_\oplus$ (Figure 3.5). After the subtraction of the two planetary signals from the RVs, a low-significance residual at 14.1 days appeared in the GLS periodogram. This peak was identified as the first harmonic ($P_{rot}/2$) of the $\approx$ 28.3-day stellar rotation, as derived from *TESS* photometry and the activity indexes extracted by HIRES (see MacDougall et al. 2022 for the details). With the addition of HARPS-N RVs, the highest peak in the GLS of the RV residuals of any 2-planet model (both with free or fixed eccentricity) is clearly shifted towards a periodicity of $\approx$13.1 days, with very high significance (FAP $\ll$ 0.01%), and it is surrounded by other peaks, including one at $\approx$14.5 days (similar to the period identified by HIRES) as represented by the GLS *clock* I created (Figure 3.6). According to my preliminary analysis, a third planet, TOI-1272 d, is more likely to be the source of the 13-day peak, as a simple 3-planet model appears statistically favoured over any 2-planet model, including one with a GP kernel to treat the 14.5-days signal as stellar activity. Moreover, the 14.5-days signal is still present in the RV residuals of the 3-planet model (without GPs), suggesting that the two signals are of different nature, even though they are close. If TOI-1272 d exists, then its minimum mass is $\approx$ 15 $M_\oplus$ and it would be almost exactly on a 3:2 resonance with TOI-1272 c. In any case, the combined RV data set,

along with *TESS* photometry, has allowed me and Pinamonti (paper in prep.) not only to identify a promising new planet in the system, but also to better constrain the two inner planets parameters, such as the eccentricity of TOI-1272 b ($e_b = 0.29 \pm 0.04$) and the mass of TOI-1272 c (which is a bit lower than measured with HIRES, at $\approx 21\, M_\oplus$), and to highlight a potential linear trend in the RVs.

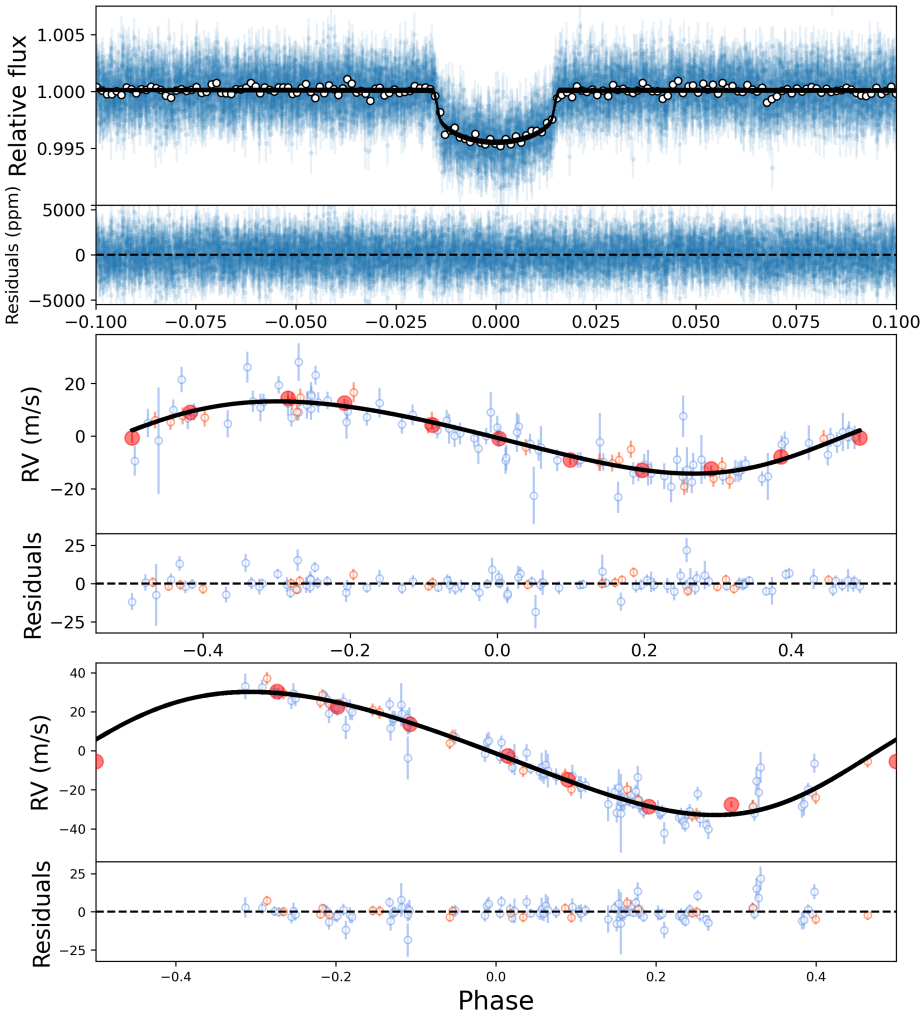

Figure 3.7: On the upper panel, the *TESS* transits of TOI-1694 b are phase-folded, and their best fit is displayed by a black line with its residuals below. The bottom panels show, respectively, the best-fit RV models of TOI-1694 b and TOI-1694 c (with HIRES data in orange and HARPS-N in blue), along with their residuals. The red points represent averages of the RVs.

Similarly, the early K dwarf star TOI-1694 was also found to host at least two planets with HIRES data (Van Zandt et al., 2023). TOI-1694 b was revealed to be a super-Neptune of radius $5.44 \pm 0.18\, R_\oplus$ (from the *TESS* DV report) and mass $26.1 \pm 2.2\, M_\oplus$, at the edge of the hot-Neptune desert, while TOI-1694 c is a gas giant with the mass of Jupiter ($M_c \sin i = 1.05 \pm 0.05\, M_{jup}$) on a moderate elliptic orbit ($e_c = 0.18 \pm 0.05$) with a long orbital period of 389.2 ± 3.9 days (therefore, a Cold Jupiter). In this case, my preliminary joint analysis (Pinamonti, Naponiello in prep.) of RVs and photometry (which was not performed in Van Zandt et al. 2023), HARPS-N RVs included, finds better constraints for all the parameters, and no residual signal is present in the data. In my analysis (refer to Figure 3.7), the eccentricity of TOI-1694 c is lower than previously reported ($e_c = 0.135 \pm 0.029$), while TOI-1694 b is also revealed to be eccentric ($e_b = 0.123 \pm 0.025$) and

thus slightly more massive, $M_p = 29.2 \pm 1.5\,M_\oplus$, with a bulk density of $1.06 \pm 0.08\,\mathrm{g\,cm^{-3}}$. At the same time, I have reassessed both the period and the mass of TOI-1694 c ($P_c = 382.8 \pm 2.4$ days, $M_c \sin i = 0.98 \pm 0.04\,M_{jup}$).

3.4 A sub-Neptune orbiting a thick disk star in a wide binary system: TOI-5076 b

My collaborators and I observed the nearby K2 V star TOI-5076 with HARPS-N from August 2022 to March 2023 and obtained a total of 44 spectra and RVs. TOI-5076 is part of a wide binary system, with the stellar companion being at 2178 au of distance (which shouldn't affect the architecture of its planetary system – Montalto et al, submitted), and is also part of a metal-rich population of neighbour stars with kinematics that make it consistent with old, thick disk (or thin-to-disk transition) stars. This makes TOI-5076 b one of the first warm, transiting Neptune-like planets that is not orbiting around a thin disk star (Biazzo et al., 2022).

The combined analysis of *TESS* photometry and HARPS-N RVs (see Figure 3.8) reveals that TOI-5076 b has a radius of $3.2 \pm 0.3\,R_\oplus$, a mass of $15 \pm 2\,M_\oplus$ and thus a bulk density of $2.5 \pm 0.8\,\mathrm{g\,cm^{-3}}$, and it orbits every 23.445 ± 0.001, with a very uncertain eccentricity of $e_b = 0.2 \pm 0.1$ (M. Montalto et al, submitted). Using its physical parameters, we can infer that TOI-5076 b is either a pure water world or it is composed of an Earth-like rocky core ($\approx 50\%$ by mass) with a H_2O layer (also $\approx 50\%$ by mass) and possibly a thin layer of H_2 envelope on top, though alternatively its core could also amount for 98% of its mass, with the remaining mass could be packed in a H_2 envelope.

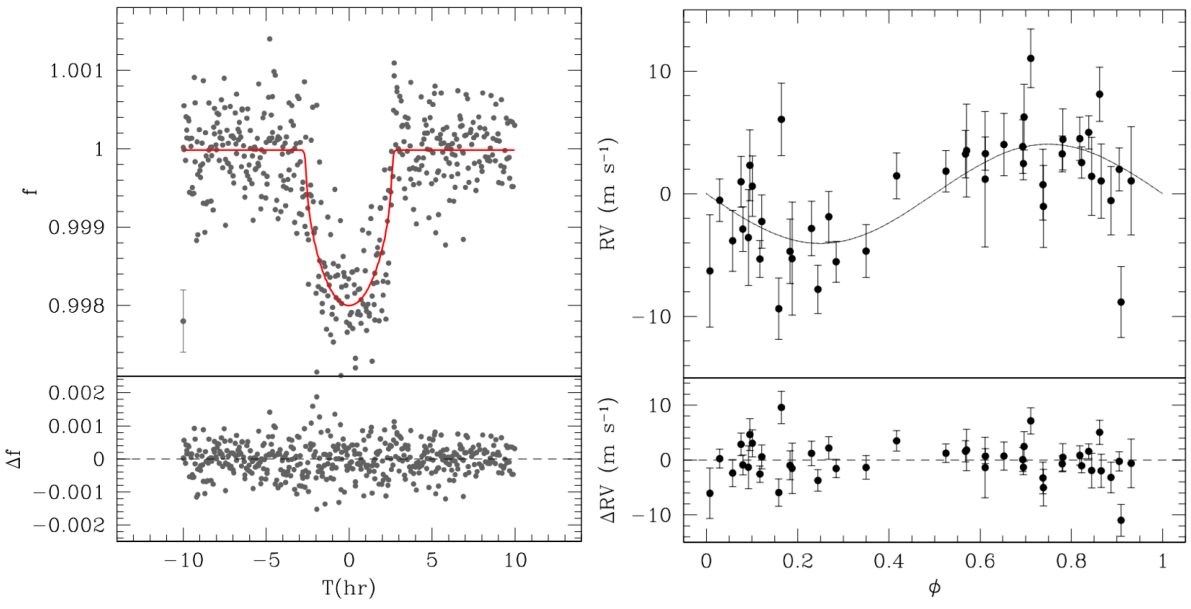

Figure 3.8: On the left, the phase-folded transits of TOI-5076 b along with their best-fit in red, and the residuals at the bottom. On the right, the phase-folded RVs as taken by HARPS-N, along with the best-fit (black line) and their residuals. Figure courtesy of M. Montalto et al (submitted).

3.5 The sub-Neptune TOI-2443 b

TOI-2443 is a K dwarf star that my collaborators and I have followed from July 2021 to January 2023, acquiring a total of 96 observations. My preliminary combined analysis of *TESS* photometry and HARPS-N RVs (Figure 3.10) uncovers the smallest planet of the sample, a sub-Neptune with radius $2.72 \pm 0.27\,R_\oplus$ and mass $6.3 \pm 1.3\,M_\oplus$, or a bulk density of 1.7 ± 0.7 g cm^{-3} (Naponiello et al, in prep.). Using the GLS periodogram, I found a peak at ≈ 53 days in the $\log R'_{\rm HK}$, similarly to the FWHM and the Contrast activity indexes (see Figure 3.9). A peak at ≈ 26.5 (53/2) days can be found instead in the residuals of the one-planet RV model, along with a weaker, but significant peak at 13.25 (53/4) days. The corresponding RV signal at 26.5 days has a weak amplitude of $2 - 3\,{\rm m\,s^{-1}}$, which is compatible with the activity of a medium-aged star, so together with the information extracted from the activity indexes, I interpret this peak as being the stellar rotation period (with the 53 and 13.25 peaks being respectively its $2\times$ and $1/2\times$ harmonics). However, this weak signal is still comparable in amplitude to the signal of TOI-2443 b, which is orbiting every 15.668662 ± 0.000008 days, or close to $P_{\rm rot}/2$, therefore in the combined analysis I employed a quasi-periodic GP (see Section 2.5) to disentangle the two contributions and to better constrain the planetary parameters. In my preliminary analysis, I found a small (not very significant) statistical advantage for the eccentric model compared to the circular one. A hint that the orbit might be eccentric also comes from the stellar density, which in the circular case results to be much lower than expected (see Section 2.6), although the overall evidence is not yet sufficient to state it with certainty (since $e_{\rm b} = 0.22 \pm 0.10$).

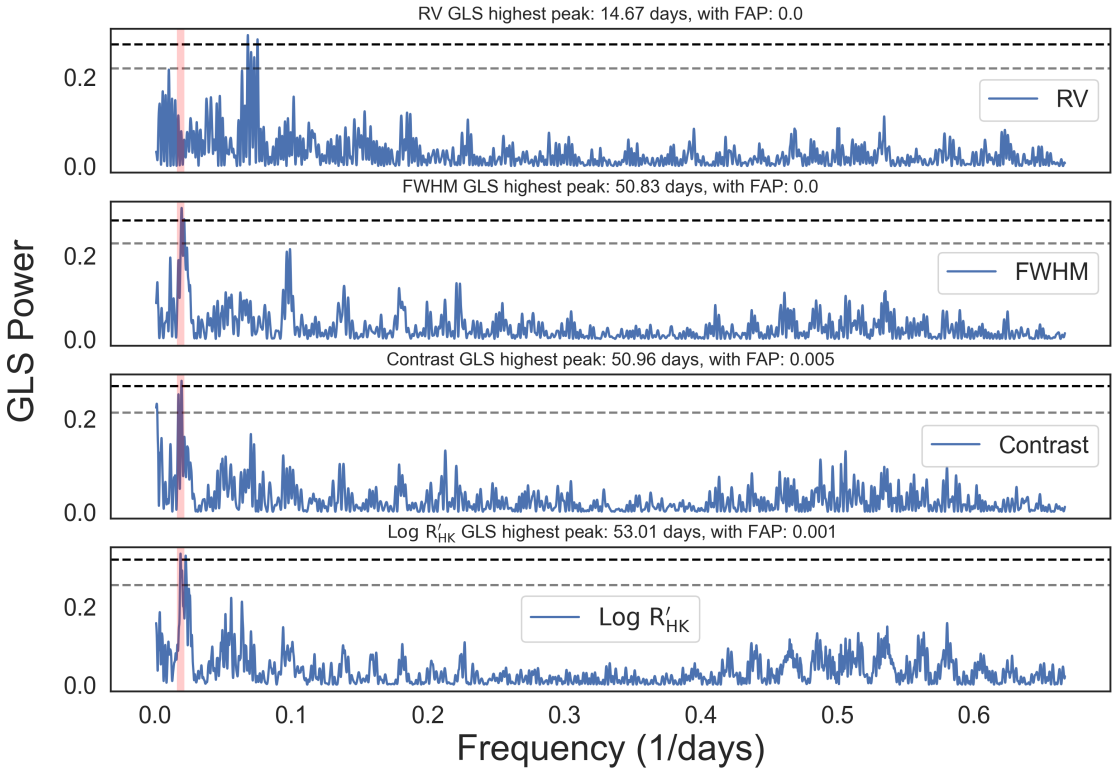

Figure 3.9: GLS periodogram results for the RV, FWHM, Contrast and $\log R'_{\rm HK}$ of TOI-2443. The peak at 53 days is highlighted in red.

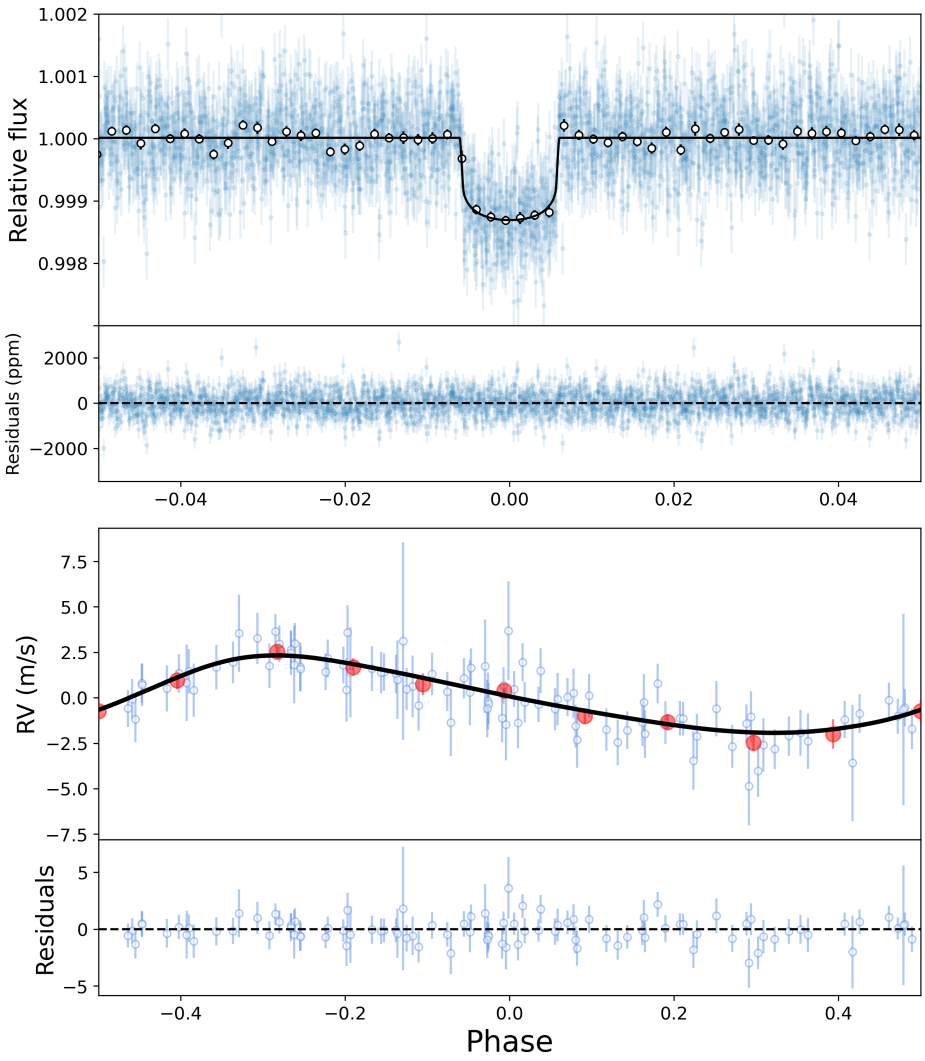

Figure 3.10: *Top panel*: the *TESS* transits of TOI-2443 b are phase-folded and their best fit is displayed by a black line along with its residuals below, in my preliminary joint analysis. *Bottom panel*: The top part shows the phased HARPS-N RV measurements together with our best-fitting model (zero-phase corresponds to the time of mid-transit); the bottom part shows the velocity O–C residuals from the best fit.

First result as leading author: the TOI-1422 system

The stellar system TOI-1422 was selected as a candidate by the GAPS team (A. S. and A. S. B.) before the start of this PhD thesis, however the analysis of this Neptune-sized hosting system was entrusted to myself after the experience gained in analyzing the TOI-1710 system (Section 3.2) and the fruitful collaboration that lead to its publication (König et al., 2022). In particular, I was responsible for the combined analysis of both the *TESS* light curve and HARPS-N RVs. I also conducted the activity indexes analysis, and I discovered the extra transit in *TESS* light curve. Finally, I handled the collaboration with all the co-authors and teams involved, and I wrote the manuscript. Notably, L. M., A. S. B., A. S. and M. D. supervised the work and contributed to writing the manuscript. A. S. B. and K. B. determined the stellar parameters, while L. Z. analyzed the planet's composition.

Note: the upcoming chapter serves as a continuation of Chapter 3, and has been formatted as a standalone chapter only for improved indexing visualization.

Chapter 4

A puffy and warm Neptune-sized planet and an outer Neptune-mass candidate orbiting the solar-type star TOI-1422.

Astronomy & Astrophysics 667, A8 (2022)

Authors

L. Naponiello[1,2], L. Mancini[1,3,4], M. Damasso[3], A. S. Bonomo[3], A. Sozzetti[3], D. Nardiello[6,7], K. Biazzo[5], R. G. Stognone[8], J. Lillo-Box[9], A. F. Lanza[14], E. Poretti[18,19], J. J. Lissauer[35,36], L. Zeng[10,11], A. Bieryla[32], G. Hébrard[21,22], M. Basilicata[1], S. Benatti[15], A. Bignamini[12], F. Borsa[18], R. Claudi[7], R. Cosentino[19], E. Covino[13], A. de Gurtubai[19], X. Delfosse[24], S. Desidera[7], D. Dragomir[33], J. D. Eastman[32], Z. Essack[30,31], A. F. M. Fiorenzano[19], P. Giacobbe[3], A. Harutyunyan[19], N. Heidari[25,26,23], C. Hellier[39], J. M. Jenkins[34], C. Knapic[12], P.-C. König[20,21], D. W. Latham[32], A. Magazzù[37], A. Maggio[15], J. Maldonado[15], G. Micela[15], E. Molinari[16], M. Molinaro[12], E. H. Morgan[28], C. Moutou[27], V. Nascimbeni[7], E. Pace[2], I. Pagano[14], M. Pedani[19], G. Piotto[17], M. Pinamonti[3], E. V. Quintana[29], M. Rainer[18], G. R. Ricker[31], S. Seager[28,30,40], J. D. Twicken[34,35], R. Vanderspek[28], and J. N. Winn[38].

[1] Department of Physics, University of Rome "Tor Vergata", Via della Ricerca Scientifica 1, 00133, Rome, Italy

[2] Department of Physics and Astronomy, University of Florence, Largo Enrico Fermi 5, 50125 Firenze

[3] INAF – Turin Astrophysical Observatory, via Osservatorio 20, 10025, Pino Torinese, Italy

[4] Max Planck Institute for Astronomy, Königstuhl 17, 69117 – Heidelberg, Germany

[5] INAF – Osservatorio Astronomico di Roma, via Frascati 33, 00040, Monte Porzio Catone (RM), Italy

[6] Aix-Marseille Université, CNRS, CNES, LAM, Marseille, France

[7] INAF – Osservatorio Astronomico di Padova, Vicolo dell'Osservatorio 5, 35122, Padova, Italy

[8] Dipartimento di Fisica, Universitá degli Studi di Torino, via Pietro Giuria 1, 10125, Torino, Italy

[9] Centro de Astrobiología, Depto. de Astrofísica, ESAC campus, 28692, Villanueva de la Cañada (Madrid), Spain

[10] Center for Astrophysics, Harvard & Smithsonian, 60 Garden Street, Cambridge, MA 02138, USA

[11] Department of Earth and Planetary Sciences, Harvard University, 20 Oxford Street, Cambridge, MA 02138, USA

[12] INAF – Osservatorio Astronomico di Trieste, via Tiepolo 11, 34143, Trieste, Italy

[13] INAF – Osservatorio Astronomico di Capodimonte, Salita Moiariello 16, 80131, Naples, Italy

[14] INAF – Osservatorio Astrofisico di Catania, via S. Sofia 78, 95123, Catania, Italy

[15] INAF – Osservatorio Astronomico di Palermo, Piazza del Parlamento, 1, 90134, Palermo, Italy

[16] INAF – Osservatorio Astronomico di Cagliari, via della Scienza 5, 09047, Selargius (CA), Italy

[17] Dipartimento di Fisica e Astronomia "Galileo Galilei" – Università di Padova, Vicolo dell'Osservatorio 2, 35122, Padova, Italy

[18] INAF – Osservatorio Astronomico di Brera, Via E. Bianchi 46, 23807, Merate (LC), Italy

[19] Fundaciòn Galileo Galilei - INAF, Rambla Josè Ana Fernandez Pérez 7, 38712 Breña Baja, TF, Spain

[20] European Southern Observatory, Karl-Schwarzschild-Straße 2, D-85748 Garching, Germany

[21] Institut d'Astrophysique de Paris, CNRS, UMR 7095 & Sorbonne Université, UPMC Paris 6, 98bis Bd Arago, 75014 Paris, France

[22] Observatoire de Haute-Provence, CNRS, Université d'Aix-Marseille, 04870 Saint-Michel-l'Observatoire, France

[23] Aix-Marseille Université, CNRS, CNES, LAM, Marseille, France

[24] Université Grenoble Alpes, CNRS, IPAG, 38000 Grenoble, France

[25] Department of Physics, Shahid Beheshti University, Tehran, Iran

[26] Laboratoire J.-L. Lagrange, OCA, Université de Nice-Sophia Antipolis, CNRS, Campus Valrose, 06108 Nice Cedex 2, France

[27] IRAP, Université de Toulouse, CNRS, UPS, CNES, F-31400 Toulouse, France

[28] Department of Physics and Kavli Institute for Astrophysics and Space Research, Massachusetts Institute of Technology, Cambridge, 02139, USA

[29] NASA Goddard Space Flight Center, 8800 Greenbelt Road, Greenbelt, MD 20771, USA

[30] Department of Earth, Atmospheric and Planetary Sciences, Massachusetts Institute of Technology, Cambridge, MA 02139, USA

[31] Kavli Institute for Astrophysics and Space Research, Massachusetts Institute of Technology, Cambridge, MA 02139, USA

[32] Harvard-Smithsonian Center for Astrophysics, 60 Garden Street, Cambridge, MA 02138, USA

[33] Department of Physics and Astronomy, University of New Mexico, 210 Yale Blvd NE, Albuquerque, NM 87106, USA

[34] NASA Ames Research Center, Moffett Field, CA 94035, USA

[35] SETI Institute, Mountain View, CA 94043, USA

[36] Space Science & Astrobiology Division MS 245-3

[37] INAF-Telescopio Nazionale Galileo, Apartado 565, E-38700, Santa Cruz de La Palma, Spain

[38] Department of Astrophysical Sciences, Princeton University, Princeton, NJ 08544, USA

[39] Astrophysics Group, Keele University, Staffordshire, ST5 5BG, UK

[40] Department of Aeronautics and Astronautics, MIT, 77 Massachusetts Avenue, Cambridge, MA 02139, USA

[41] INAF – Osservatorio Astrofisico di Arcetri, Largo E. Fermi 5, 50125, Florence, Italy.

Abstract

Neptunes represent one of the main types of exoplanets and have chemical-physical characteristics halfway between rocky and gas giant planets. Therefore, their characterization is important for understanding and constraining both the formation mechanisms and the evolution patterns of planets. We investigate the exoplanet candidate TOI-1422 b, which was discovered by the *TESS* space telescope around the high proper-motion G2 V star TOI-1422 ($V = 10.6$ mag), 155 pc away, with the primary goal of confirming its planetary nature and characterising its properties. We monitored TOI-1422 with the HARPS-N spectrograph for 1.5 years to precisely quantify its radial velocity (RV) variation. We analyse these RV measurements jointly with *TESS* photometry and check for blended companions through high-spatial resolution images using the AstraLux instrument. We estimate that the parent star has a radius of $R_\star = 1.019^{+0.014}_{-0.013}\,R_\odot$, and a mass of $M_\star = 0.981^{+0.062}_{-0.065}\,M_\odot$. Our analysis confirms the planetary nature of TOI-1422 b and also suggests the presence of a Neptune-mass planet on a more distant orbit, the candidate TOI-1422 c, which is not detected in *TESS* light curves. The inner planet, TOI-1422 b, orbits on a period of $P_\mathrm{b} = 12.9972 \pm 0.0006$ days and has an equilibrium temperature of $T_\mathrm{eq,b} = 867 \pm 17$ K. With a radius of $R_\mathrm{b} = 3.96^{+0.13}_{-0.11}\,R_\oplus$, a mass of $M_\mathrm{b} = 9.0^{+2.3}_{-2.0}\,M_\oplus$ and, consequently, a density of $\rho_\mathrm{b} = 0.795^{+0.290}_{-0.235}\,\mathrm{g\,cm^{-3}}$, it can be considered a warm Neptune-sized planet. Compared to other exoplanets of a similar mass range, TOI-1422 b is among the most inflated, and we expect this planet to have an extensive gaseous envelope that surrounds a core with a mass fraction around $10\% - 25\%$ of the total mass of the planet. The outer non-transiting planet candidate, TOI-1422 c, has an orbital period of $P_\mathrm{c} = 29.29^{+0.21}_{-0.20}$ days, a minimum mass, $M_\mathrm{c} \sin i$, of $11.1^{+2.6}_{-2.3}\,M_\oplus$, an equilibrium temperature of $T_\mathrm{eq,c} = 661 \pm 13$ K and, therefore, if confirmed, could be considered as another warm Neptune.

Keywords. planetary systems – techniques: photometric – techniques: spectroscopic – techniques: radial velocities stars: individual: TOI-1422 – method: data analysis.

4.1 Introduction

Exoplanetary science has expanded quickly from the simple detection of new worlds to their in-depth characterization. This characterization is especially feasible for planets orbiting bright stars on a plane almost aligned to our line of sight, meaning that their radius and mass can be derived by transit photometry and radial velocity (RV) measurements, respectively. The population of known transiting planets has increased significantly in the last two decades, mainly thanks to dedicated ground-based surveys, which were then followed by surveys from space that turned out to be much more efficient, considering the total number of discoveries. Thus far, the *Kepler* and the K2 space missions (Borucki et al., 2010, Howell et al., 2014) have had a very important impact on the exoplanet field by discovering thousands of confirmed and candidate planets, many of which are not amenable to RV follow-up due to the faintness of their host stars. The Transiting Exoplanet Survey Satellite (*TESS*) (Ricker et al., 2014), currently at the end of its first extended mission and with a second one already proposed, was designed to target nearby and bright stars over a large portion of the sky (around 85% sky coverage during the primary mission alone) because such stars are easier to follow up by means of RV, and result in refined measurements of their own exoplanet masses, atmospheres, sizes, and therefore, densities. The opportunity to use a large exoplanet sample such as that of *Kepler*, which is based on homogeneous data and has minimal pollution from false positives ($< 10\%$, (Fressin et al., 2013)), has allowed us to distinguish between several distinct exoplanet regimes (Buchhave et al., 2014, Weiss and Marcy, 2014, Zeng et al., 2019): the terrestrial-like planets ($R_\mathrm{p} < 1.7\,R_\oplus$), the gas dwarf planets with rocky cores and hydrogen–helium envelopes, the H_2O-dominated ices and fluid water worlds (both of the latter two classes have $1.7\,R_\oplus < R_\mathrm{p} < 3.9\,R_\oplus$) and the ice or gas giant planets ($R_\mathrm{p} > 3.9\,R_\oplus$).

Planet occurrence around main-sequence stars has been investigated thanks to Doppler surveys (e.g. (Cumming et al., 2008, Wright et al., 2012)). In particular, the Keck Eta-Earth survey (Howard et al., 2010) and the CORALIE+HARPS survey (Mayor et al., 2011) first explored the domain of low-mass ($3 - 30\,M_\oplus$) close-in ($P_\mathrm{orb} \sim 50$ days) planets. These planets turned out to be an order of magnitude more common than giant planets. Other studies for determining the occurrence rates of planets, based on the *Kepler* sample, agree that for planets with less than a 1-year orbital period, their mean number per star is higher within the radius range $1\,R_\oplus < R_\mathrm{p} < 4\,R_\oplus$ rather than the range $4\,R_\oplus < R_\mathrm{p} < 16\,R_\oplus$, (Fressin et al., 2013, Howard et al., 2012, Petigura et al., 2013). The subsequent and gradual refinement of parent-star properties (especially thanks to high-resolution stellar spectra) revealed a clear bimodality of the radius distribution of close-in ($P < 100$ days), small-sized ($R_\mathrm{p} < 4.0\,R_\oplus$) planets orbiting bright, main-sequence solar-type stars (Fulton and Petigura, 2018, Petigura et al., 2017, Van Eylen et al., 2018)[1]. These two quite distinct populations were identified as 'super-Earths' ($R_\mathrm{p} < 1.5\,R_\oplus$) and 'sub-Neptunes' ($R_\mathrm{p} = 2 - 3\,R_\oplus$), which are also represented in the intermediate region ($R_\mathrm{p} = 1.5 - 2\,R_\oplus$) with fewer planets. However, it is better to stress that, since we do not know for sure what they are made of, the space of physical

[1]For a possible explanation of the radius gap, see (Modirrousta-Galian et al., 2020)

parameters (R_p, M_p), for which the previous terms apply, are not strictly defined.

The advantage of studying transiting planets is the possibility, in many cases, to measure both the planetary radius and mass, and therefore determine their density and bulk composition. Knowing the structural properties, one should be able to distinguish among the various scenarios of exoplanet formation and evolution. Unfortunately, theoretical models (e.g. (Bitsch et al., 2019, Turbet et al., 2020)) tell us that the mass-radius relationships for small planets present degeneracy due to the vastness of possible different compositions and amounts of rock, ice, and gas, especially in the transition between rocky super-Earths and Neptune-like planets (e.g. (Lozovsky et al., 2018, Miller-Ricci et al., 2009)). A detailed investigation of the mass-radius relation for small planets can be useful for throwing light on several open questions, such as the diversity of planet core masses and compositions, or where they form (in situ or beyond the snowline), and the existence of the radius gap. We refer the reader to the recent review by (Biazzo et al., 2022) for an exhaustive discussion on this topic. It is therefore clear how RV follow-up observations and planetary-mass measurements play an important role in understanding this process and why there is currently a tremendous effort in this field by many teams (e.g. KESPRINT: (Gandolfi et al., 2018); HARPS-N consortium: (Cloutier and Eastman, 2020); NCORES: (Armstrong et al., 2020); TESS-Keck Survey: (Chontos and Murphy, 2022); GAPS: (Carleo et al., 2021)) to confirm TESS small-planet candidates.

Probing the chemical composition of the atmosphere of a large number of sub-Neptune planets would also be helpful to unravel the skein. Various techniques (such as high-resolution spectroscopy, transmission, and emission spectroscopy) have been implemented and applied successfully using the Hubble Space Telescope (HST) instruments or the high-resolution spectrographs mounted on large-class ground-based telescopes (e.g. CRIRES: (Snellen et al., 2010); HARPS: (Wyttenbach et al., 2015); LDSS3C: (Diamond-Lowe et al., 2018); GIANO: (Brogi et al., 2018); CARMENES: (Casasayas-Barris et al., 2019); HARPS-N: (Pino et al., 2020); ESPRESSO: (Borsa et al., 2021)). Unfortunately, these techniques for probing the planetary atmospheres are currently effectively applicable only to giant planets, as we know only a few sub-Neptune planets for which the transmission-spectrum signal can be detected with a sufficient signal-to-noise ratio (S/N) that allows us to discriminate between different atmospheric models. The featureless transmission spectra of GJ 436 b (Knutson et al., 2014) and GJ 1214 b (Kreidberg et al., 2014) are emblematic. The situation should improve soon thanks to the James Webb Space Telescope (JWST) (Barstow et al., 2015), which is about to go into operation, and with the next generation of space-based and large ground-based telescopes (Ariel: (Tinetti et al., 2021); ELT: (Ramsay et al., 2021); TMT: (Skidmore et al., 2015)). In the meantime, it is important that we continue to work to uncover new exoplanets, especially those of small size ($R_\mathrm{p} < 5\,R_\oplus$) that orbit bright ($V < 11$ mag) main-sequence dwarf stars. This is currently possible thanks to the large number of planet candidates (more than 5000) that *TESS* is discovering at the present time. The recent detection of water vapour in the atmosphere of the super-Neptune TOI-674 b with the HST (Brande et al., 2022) is a successful example of this effort.

On the 6 November 2019, the *TESS* target star TIC 333473672 was officially named TOI-1422 (*TESS* Object of Interest; (Guerrero et al., 2021)), following the Data Validation Report Summary (DRS) produced by the *TESS* Science Processing Operations Center (SPOC) (Jenkins et al., 2016)

pipeline at the NASA Ames Research Center through the Transiting Planet Search (TPS; (Jenkins, 2002, Jenkins et al., 2010, 2020)) and Data Validation (DV; (Twicken et al., 2018), (Li et al., 2019)) modules. In particular, TOI-1422 01 was flagged as a potential planet with an orbital period of 13.0020 ± 0.0040 days, a transit depth of 1422 ± 94 ppm (parts per million), and a corresponding radius of 3.85 ± 0.90 $R_\oplus$, which is compatible with Neptune's radius. The candidate passed all SPOC DV diagnostic tests, and, furthermore, all TIC (version 8) objects other than the target star were excluded as sources of the transit signal through the difference image centroid offsets (Twicken et al., 2018). The long-term, multi-programme Global Architecture of Planetary Systems (GAPS) (Covino et al., 2013, Poretti et al., 2016) exploits Doppler measurements taken with the High Accuracy Radial velocity Planet Searcher for the Northern hemisphere (HARPS-N) (Cosentino et al., 2012) instrument at the Telescopio Nazionale Galileo (TNG) in La Palma (Spain). This high-resolution spectrograph (resolving power $R \approx 115\,000$) delivers the highest RV precision (~ 1 m s^{-1}) currently achievable in the northern hemisphere. One of the aims of the GAPS programme is to confirm and obtain an accurate mass determination of planets having an intermediate-mass between super-Earths and super-Neptunes; for this reason, TOI-1422 was selected for RV follow-up observations, which started in June 2020.

In the present work, we report the results of our measurements and analyses that allowed us to confirm TOI-1422 as a new planetary system. The paper is organized as follows: Section 4.2 contains the details of the instruments, and the photometric and RV measurements; the results of our analyses are presented in Sect. 4.3 and discussed in Sect. 4.4; and we finally address the conclusions in Sect. 4.5.

4.2 Observations and data reduction

4.2.1 TESS photometry

Since late July 2018, *TESS* has observed more than 200 000 stars with its four wide-field optical Charged-Coupled Devices (CCD) cameras (24 × 96 degrees), each having a focal ratio of $f/1.4$ and a broad-band filter range between 600 and 1000 nm. The pre-selected target TIC 333473672 was observed in Sectors 16 and 17 between 11 September 2019 and 2 November 2019, and the first of a total of four transiting events were recorded on 19 September 2019. The two-minute cadence photometry of TOI-1422 from *TESS* spans a total of ≈ 50 days and to analyse it, we used the Presearch Data Conditioning Simple Aperture Photometry (PDC-SAP; (Stumpe et al., 2012, 2014), (Smith et al., 2012)) light curve, which is provided by the *TESS* SPOC pipeline and retrieved through the Python package `lightkurve` (Lightkurve Collaboration et al., 2018) from the Mikulski Archive for Space Telescopes (MAST). We jointly fitted the transit model and a Gaussian process (GP) using a simple (approximate) Matern kernel, which was implemented in the Python modelling tool `juliet`[2] (Espinoza et al., 2019) via `celerite` (Foreman-Mackey et al., 2017), of the form:

$$k(\tau_{i,j}) = \sigma^2_{\rm GP}\, M(\tau_{i,j},\, \rho) + (\sigma_i^2 + \sigma_w^2)\, \delta_{i,j}\,, \tag{4.1}$$

[2] `https://juliet.readthedocs.io`

where σ_i is the error bar of the i-th data point, $\sigma_{\rm GP}$ the amplitude of the GP in parts per million (ppm), σ_w an added jitter term (in ppm), $\delta_{i,j}$ the Kronecker's delta, $k(\tau_{i,j})$ the element i,j of the covariance matrix as a function of $\tau_{i,j} = |t_i - t_j|$, with t_i and t_j being the i,j GP regressors (i.e. the observing times), while

$$M(\tau_{i,j},\, \rho) = (1 + 1/\epsilon)\, e^{-[1-\epsilon]\sqrt{3}\tau_{i,j}/\rho} + (1 - 1/\epsilon)\, e^{-[1+\epsilon]\sqrt{3}\tau_{i,j}/\rho} \tag{4.2}$$

is the kernel with its characteristic time scale ρ. The parameter ϵ controls the quality of the approximation since, in the limit $\epsilon \to 0$, Eq. (4.2) becomes the Matern-3/2 function. In `juliet`, the possible polluting sources inside the *TESS* aperture[3] (Fig. 4.1), which might result in a smaller transit depth compared to the real one, are taken into account with a dilution factor (D) that, in this case, has been neglected because the PDC-SAP photometry is already corrected for dilution from other objects contained within the aperture using the Create Optimal Apertures (COA) module (Bryson et al., 2010, 2020)[4]. In order to efficiently sample the whole plausible zone in the (b, k) plane, where b is the impact parameter and k is the planet-to-star radius ratio, we used the (r_1, r_2) parametrization described in (Espinoza, 2018). This is the same approach that we adopted for the modelling of the transits in the joint analysis with the RVs (see Sect. 4.3.3). Moreover, here we make use of the limb-darkening parametrizations of (Kipping, 2013) for two-parameter limb-darkening laws ($q_1, q_2 \to u_1, u_2$).

The PDC-SAP light curve of TOI-1422 and its detrending are plotted in Fig. 4.2. We also analysed the SPOC SAP photometry (Morris et al., 2020, Twicken et al., 2010), which presents a small long-term variability that might be due to systematics, but no other feature or modulation can be discerned within the experimental uncertainties, aside from a possible single extra transit event, which is discussed at the end of Sect. 4.3.4, and a steep flux drop at the end of both the SAP and PDC-SAP light curves, which are probably due to high levels of background noise.

4.2.2 High-spatial resolution imaging - AstraLux

We observed TOI-1422 with the AstraLux high-spatial resolution camera (Hormuth et al., 2008), located at the 2.2 m telescope of the Calar Alto Observatory (CAHA, Almería, Spain) using the lucky-imaging technique. This technique obtains diffraction-limited images by acquiring thousands of short-exposure frames and selecting those with the highest Strehl ratio (Strehl, 1902) to finally combine them into a co-added high-spatial resolution image. We observed this target on the night of 29 September 2021 under good weather conditions with a mean seeing of 1 arcsec, and obtained 50 000 frames with 20 ms exposure time in the Sloan Digital Sky Survey z filter (SDSSz), with a field of view windowed to 6×6 arcsec. The datacube was reduced by the instrument pipeline (Hormuth et al., 2008) and we selected the best quality 10% frames to produce the final high-resolution image. We obtained the sensitivity limits of the co-added image by using our own

[3] `tpfplotter` is a python package developed by J. Lillo-Box and publicly available on www.github.com/jlillo/tpfplotter.

[4] Since the release of the light curve products from Year 2, the SPOC background estimation algorithm has been updated due to an over-correction bias, which was significant for dim and/or crowded targets. For this particular TOI, we estimated this over-correction to be negligible for the planetary radius estimation as it is significantly smaller than the transit depth uncertainty.

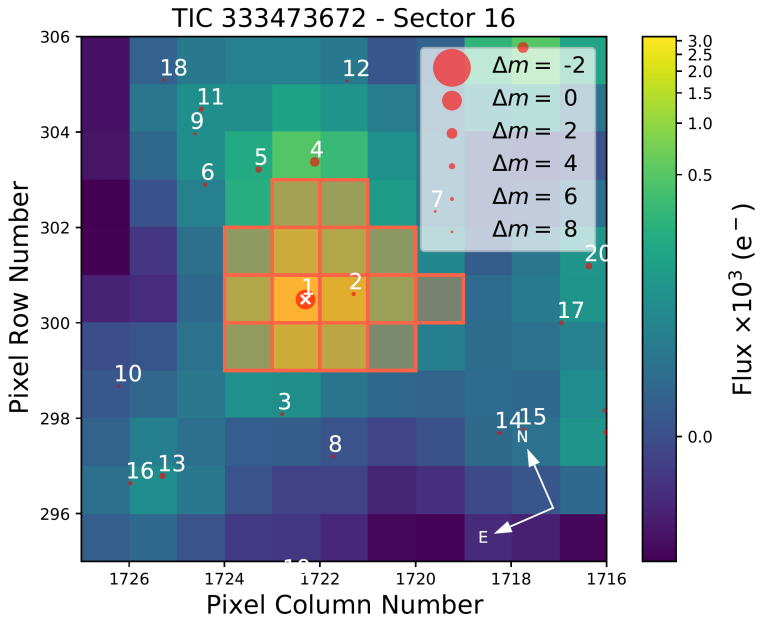

Figure 4.1: Target pixel file from the *TESS* observation of Sector 16, made with `tpfplotter` (Aller et al., 2020) and centred on TOI-1422, which is marked with a white cross. The SPOC pipeline aperture is shown by shaded red squares, and the *Gaia* satellite eDR3 catalogue (Brown et al., 2018, Prusti et al., 2016) is also overlaid with symbol sizes proportional to the magnitude difference with TOI-1422. The difference image centroid locates the source of the transits within 1.89 ± 5 arcsec of the target star's location, as reported by the TicOffset for the multi-sector DV report for this system.

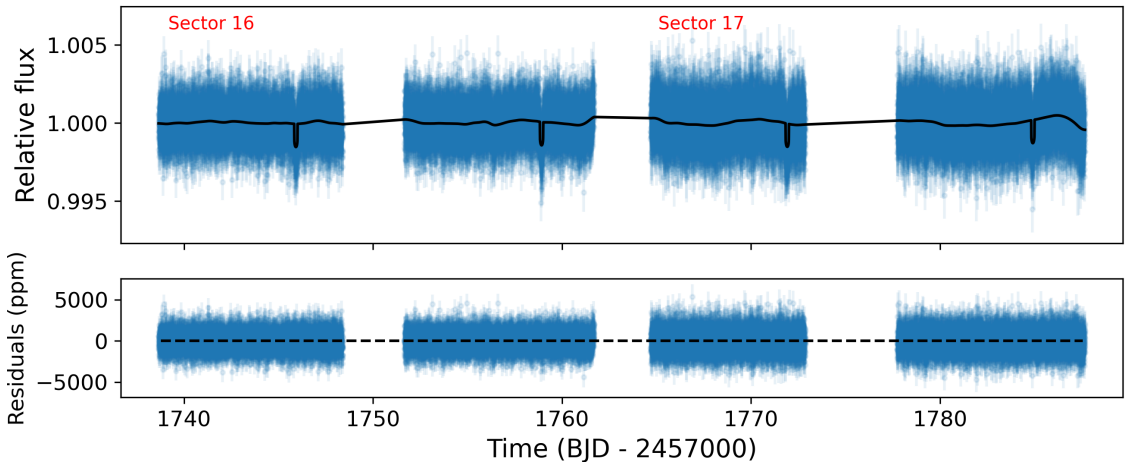

Figure 4.2: Light curve of TOI-1422 as collected by *TESS* in Sectors 16 and 17 with a 2-minute cadence. *Top panel:* Light curve from the PDC-SAP pipeline. The black line represents the best-fit model obtained through GP detrending, as detailed in Sect. 4.2.1. *Bottom panel:* Residuals of the best-fit model in parts per million.

developed ASTRASENS package[5] with the procedure described in (Lillo-Box et al., 2012, 2014). The 5σ sensitivity curve is shown in Fig. 4.3. We could discard sources down to 0.2 arcsec with a magnitude contrast of $\Delta Z < 4$ mag, corresponding to a maximum contamination level of 2.5%. By using this high-spatial resolution image, we also estimated the probability of an undetected blended source. This probability (fully described in (Lillo-Box et al., 2014)) is called the blended source confidence (BSC). We used a python implementation of this approach (`bsc`, by J. Lillo-Box), which uses the TRILEGAL[6] galactic model (v1.6; Girardi et al., 2012) to retrieve a simulated source population of the region around the corresponding target[7]. This simulated population was used to compute the density of stars around the target position (radius $r = 1°$) and derive the probability of chance alignment at a given contrast magnitude and separation. When applied to the TOI-1422 location, we used a maximum contrast magnitude of $\Delta m_{\rm b,max} = 6.97$ mag in the SDSSz passband, corresponding to the maximum contrast of a blended eclipsing binary that could mimic the observed transit depth of planet b ($\sim$ 1000 ppm). Thanks to our high-resolution image, we estimated the probability of an undetected blended source to be 0.28%. The probability of such an undetected source being an appropriate eclipsing binary was thus even lower and consequently, we could assume that the transit signal was not due to a blended eclipsing binary.

4.2.3 HARPS-N radial velocities

Between June 2020 and January 2022, we collected a total of 112 RV measurements of TOI-1422 with HARPS-N (Table 4.3). The RVs were calculated using the TERRA pipeline (Anglada-Escudé and Butler, 2012), version 1.8, through the YABI workflow interface (Hunter et al., 2012), which is

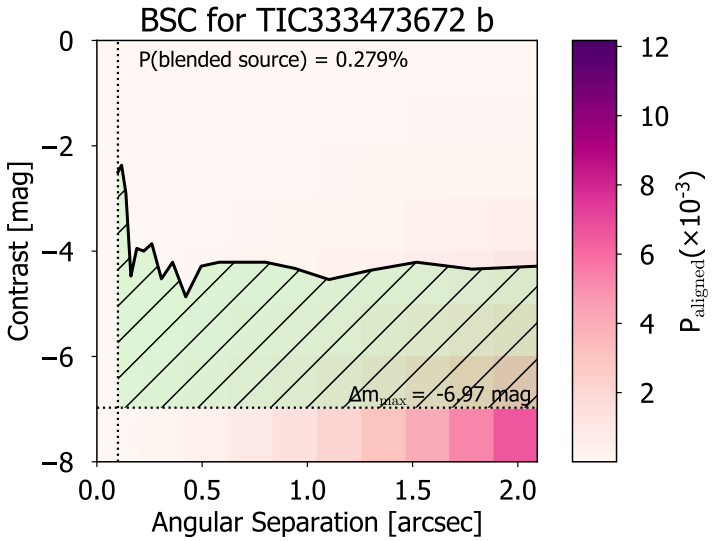

Figure 4.3: Blended source confidence (BSC) curve from the AstraLux SDSSz image (solid black line). The color on each angular separation and contrast bin represent the probability of a source aligned at the location of the target, based on the TRILEGAL model. The horizontal dotted line shows the maximum contrast of a blended binary that is capable of imitating the planet's transit depth. The green region represents the regime that is not explored by the high-spatial resolution image. The BSC curve corresponds to the integration of $P_{\rm aligned}$ over this region.

[5] `https://github.com/jlillo/astrasens`
[6] `http://stev.oapd.inaf.it/cgi-bin/trilegal`
[7] This is done in python by using the astrobase implementation by (Bhatti et al., 2020).

maintained by the Italian center for Astronomical Archive (IA2). TERRA is an algorithm based on the template matching technique, and is preferred for the RVs retrieval in this paper over the standard Data Reduction Software (DRS) pipeline, which returned a slightly lower overall RV precision[8] on this target. We used the RVs calculated using all the spectral orders, and from the full sample of RVs, we removed four points following Chauvenet's criterion. TERRA RVs have an average measurement error of $2.6\,\mathrm{m\,s^{-1}}$, a root mean square error of $4.5\,\mathrm{m\,s^{-1}}$, and a $\mathrm{S/N} \approx 35$, measured at a reference wavelength of 5500 Å. A long linear trend is evident in HARPS-N RV data, as we discuss in Sect. 4.3.2.

TOI-1422 was also observed with the SOPHIE instrument, a stabilized échelle spectrograph mounted at the 193-cm Telescope of Observatoire de Haute-Provence in France ((Perruchot et al., 2008), (Bouchy, F. et al., 2013)). However, for signals of low semi-amplitudes such as those we discuss in this work, the RV measurements of SOPHIE, due to higher uncertainties compared to HARPS-N, do not increase the significance of the results presented in Sect. 4.5, and therefore have not been utilized.

4.3 System characterization

4.3.1 Parent star

From the co-added spectrum built from individual HARPS-N spectra extracted with the standard DRS pipeline, we derived the following atmospheric parameters of the planet's host star TOI-1422: effective temperature T_{eff}, surface gravity $\log g$, microturbulence velocity ξ, iron abundance [Fe/H], and rotational velocity $v \sin i_\star$. For T_{eff}, $\log g$, ξ, and [Fe/H], we applied a method based on equivalent widths of iron lines taken from (Biazzo et al., 2015) and the spectral analysis package MOOG ((Sneden, 1973); version 2017). The (Castelli and Kurucz, 2003) grid of model atmospheres was adopted. T_{eff} and ξ were derived by imposing that the abundance of Fe I was not dependent on the line excitation potentials and the reduced equivalent widths (i.e. EW/λ), respectively, while $\log g$ was obtained by imposing the Fe I/Fe II ionization equilibrium condition. The $v \sin i_\star$ was measured with the same MOOG code, by applying the spectral synthesis of three regions around 5400, 6200, and 6700 Å, and adopting the same grid of model atmosphere after fixing the macroturbulence velocity to the value of $3.4\,\mathrm{km\,s^{-1}}$ from the relationship by (Doyle et al., 2014). From these results, the star can be classified as a G2 V dwarf with a low projected rotation velocity $v \sin i_\star$ of $1.9 \pm 0.8\,\mathrm{km\,s^{-1}}$, implying a maximum rotation period of 27^{+19}_{-8} d at 1σ. Analogously, using an empirical relation based on the Full Width at Half Maximum (FWHM)[9] derived by the HARPS-N DRS, we find $v \sin i_\star \sim 2.2\,\mathrm{km\,s^{-1}}$.

The field of TOI-1422 was also observed in 2004, 2006, and 2007 during the WASP transit-search survey (Pollacco et al., 2006). A total of 20 000 photometric data points were obtained by observing the field every ~ 15 min on clear nights, over spans of ~ 120 days in each year. We searched the data

[8] For a comparison of the performances of TERRA vs DRS see (Perger, M. et al., 2017)

[9] This relation was calibrated using a set of well-aligned transiting exoplanet systems, for which we could infer $v \sin i_\star$ as equal to their equatorial velocities. We estimate the equatorial velocities from the stellar radii and rotational period, and correlated these values directly to the FWHMs.

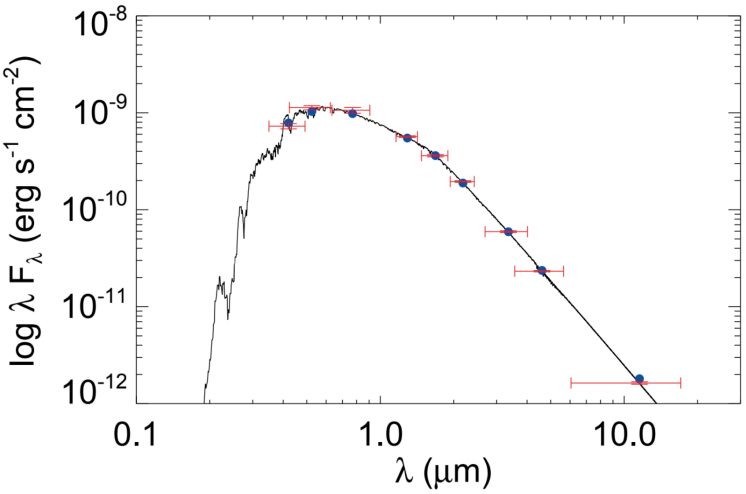

Figure 4.4: Spectral energy distribution computed for TOI-1422, where the black curve is the most likely atmospheric stellar model and the blue dots correspond to the model fluxes over each passband. The horizontal and vertical red error bars represent, respectively, the effective width of the passbands and the reported photometric measurement uncertainties (refer to the magnitudes in Table 4.1).

for any rotational modulation using the methods from (Maxted et al., 2011) and found no significant periodicity between 1 and 100 days, with a 95%-confidence upper limit on the amplitude of 2 mmag. The TESS light curve shows no modulation either (Sect. 4.2.1), confirming that the star is rather magnetically quiet over a period of $\sim$100 days. Moreover, the spectrum of TOI-1422 clearly shows a lithium line at $\lambda = 6707.8$ Å. We therefore estimated the lithium abundance $\log A(\mathrm{Li})_{\mathrm{NLTE}}$ by measuring the lithium *EW* and considering our T_{eff}, $\log g$, ξ, and [Fe/H] previously derived together with the NLTE corrections by (Lind et al., 2009). The value of the lithium abundance is listed in Table 4.1 and its position in a $\log A(\mathrm{Li})$-T_{eff} diagram is compatible with the M67 open cluster *advanced age* ($\sim$ 4.5 Gyr; see (Pasquini et al., 2009)) in agreement with the star's low activity level. The physical parameters of TOI-1422 are also displayed in Table 4.1 and were determined with the EXOFASTv2 Bayesian code (Eastman et al., 2017, 2019), by fitting the stellar spectral energy distribution (SED) and by employing the MESA Isochrones and Stellar Tracks (Dotter, 2016) to more precisely constrain the stellar mass. In addition, in the table we report the stellar magnitudes used for the SED modelling, while the SED best fit is shown in Fig. 4.4. Gaussian priors were imposed on the *Gaia* eDR3 parallax (Gaia Collaboration, 2021) as well as on the T_{eff} and [Fe/H], as derived above from the analysis of the HARPS-N spectra. An upper limit was set on the V-band extinction, A_{V}, from reddening maps (Schlafly and Finkbeiner, 2011, Schlegel et al., 1998).

4.3.2 RV and activity indexes periodogram analysis

We computed the generalized Lomb-Scargle (GLS) periodogram for the HARPS-N RVs and different stellar activity indexes[10] using the Python package `astropy` v.4.3.1 (Price-Whelan and The Astropy Collaboration, 2018). The periodogram of the RVs shows the main peak around 29 days, and a significant peak at 13 days (TOI-1422 b transiting period), after correcting for a linear trend

[10]The FWHM and the Bisector inverse span (BIS) are calculated using the cross correlation function (CCF) derived by the DRS pipeline. We also analysed the chromospheric $\log R'_{\mathrm{HK}}$ index, and additional activity diagnostics derived from the spectroscopic lines He I, Na I, Ca I, Hα06 and Hα16 as defined in the code `ACTIN` (`https://github.com/gomesdasilva/ACTIN` v.1.3.9, (Gomes da Silva et al., 2018), which has been used for the calculation. In particular, the two H-alpha indices have 1.6 and 0.6 Åband-pass width, respectively.

Table 4.1: TOI-1422 parameters.

Parameter	Unit	Value	Source
Cross-identifications			
TOI	.....	TOI-1422	TOI catalogue
TIC ID	.....	333473672	TIC
Tycho	.....	3235-00524-1	Tycho
2MASS ID	.....	J23365789+3938218	2MASS
Gaia ID	.....	1920333449169516288	Gaia eDR3
Astrometric properties			
R.A.	J2016	354.240817	Gaia eDR3
Dec	J2016	+39.639275	Gaia eDR3
Parallax	mas	6.4418 ± 0.0138	Gaia eDR3
μ_α	$\mathrm{mas\,yr^{-1}}$	-67.564 ± 0.015	Gaia eDR3
μ_δ	$\mathrm{mas\,yr^{-1}}$	-31.180 ± 0.011	Gaia eDR3
Distance	pc	$154.56^{+0.037}_{-0.027}$	VizieR
Photometric properties			
B_T	mag	11.31 ± 0.07	Tycho
V_T	mag	10.62 ± 0.05	Tycho
J	mag	9.585 ± 0.022	2MASS
H	mag	9.275 ± 0.030	2MASS
K_S	mag	9.190 ± 0.022	2MASS
i'	mag	10.311 ± 0.075	APASS
$W1$	mag	9.161 ± 0.023	AllWISE
$W2$	mag	9.201 ± 0.020	AllWISE
$W3$	mag	9.161 ± 0.033	AllWISE
A_V	mag	< 0.077	This work
Stellar parameters			
$L_\star$	$L_\odot$	1.116 ± 0.037	This work
$M_\star$	$M_\odot$	$0.981^{+0.062}_{-0.065}$	This work
$R_\star$	$R_\odot$	$1.019^{+0.014}_{-0.013}$	This work
T_eff	K	5840 ± 62	This work
$\log g_\star$	cgs	4.41 ± 0.11	This work
ξ	$\mathrm{km\,s^{-1}}$	0.89 ± 0.07	This work
[Fe/H]	dex	-0.09 ± 0.07	This work
Spectral type[(a)]		G2 V	This work
$\rho_\star$	$\mathrm{g\,cm^{-3}}$	1.3 ± 0.1	This work
$v \sin i_\star$	$\mathrm{km\,s^{-1}}$	1.7 ± 0.4	This work
$\log A(\mathrm{Li})_\mathrm{NLTE}$		1.97 ± 0.05	This work
$\log R'_\mathrm{HK}$	dex	-4.95 ± 0.03	This work
Age	Gyr	$5.1^{+3.9}_{-3.1}$	This work

References: TESS Primary Mission TOI catalogue (Guerrero et al., 2021); TIC (Stassun, 2019, Stassun et al., 2018); Tycho (Høg et al., 2000); 2MASS (Skrutskie et al., 2006); Gaia eDR3 (Gaia Collaboration, 2021); AllWISE (Cutri et al., 2021); APASS (Henden et al., 2015); VizieR Online Data catalogue (Bailer-Jones et al., 2021).

Notes: Spectral type defined according to the stellar spectral classification of (Gray and Corbally, 2009).

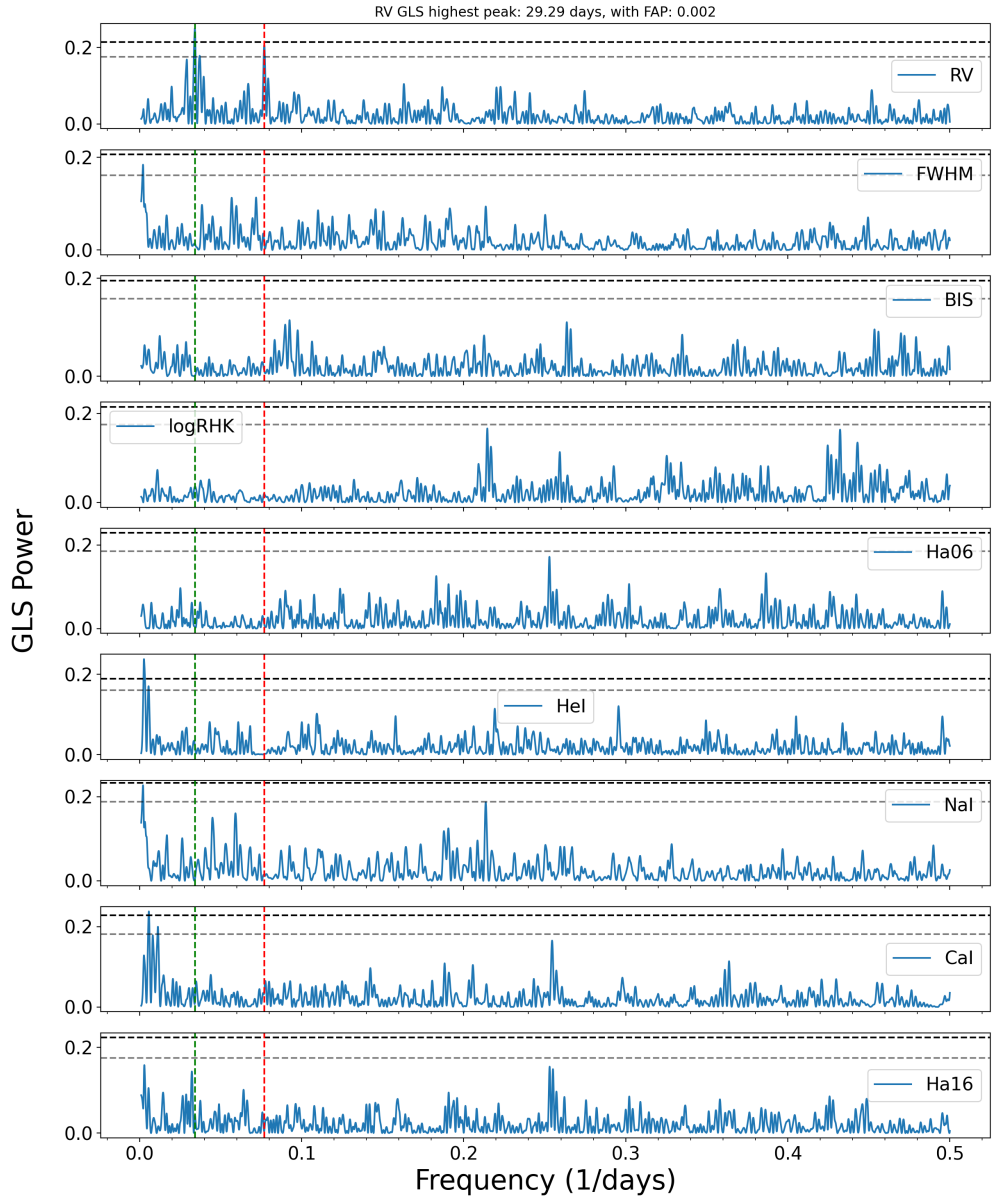

Figure 4.5: GLS periodogram of HARPS-N RVs and of various activity indexes specified in the labels, after the removal of a linear trend (Sect. 4.3.2). The main peak of the RV GLS periodogram and that of the TOI-1422 b period are highlighted with a green and a red dashed line, respectively. They do not overlap with any of the peaks from the indexes, which in general do not suggest any clear stellar rotation period. The period corresponding to the highest peak in the RV GLS periodogram, and its False Alarm Probability (FAP), are written on the top of the first panel, while the horizontal dashed lines remark the 10% and 1% confidence levels (evaluated with the bootstrap method), respectively. The three peaks surrounding the RVs main frequency can all be explained as aliases of the 29-day signal due to the two highest frequencies of the window function (190 and 390.3 days, as shown in Fig. 4.16 and Fig. 4.17).

of $\sim 4\,\mathrm{m\,s^{-1}\,yr^{-1}}$, observed in HARPS-N data. No index shows signs of the 29-day periodicity, but a linear trend is also present in the FWHM and $\log R'_{\mathrm{HK}}$ (see Fig. 4.15), with the former correlating the most with the RVs, unveiling a moderate Spearman coefficient (Spearman, 1904) of 0.41 (p-value 0.01%). Therefore, in order to explain the nature of the main peak in the RVs, we present the GLS periodogram of these coefficients posterior to the removal of their linear trends in Fig. 4.5 (see Fig. 4.16 for a closer look at the RVs panel), but again no trace of the 29-day signal is found. We also performed a GP regression analysis, using a quasi-periodic model, of the $\log R'_{\mathrm{HK}}$ index

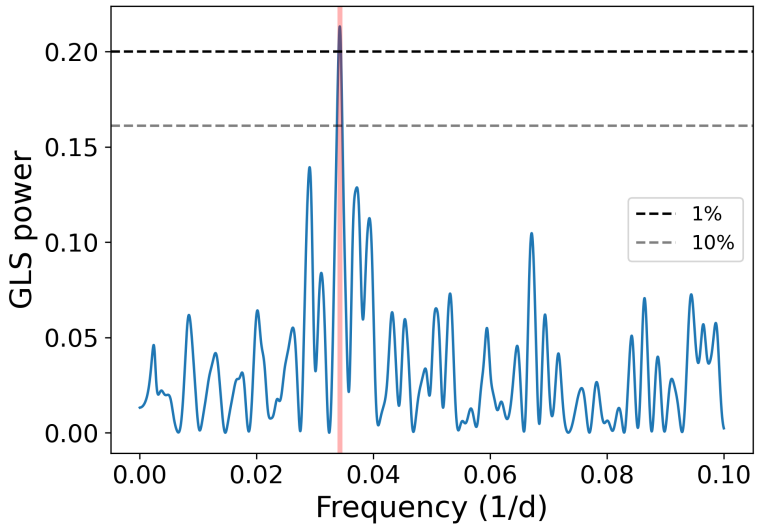

Figure 4.6: GLS periodogram of the transiting one-planet model RV residuals. The main peak is highlighted in red and corresponds to a period of 29.2 days, with a FAP of 0.45% (evaluated with the bootstrap method), while the horizontal dashed lines show the 10% and 1% confidence levels.

corrected for the linear trend over the time series, and find no evidence of any particular periodic modulation in the posterior distribution of the periodic time-scale hyper-parameter. In short, there is no evidence pointing to a specific periodic rotation of the star TOI-1422, other than the tentative estimation from $v \sin i_\star$.

A query from the Gaia eDR3 archive returns astrometric excess noise and renormalized unit weight error (RUWE) values of 80 μas and 1.09, respectively, for TOI-1422. Thus, the star is astrometrically quiet. The analysis of Sect. 4.2.2 rules out the existence of obvious sub-arcsec stellar companions, and no co-moving objects are present in Gaia eDR3 data in a 600 arcsec radius. The linear trend seen in the RV data, along with a few activity indexes, can therefore be explained by long star magnetic activity, rather than by the presence of a companion[11].

4.3.3 RV and photometry joint analysis

A joint transit and RV analysis was carried out with `juliet`, which employs different Python tools: `batman`[12] (Kreidberg, 2015) for the modelling of transits, `RadVel`[13] (Fulton et al., 2018) for the modelling of RVs, and stochastic processes, which are treated as GPs with the packages `george`[14] (Ambikasaran et al., 2015) and `celerite`[15]. The RV model that we used in `juliet` is the following:

$$M(t) = K(t) + \epsilon(t) + \overline{\mu} + A\,t + B\,, \tag{4.3}$$

where $\epsilon(t)$ is a noise model for the HARPS-N instrument, here assumed to be white-gaussian noise, in other words $\epsilon(t) \approx N(0, \sigma(t)^2 + \sigma_w^2)$, with $\sigma(t)^2$ being the formal uncertainty of the RV point

[11] In this case, at a projected separation of 0.1 arcsec ($\sim$ 15 au at the distance of TOI-1422), the lower limit of the AstraLux imaging data, a maximum RV slope of the magnitude measured in this work would be produced by a companion of $\sim 30\,M_{\rm Jup}$ (i.e. either a very low-mass star or a massive sub-stellar companion).

[12] `https://lweb.cfa.harvard.edu/~lkreidberg/batman`

[13] `https://radvel.readthedocs.io`

[14] `https://george.readthedocs.io`

[15] `https://celerite.readthedocs.io`

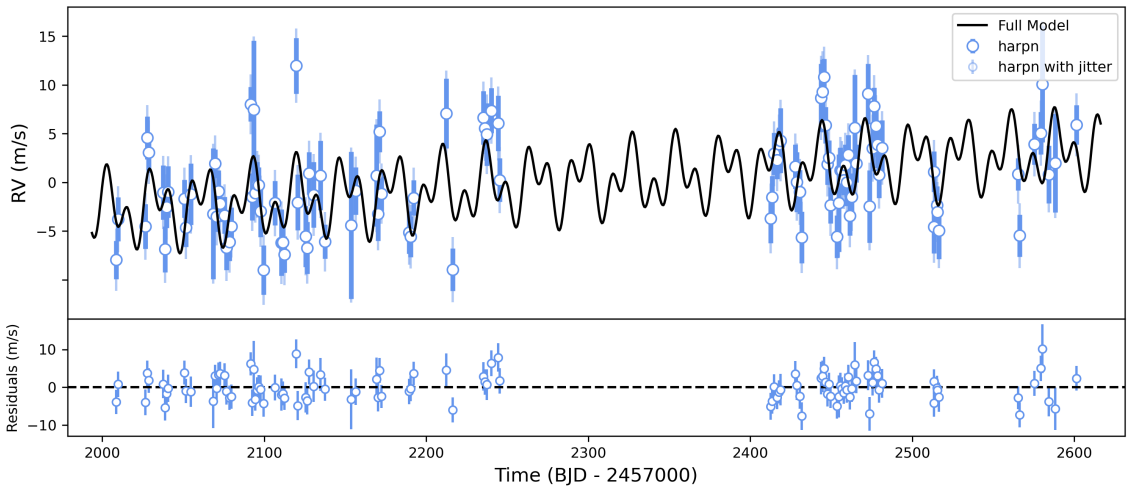

Figure 4.7: RV measurements of TOI-1422 versus time are shown on the top panel, while their residuals over the model fit are in the bottom panel. The circles with blue error bars are the RV data taken with HARPS-N. The large and small error bars indicate σ_t and σ_w (the added jitter term), respectively. In the top panel, the black line represents the two-planet model fit.

at time t, σ_w^2 being an added jitter term, and $N(\mu, \sigma^2)$ denoting a normal distribution with mean μ and variance σ^2. $K(t)$ is the Keplerian model of the RV star perturbations due to the orbiting planet, $\overline{\mu}$ is the systemic velocity linked to the instrument, and the coefficients A, B (also referred to as RV slope and RV intercept) represent an additional linear trend used for modelling non-Keplerian signals with a period longer than the observation span. For a total number of data points N, we assumed the model likelihood to follow the likelihood of an N-dimensional multi-variate Gaussian:

$$ln\, p(\vec{y}|\vec{\theta}) = -\frac{1}{2}[N\, ln\, 2\pi + ln\, |\Sigma| + \vec{r}^T \Sigma^{-1} \vec{r}]\,, \tag{4.4}$$

where $\vec{y}$ and $\vec{\theta}$ are vectors containing, respectively, all the RV data points and instrumental parameters, while $\vec{r}$ is the residual vector given by

$$r\,(t_i) = y\,(t_i) - M\,(t)\ . \tag{4.5}$$

The elements of the covariance matrix Σ are:

$$\Sigma(t_i, t_j) = k(\mu_i, \mu_j) + (\sigma_w^2 + \sigma_t^2)\delta_{t_i,t_j}\,, \tag{4.6}$$

with k equal to any GP kernel model, or zero for a pure white-noise one. In order to estimate the Bayesian posteriors and evidence, $\mathcal{Z}$, of different models, we used the dynamic nested sampling package `dynesty` (Speagle, 2020), which adaptively allocates samples based on a posterior structure and, at the same time, estimates evidence and sampling from multi-modal distributions. In general, dynamic nested sampling algorithms sample a dynamic number of live points from the prior 'volume' and sequentially replace the point with the lowest likelihood with a new one, while updating the Bayesian evidence by the difference $\Delta\mathcal{Z}$. Usually, the stopping criterion is a defined value of $\Delta\mathcal{Z}$, below which the algorithm is said to have converged ($\Delta\mathcal{Z} \approx 0.5$). However, here we used the default criterion described in Sect. 3.4 of (Speagle, 2020).

In order to reveal the transiting object suggested by the TESS light curve, we first ran the RV and photometry joint analysis with a simple one-planet model, using the parameters in the DVR produced by the SPOC pipeline as transit-related priors, both with a fixed null and uniformly-sampled eccentricity via the parametrization $S_1 = \sqrt{e}\sin\omega,\ S_2 = \sqrt{e}\cos\omega$, which is described in (Eastman et al., 2013). All the priors are defined in Table 4.4. In particular, we set Gaussian priors on both the limb-darkening coefficients (from (Claret, A., 2017)) and the star mean density $\rho_\star$ (from Sect. 4.3.1), which was implemented here instead of the scaled semi-major axis, $a/R_\star$, because the latter can be recovered using Kepler's third law using only the period of the respective planet, which is a direct result of any `juliet` run. In this way, from the single value of $\rho_\star$ we can evenly derive $a/R_\star$ in the case of multiple planets.

The best one-planet RV model fit is found with $e = 0$ ($\Delta \ln \mathcal{Z}^{e_b=0}_{e_b\neq 0} = 0.7$), but the scatter of the residuals is higher than the average photon-noise uncertainties for this kind of star. In fact, the same peak of 29 days, which was found in the RV GLS periodogram, is also distinctly found in the residuals of the transiting one-planet model (see Fig. 4.6). Consequently, we proceeded to test two-planet models, whose priors are summed in Table 4.5. Since they have comparable statistical significance ($\Delta \ln \mathcal{Z}^{e_{b,c}=0}_{e_{b,c}\neq 0} = 0.4$), we use the results of the eccentric model for the rest of the paper. The two-planet eccentric model is plotted on top of the RVs in Fig. 4.7, along with its residuals. TOI-1422 b RV semi-amplitude and orbital period are found to be $K_\mathrm{b} = 2.47^{+0.50}_{-0.46}$ m/s and $P_\mathrm{b} = 12.9972 \pm 0.0006$ days, respectively. The second planet, candidate TOI-1422 c, has an RV semi-amplitude of $K_\mathrm{c} = 2.36^{+0.42}_{-0.40}$ m/s, orbital period of $P_\mathrm{c} = 29.29^{+0.21}_{-0.20}$ days and $T_{0,\mathrm{c}} = 2458776.6 \pm 4.6$ BJD (see the posteriors in Fig. 4.14 and Table 4.6). The eccentricities turn out to be $e_\mathrm{b} = 0.04^{+0.05}_{-0.03}$ and $e_\mathrm{c} = 0.14^{+0.17}_{-0.10}$, but it is important to note that when they are fixed to zero, the orbital parameters of TOI-1422 b and TOI-1422 c remain, within 1-σ, compatible with those of the eccentric model.

4.3.4 Results

TOI-1422 c's orbital period explains both the main peak found in the residuals of the one-planet model (Fig. 4.6) and in the RV GLS periodogram (Fig. 4.5); it is also in 9:4 orbital resonance with the first planet. The difference between the Bayesian evidence of the two-planet eccentric model and the one-planet model ($\Delta \ln \mathcal{Z}^{2p}_{1p} = 5.1$) is barely above the *very strong* evidence threshold defined in (Kass and Raftery, 1995) ($\Delta \ln \mathcal{Z} > 5$), so even if the existence of candidate planet c remains unproven, we believe the two-planet model is currently the better one to explain the 29-day signal observed in the RVs, due to the lack of evidence of star activity. Furthermore, the two-planet analysis was replicated with different numbers of data points in order to understand how and if new measurements were impacting the significance of the second planet detection. As shown in Fig. 4.11, both the RV semi-amplitude and the period seem to stabilize after ≈ 60 measurements, which matches the beginning of the second observation season, while the significance of the 29-day peak also grows (Fig. 4.18). It is noteworthy to mention that the GLS periodogram of the residuals of the two-planet model does not show peaks below 50% FAP, and hence does not suggest the presence of additional detectable signals.

A phase-folded plot of both the transit and the RVs is shown in Fig. 4.9 for the eccentric two-

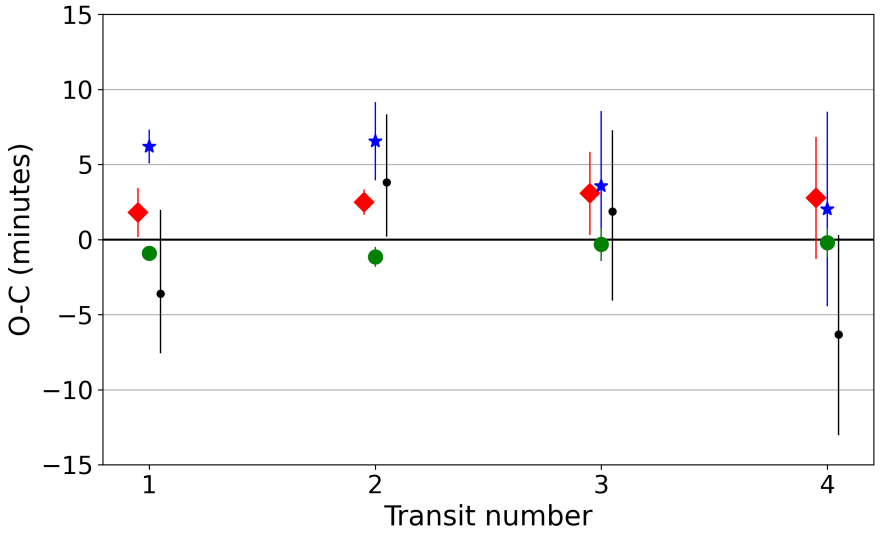

Figure 4.8: Residuals for the mid-transit timings of TOI-1422 b versus a linear ephemeris, with 1-σ error bars, are plotted in black. The green circles, red diamonds, and blue stars represent TTV predictions in the cases of null, average, or maximum eccentricities, respectively, with the error bars showing the uncertainty due to $T_{0,c}$ (see Table 4.2). The points have been slightly shifted on the x-axis to allow for more visibility.

planet model. The radius for TOI-1422 b was calculated with the transformations provided by (Espinoza, 2018) and, using the stellar radius from Sect. 4.3.1, its revised value turns out to be $R_{\rm b} = 3.96^{+0.13}_{-0.11}\,R_{\oplus}$. Using the stellar radius from Table 4.1, we derived the mass of both objects to be $M_{\rm b} = 9.0^{+2.3}_{-2.0}\,M_{\oplus}$ and $M_{\rm c}\sin i_c = 11.1^{+2.6}_{-2.3}\,M_{\oplus}$. Their final parameters are reported in Table 4.2. An independent joint analysis of the HARPS-N RVs and *TESS* photometry, after the transits were normalized through a local linear fitting, was also performed with a DE-MCMC method (Eastman et al., 2013, 2019), following the same implementation as in (Bonomo et al., 2014, 2015). The obtained results are consistent, within 1-σ, with those reported in Table 4.2.

In order to evaluate possible transit time variations (TTVs) due to the influence of candidate TOI-1422 c over TOI-1422 b, we plot the four mid-transit times minus their expected values (based on the two-planet eccentric model) in Fig. 4.8, along with different TTV predictions made with the code described in (Agol and Deck, 2016). Unfortunately, there are not enough transits to draw any conclusions, as all the delays are compatible with zero within 1-σ. Therefore, further precise monitoring of TOI-1422 b transits is encouraged in order to confirm the existence of TOI-1422 c and, overall, better characterize the planetary system.

4.3.5 Other transit events

In the search for TOI-1422 c transits, we found a possible single transit-like event around 2 458 756.35 BTJD days, as shown in Fig. 4.10, which can not be related to either TOI-1422 b or TOI-1422 c. We fitted this potential transit using the light curve from the pipeline PATHOS (Nardiello et al., 2019) and retrieved a possible radius of $R_{\rm d} = 2.82^{+0.38}_{-0.05}\,R_{\oplus}$, which is compatible with the transit depth observed in the PDC-SAP and SAP light curves as well. The duration of the transit suggests an orbital period longer than that for TOI-1422 c, but this is very uncertain, while the lack of other transits in the TESS light curve suggests an orbital period between 17-22, or longer than, 35 days, thus incompatible with that of TOI-1422 c. PATHOS is a PSF-based approach to TESS

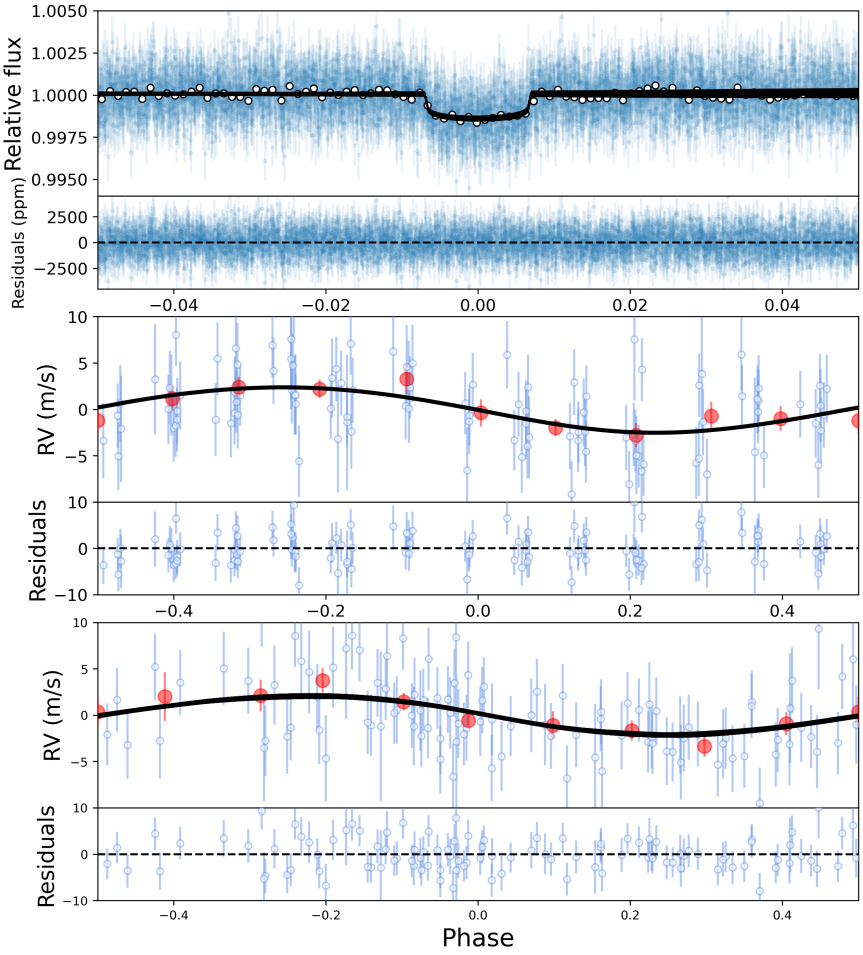

Figure 4.9: *TESS* light curve and RV curves phase-folded. **Top panel:** TOI-1422 b transit, compared to the best-fitting model. **Bottom panels:** HARPS-N RV data phase-folded to the period of planet b (middle) and candidate c (bottom), along with their residuals over the model. The red circles represent the average value of phased RV data points.

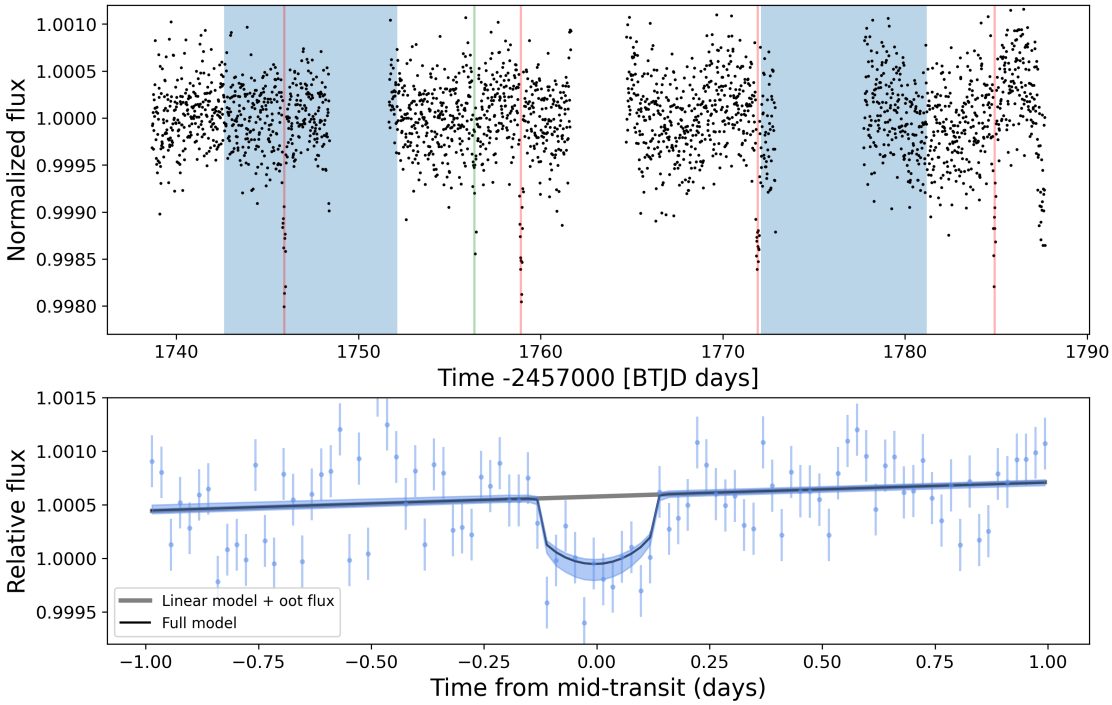

Figure 4.10: PDC-SAP and PATHOS light curves. *Top panel:* TOI-1422 b transits highlighted in red in the PDC-SAP light curve, and the expected TOI-1422 c transits, with their uncertainties, highlighted in blue. A single planetary-transit event is also marked with a vertical line green, and is discussed at the end of Sect. 4.3.4). *Bottom panel:* Single transit-like event as seen in the PATHOS light curve and the corresponding fit.

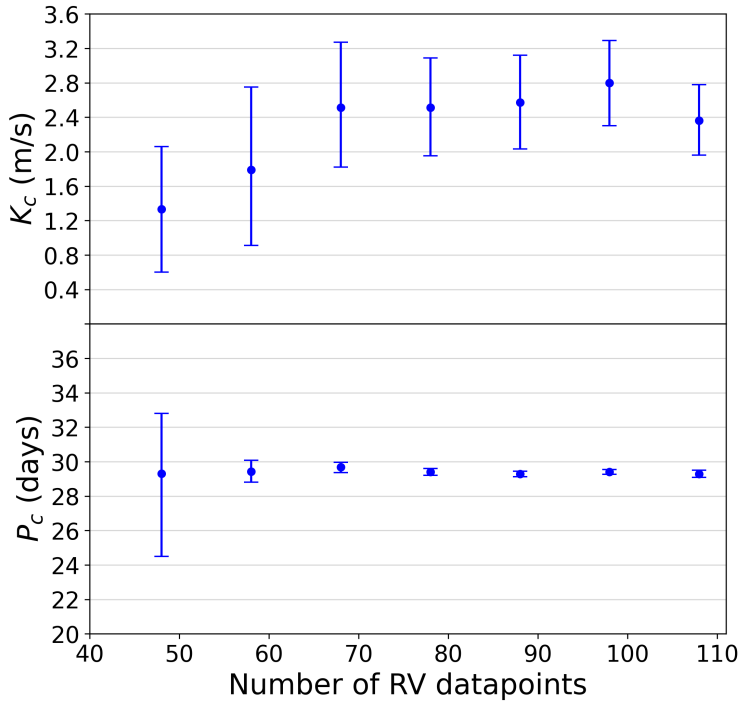

Figure 4.11: RV semi-amplitude K and orbital period P, along with their 1-σ error bars, for candidate planet c, as functions of the number of data points used for the two-planet eccentric model analysis with `juliet`.

Table 4.2: Best-fit median values, with upper and lower 68% credibility bands as errors, of the fitted and derived parameters for TOI-1422 b and TOI-1422 c, as extracted from the posterior distribution of the two-planet eccentric model (Table 4.6 and Fig. 4.14).

	TOI-1422 b	TOI-1422 c
Transit and orbital parameters		
K ($\mathrm{m\,s^{-1}}$)	$2.47^{+0.50}_{-0.46}$	$2.36^{+0.42}_{-0.40}$
$P_{\rm orb}$ (days)	12.9972 ± 0.0006	$29.29^{+0.21}_{-0.20}$
T_0 (BJD)	$2\,458\,745.9205^{+0.0012}_{-0.0011}$	$2\,458\,776.6^{+4.6}_{-4.5}$
T_{14} (hours)	4.52 ± 0.16	–
$R_{\rm p}/R_\star$	$0.0356^{+0.0007}_{-0.0005}$	–
b	$0.19^{+0.11}_{-0.10}$	–
i (deg)	$89.52^{+0.26}_{-0.28}$	–
$a/R_\star$	$22.72^{+0.31}_{-0.40}$	$39.05^{+0.50}_{-0.73}$
q_1	$0.28^{+0.11}_{-0.08}$	–
q_2	$0.30^{+0.05}_{-0.05}$	–
$\sqrt{e}\sin\omega$	$0.018^{+0.108}_{-0.095}$	$0.120^{+0.221}_{-0.233}$
$\sqrt{e}\cos\omega$	$-0.149^{+0.153}_{-0.128}$	$-0.070^{+0.349}_{-0.304}$
Derived parameters		
$M_{\rm p}$ ($M_\oplus$)	$9.0^{+2.3}_{-2.0}$	–
$M_{\rm p}\sin i$ ($M_\oplus$)	–	$11.1^{+2.6}_{-2.3}$
$R_{\rm p}$ ($R_\oplus$)	$3.96^{+0.13}_{-0.11}$	–
$\rho_{\rm p}$ ($\mathrm{g\,cm^{-3}}$)	$0.795^{+0.290}_{-0.235}$	–
$\log g_p$ (cgs)	$2.75^{+0.08}_{-0.14}$	–
a (AU)	0.108 ± 0.003	0.185 ± 0.006
$T_{\rm eq}^{(\ddagger)}$ (K)	867 ± 17	661 ± 13
u_1	$0.32^{+0.12}_{-0.10}$	–
u_2	$0.21^{+0.10}_{-0.08}$	–
e	$0.04^{+0.05}_{-0.03}$	$0.14^{+0.17}_{-0.10}$
ω (deg)	153^{+20}_{-56}	99^{+63}_{-64}

Notes: $^{(\ddagger)}$ This is the equilibrium temperature for a zero Bond albedo and uniform heat redistribution to the night side.

data that minimizes the dilution effects in crowded environments, and here it is utilized to extract high-precision photometry of TOI-1422 to independently confirm the presence of this transit even after the application of a different neighbour-subtraction technique. Neither the single transit nor TOI-1422 b transits show correlation with the X,Y pixels and the sky background signal (Fig. 4.19), and the single transit depth also does not change with different photometric apertures (Fig. 4.20). Nevertheless, the three-planet model for the joint transit-RV analysis is not statistically significant and the lack of other transits makes the suggestion of another candidate impossible to justify.

However, no transit compatible with the expected $T_{0,c}$ and P_c evaluated with the RV and photometry joint analysis, was found in the SPOC (both SAP and PDC-SAP) light curves, even though a small part of the supposed transiting window was missed by *TESS*. When we take into account both the time-span of the *TESS* light curve and TOI-1422 c expected (non-grazing) transit duration, the probability that such transits would have been missed can be estimated to be around 1% and 7%, with 1σ and 3σ uncertainty, respectively, on $T_{0,c}$. Other than misaligned orbits, another possible explanation for the lack of TOI-1422 c transits is that despite its mass, which is greater than that of planet b, its size could be much smaller (similar to the high-density sub-Neptune, BD+20594b of (Espinoza et al., 2016)), as any object with a radius approximately below $2.8 R_\oplus$ might be disguised in the light curve noise (as proven by the, so far undetected and uncertain, single transit-like event). Ultimately, it remains unknown if candidate planet c is transiting or not, so further high-precision long photometric follow-up observations will be important to clear up this possibility, along with the nature of the single transit event. The new *TESS* observations of this target, during Sector 57, are definitely welcome as they might shed some light on both matters.

4.4 Discussion

4.4.1 Orbital resonance

As we have seen, candidate c is within 1-σ, in 9:4 orbital resonance with planet b. This is likely coincidental since the resonance is fifth-order, and thus very weak, unless one of the planets is quite eccentric[16] or the mutual inclination is high. The exact 9:4 (or 2.25) resonance is within uncertainty, perhaps only because the uncertainty of the orbial period of TOI-1422 c is large compared to the tight period uncertainties of transiting planets. As a matter of fact, period ratios a little above two have been found within many exoplanetary systems (Winn and Fabrycky, 2015), but it is also possible that the 9:4 resonance is actually the result of a resonant chain of three planets in first-order 3:2 resonances among each other, with the middle one yet to be seen. If that is the case, since the period ratios of Kepler planets near first-order resonances are usually slightly wide of resonance, the likely orbital period for this unknown exoplanet would be slightly more than 19.5 days, and thus compatible with the observed single transit discussed in Sect. 4.3.4. Given this orbital period and assuming that an RV semi-amplitude roughly up to $2\,\mathrm{m\,s^{-1}}$ might be hidden in the residuals of the two-planet model, this middle object should not have a mass higher than $\approx 8\,M_\oplus$, or a density higher than $\approx 2\ \mathrm{g\,cm^{-3}}$.

[16] We note that, even with the e's suggested by the eccentric fits, which are unusually high compared to most multi-transiting planetary systems according to (Xie et al., 2016), the 9:4 would not be as strong as a first-order resonance.

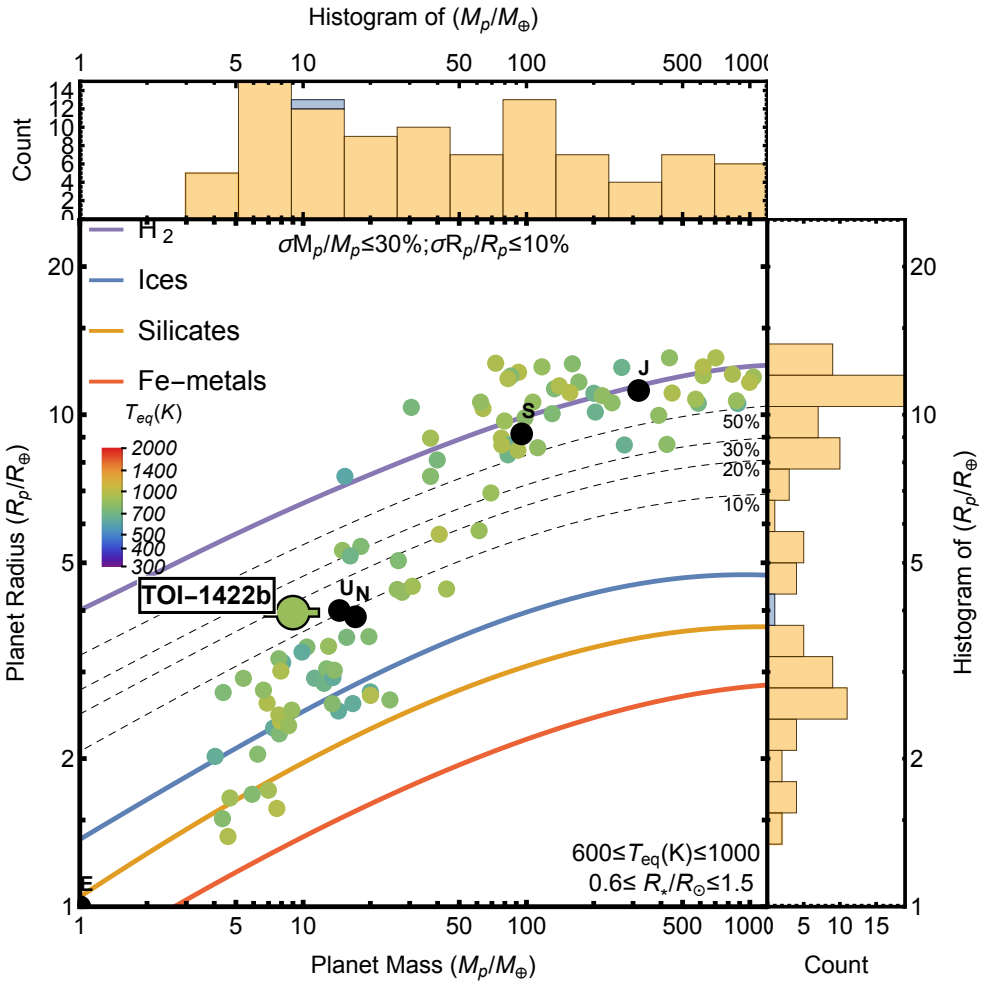

Figure 4.12: Planetary masses and radii of the known transiting exoplanets (values taken from the Transiting Extrasolar Planet catalogue, TEPCat) (Southworth, 2010, 2011) with equilibrium temperature $T_{\rm eq}$ between 600 and 1000 K and host star radius between 0.6 and 1.5 $R_\odot$. Different lines correspond to different mass fractions of relatively cold hydrogen envelopes. The *ice giants* of the Solar System are displayed in filled black circles. TOI-1422 b is on the low-density envelope of planets with precise mass and/or radius estimations ($\sigma M_p/M_p \leq 30\%$; $\sigma R_p/R_p \leq 10\%$), one of the reasons that make it potentially valuable for transit spectroscopy.

4.4.2 Mass-radius diagram and internal structure of planet b

TOI-1422 b is one of the puffier planets with a density of $\sim 0.8\,\mathrm{g\,cm^{-3}}$, which is close to that of Saturn and, therefore, lower than most exoplanets in this mass range. It lies towards the upper-left corner of the mass-radius diagram (Fig. 4.12), making it very similar to Kepler-36 c (Vissapragada et al., 2020) and especially to Kepler-11 e (Lissauer et al., 2013), which even shares the same kind of host star but is on a longer orbit. On one hand, it has a similar radius compared to Neptune and Uranus in our solar system, but on the other hand, its mass is only about $50\% - 60\%$ that of our ice giants. Thus, an extensive gaseous envelope, surrounding a massive core, is expected to be found in TOI-1422 b. More precisely, the mass fraction of this envelope is expected to be around $10\% - 25\%$ of the total mass of the planet (using the equations of state from (Becker et al., 2014)), suggesting that the atmosphere has not been blown away by the stellar wind. The nature of this extensive envelope as well as its core requires further investigation. For this purpose, we assess the expected

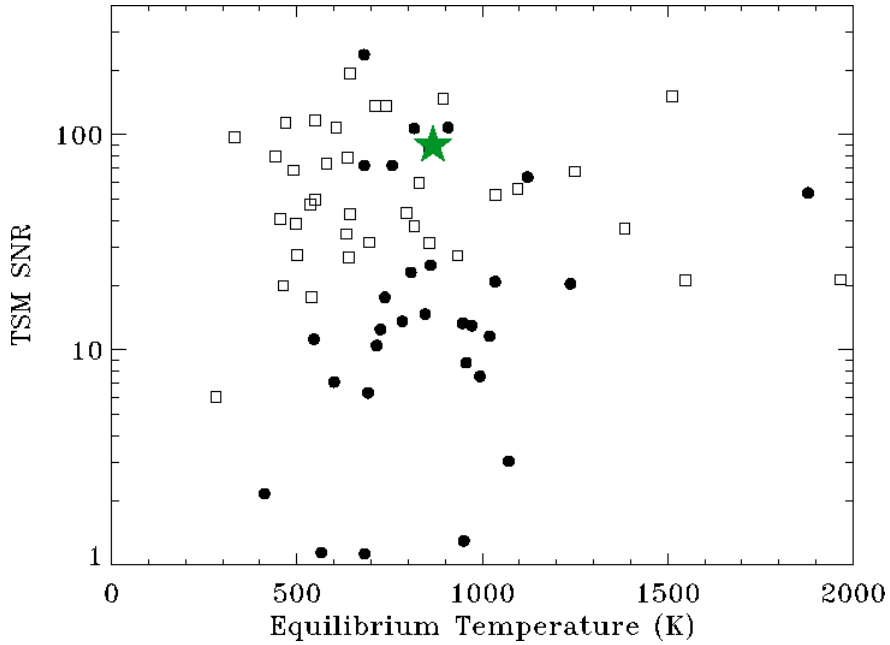

Figure 4.13: Transmission spectroscopy observations (TSM) values with the JWST over the equilibrium temperature for planets with a measured mass in the radius range $2.75 < R_{\oplus} < 4.0$, including TOI-1422 b (green star). Filled black dots and empty squares identify the sample of planets around stars with $T_{eff} > 5400\,K$ and $T_{eff} < 5400\,K$, respectively.

S/N of the *JWST*/NIRISS measurements[17] of TOI-1422 b transits compared to planets of similar sizes, by evaluating the transmission spectroscopy metric (TSM) defined in (Kempton et al., 2018):

$$\mathrm{TSM} = (\text{Scale factor}) \times \frac{R_{\oplus}^3\, T_{\mathrm{eq}}}{M_{\oplus}\, R_{\star}^2} \times 10^{-0.2\,J}\,, \tag{4.7}$$

where the scale factor is a dimensionless normalization constant, equal to 1.28 for planets with $2.75 < R_{\oplus} < 4.0$, and J is the apparent magnitude of the host star in the J band (a filter that is near the middle of the NIRISS bandpass). As a result (Fig. 4.13), TOI-1422 b ranks fourth[18] among Neptunes ($2.75 < R_{\oplus} < 4.0$) orbiting G-F dwarfs ($T_{eff} > 5400$K), but being the one with the lowest density, it is definitely an interesting candidate for atmospheric characterization by the *JWST*.

4.5 Conclusions

In this paper, we have confirmed the planetary nature of the *TESS* transiting planet TOI-1422 b, which turns out to be a low-density and warm Neptune-sized planet orbiting an astrometrically, and overall magnetically, quiet G2 V star. Therefore, TOI-1422 b is the latest addition to the low-populated range of exoplanets with the size of Neptune, but with Saturn-like density. In order to well constrain the mass of TOI-1422 b, a long RV monitoring with more than a hundred observations was necessary with the HARPS-N instrument at the TNG in La Palma, which resulted in fully characterized orbital and physical parameters of this new planetary system. On top of that, our RV

[17] From a 10-hour observing programme assuming a cloud-free, solar-metallicity, H_2-dominated atmosphere.

[18] Following TOI-561 c (Lacedelli et al., 2020, 2022), HD 136352 c (Delrez et al., 2021, Kane et al., 2020) and HD 63935 b (Scarsdale et al., 2021)

measurements also suggest the presence in the system of a possibly non-transiting, heavier candidate planet, TOI-1422 c, in a weak 9:4 orbital resonance with its inner brother, which will require further study to validate.

Appendix A: HARPS-N RV datapoints

Appendix B: Priors and posteriors

Appendix C: Corner plots

Appendix D: Additional plots

Table 4.3: HARPS-N RV data points and activity indexes (used in Fig. 4.5) obtained with the TERRA reduction pipeline between June 8, 2020 and January 21, 2022. The four lines in bold highlight the RV data points that have been removed because they do not fit Chauvenet's criterion.

BJD_{UTC} $-2457000\,[days]$	RV	$\pm1\sigma_{RV}$ $[m\,s^{-1}]$	FWHM –	BIS$^{(\dagger)}$ –	Exp.$^{(*)}$ [sec]	S/N –	$I_{Ca\ ii}$ –	$I_{H\alpha06}$ –	$I_{He\ i}$ –	$I_{Na\ i}$ –	$I_{Ca\ i}$ –	$I_{H\alpha16}$ –
2008.69349316	-7.95	1.95	7174.86	-7.56	900	42.8	0.549907	0.084427	0.097028	0.180378	0.527652	0.683496
2009.71160774	-3.78	2.25	7181.28	-6.09	900	34.3	0.555074	0.078803	0.097526	0.179596	0.522912	0.63963
2026.66187880	-4.51	2.31	7164.91	0.894	900	44.2	0.554022	0.082134	0.100171	0.187731	0.505988	0.687073
2027.72062839	4.586	2.2	7153.54	-4.7	900	36.4	0.558749	0.083288	0.107005	0.187897	0.530667	0.687811
2028.69301741	3.085	2.06	7178.27	-6.91	900	39.3	0.587418	0.078941	0.098429	0.181754	0.53219	0.657997
2037.70925340	-1.04	2.78	7190.11	1.317	900	27.1	0.588273	0.087717	0.10143	0.181427	0.533928	0.670313
2038.71004788	-6.86	2.35	7174.7	-12.8	900	33.8	0.589738	0.08641	0.102117	0.18419	0.531931	0.671326
2039.71645615	-2.51	2.17	7176.79	-5.84	900	40.5	0.590585	0.078021	0.099401	0.182083	0.530063	0.658114
2040.70404346	-0.98	2.65	7182.67	-18.1	900	31.6	0.593109	0.085039	0.099033	0.182093	0.528559	0.650582
2050.69789104	-1.68	1.94	7172.47	-1.01	900	40.2	0.594075	0.087503	0.099635	0.183098	0.534144	0.666092
2051.69861363	-4.63	1.99	7177.72	-11.5	900	38.6	0.591485	0.076251	0.099171	0.182165	0.525447	0.654697
2054.72404480	-1.22	3.15	7162.98	-4.59	900	30.1	0.564703	0.094168	0.100699	0.182831	0.523618	0.663779
2068.61577511	-3.21	6.73	7165.8	-6.58	900	12.7	0.584758	0.089195	0.098718	0.179674	0.52911	0.641145
2069.66437348	1.928	1.46	7167.86	-1.31	900	52.5	0.562065	0.080459	0.103277	0.183022	0.530759	0.690607
2070.70250746	-3.5	1.57	7172.32	-3.47	900	47.8	0.561804	0.078625	0.09964	0.18108	0.529827	0.668034
2071.70780293	-0.88	2.12	7195.44	-4.27	900	39.4	0.589073	0.083154	0.099452	0.180534	0.52584	0.65915
2072.70309705	-2.2	1.86	7185.56	-14.3	900	42.3	0.557986	0.082279	0.098576	0.180502	0.525855	0.654666
2075.63970105	-3.37	1.9	7169.71	0.109	900	45.6	0.594915	0.083487	0.100564	0.181682	0.527055	0.685465
2076.71092255	-6.68	2.31	7174.73	-9.8	900	33.1	0.554061	0.07931	0.103664	0.184892	0.530864	0.665231
2078.68129258	-6.1	1.94	7175.62	-16.9	900	44.2	0.588419	0.082137	0.100369	0.183009	0.534477	0.67444
2079.69077171	-4.53	1.95	7176.88	-8.31	900	45.3	0.560252	0.079819	0.100953	0.183346	0.530948	0.673179
2091.68437135	8.017	1.77	7185.69	-8.84	900	41.1	0.549246	0.082682	0.099392	0.181514	0.526944	0.682402
2092.62561704	-1.48	2.43	7172.71	-7.71	900	34.1	0.581979	0.086567	0.100783	0.183421	0.530712	0.666342
2093.65087003	7.487	7.04	7164.43	-16.6	900	13.4	0.564012	0.107488	0.101191	0.188208	0.50388	0.653611
2094.60798244	-1.1	1.7	7168.72	-6.22	900	42.4	0.5533	0.084541	0.100049	0.184004	0.527844	0.70821
2095.61169299	-0.2	2.3	7152.3	3.952	900	36.4	0.585249	0.077758	0.105133	0.187703	0.525175	0.697218
2096.62962752	-0.29	1.86	7166.3	-11.5	900	46.4	0.541437	0.080363	0.09865	0.182509	0.530522	0.677679
2097.66412402	-2.95	2.64	7180.27	-4.25	900	33.7	0.55499	0.084606	0.102655	0.182256	0.527347	0.650539
2099.63975353	-8.99	2.53	7178.63	-1	900	32.3	0.511441	0.083238	0.09935	0.183486	0.53274	0.664088
2106.65854394	-2.12	2.29	7175.27	-17.8	900	34.3	0.542303	0.089511	0.101622	0.184597	0.529016	0.670419
2110.71566068	-6.18	3.41	7186.25	5.57	900	25.3	0.512902	0.082166	0.101099	0.184164	0.530842	0.67291
2111.55269319	-6.16	1.92	7162.99	-2.12	900	41	0.525014	0.080415	0.100104	0.185605	0.529595	0.68975
2112.58796961	-7.39	1.88	7169.58	-11.6	900	40	0.534984	0.083924	0.099656	0.182888	0.53337	0.680635
2119.69014174	11.98	2.85	7190.32	-9.13	900	25.8	0.545065	0.087481	0.098395	0.182445	0.534123	0.626241
2120.67679558	-2.05	2.87	7208.68	-6.74	900	27.8	0.528515	0.086578	0.102032	0.186926	0.532501	0.627348
2125.54442015	-5.53	3.13	7169.97	-3.52	900	28.1	0.555249	0.085601	0.101368	0.186582	0.523009	0.665638
2126.56835804	-6.72	2.67	7174.3	-16.4	1200	32.1	0.567202	0.083452	0.099046	0.183561	0.527745	0.651399
2127.63415799	0.931	2.18	7180.78	-4.92	900	35.3	0.539365	0.085257	0.098857	0.18364	0.524582	0.655533
2130.59628332	-1.27	3.36	7187.06	-7.56	900	23.7	0.576932	0.083983	0.098713	0.183139	0.531644	0.651165
2134.62011272	0.717	3.58	7200.6	-10.9	900	22.7	0.580358	0.091434	0.100845	0.184286	0.525551	0.661751
2137.55086797	-6.08	1.75	7184.04	-1.32	900	39.9	0.587977	0.087623	0.097656	0.18263	0.528299	0.65772
2153.56077137	-4.39	7.54	7144.15	-24	900	14.5	0.561764	0.077853	0.102889	0.189554	0.527182	0.670189
2156.53992496	-0.87	2.45	7194.74	-1.33	900	34.9	0.596947	0.089431	0.103586	0.187334	0.531839	0.639791
2157.58172574	**15.06**	**6.49**	**7189.21**	**8.093**	**900**	**15.9**	**0.554652**	**0.093102**	**0.098102**	**0.18062**	**0.525648**	**0.651384**
2169.31333487	0.713	5.22	7202.4	-9.03	900	19.2	0.569926	0.086208	0.102926	0.186679	0.532988	0.706365
2170.34375539	-3.22	2.75	7181.57	-5.96	900	26.3	0.573886	0.092071	0.106226	0.189905	0.524569	0.677237
2171.31709456	5.22	2.1	7199.72	-2.35	900	40	0.567555	0.080705	0.097921	0.182549	0.526484	0.643617
2172.31291994	-1.16	1.78	7183.03	-13.1	900	51.7	0.602331	0.082135	0.100467	0.184348	0.521872	0.655749
2189.39389821	-5.12	2.18	7187.35	0.742	900	34.9	0.553612	0.087636	0.106345	0.186232	0.524683	0.636639
2190.35888875	-5.56	2.1	7181.28	-1.38	900	37.8	0.553642	0.08599	0.10436	0.185399	0.52397	0.649955
2192.33613311	-1.58	1.8	7190.22	-4.64	900	41.2	0.594328	0.086471	0.099245	0.182607	0.521139	0.661821
2212.37354384	7.092	3.59	7203.08	-9.36	900	23.9	0.593524	0.09262	0.102766	0.183774	0.521448	0.630614
2213.42063681	**16.78**	**4.42**	**7211.7**	**3.168**	**900**	**19**	**0.596428**	**0.099179**	**0.101745**	**0.181668**	**0.520206**	**0.654342**
2216.40383735	-8.94	2.19	7203.82	-10.3	900	33.9	0.594565	0.089359	0.100295	0.182115	0.519823	0.629985
2235.36719701	6.639	2.74	7177.77	0.334	900	25.5	0.595733	0.091527	0.101648	0.182908	0.520753	0.626604
2236.31768047	5.56	2.2	7188.86	-8.92	900	38.7	0.567033	0.087864	0.100285	0.182334	0.518575	0.610068
2237.32364626	4.933	3.21	7181.9	-17.9	1200	28.2	0.559051	0.086238	0.104913	0.186654	0.525845	0.664309
2239.31266431	**21.6**	**2.85**	**7219.49**	**1.592**	**900**	**31.5**	**0.591982**	**0.088633**	**0.099598**	**0.180553**	**0.524177**	**0.630278**
2240.31312271	7.368	2.31	7208.34	-2.51	900	37.6	0.594946	0.081703	0.10278	0.183971	0.522467	0.662409
2244.31706817	6.052	2.84	7195.35	0.352	900	32.5	0.594812	0.084492	0.100398	0.18777	0.524697	0.655945
2245.31980936	0.237	2.24	7209.07	-5.47	900	34.9	0.589965	0.087524	0.103149	0.183372	0.519622	0.663637
2246.32103509	**27.1**	**7.78**	**7248.46**	**34.51**	**1200**	**12.7**	**0.594927**	**0.090211**	**0.100742**	**0.184404**	**0.521228**	**0.74003**
2412.68868670	-3.7	2.54	7163.71	-3.37	900	32.8	0.550281	0.090724	0.100293	0.183955	0.523314	0.6709
2413.66378329	-1.5	2.16	7179.72	-6.74	900	34.4	0.558588	0.088191	0.099293	0.1792	0.526702	0.652927
2414.68886021	2.937	2.15	7166.9	4.331	900	37.1	0.555402	0.084723	0.098655	0.183102	0.530929	0.676626
2416.63114629	2.289	1.95	7191.8	-11.7	900	48	0.584258	0.083699	0.099042	0.180173	0.526418	0.68478
2417.65137234	3.912	1.73	7191.95	-8.14	900	40.8	0.583166	0.087257	0.098779	0.18156	0.52857	0.664774
2418.65486069	4.286	3.33	7195.12	-13.2	900	21.6	0.587824	0.10659	0.10043	0.180994	0.498526	0.662161
2427.73181821	1.618	2.29	7191.43	-0.36	900	34.2	0.595541	0.089463	0.100339	0.183087	0.530979	0.649579
2428.66018094	0.03	3.07	7187.2	-11.9	900	28.1	0.587265	0.089537	0.098082	0.181868	0.526651	0.668995
2430.66988978	-0.96	2.26	7186.32	-3.5	900	36	0.558113	0.085708	0.102817	0.184679	0.529491	0.668573
2431.71360583	-5.64	2.64	7190.54	-22.7	900	32.1	0.550955	0.07889	0.100986	0.181203	0.529026	0.662741
2443.66087057	8.667	3.5	7188.34	-4.35	900	25.2	0.590039	0.092999	0.096614	0.179042	0.526005	0.696157
2444.57982389	9.299	3.32	7180.37	-2.39	900	26.8	0.589859	0.091057	0.098188	0.179557	0.522807	0.666047
2445.59632825	10.81	1.86	7178.02	-8.87	900	36.9	0.557645	0.085087	0.10075	0.181234	0.528886	0.678235
2446.60873425	5.874	1.87	7182.03	2.719	900	45	0.552972	0.085681	0.101935	0.183638	0.525628	0.682197
2447.61736597	1.855	2.1	7181.21	-2	900	39.9	0.585974	0.086557	0.101268	0.182021	0.529423	0.6903
2448.59166621	2.524	1.79	7183.26	-6.53	900	46.5	0.550409	0.081722	0.099201	0.181717	0.528627	0.676518
2449.61666267	-2.34	1.85	7181.85	-9.02	900	46.7	0.55726	0.081361	0.100242	0.183494	0.527072	0.693437
2453.58138876	-5.57	2.17	7179.71	-10.5	900	38.1	0.576	0.087524	0.101564	0.182982	0.529699	0.666481
2454.66732062	-2.11	5	7157.53	-13.6	900	16.4	0.534792	0.105417	0.106316	0.188685	0.531533	0.672621
2455.68136136	1.242	2.34	7201.87	-15	900	37.6	0.559782	0.085698	0.097922	0.182038	0.527513	0.642527
2456.70358427	1.194	1.71	7193.3	-2.59	900	39.1	0.539261	0.083335	0.100678	0.18192	0.526882	0.654302
2457.65444875	0.232	1.53	7186.93	-4.04	900	45.9	0.544456	0.082158	0.103781	0.185289	0.52979	0.678245
2458.62416725	1.797	2.1	7191.62	-2.73	900	42.5	0.571849	0.083688	0.10082	0.181891	0.525159	0.670374
2459.58868774	0	2.42	7166.31	-9.47	900	32	0.534143	0.084143	0.101018	0.183983	0.531303	0.671843
2460.68008744	2.859	2	7199.43	-10	900	39	0.567005	0.085291	0.09952	0.182178	0.53004	0.641539
2461.61247483	-3.43	2.01	7177.71	-14.6	900	39.8	0.531283	0.081882	0.101482	0.18371	0.532312	0.662684
2462.59699290	-1.49	2.41	7193.46	-10.2	900	34	0.53251	0.091757	0.1007	0.182059	0.53047	0.678952
2464.59087617	5.604	5.45	7198.52	-24.4	900	17.8	0.536789	0.095036	0.099161	0.183787	0.528055	0.686225
2465.55285533	1.953	1.95	7189.61	-10.6	900	37.5	0.525385	0.081987	0.102391	0.184078	0.528833	0.659363
2472.64437339	9.088	3.09	7206.96	-15.6	900	28.8	0.582423	0.088182	0.102267	0.18471	0.526636	0.671635
2473.58211801	-2.46	3.71	7182.04	-22.5	900	24	0.548713	0.090743	0.100974	0.184532	0.522132	0.670676
2475.57083577	3.505	2.35	7184.54	-16.3	1800	32.2	0.580897	0.092011	0.101234	0.182594	0.528772	0.656172
2476.56282582	7.827	1.91	7191.68	-6.25	900	44	0.556952	0.083328	0.09885	0.181388	0.523729	0.660628
2477.54247641	5.777	1.95	7190.45	-13.2	900	40.1	0.584375	0.084401	0.105974	0.188686	0.528026	0.684554
2478.53938306	3.887	2.42	7199.21	1.209	900	33.4	0.542519	0.091376	0.099644	0.180595	0.522094	0.662569
2479.53060547	0.796	2.4	7200.54	-6.9	900	35.5	0.578876	0.086324	0.099936	0.181075	0.527574	0.654195
2481.49382164	3.548	2.82	7186.71	-6.58	900	31.2	0.53899	0.091801	0.101227	0.183502	0.527366	0.676158
2513.44982261	1.106	2.07	7176.01	-3.44	900	41.6	0.561363	0.088328	0.100405	0.183709	0.523996	0.678603
2513.50218232	-4.57	2.69	7172.76	-4.86	900	33.2	0.566953	0.08974	0.10596	0.188059	0.524511	0.666513
2515.41917706	-2.34	1.93	7184.92	-5.97	900	41.7	0.564153	0.089897	0.101247	0.182411	0.526736	0.673459
2515.44453511	-3.02	1.76	7178.72	-6.73	900	49.2	0.567076	0.088259	0.098628	0.181831	0.520853	0.679953
2516.53077561	-4.93	2.92	7190.8	1.972	900	31.9	0.602149	0.092247	0.099896	0.182444	0.527717	0.666103
2565.36649887	0.845	1.64	7187.23	-3.3	900	54.5	0.596593	0.088658	0.09841	0.180042	0.522949	0.675468
2566.34542939	-5.47	2.15	7179.09	-6.14	900	45.4	0.601739	0.091592	0.099575	0.18055	0.525212	0.678527
2575.40497038	3.93	2.12	7181.99	-8.36	900	40.1	0.566264	0.087701	0.098051	0.182169	0.523518	0.671318
2579.38524573	5.059	2.18	7191.98	-5.62	900	38.3	0.562049	0.089366	0.104764	0.183719	0.525329	0.674917
2580.41266409	10.09	5.97	7187.22	4.876	900	19.9	0.572011	0.107006	0.107628	0.185394	0.52275	0.687077
2584.33980519	0.821	2.95	7183.34	0.433	900	29.2	0.56581	0.092026	0.104575	0.185035	0.514433	0.687819
2588.34483394	1.991	5.05	7181.58	9.001	900	19.2	0.560173	0.094073	0.110324	0.186892	0.524911	0.680451
2601.31675212	5.918	2.03	7196.44	-6.76	900	45.2	0.565656	0.087291	0.10094	0.17769	0.523886	0.667702

Notes: $^{(*)}$ Duration of each individual exposure. $^{(\dagger)}$ Bisector spans; error bars are twice those of RVs.

Table 4.4: Prior volume for the parameters of the one-planet model fit of Sect. 4.2.3 processed with `juliet`. $\mathcal{U}(a, b)$ indicates a uniform distribution between a and b; $\mathcal{L}(a, b)$ a log-normal distribution, $\mathcal{N}(a, b)$ a normal distribution, and $\mathcal{T}(a, b)$ a truncated normal distribution (where lower possible value equals zero) with mean a and standard deviation b.

Parameter		Prior distribution
Keplerian Parameters:		
$\rho_\star$	[kg/m^3]	$\mathcal{N}(1300,\ 100)$
$T_{0,b}$	[BJD]	$\mathcal{N}(2458745.921,\ 0.003)$
P_b	[days]	$\mathcal{N}(12.998,\ 0.002)$
e_b^*		0
ω_b^*		90
Transit Parameters:		
$R_\mathrm{p}/R_\star$		$\mathcal{U}(0.0,\ 1.0)$
D		1.0
q_1		$\mathcal{N}(0.31,\ 0.30)$
q_2		$\mathcal{N}(0.25,\ 0.10)$
Light curve GP Hyperparameters:		
σ_{TESS}	[ppt]	$\mathcal{L}(10^{-3},\ 10)$
ρ_{TESS}	[days]	$\mathcal{L}(10^{-1},\ 10)$
RV parameters:		
K_b	[m/s]	$\mathcal{U}(0.0,\ 10.0)$
$\sigma_{\mathsf{HARPS\text{-}N}}$	[m s^{-1}]	$\mathcal{U}(0,\ 10)$
A	[m s^{-1} days^{-1}]	$\mathcal{U}(-1,\ 1)$
B	[m s^{-1}]	$\mathcal{U}(-20,\ 20)$

Notes:$^{(*)}$ In the case of non-null eccentricity, the priors were set as follows: $(\sqrt{e}\,\sin\omega, \sqrt{e}\,\cos\omega)$ in $\mathcal{U}(-1.0,\ 1.0)$.

Table 4.5: Prior volume for the parameters of the two-planet model fit of Sect. 4.2.3 processed with `juliet`.

Parameter		Prior distribution
Keplerian Parameters:		
$\rho_\star$	[kg/m^3]	$\mathcal{N}(1300,\ 100)$
$T_{0,b}$	[BJD]	$\mathcal{N}(2458745.921,\ 0.003)$
P_b	[days]	$\mathcal{N}(12.998,\ 0.002)$
$T_{0,c}$	[BJD]	$\mathcal{N}(2458740,\ 2458790)$
P_c	[days]	$\mathcal{U}(1,\ 100)$
$(e_b, e_c)^*$		0
$(\omega_b, \omega_c)^*$		90
Transit Parameters:		
$R_\mathrm{p}/R_\star$		$\mathcal{U}(0.0,\ 1.0)$
D		1.0
q_1		$\mathcal{N}(0.31,\ 0.30)$
q_2		$\mathcal{N}(0.25,\ 0.10)$
Light curve GP Hyperparameters:		
σ_{TESS}	[ppt]	$\mathcal{L}(10^{-3},\ 10)$
ρ_{TESS}	[days]	$\mathcal{L}(10^{-1},\ 10)$
RV parameters:		
K_b	[m/s]	$\mathcal{U}(0.0,\ 10.0)$
K_c	[m/s]	$\mathcal{U}(0,\ 10)$
$\sigma_{\mathsf{HARPS\text{-}N}}$	[m s^{-1}]	$\mathcal{U}(0,\ 10)$
A	[m s^{-1} days^{-1}]	$\mathcal{U}(-1,\ 1)$
B	[m s^{-1}]	$\mathcal{U}(-20,\ 20)$

Notes:$^{(*)}$ In the case of non-null eccentricity, the priors were set as follows: $(\sqrt{e}\sin\omega, \sqrt{e}\cos\omega)$ in $\mathcal{U}(-1.0,\ 1.0)$.

Table 4.6: Posterior's result for the parameters of the two-planet eccentric model fit of Sect. 4.2.3 processed with `juliet`.

Parameter		Value ($\pm 1\sigma$)
Keplerian Parameters:		
$\rho_\star$	[kg/m^3]	1312^{+55}_{-68}
$a_b/R_\star$		$22.72^{+0.31}_{-0.40}$
$a_c/R_\star$		$39.05^{+0.50}_{-0.73}$
$T_{0,b}$	[BJD]	$2458745.9205^{+0.0012}_{-0.0011}$
P_b	[days]	12.9972 ± 0.0006
$T_{0,c}$	[BJD]	$2458776.6^{+4.5}_{-4.6}$
P_c	[days]	$29.29^{+0.21}_{-0.20}$
Transit Parameters:		
$R_{\mathrm{p_b}}/R_\star$		$0.0356\pm^{+0.0007}_{-0.0005}$
q_1		$0.28^{+0.11}_{-0.08}$
q_2		$0.30^{+0.05}_{-0.05}$
b_b		$0.19^{+0.11}_{-0.10}$
i_b	[deg]	$89.52^{+0.26}_{-0.28}$
Light curve GP Hyperparameters:		
σ_{TESS}	[ppt]	$0.19^{+0.03}_{-0.02}$
ρ_{TESS}	[days]	$0.76^{+0.19}_{-0.15}$
RV parameters:		
K_b	[m/s]	$2.47^{+0.50}_{-0.46}$
K_c	[m/s]	$2.36^{+0.42}_{-0.40}$
$\sigma_{\mathsf{HARPS\text{-}N}}$	[m s^{-1}]	$2.93^{+0.35}_{-0.32}$
A	[m s^{-1} days^{-1}]	0.0110 ± 0.0015
B	[m s^{-1}]	-9.1 ± 1.3

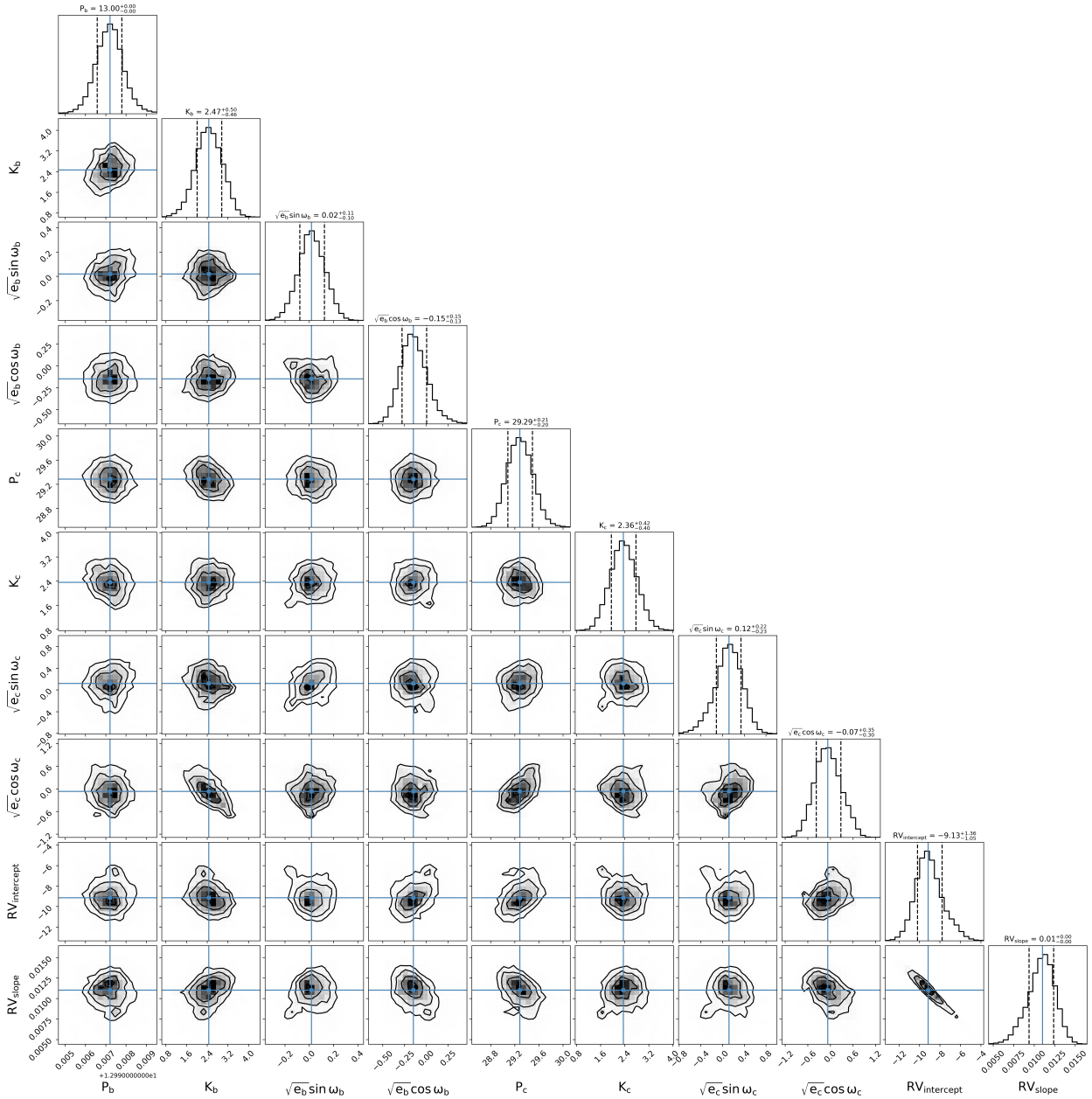

Figure 4.14: Corner plot for the posterior distribution of the joint transit and RV analysis of Sect. 4.3.3 in the case of two planets, elaborated with `juliet`.

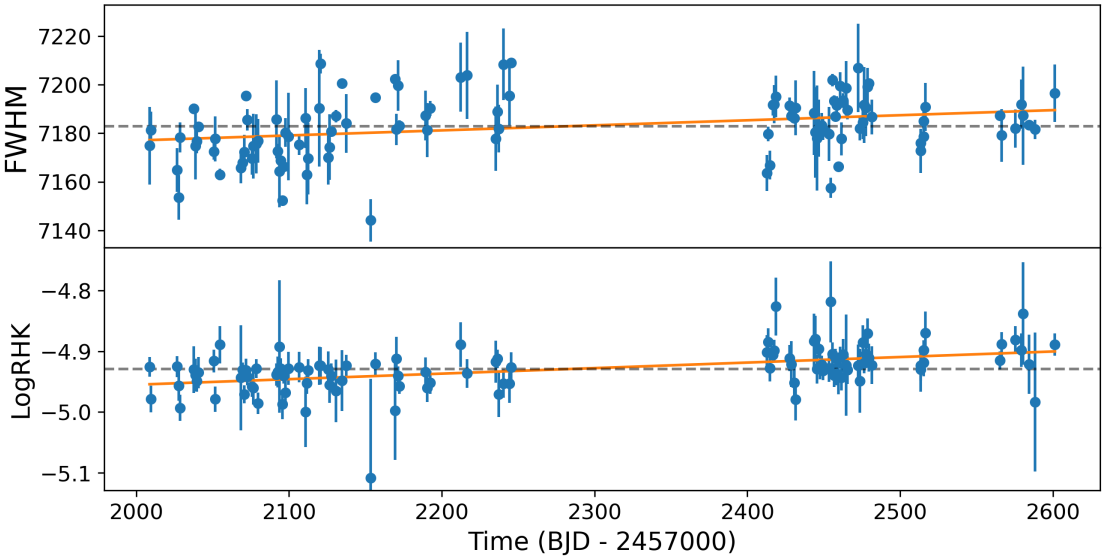

Figure 4.15: FWHM and $\log R'_{\rm HK}$ are plotted over time respectively in the upper and lower panel, along with their linear trends (orange line) and average value (dashed grey line).

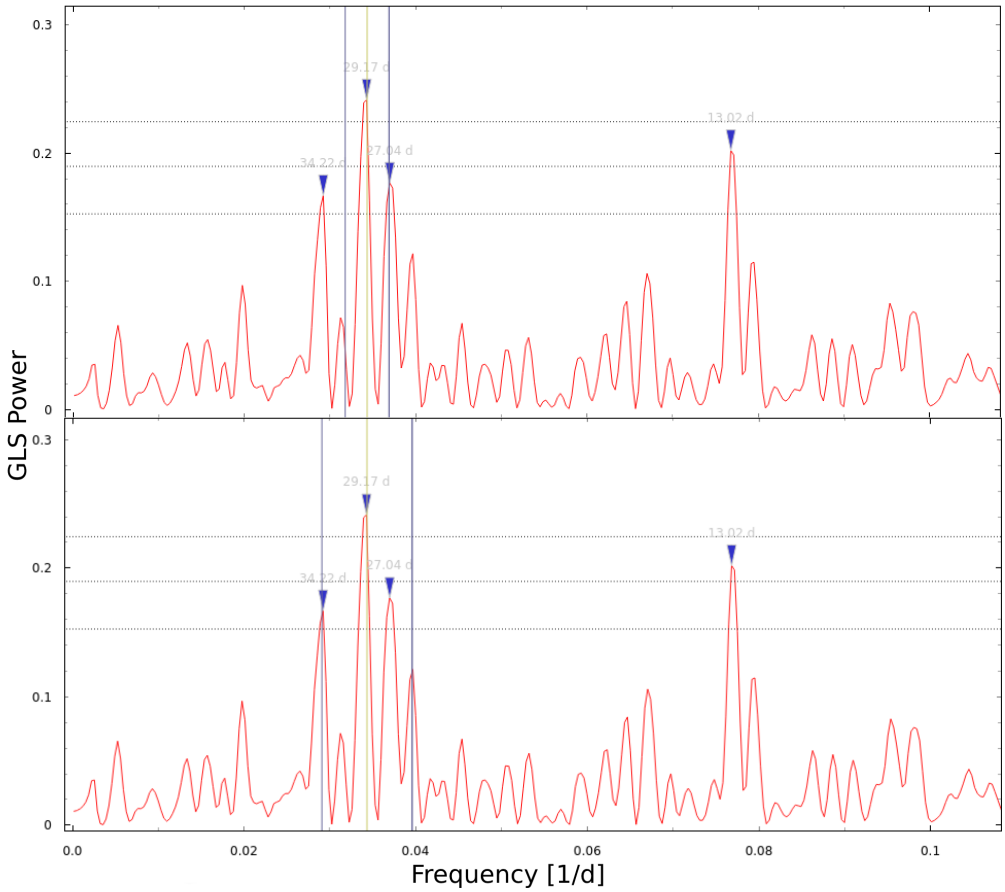

Figure 4.16: Close-up look of the RV GLS periodogram, executed with the publicly available tool Exo-Striker ((Trifonov, 2019); `https://github.com/3fon3fonov/exostriker`) after the removal of a linear trend. The two vertical blue lines, around the 29-day signal (indicated by a vertical yellow line), show the main peak aliases due to the two highest frequencies of the window function, in the upper and bottom panels. The three horizontal dotted lines represent the 10%, 1%, and 0.1% FAP levels.

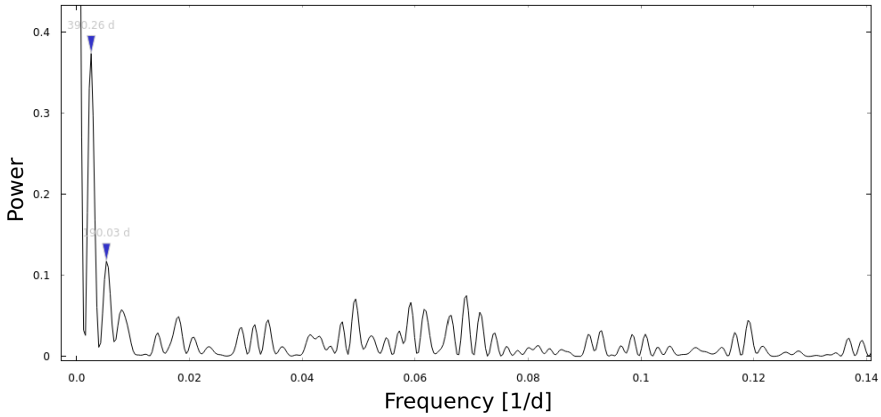

Figure 4.17: Window function of the HARPS-N RV measurements, as evaluated with Exo-Striker. The two highest peaks, excluding the 1-day peak and frequencies close to zero, are indicated by the respective labels.

Figure 4.18: Unnormalized GLS power for a different number of HARPS-N observations. The power of the 29-day signal increases with more observations. The vertical dashed red and green lines indicate TOI-1422 b and TOI-1422 c orbital periods, respectively, while the horizontal dashed lines signal the 10% and 1% confidence levels, respectively (evaluated with the bootstrap method).

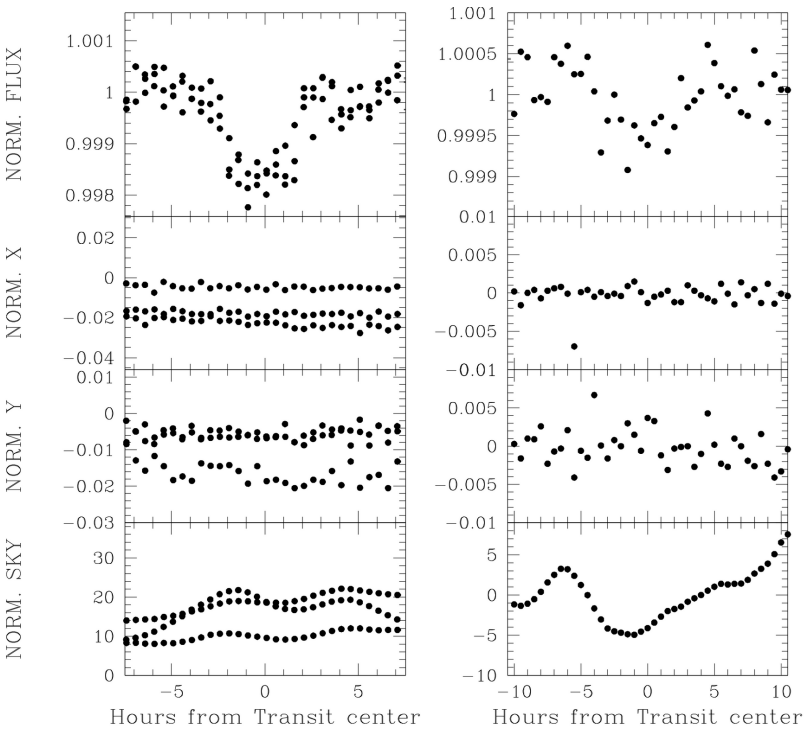

Figure 4.19: TOI-1422 b transits, as seen with PATHOS, folded on the first row of the left column and the single transit event on the right one, with X/Y and the sky background in the following rows, showing no correlation with the transits.

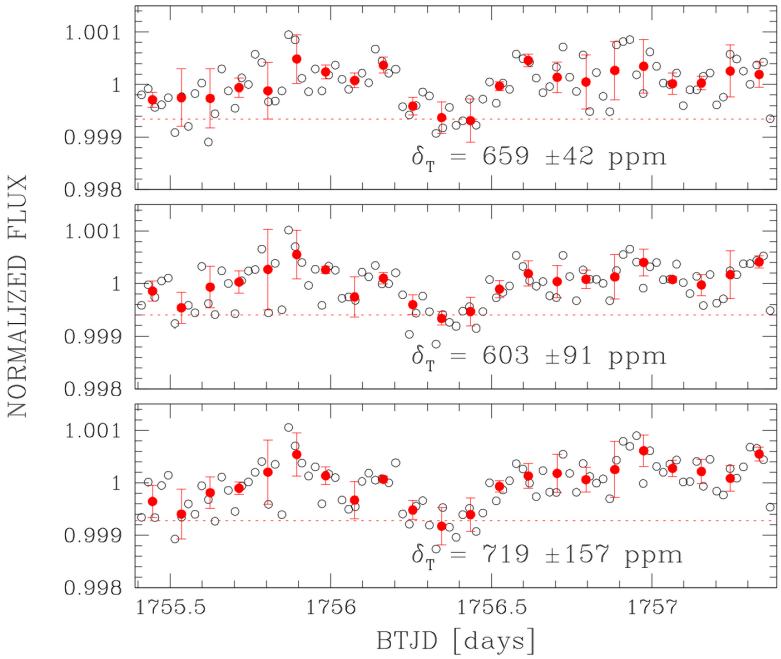

Figure 4.20: Single transit depth from PATHOS in different apertures, with the three rows showing the transit depth at an aperture radius of 2, 3, and 4 pixels, respectively.

Second result as leading author: the discovery of TOI-1853 b

The stellar system TOI-1853 was selected as a candidate by myself at the start of this PhD thesis (along with A. S. and A. S. B.). I took charge of the analysis of this Neptune-sized hosting system right after the publication of the TOI-1422 paper (Naponiello et al., 2022). In particular, I was responsible for the combined analysis of the *TESS* light curve, ground-based light curves and HARPS-N RVs. I also explored the content of the activity indexes. Finally, I handled the collaboration with all the co-authors and teams involved, and I wrote the manuscript. Notably, A. S. and A. S. B. scheduled the HARPS-N observations within the GAPS consortium. L. M., A. S. B., A. S. and M. D. supervised the work and contributed to writing the manuscript. X. D. reduced HARPS-N spectra. M. P. estimated the detection function of HARPS-N RVs. A. S. B. and K. B. determined the stellar parameters. A. W. M. and C. Z. performed and analyzed SOAR observations, while J. E. S., S. B. H., K. V. L. and R. M. obtained and reduced the Gemini data. D. R. C and C. Z. contributed to writing the high-resolution imaging section. E. G. is the Keck data collector. A. M. performed the simulations and contributed to writing the formation scenario with the help of J. J. L., while J. D., Z. L. and P. C. computed the body collision simulations. L. Z. analyzed the planet's composition. K. A. C. scheduled the LCO observations, performed data reduction along with R. P. S., and contributed to writing the light curve follow-up sections. J. F. K. performed the ULMT observations and their data reduction. E. L. N. J. performed the joint MCMC analysis of the LCO and ULMT light curves. E. Pal. obtained the data of MuSCAT2. D. L. and A. Ma. analyzed the evolutionary history of the atmosphere. P. C. estimated the transmission spectral signals observed by JWST. A. L. computed the lifetime of the planet.

Note: the upcoming chapter serves as a continuation of Chapter 3, and has been formatted as a standalone chapter only for improved indexing visualization.

Figure 4.21: Selection of online press releases for TOI-1853 b (Naponiello et al. 2023, Nature): the most massive and dense Neptune-sized planet ever found!

Chapter 5

A super-massive Neptune-sized planet

Nature, 622, pages 255–260 (2023)

Authors

Luca Naponiello[1,2,3,4], Luigi Mancini[1,4,5], Alessandro Sozzetti[4], Aldo S. Bonomo[4], Alessandro Morbidelli[6], Jingyao Dou[7], Li Zeng[8,9], Zoe M. Leinhardt7, Katia Biazzo[10], Patricio E. Cubillos[4,11], Matteo Pinamonti[4], Daniele Locci[12], Antonio Maggio[12], Mario Damasso[4], Antonino F. Lanza[13], Jack J. Lissauer[14,15], Karen A. Collins[8], Philip J. Carter[12], Eric L. N. Jensen[16], Andrea Bignamini[17], Walter Boschin[18,19,20], Luke G. Bouma[21], David R. Ciardi[21], Rosario Cosentino[18], Silvano Desidera[22], Xavier Dumusque[23], Aldo F. M. Fiorenzano[18], Akihiko Fukui[19,24], Paolo Giacobbe[4], Crystal L. Gnilka[14,21], Adriano Ghedina[18], Gloria Guilluy[4], Avet Harutyunya[18], Steve B. Howell[14], Jon M. Jenkins[14], Michael B. Lund[21], John F. Kielkopf[25], Katie V. Lester[14], Luca Malavolta[22,26], Andrew W. Mann[27], Rachel A. Matson[28], Elisabeth C. Matthews[5], Domenico Nardiello[22], Norio Narita[19.24.29], Emanuele Pace[2], Isabella Pagano[13], Enric Palle[19,20], Marco Pedani[18], Sara Seager[9,30,31], Joshua E. Schlieder[32], Richard P. Schwarz[8], Avi Shporer[30], Joseph D. Twicken[14,33], Joshua N. Winn[34], Carl Ziegler[35], Tiziano Zingales[22,26].

[1] Department of Physics, University of Rome "Tor Vergata", Rome, Italy

[2] Department of Physics and Astronomy, University of Florence, Florence, Italy

[3] Department of Physics, Sapienza University of Rome, Italy

[4] INAF, Turin Astrophysical Observatory, Pino Torinese, Italy

[5] Max Planck Institute for Astronomy, Heidelberg, Germany

[6] Laboratoire Lagrange, Université Cote d'Azur, CNRS, Observatoire de la Côte d'Azur, France

[7] School of Physics, H. H. Wills Physics Laboratory, University of Bristol, Bristol, UK

[8] Center for Astrophysics, Harvard & Smithsonian, Cambridge, MA, USA

[9] Department of Earth and Planetary Sciences, Harvard University, Cambridge, MA, USA

[10] INAF – Rome Astronomical Observatory, Monte Porzio Catone, Italy

[11] Space Research Institute, Austrian Academy of Sciences, Graz, Austria

[12] INAF – Palermo Astronomical Observatory, Palermo, Italy

[13] INAF – Catania Astrophysical Observatory, Catania, Italy

[14] NASA Ames Research Center, Moffett Field, CA, USA

[15] Department of Earth & Planetary Sciences, Stanford University, Stanford, CA, USA

[16] Department of Physics & Astronomy, Swarthmore College, PA, USA

[17]INAF – Trieste Astronomical Observatory, Trieste, Italy

[18] Fundación Galileo Galilei - INAF, Tenerife, Spain

[19] Instituto de Astrofísica de Canarias (IAC), Tenerife, Spain

[20] Departamento de Astrofísica, Universidad de La Laguna (ULL), Tenerife, Spain

[21] NASA Exoplanet Science Institute-Caltech/IPAC, Pasadena, CA, USA
[22] INAF - Padova Astronomical Observatory, Padova, Italy
[23] Observatoire de Geneéve, Université de Geneéve, CH-1290 Versoix, Switzerland
[24] Komaba Institute for Science, The University of Meguro, Japan
[2] Department of Physics and Astronomy, University of Louisville, KY, USA
[26] Department of Physics and Astronomy, University of Padova, Padova, Italy
[27] Department of Physics and Astronomy, The University of North Carolina, NC, USA
[28] U. S. Naval Observatory, Washington, D.C., USA
[29] Astrobiology Center, Osawa, Mitaka, Japan
[30] Department of Physics and Kavli Institute for Astrophysics and Space Research, MIT, MA, USA
[31] Department of Aeronautics and Astronautics, MIT, Cambridge, MA, USA
[32] NASA Goddard Space Flight Center, Greenbelt, MD, USA
[33] SETI Institute, Mountain View, CA, USA
[34] Department of Astrophysical Sciences, Princeton University, NJ, USA
[35] Dep. of Physics, Engineering and Astronomy, Stephen F. Austin State University, TX, USA.

Abstract

Neptune-size planets exhibit a wide range of compositions and densities, depending on factors related to their formation and evolution history, such as the distance from their host stars and atmospheric escape processes. They can vary from relatively low-density planets with thick hydrogen-helium atmospheres (Cubillos et al., 2017, Leleu et al., 2023) to higher-density planets with a significant amount of water or a rocky interior with a thinner atmosphere, like HD 95338 b (Díaz et al., 2020), TOI-849 b (Armstrong et al., 2020) and TOI-2196 b (Persson et al., 2022). The discovery of exoplanets in the hot-Neptune desert (Mazeh et al., 2016), a region close to the host stars with a deficit of Neptune-sized planets, provides insights into the formation and evolution of planetary systems, including the existence of this region itself. Here we report observations of the transiting planet TOI-1853 b, which has a radius of 3.46 ± 0.08 Earth radii and orbits a dwarf star every 1.24 days. This planet has a mass of 73.2 ± 2.7 Earth masses, almost twice that of any other Neptune-sized planet known so far, and a density of 9.7 ± 0.8 grams per cubic centimetre. These values place TOI-1853 b in the middle of the Neptunian desert and imply that heavy elements dominate its mass. The properties of TOI-1853 b present a puzzle for conventional theories of planetary formation and evolution, and could be the result of multiple proto-planet collisions or the final state of an initially high-eccentricity planet that migrated closer to its parent star.

5.1 Main

TOI-1853 is a dwarf star with a V-band optical brightness of 12.3 magnitudes, located 167 pc from the Sun. It was photometrically monitored by the *TESS* space telescope and the analysis of its light curve showed transit-like events compatible with a planet candidate (see Methods 5.2.1), designated as TOI 1853.01, having a short orbital period of 1.24 days and a Neptune-like radius. We ruled out a nearby eclipsing binary (NEB) blend as the potential source of the TOI-1853.01 detection in the wide *TESS* pixels, by monitoring extra transit events with the higher angular resolution of three ground-based telescopes: MuSCAT2, ULMT and LCOGT (see Methods 5.2.2). As part of the standard process for validating transiting exoplanets and assessing the possible contamination of companions on the derived planetary radii (Ciardi et al., 2015), we observed TOI-1853 with near-infrared adaptive optics imaging, using the NIRC2 instrument on the Keck-II telescope, and

with optical speckle imaging, using the ʻAlopeke speckle imaging camera at Gemini North, and the High Resolution Imaging on the 4.1 m Southern Astrophysical Research (SOAR) telescope. No nearby stars bright enough to significantly dilute the transits were detected within 0.5″, 1″ and 3″ of TOI-1853 in the Gemini, Keck and SOAR observations, respectively (see Methods 5.2.3). Using Gaia DR3 data (Gaia Collaboration, 2021) we also found that the astrometric solution is consistent with the star being single (see Methods 5.2.4).

In the context of the Global Architecture of Planetary Systems programme (König et al., 2022, Naponiello et al., 2022), we monitored TOI-1853 with the HARPS-N spectrograph (Cosentino et al., 2012), at the Telescopio Nazionale Galileo in La Palma, with the aim of measuring variations of its radial velocity (RV), i.e. its velocity projected along the line-of-sight. The HARPS-N data reduction software pipeline provided wavelength-calibrated spectra (see Methods 5.2.5), which we used to determine the stellar atmospheric properties. TOI-1853 is a quiet K2 V star with effective temperature $T_{\rm eff} = 4985 \pm 70$ K, surface gravity $\log g = 4.49 \pm 0.11$ dex, iron abundance [Fe/H] $= 0.11 \pm 0.08$ dex, and solar Fe/Si - Mg/Si ratios (see Methods 5.2.6). Furthermore, we determined a mass of $M_\star = 0.837 \pm 0.039$ solar masses ($M_\odot$), a radius of $R_\star = 0.808 \pm 0.013$ solar radii ($R_\odot$), and an advanced, though uncertain, stellar age of $7.0^{+4.6}_{-4.3}$ Gyr (Table 5.1). We computed the Generalised Lomb-Scargle periodogram of the HARPS-N RVs and found a significant peak (with False Alarm Probability - FAP $\ll 0.1\%$) at a frequency of $\approx 0.8\,{\rm d}^{-1}$ that matches the transit period and the phase of the planet candidate (see Methods 5.2.7). To determine the main physical and orbital parameters of the system, we performed a global transit and RV joint analysis (see Methods 5.2.8). Fig. 5.1 displays both the *TESS* photometric light curve and HARPS-N RV data, as a function of time and orbital phase. We measured the radius of the companion to be 3.46 ± 0.08 Earth radii ($R_\oplus$), with a mass of 73.2 ± 2.7 Earth masses ($M_\oplus$), thus confirming the planetary nature of TOI-1853.01, hereafter TOI-1853 b. These values imply a bulk density of $9.74^{+0.82}_{-0.76}$ g cm^{-3} (≈ 6 times that of Neptune) and surface gravity of $g_{\rm p} = 60.1^{+3.8}_{-3.6}$ m s^{-2} (≈ 5.5 times that of Neptune), as detailed in Table 5.1. Despite its short orbital period, TOI-1853 b may survive during the remaining main-sequence lifetime of its host star (see Methods 5.2.10).

The exceptional properties of TOI-1853 b are clearly evident in comparison with the currently known exoplanet population (Fig. 5.2). Objects with the same density of TOI-1853 b are rare, typically super-Earths, while planets with the same mass usually have radii more than twice as large. Furthermore, it occupies a region of the mass-orbital period space of hot planets that was previously devoid of objects, corresponding to the driest area of the hot-Neptune desert (Owen and Lai, 2018). TOI-1853 b is twice as massive as the two runners-up with similar radius in the radius-mass diagram (Fig. 5.2), i.e. the ultra-hot ($P = 0.76$ days) Neptune-sized TOI-849 b (Armstrong et al., 2020) and the warm ($P = 55$ days) Neptune HD 95338 b (Díaz et al., 2020). While for HD 95338 b and TOI-849 b the atmospheric mass fraction is expected to be at most $\sim 5 - 7\%$ (Kubyshkina and Fossati, 2022) and $\sim 4\%$ (Armstrong et al., 2020), respectively, TOI-1853 b is best described as a bare core of half water–half rock with no or negligible envelope, or as having at most 1% atmospheric H/He mass fraction on top of a 99% Earth-like rocky interior (Fig. 5.2) (see Methods 5.2.11). The characteristic pressure of its deep interior is estimated to reach ~ 5000 GPa (50 times the core-mantle boundary pressure of Earth), where most elements and their compounds are ex-

pected to metalize due to the reduced spacings of neighbouring atoms under extreme compression. TOI-1853 b's metallic core could be surrounded by a mantle of H_2O in a high-pressure ice phase and, possibly, in the supercritical fluid form (Zeng et al., 2021). However, the properties of matter at such high central pressures are still quite uncertain and compositional mixing (Bodenheimer et al., 2018, Kovačević et al., 2022, Stevenson et al., 2022, Vazan et al., 2022) might be present rather than distinct layers as postulated by standard models (Dorn et al., 2017, Zeng et al., 2019). If TOI-1853 b is a water-rich world, its upper structure could be described in terms of a hydrosphere with variable mass fractions of supercritical water on top of a mantle-like interior (Mousis et al., 2020). While existing structural models of Neptunes addressing this possibility do not encompass objects with a mass similar to that of TOI-1853 b, atmospheric characterization measurements with the James Webb Space Telescope might be telling. For instance, by combining three secondary-eclipse observations with the NIRSpec/G395H instrument we could constrain the CO_2 absorption feature at 4.5 μm, whose strength is a tracer of atmospheric metallicity. Transmission observations are more challenging; however, NIRISS/SOSS might be able to detect the series of H_2O absorption bands in the $0.9 - 2.8\,\mu$m range, which would distinguish a thin H_2-dominated atmosphere from an H_2O-dominated atmosphere (see Methods 5.2.15).

Explaining the formation of such a planet is challenging due to the substantial abundance of heavy elements involved. Pebble accretion, which is the most efficient growth process for massive planets, shuts off when the core is massive enough to disrupt the gas disk (Lambrechts and Johansen, 2014), and accreting solids beyond this mass requires a different process. The planetesimal isolation mass for runaway growth (Safronov, 1972) as well post-isolation growth (Lissauer, 1987) would require exceedingly and unrealistically high surface densities to grow a planet composed almost entirely of condensable material in situ. Thus, the growth of a planet like TOI-1853 b by planetesimal accretion alone appears unrealistic as well. One possibility is that a system of small planets migrated from the distant regions of the disk towards its inner edge, which could have loaded the inner disk of solid mass. After the disappearance of gas from the disk, the system became unstable, leading to several mutual collisions among the small planets and eventually forming a planet with a large mass of heavy elements, by growth-dominated collisions (Fig. 5.3). A preliminary, indicative simulation (see Methods 5.2.12) shows that the formation of a planet with a large mass of heavy elements by accreting several solid-rich planets is possible, even though growth into a single planet in the system is an unlikely event. More detailed hydrodynamic simulations also suggest that a final high-speed giant impact between two massive proto-planets is needed to account for the atmosphere-poor structure of TOI-1853 b (see Methods 5.2.13). Moreover, groups of small planets carrying cumulatively $\sim 100\,M_\oplus$ in proto-planetary disks might be rare, although the *Kepler*-mission results indicate this scenario is not unrealistic (Sun et al., 2019).

Another possible formation scenario is based on the jumping-model (Beaugé and Nesvorný, 2012), in which at least three giant planets form at a few au from their parent star. After the disappearance of the disk, this system becomes unstable and suffers mutual scattering, leading to high-eccentricity orbits for the surviving planets, which then can be circularized by tidal damping at perihelion passages. If the inner disk initially contained a lot of solid mass, in the form of planetesimals or small proto-planets, the innermost planet would have engulfed a large fraction of it near perihelion

(Fig. 5.3). To test this possibility, we simulated an eccentric Jupiter-mass planet with an initial budget of 20 to 40 $M_\oplus$ in heavy elements and found that it can accrete an additional $30 - 40\,M_\oplus$ (see Methods 5.2.12). Then, we investigated the atmosphere's evolutionary history and concluded that the current planet's structure cannot be the result of photo-evaporation processes due to the high surface gravity, but might be the result of Roche Lobe Overflow (Owen and Lai, 2018) (see Methods 5.2.14). Thus, an initially massive H/He dominated giant planet TOI-1853 b could have lost the bulk of its envelope mass due to tidal stripping (Beaugé and Nesvorný, 2013) near periastron passage during the high-eccentricity migration. The planet that we see now may have survived very close passages to its parent star from early in the system's history since the host star would have shrunk to a size of less than 2 $R_\odot$ well before reaching the main sequence. Tidal heating of a young giant planet still hot from accretion would have further expanded its envelope, facilitating the escape of light gases from the original atmosphere (Beaugé and Nesvorný, 2013, Owen, 2019, Owen and Lai, 2018).

In any case, the anomalous mass-radius and mass-period combinations of TOI-1853 b are challenging to explain with conventional models of planet formation and evolution. The local merging of solid-rich proto-planets rarely develops into a single planet, while the migration scenario would have removed all objects within ∼1 au, so we computed the sensitivity limits of HARPS-N RVs to additional planetary companions (see Methods 5.2.9) and found that we can only exclude, with a 90% confidence level, the presence of companions of masses $> 10\,M_\oplus$ up to orbital periods of $\lesssim 10$ days and with masses $> 30\,M_\oplus$ up to $\lesssim 100$ days (or ∼0.4 au). Further RV monitoring is thus needed to firmly exclude the presence of other planets within ∼1 au in order to constrain TOI-1853 b formation, while future atmospheric characterization attempts could decipher its composition, allowing us to unveil the history of the densest Neptune-sized planet currently known.

5.2 Methods

5.2.1 TESS photometric data

The star TIC 73540072, or TOI-1853, was observed by *TESS* in Sector 23 at a 30-minute full-frame images (FFI) cadence in early 2020, and in Sector 50 at a 2-minute cadence in early 2022. The transit signal was first identified in the Quick-Look Pipeline (QLP) (Huang and Vanderburg, 2020), and later promoted to *TESS* Object of Interest, TOI-1853.01, planet candidate status by the *TESS* Science Office (Guerrero et al., 2021). The Science Processing Operations Center (SPOC) (Caldwell et al., 2020, Jenkins et al., 2016) pipeline retrieved the 2-minute Simple Aperture Photometry (SAP) and Presearch Data Conditioning Simple Aperture Photometry (PDC-SAP (Smith et al., 2012, Stumpe et al., 2014)) light curves. The transit signal was identified through the Transiting Planet Search (TPS (Jenkins, 2002, Jenkins et al., 2020)) and passed all diagnostic tests in the Data Validation (Li et al., 2019, Twicken et al., 2018) (DV) modules. All TIC objects, other than the target star, were excluded as sources of the transit signal through the difference image centroid offsets (Twicken et al., 2018). Here, for the global joint transit-RV analysis of the system, we adopted the PDC-SAP light curves: SPOC for S23 and TESS-SPOC High-Level Science Product (HLSP) (Caldwell et al., 2020) for S50, where, unlike SAP or QLP light curves, long-term trends were already removed using the so-called Co-trending Basis Vectors (CBVs). The light curve of S23

Table 5.1: Stellar and planetary properties. The uncertainties represent the 68% confidence intervals (one standard deviation or σ) for each value. The equilibrium temperature is estimated for a zero Bond albedo, in the assumption of uniform heat redistribution to the night side. The eccentricity upper limit is constrained at the confidence level of 3σ.

Parameters	**Nomenclature**	**Unit**	**Value**
Stellar			
Spectral class			K2.5 V
Right ascension (J2020)	RA		14:05:50.24
Declination (J2020)	Dec		+16:59:32.53
B-band magnitude		mag	13.100 ± 0.031
V-band magnitude		mag	12.276 ± 0.092
J-band magnitude		mag	10.582 ± 0.021
H-band magnitude		mag	10.175 ± 0.018
K-band magnitude		mag	10.055 ± 0.019
$WISE1$-band magnitude		mag	9.997 ± 0.023
$WISE2$-band magnitude		mag	10.057 ± 0.019
$WISE3$-band magnitude		mag	9.956 ± 0.054
Parallax	π	mas	6.022 ± 0.016
Distance	d	pc	$166.8^{+0.9}_{-0.5}$
Projected rotational velocity	$v \sin i$	$\mathrm{km\,s^{-1}}$	1.3 ± 0.9
Chromospheric activity indicator	$\log R'_{\mathrm{HK}}$	dex	-4.73 ± 0.06
Mass	$M_\star$	$M_\odot$	0.837 ± 0.039
Radius	$R_\star$	$R_\odot$	0.808 ± 0.013
Luminosity	$L_\star$	$L_\odot$	0.3696 ± 0.0093
Effective temperature	T_{eff}	K	4985 ± 70
Surface gravity	$\log g$	dex	4.49 ± 0.11
Iron abundance	[Fe/H]	dex	0.11 ± 0.08
Magnesium abundance	[Mg/H]	dex	0.09 ± 0.06
Silicon abundance	[Si/H]	dex	0.14 ± 0.06
Planetary			
Orbital period	P	days	$1.2436258^{+0.0000015}_{-0.0000015}$
Radial velocity semi-amplitude	K	$\mathrm{m\,s^{-1}}$	$48.8^{+1.1}_{-1.0}$
Eccentricity	e		< 0.03
Argument of periastron	ω	degrees	unconstrained
Impact parameter	b		$0.52^{+0.04}_{-0.04}$
Reference epoch of mid-transit	T_0	$\mathrm{BJD_{TDB}}$	$2\,459\,690.7420 \pm 0.0006$
Transit duration	T_{14}	hours	1.19 ± 0.03
Orbital semi-major axis	a	au	0.0213 ± 0.0005
Orbital inclination	i	degrees	$84.7^{+0.4}_{-0.4}$
Mass	M_{p}	$M_\oplus$	$73.2\ ^{+2.7}_{-2.7}$
Radius	R_{p}	$R_\oplus$	3.46 ± 0.08
Density	ρ_{p}	$\mathrm{g\,cm^{-3}}$	$9.74^{+0.82}_{-0.76}$
Surface gravity	g	$\mathrm{m\,s^{-2}}$	$60.1^{+3.8}_{-3.6}$
Equilibrium temperature	T_{eq}	K	1479 ± 25

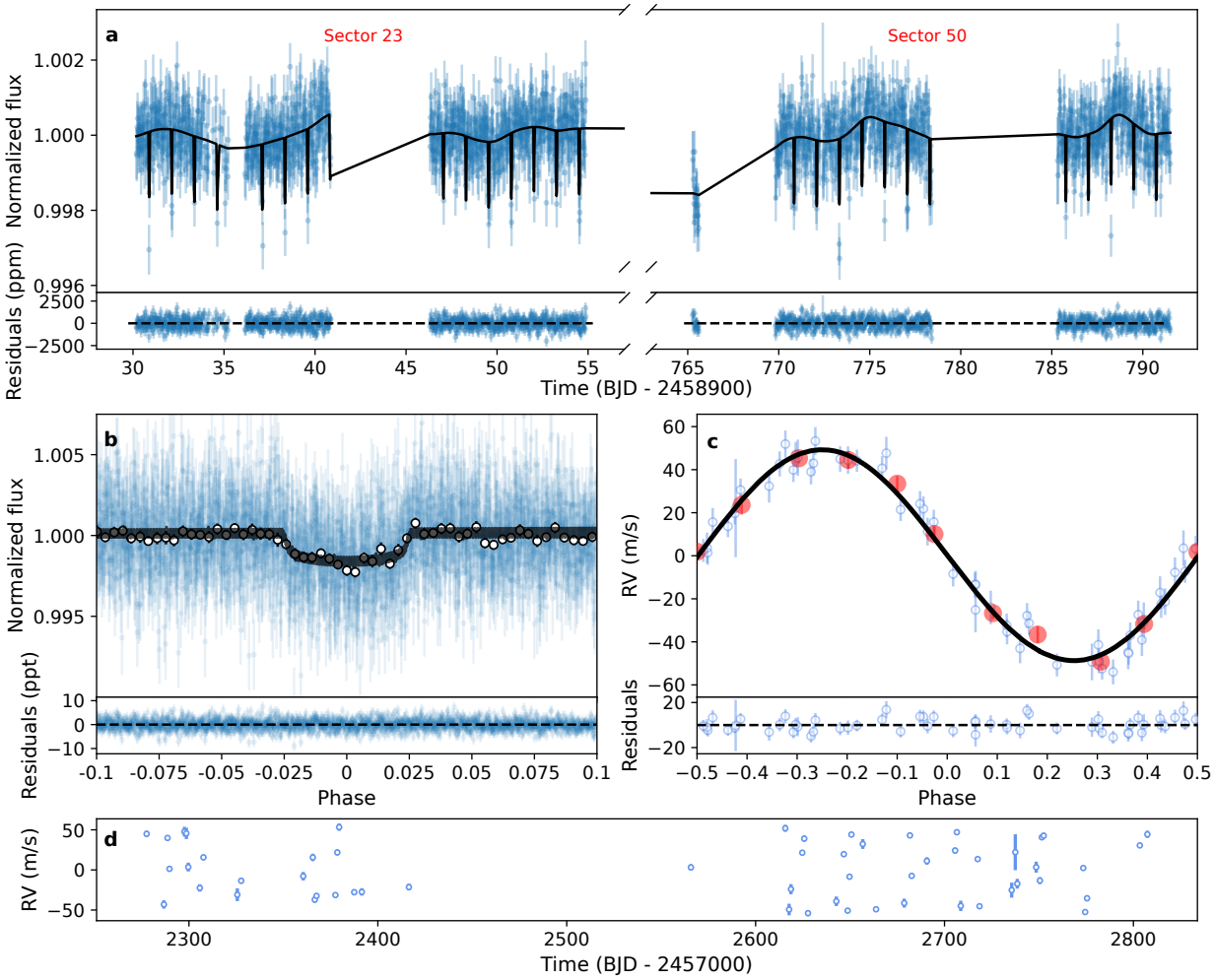

Figure 5.1: Light curve and Radial Velocities. (a) TESS light curve of TOI-1853, (b) Phase curve of all TESS transits fitted separately, (c) Phase curve of all the RVs, (d) HARPS-N RVs. The light curves are binned at a 30-minute cadence for clarity. Data points marked with anomaly flags (i.e. Coarse Point, Straylight, Impulsive Outliers and Desaturation events) were excluded from the light curve. In panel (c), the average of ≈ 6 radial velocity measurements are indicated by red dots. In all panels, the error bars represent one standard deviation, while in (a), (b) and (c) the best-fitting model is shown in black along with its residuals below.

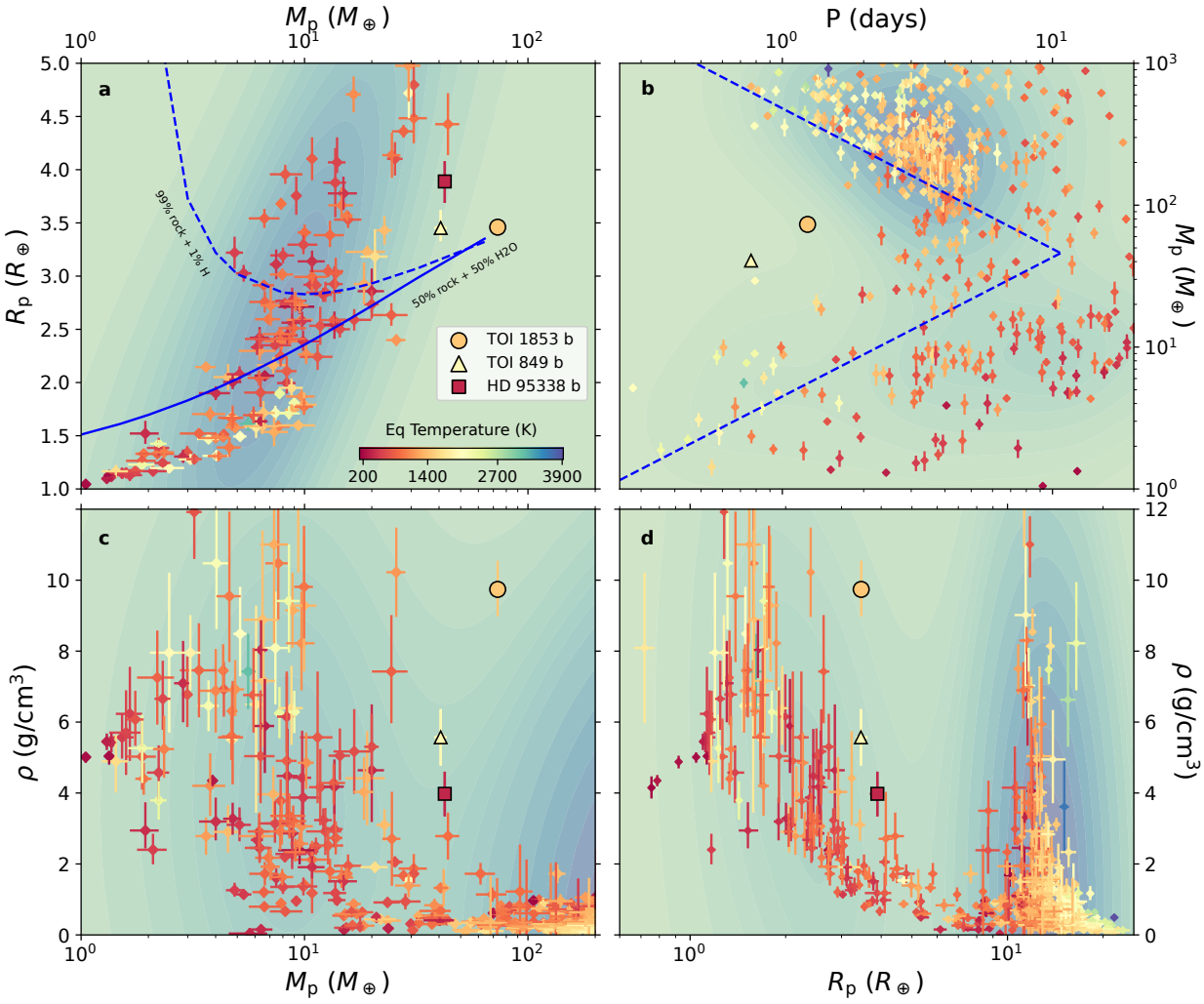

Figure 5.2: Diagrams of known transiting exoplanets. The properties of known exoplanets have been extracted from TEPCat (Southworth, 2011) and displayed as diamonds, their color being associated with their equilibrium temperature. Horizontal and vertical error bars represent one standard deviation. TOI-1853 b, TOI-849 b and HD 95338 b are displayed as a circle, triangle and square respectively. (a) Radius-mass diagram with blue lines representing different internal compositions [**dashed**: 99% Earth-like rocky interior + 1% H layer (at temperature and pressure of 1000 K, 1 mbar); **solid**: 50% Earth-like + 50% water]. (b) Period-mass diagram, where the blue dashed lines enclose the Neptunian desert (Mazeh et al., 2016) ($P_{orb} \approx 55$ days for HD 95338 b). (c) Mass-density diagram. (d) Radius-density diagram.

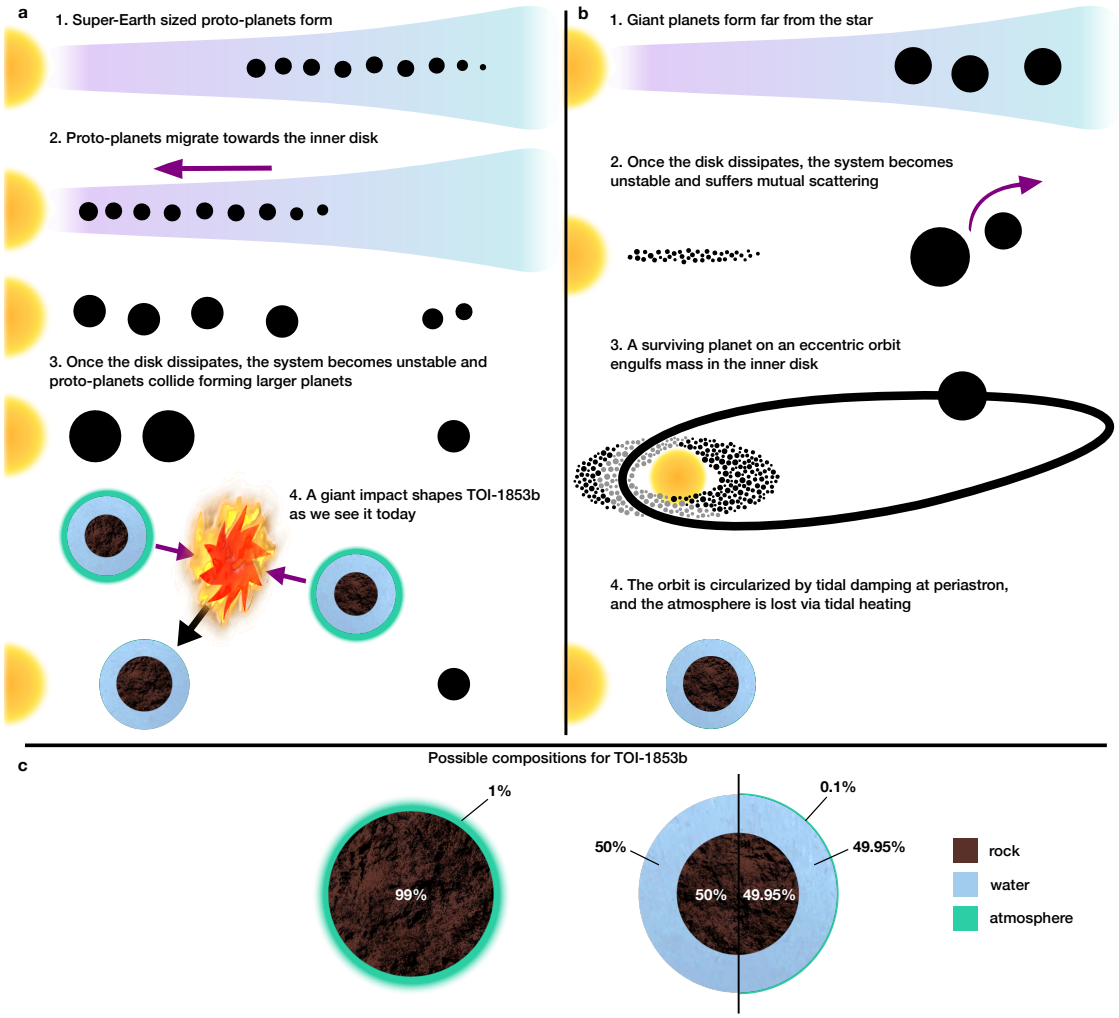

Figure 5.3: Formation scenarios. Two possible pathways for the formation of TOI-1853 b are displayed: in panel (a) the merging of Super-Earth-sized proto-planets ends up in a giant collision, generating with high probability a planetary companion within ∼1 au; in panel (b) distant giant planets undergo mutual scattering after the disk dissipation and the surviving one eventually settles into a highly elliptical orbit. Over time, tidal stripping causes the planet to lose its atmosphere, and tidal damping at periastron circularizes its orbit. Both pathways eventually lead to TOI-1853 b, for which three likely compositions are displayed on panel (c).

was supersampled (Kipping, 2010) at 2 minutes for the global analysis in order to properly account for the longer cadence compared to S50 and the ground-based follow-up light curves. The transit depths are found to be consistent within different *TESS* extraction pipelines, including *PATHOS* (Nardiello et al., 2019), and with ground-based photometry.

5.2.2 Ground-based photometric follow-up

The *TESS* pixel scale is ~ 21 arcsec pixel^{-1} and photometric apertures extend out to multiple pixels, generally causing multiple stars to blend in the *TESS* aperture. To rule out the NEB-blend scenario and attempt to detect the signal on-target, we observed the field as part of the *TESS* Follow-up Observing Program Sub Group 1 (TFOP (Collins, 2019)). We observed full transit windows of TOI-1853 b on May 25, 27 and June 27 2020 respectively with the MuSCAT2 imager (Narita et al., 2018) installed at the 1.52 m Telescopio Carlos Sanchez in the Teide Observatory (in g, r, i, and z_s bands), with the 0.61 m University of Louisville Manner Telescope (ULMT) located at Steward Observatory (through a Sloan-r' filter) and with the Las Cumbres Observatory Global Telescope (LCOGT (Brown et al., 2013)) 1.0 m network node at Siding Spring Observatory (through a Sloan-g' band filter). We extracted the photometric data with `AstroImageJ` (Collins et al., 2017) and measured transit depths across multiple optical bands consistent with an achromatic transit-like event and compatible with *TESS* well within 1σ. We ruled out an NEB blend as the cause of the TOI-1853 b detection for all the surrounding stars, and included the detrended ground-based observations in the global fit (Fig. 5.5).

5.2.3 High Resolution Imaging

As part of the standard process for validating transiting exoplanets to assess the possible contamination of bound or unbound companions on the derived planetary radii (Ciardi et al., 2015), we observed TOI-1853 with near-infrared adaptive optics (AO) imaging at Keck and with optical speckle imaging at Gemini and SOAR. We performed observations at the Keck Observatory with the NIRC2 instrument on Keck-II behind the natural guide star AO system (Wizinowich et al., 2000) on 2020-05-28 UT in the standard 3-point dither pattern. The dither pattern step size was $3''$ and was repeated twice, with each dither offset from the previous dither by $0.5''$. NIRC2 was used in the narrow-angle mode with a full field of view of $\sim 10''$ and a pixel scale of approximately $0.0099442''$ per pixel. The Keck observations were made in the narrowband Br-γ filter ($\lambda_O = 2.1686; \Delta\lambda = 0.0326$ μm) with an integration time of 15 seconds for a total of 135 seconds on the target. The final resolutions of the combined dithers were determined from the full width at half maximum (FWHM) of the point spread functions: $0.053''$. The sensitivities of the final combined AO image (Fig. 5.6) were determined by injecting simulated sources azimuthally around the primary target every 20° at separations of integer multiples of the central source's FWHM (Furlan et al., 2017).

We observed TOI-1835 with the ʻAlopeke speckle imaging camera at Gemini North (Scott et al., 2021, Ziegler et al., 2019), obtaining seven sets of 1000 frames (2020-06-10 UT), with each frame having an integration time of 60 ms, in each of the instrument's two bands (Howell et al., 2011) (centred at 562 nm and 832 nm). The observations of the target reach a sensitivity in the blue

channel of 5.2 mag, while in the red channel of 6.3 mag at separations of 0.5 arcsec, and show no evidence of additional point sources. We also searched for stellar companions to TOI-1853 with speckle imaging on the 4.1-m SOAR telescope (Tokovinin, 2018) on 2021-02-27 UT, observing in Cousins-I band, similar to the TESS bandpass. This observation was sensitive to a 4.7-magnitude fainter star at an angular distance of 1 arcsec from the target (Fig. 5.6).

5.2.4 Gaia

Gaia DR3 astrometry (Gaia Collaboration, 2021) provides additional information on the possibility of inner companions that may have gone undetected by high-resolution imaging. For TOI-1853, Gaia found a Renormalised Unit Weight Error (RUWE) of 1.08, indicating that the Gaia astrometric solution is consistent with the star being single (Ziegler et al., 2019). In addition, in the Gaia archive, we identified no sources within 40 arcsec from the target ($\approx$ 7000 au at the distance of TOI-1853) and, therefore, no potentially widely separated companions with the same distance and proper motion.

5.2.5 Spectroscopic data

We gathered 56 spectra of TOI-1853 with HARPS-N (High Accuracy Radial velocity Planet Searcher for the Northern hemisphere (Cosentino et al., 2012)) between February 2021 and August 2022 (Table 5.2), within the GAPS programme, and reduced them using the updated online Data Reduction Software (DRS) v2.3.5 (Dumusque, 2021). A different pipeline based on the template matching technique, TERRA v1.8 (Anglada-Escudé and Butler, 2012), gave comparable errors and resulted in a fully consistent mass determination. We observed the star in OBJ_AB mode, with fiber A on the target and fiber B on the sky to monitor possible contamination by moonlight, which we deemed negligible (Malavolta et al., 2017). We extracted the RVs by cross-correlating the HARPS-N spectra with a stellar template close to the stellar spectral type. The median (mean) of the formal uncertainties of the HARPS-N RVs is 3.8 (4.6) m s^{-1}; the RV scatter of 34 m s^{-1} reduces to 4.5 m s^{-1} after removing the planetary signal. Our observations had average airmass, signal-to-noise ratio and exposure time of 1.25, 18 and 1200 seconds, respectively.

5.2.6 Stellar analysis

We derived spectroscopic atmospheric parameters exploiting the co-added spectrum of TOI-1853. In particular, we measured effective temperature ($T_{\rm eff}$), surface gravity ($\log g$), microturbulence velocity (ξ), and iron abundance ([Fe/H]) through a standard method based on measurements of equivalent widths (EWs) of iron lines (Biazzo et al., 2015, Biazzo et al., 2022). We then adopted the grid of model atmospheres (Castelli and Kurucz, 2003) with new opacities and the spectral analysis package MOOG (Sneden, 1973) version 2017. $T_{\rm eff}$ was derived by imposing that the abundance of Fe I is not dependent on the line excitation potentials, ξ by obtaining the independence between Fe I abundance and the reduced iron line EWs, and $\log g$ by the ionization equilibrium condition between Fe I and Fe II.e We also computed the elemental abundance of magnesium and silicon, with respect to the Sun (Biazzo et al., 2022), using the same code and grid of models. The elemental ratios [Mg/Fe] and [Si/Fe] have solar values within the errors, with no evident enrichment in none of these elements with respect to the others. The stellar projected rotational velocity ($v \sin i$) was obtained

through the spectral-synthesis technique of three regions around 5400, 6200, and 6700 Å(Biazzo et al., 2022). By assuming a macroturbolence velocity (Brewer et al., 2016) $v_{\rm macro} = 1.8\,{\rm km\,s^{-1}}$, we found $v \sin i = 1.3 \pm 0.9\,{\rm km\,s^{-1}}$, which is below the HARPS-N spectral resolution, thus suggesting an inactive, slowly rotating star, unless it is observed nearly pole-on.

Finally, we determined the stellar physical parameters with the EXOFASTv2 tool (Eastman et al., 2017), which simultaneously adjusts the stellar radius, mass and age in a Bayesian differential evolution Markov chain Monte Carlo (DE-MCMC) framework (Ter Braak, 2006b), through the modelling of the stellar Spectral Energy Distribution (SED) and the use of the MESA Isochrones and Stellar Tracks (MIST) (Paxton et al., 2015). To sample the stellar SED we used the APASS Johnson B, V and Sloan g', r', i' magnitudes (Henden et al., 2016), the 2-MASS near-infrared J, H and K magnitudes (Cutri et al., 2003), and the WISE W1, W2, W3 infrared magnitudes (Cutri et al., 2021). We imposed Gaussian priors on the $T_{\rm eff}$ and [Fe/H] as derived from the analysis of the HARPS-N spectra, and on the Gaia DR3 parallax 6.0221 ± 0.0159 mas (Gaia Collaboration, 2022). We used uninformative priors for all the other parameters, including the V-band extinction A_V, for which we adopted an upper limit of 0.085 from reddening maps (Schlafly and Finkbeiner, 2011). Fig. 5.7 displays the best fit of the stellar SED. In doing so, we derived a mass of $M_\star = 0.837 \pm 0.038\ M_\odot$, a radius of $R_\star = 0.808 \pm 0.009\ R_\odot$, and an age of $\tau = 7.0^{+4.6}_{-4.3}$ Gyr. To evaluate the uncertainties inherent in stellar models, we determined the stellar parameters with two additional stellar evolutionary tracks, namely Yonsie-Yale (Demarque et al., 2004) (Y2) and Dartmouth (Dotter et al., 2008), finding $M_\star = 0.835 \pm 0.029\ M_\odot$, $R_\star = 0.807 \pm 0.009\ R_\odot$, $\tau = 8.0^{+3.8}_{-4.4}$ Gyr, and $M_\star = 0.849 \pm 0.025\ M_\odot$, $R_\star = 0.792^{+0.005}_{-0.004}\ R_\odot$, $\tau = 4.6 \pm 2.8$ Gyr, respectively. We then summed in quadrature to the EXOFASTv2 uncertainties on $M_\star$ and $R_\star$ the standard deviations of 0.009 $M_\odot$ and 0.009 $R_\odot$ from the MIST, Y2, and Dartmouth stellar models, to obtain the adopted mass and radius of $M_\star = 0.837 \pm 0.039\ M_\odot$ and $R_\star = 0.808 \pm 0.013\ R_\odot$.

5.2.7 RV and activity indicators periodograms

Simultaneously with the RVs, we extracted the time series of several stellar activity indices (Fig. 5.1): the FWHM, contrast and bisector (BIS) span of the CCF (Cross-Correlation Function) profile, as well as the Mount Wilson index ($S_{\rm MW}$) and the spectroscopic lines Hα, Na and Ca. We computed the Generalized Lomb-Scargle (GLS) periodogram, with `astropy` v.4.3.1 (Price-Whelan and The Astropy Collaboration, 2018, Zechmeister and Kürster, 2009), for both the RVs and the activity indexes, which can be inspected in Fig. 5.1. In the RVs, we found the most significant peak at 1.24 days (FAP $\ll 0.1\%$), i.e. the expected transiting period of TOI-1853 b. This signal is not attributable to stellar activity since none of the measured activity indicators shows a similar periodicity or harmonics. Two strong peaks appear at the frequencies of the 1d aliases of the planetary period (for example $f_{\rm alias} = f_{1\,\rm d} - f_{1.24\,\rm d}$, giving rise to a period of $P_{\rm alias} \approx 5.1$ days), which are no longer seen when the signal of TOI-1853 b is subtracted, along with any other peak with FAP $\lesssim 5\%$. The activity indicators do not show signals with FAP $\gtrsim 0.1\%$.

5.2.8 Joint transit and RV analysis

For the joint transit-RV analysis of TOI-1853 b, we employed the modelling tool `juliet` (Espinoza et al., 2019), which makes use of `batman` (Kreidberg, 2015) for the modelling of transits, `RadVel` (Fulton et al., 2018) for the modelling of RVs and correlated variations which are treated as GPs with the packages `george` (Ambikasaran et al., 2015) and `celerite` (Foreman-Mackey et al., 2017). We exploited the dynamic nested sampling package, `dynesty` (Speagle, 2020), to compute Bayesian posteriors and evidence ($\mathcal{Z}$) for the models. Even though by default the *TESS* PDC-SAP photometry is already corrected both for dilution from other objects contained within the aperture using the Compute Optimal Aperture (COA) module (Bryson et al., 2020), and major systematic errors, we corrected it for minor fluctuations that were still observable in the light curve (Fig. 5.1). In particular, we normalized it by fitting a simple (approximate) Matern GP (Gaussian Process) kernel (Espinoza et al., 2019). We also analysed the SPOC SAP photometry (Morris et al., 2020, Twicken et al., 2010), which is not corrected for long trends and found no significant change in the transit depths, or any conclusive evidence of the stellar rotation period over the brief time coverage of both sectors.

We constructed a transit light curve model with the usual planetary orbital parameters: period P, time of inferior conjunction T_0, eccentricity e and argument of periastron ω via the parametrization $(\sqrt{e}\sin\omega, \sqrt{e}\cos\omega)$ and the mean density of the parent star $\rho_\star$ (Espinoza et al., 2019) from our stellar analysis. For the flux of *TESS* and the on-ground light curves, we included in the global model both offsets and jitter parameters, along with two hyper-parameters of the Matern GP model: $\sigma_{\rm GP}$ and $\rho_{\rm GP}$, respectively the amplitude and the length-scale of the GP used to correct *TESS* light curves. The impact parameter [$b = (a_{\rm p}/R_\star)\cos i_{\rm p}$ for a circular orbit] and the planet-to-star radius ratio k were parameterized as (r_1, r_2) (Espinoza, 2018). Moreover, here we make use of a limb-darkening parametrization (Kipping, 2013) for the quadratic limb-darkening coefficients $(q_1, q_2 \rightarrow u_1, u_2)$, with Gaussian priors (Claret, A., 2017). Then, we include the RV model with the usual systemic velocity $\overline{\gamma}_{\rm HARPS-N}$, jitter $\sigma_{\rm HARPS-N}$, and the RV signal semi-amplitude $K_{\rm p}$.

The priors for all the parameters that are used in the joint analysis along with the estimates of the parameters' posteriors are summarized in Table 5.3, while the posterior distributions of the most relevant sampling parameters are shown as corner plots in Fig. 5.9. The addition of an RV linear term (e.g. RV intercept and slope) or RV GP models (Espinoza et al., 2019) with the simple harmonic oscillator, Matern and quasi-periodic (which had the best result of the three) kernels (Foreman-Mackey et al., 2017), did not significantly increase the Bayesian-log evidence or even worsened it ($\Delta\mathcal{Z}^{\rm quasi\,per}_{\rm base} \approx 2$, $\Delta\mathcal{Z}^{\rm linear}_{\rm base} \approx -3$), and resulted in an unconstrained value for the GP evolution time-scale. The inclusion of a second planet in the model, with a uniform orbital period prior between 2 and 500 days, did not improve the Bayesian-log evidence either ($\Delta\mathcal{Z}^{2pl}_{\rm base} \approx 0$), also resulting in an unconstrained value for the period, which is consistent with the observed lack of features in the GLS of the RV residuals after the subtraction of TOI-1853 b signal. Furthermore, in order to check for transit time variations (TTVs) we ran a simple test where the orbital period of the transit model was fixed at its best-fitting value while all the transit times were allowed to vary, finding no clear evidence of TTVs as all the transit times are compatible with their expected value within $\approx$ 1-sigma (see Supplementary materials).

5.2.9 RV detection function

We estimated the detection function of the HARPS-N RV time series by performing injection-recovery simulations, in which synthetic planetary signals were injected in the RV residuals after the subtraction of the TOI-1853 b signal. We simulated signals of additional companions in a logarithmic grid of 30×40 in the planetary mass, $M_{\rm p}$, orbital period, P, parameter space respectively, covering the ranges $1 - 1000\,M_{\oplus}$ and $0.5 - 5000$ d. For each location in the grid, we generated 200 synthetic planetary signals, drawing P and $M_{\rm p}$ from a log-uniform distribution inside the cell, T_0 from a uniform distribution in $[0, P]$, and assuming circular orbits. Each synthetic signal was then added to the RV residuals. We computed the detection function as the recovery rate of these signals, i.e. fitting the signals with either a circular-Keplerian orbit or a linear or quadratic trend, to correctly take into account long-period signals which would not be correctly identified as a Keplerian due to the short time-span of the RV observations (500 d). We adopted the Bayesian Information Criterion (BIC) to compare the fitted planetary model with a constant model: we considered the planetary signal significantly detected when $\Delta\mathrm{BIC} > 10$ in favour of the planet-induced model. The detection function was then computed as the fraction of detected signals for each element of the grid (Fig. 5.10).

5.2.10 Orbital decay

According to the current tidal theory, tidal inertial waves are presently not excited inside TOI-1853 by planet b because the rotation period of the star is certainly longer than twice the planetary orbital period (Ogilvie and Lin, 2007), while tidal gravity waves are not capable of dissipating efficiently in the central region of the star given the relatively low planetary mass (Barker, 2020). Even assuming a lower limit for the modified tidal quality factor $Q'_{\star} = 10^7$, the remaining lifetime of the planet is about 4 Gyr according to Eq. (1) of ref. (Metzger et al., 2012), or longer if we take into account equilibrium tides (Cameron and Jardine, 2018). The situation is different if the planet's orbital plane is inclined relative to the stellar equator (Lai, 2012) because a dynamical obliquity tide is expected to be excited independently of the star rotation period. Such a dynamical tide would produce a fast decay of the obliquity, while it is not equally effective in producing a decay of the orbit semi-major axis (Lai, 2012). Therefore, the effective Q'_{*}, which rules the orbital decay, can be assumed to be approximately unaffected by the stellar or planetary obliquities (see, however, Sect. 2.2 of ref. (Leconte et al., 2010), for quantification of how the obliquities affect the evolution of the semi-major axis). On the other hand, assuming $Q'_{\star} \sim 10^6$ for the dynamical obliquity tide, the e-folding damping time of the stellar obliquity would be about 1.6 Gyr, which is significantly shorter than the estimated age of the system. Therefore, any initial stellar obliquity may have had time to be damped along the lifetime of the system.

5.2.11 Composition

The planet bulk composition was constrained based on mass-radius relations derived in refs. (Zeng et al., 2019, 2021). For the calculation we adopted a second-order adapted polynomial equation of state (EOS) from ref. (Holzapfel, 2018), using EOS coefficients from ref. (Zeng et al., 2021). This is a robust estimate since any density of a condensed phase (solid or liquid) in the interior of the planet is mostly determined by pressure, which, in this case, is generated by strong self-gravitation

and weakly depends on the temperature. We assumed a completely differentiated planet with an iron (Fe) core and a mantle consisting of silicate ($MgSiO_3$) rock. The rocky interior (Fig. 5.2) was assumed to be 32.5% Fe plus 67.5% silicates, broadly consistent with cosmic element abundance ratios and those derived from the host-star abundances taken as a proxy for the proto-planetary disk composition (Table 5.1), which point to Mg:Si:Fe being close to 1:1:1. The H_2–He gaseous envelope above the rocky interior was assumed to be a cosmic mixture of 75% H_2 and 25% He by mass. Instead, the 50% H_2O curve in Fig. 5.2 corresponds to an Earth-like composition with exactly equal mass of H_2O on top. The latter component approximates the mixture of C, N, O, H-bearing material that condensed beyond the iceline of the proto-planetary disk in a water-dominated mixture of H_2O, NH_3 and CH_4. Slightly different compositions are compatible with TOI-1853 b as well, for example, a thin H_2 envelope, 0.1% by mass, might be present along with a rocky interior (49.95%) and the H_2O mantle (49.95%). We neglected both the role of miscibility and chemical reactions at the interface between rock and icy material (Kovačević et al., 2022, Vazan et al., 2022) and that of any phase transition between high-pressure ice and supercritical water (Mousis et al., 2020). Finally, neither of the possible compositions producing the mass-radius curves in Fig. 5.2 is expected to be primordial for a planet with the mass and radius of TOI-1853 b. Catastrophic events such as the ones we discuss here, i.e. multiple proto-planet collisions at the onset of dynamical instabilities upon disk disappearance or tidal disruption in a high-eccentricity migration scenario, must be invoked.

5.2.12 Formation simulations

We simulated systems of 2, 4 and 8 solid-rich planets with a total mass of 80 $M_\oplus$, using the code `swift symba5` (Duncan et al., 1998). For the first scenario of merging proto-planets, we placed the innermost planet at 0.02 au from the star, similar to TOI-1853 b, and the other planets separated by 1.5 mutual Hill radii, to ensure that the system is violently unstable. The initial eccentricities were assumed to be between 0 and 5e-2 and the inclinations between 0 and 1.4 degrees, to ensure that the system evolves in 3D and the collision probability is not artificially enhanced (see Supplementary materials). The systems with initially 2 and 4 proto-planets merged into a single planet with 80 $M_\oplus$. The system with 8 super-Earths merged into two planets of 50 and 30 $M_\oplus$ respectively. We then did a fourth simulation starting from a system of 10 super-Earths of 10 $M_\oplus$ each, which led to the formation of two planets of 70 $M_\oplus$ and 30 $M_\oplus$.

For the second scenario, we simulated a Jupiter-mass planet on an orbit with a semi-major axis at 1 au, perihelion distance at 0.02 au and inclination of 10 degrees. The planet is assumed to have a radius of 2 Jupiter radii, due to tidal heating at perihelion. We placed test particles in three rings at 0.02-0.06 au, 0.1-0.3 au and 0.5-1.5 au. In a million years, the planet engulfed 30%, 6% and 2% of the particles in the three rings, respectively (see Supplementary materials). The sharp decay of efficiency with the distance from the star is expected because the planetesimals are spread over a larger area. However, this means that the planet can accrete an additional 30-40 $M_\oplus$ if there's enough mass in the disk to begin with.

5.2.13 Detailed impact simulations

TOI-1853 b is too massive to have been formed in situ, but a single large impact, or multiple smaller ones, might have removed its atmosphere and crust during the final stages of formation, thus boosting its density. Here we consider giant impacts between super-Earths (or mini-Neptunes), as a possible explanation for the two possible internal compositions depicted in Fig. 5.2 (panel a). If all the pre-impact super-Earths in the system originally had thin atmospheres like Earth, it would be straightforward to form TOI-1853 b with 1% atmosphere on top of a 99% Earth-like rocky interior. However, for pre-impact super-Earths with thick atmospheres, the required impact velocity to remove most of the atmosphere could be as high as three times the mutual escape velocity of the two colliding bodies (Denman et al., 2020, 2022). A series of high-speed impacts ($\gtrsim 2$ mutual escape velocity) or one last catastrophic high-speed ($\gtrsim 3$ mutual escape velocity) impact could expel most of the gaseous envelope. N-body simulations show that the impact speeds of similar-sized objects are normally within two times the mutual escape velocity (Chambers, 2013, Quintana et al., 2016), but given the close distance of TOI-1853 b to its star, high-speed impacts are not impossible. If TOI-1853 b is a half water–half rock planet, the pre-impact mini-Neptunes composition could be very different. A layer of water on top of a planet could greatly enhance the loss efficiency of the atmosphere (Genda and Abe, 2005), but few studies have examined the problem in three dimensions.

In order to better understand the loss process of volatiles during these collisions, we conducted a series of smoothed particle hydrodynamics impact simulations under different conditions using `SWIFT` (Schaller et al., 2016). Assuming the initial planets have three layers (H/He on top, a water mantle, and a rocky interior), we explored three different compositions: water-rich by mass (67.5 % water, 22.5 % rock, 10 % H/He), equal rock and water (45 % rock, 45 % water, 10 % H/He), and rock-rich (67.5 % rock, 22.5 % water, 10 % H/He), with the planets' thermodynamic profiles generated using `WoMa` (Ruiz-Bonilla et al., 2020). These conditions were chosen to give a range of reasonable Neptune-like compositions for the precursor planets. The rocky interior, water, and atmosphere layers are modelled using the ANEOS forsterite (Stewart et al., 2020), AQUA water (Haldemann et al., 2020), and a mixture of hydrogen–helium (Hubbard and Macfarlane, 1980) equation of states, respectively. The ANEOS forsterite equation-of-state table was regenerated using ref. (Stewart et al., 2019) with a more dense grid (1560 grid points for density, 744 grid points for temperature) and higher maximum density ($80\,\mathrm{g\,cm^{-3}}$) to better model the high-pressure and high-density rocky interior. Each initial target contained approximately 10^6 particles, and the atmosphere layers were resolved with at least 10 particle layers. The most promising impacts were repeated with higher resolution (10^7 particles) to make sure that the post-collision results converged. The mass of the largest post-collision remnant (M_{lr}) was calculated using a known methodology (Carter et al., 2018, Marcus et al., 2009), while the maximum smoothing length h_{max} was set to $5\,R_\oplus$.

We tested various impact scenarios including head-on and oblique impacts with a pre-impact impactor to target mass ratio ranging from 0.5 to 1 and target masses of 25, 45, 50 and 60 $M_\oplus$. In Table 5.4, we provide selected results from impact simulations. We found that head-on (oblique) merging collisions, where a target and an impactor collide at a speed approximately equal to their mutual escape velocity (simulations with id from 1-3, 5-7, 9-11 in the Table 5.4), would result in the removal of at most 10% (5%) of their atmospheres. While giant impacts at approximately mutual

escape velocity are the most common, they have low atmosphere removal efficiency, and even a series of impacts may not be enough to remove the gaseous envelope completely. Therefore, the system would need to experience a sequence of mid-speed impacts ($\gtrsim$ 1.5 mutual escape velocity, simulation id 4, 8 and 12 in the Table 5.4) or at least one high-speed impact ($\gtrsim$ 2 mutual escape velocity) during its final formation stage in order to remove most of the atmosphere. Simulations 16, 17, and 18 in the Table 5.4 represent the potential final giant impact leading to the formation of TOI-1853 b, assuming that the target planet with a mass of 60 $M_\oplus$ was formed by several previous merging collisions that resulted in little or no compositional change. A high percentage of water on the initial planets would make the removal of the atmosphere more efficient, as water-rich impacts require the lowest impact velocity and have the highest atmosphere loss fraction. Although there is always some loss of water during impacts, the water loss efficiency is reduced if more water is present on the planet initially. The mass fractions of the rock in the post-collision remnant tend to increase in all three impact composition setups, confirming that rock is less likely to be lost due to the core being in the centre and being less compressible than water and the atmosphere.

Considering the results shown in Table 5.4, we expect that the post-collision remnant could have half water and half rock (with a very thin or negligible atmosphere) if the initial planets contained more water than in the equal rock and water case (simulation id 17 Table 5.4) but not as much as the water-rich planet (simulation id 16). If TOI-1853 b is a half-rock and half-water planet, these impact simulations can be used to infer the composition of either the planets prior to the final impact or the primordial disk that supplied the material from which TOI-1853 b accreted. Generating a pure rock post-collision remnant requires a higher impact speed, as the atmosphere removal efficiency for rock-rich planets is relatively low. Scaling laws (Denman et al., 2020), applied in the mass regime of TOI-1853 b, suggest that the impact energies required to remove a large fraction of the atmosphere will be in the super-catastrophic regime, and the initial planet would need $\sim$ 10 times the final mass to produce a rocky planet with a thin atmosphere. Therefore, if TOI-1853 b is mainly composed of rock, then there would need to have been a greater mass budget in the disk initially, as a higher velocity impact would have ejected much more mass. A water-rich composition for TOI-1853 b is likely easier to produce via impacts than a water-free super-Earth composition.

5.2.14 Atmospheric evaporation

We have considered two possible evaporation mechanisms: photo-evaporation induced by high-energy irradiation, or Roche Lobe Overflow (RLO). At the present age, the Jeans escape parameter ($\propto M_\mathrm{p}/R_\mathrm{p}T_\mathrm{eq}$) (Fossati et al., 2017) resulted $\Lambda \gtrsim 100$, adopting the planetary parameters in Table 5.1. Such a high value indicates that the atmosphere of TOI-1853 b is in hydrodynamic stability against photo-evaporation, thanks to the deep gravitational potential well of the planet. To explore its evolution, we adapted a numerical code developed for studying single systems (Locci et al., 2019, Maggio et al., 2022), considering the following three scenarios: rocky interior + an H_2-dominated envelope (1% by mass), 49.95% rocky interior + 49.95% water mantle + 0.1% H_2-dominated envelope, 50% rocky interior + 50% water mantle and no envelope. For each case, we created a synthetic population of young planets (10 Myr old) with different atmospheric mass fractions, ranging from 0, 0.1% or 1% (depending on the case) to around 75% of the current planetary mass. At any age, the planet's radius is the sum of a fixed core radius plus a time-dependent envelope radius.

During the evolutionary history, which we followed up to 7 Gyr, planet contraction occurs due to gravitational shrinking and to the possible mass loss via atmospheric evaporation. Assuming a Jupiter-like albedo, $A = 0.5$, we found that none of the planets is either initially, or later becomes, hydro-dynamically unstable. Larger radii imply lower values of the Jeans escape parameter, but this is compensated by the lower equilibrium temperatures until the host star reaches the main sequence at an age of ~ 200 Myr. In the extreme case of zero Bond albedo, planets with initial mass $\leq 180\,M_\oplus$ and $\geq 75\,M_\oplus$ can be hydro-dynamically unstable ($\Lambda < 80$). We explored the cases near the lowest initial mass ($\sim 75\,M_\oplus$) or the lowest initial value of the Jeans parameter ($\Lambda \sim 60$), but we found that in all these cases the total mass loss and the radius contraction are not sufficient to recover the assumed planetary structure at the current age.

In order to investigate the possible mass loss due to RLO, we computed the volume-averaged Roche radius R_L (Eggleton, 1983), during the different evolutionary histories of the planet described above. It resulted always larger than $1.8R_\mathrm{p}$ at the start of the evolution ($t = 10$ Myr), for any value of the assumed initial mass. At later ages, the Roche radius tends to increase due to any possible mechanism of mass loss. For comparison, we evaluated the outer limit of the atmosphere, i.e. the so-called exobase ($p_\mathrm{b} \sim 10^{-12}$ bar), by scaling the thermal escape parameter (Koskinen et al., 2022) $\Gamma = GM_\mathrm{p}\mu m_\mathrm{H}/kT_1 r$, where $\mu = 2.3$ is the mean molecular weight and $T_1 = T_\mathrm{eq}$, assuming an isothermal atmosphere in hydrostatic equilibrium and $r_1 = R_\mathrm{p}$ at $p = 1$ bar. We found that the exobase is located at $r_\mathrm{b} = 1.1\,R_\mathrm{p}$, and hence always below the Roche radius. Finally, we computed the orbital period at which a planetary companion would begin losing mass as a result of RLO, given by $P_\mathrm{RL} = 0.4\rho^{-1/2}$ d (Jackson et al., 2017, Rappaport et al., 2013), where ρ is the mean planet density. This critical period resulted always shorter than 0.5 days. Assuming that the planet is not migrating during the evolution, the critical period remains also shorter than the orbital period, and hence no RLO should occur. This result is due to the very large density of the planet, with respect to standard models. As a countercheck, we verified that the critical period would become equal to or larger than the orbital period if the past density of the planet was lower than ~ 0.1 g cm^{-3}. In our grid of models, the planetary radius remains in the range 4–12 $R_\oplus$ for envelope mass fractions up to 75% the current planetary mass, while the critical density would require radii from 16 to 25 $R_\oplus$. We conclude that RLO processes could have contributed to the loss of TOI-1853 b envelope only if the planet was closer to the star in the past, which for a circular orbit corresponds to $P_{orb} \approx 0.5$ days, almost half of the current one. For this to be true, the planet should have later migrated to its current position in agreement with the high-eccentricity formation scenario, for which planets roughly circularize at twice the periastron distance of the initial eccentric orbit.

5.2.15 Spectral atmospheric characterisation prospects

We explored whether JWST is able to detect spectroscopic signatures of a TOI-1853 b-like planet. According to the transit and emission spectroscopic metrics (Kempton et al., 2018), TOI-1853 b is at the lower-end distribution of targets selected for transmission. For emission instead, TOI-1853 b is comparable to the bulk of the selected JWST secondary eclipse observations (Fig. 5.11). We generated synthetic spectra for TOI-1853 b using the open-source Pyrat Bay modelling framework (Cubillos and Blecic, 2021). We considered two extreme cases based on the scenarios previously

explored: 1) a planet with a rocky interior and a 1% H_2 atmosphere and 2) a planet with a 50% rocky interior, 40% H_2O mantle, and a 10% H_2O supercritical steam atmosphere. Given the lack of atmospheric composition constraints other than the bulk density of the planet, we adopted a generic solar composition with scaled heavy-element metallicities such that we match the atmospheric mass fraction of the H_2-dominated and the heavy-element-dominated atmosphere. Based on the planet's equilibrium temperature, we assumed an isothermal temperature profile for transmission and a radiative-equilibrium profile for emission. We computed the molecular composition assuming thermochemical equilibrium. We considered the main opacity sources expected for exoplanets in the infrared, i.e.: from molecular line lists (Rothman et al., 2010, Tennyson et al., 2020) (pre-processed with the `repack` package (Cubillos, 2017)), collision induced absorption (Borysow et al., 2001, 1988), and Rayleigh scattering (Kurucz, 1970). We then simulated JWST transmission and emission observations with `PandExo` (Batalha et al., 2017) for all instruments on board.

Fig. 5.11 shows our model spectra of TOI-1853 b along with the simulated JWST observations combining three visits with each instrument to enhance the signal-to-noise ratios. Either transmission or emission spectroscopic characterisation efforts will be challenging. According to the adopted synthetic models, NIRISS/SOSS and NIRSpec/G395H are the most favourable instruments to detect spectral features based on their spectral coverage and S/N ratios. Additionally, NIRSpec/G235H provides the best S/N ratio at ∼2–3 μm. The transmission spectra present the largest spectral features for metallicities ranging from $0.01 - 50.0\times$ solar. For larger metallicities, the amplitude of the features starts to flatten as the mean molecular mass of the atmosphere increases. Notable spectral features are the H_2O bands at 1.0–2.5 μm and a strong CO_2 band at 4.5 μm for super-solar metallicities. Certainly, the presence of clouds and hazes would complicate the interpretation of these observations as they can also flatten the spectral features, though they tend to be more prevalent for lower-temperature atmospheres (Morley et al., 2015). The emission spectra seem to provide more identifiable features than in transmission (as confirmed by the relatively better spectroscopic metric). Under the assumption of equilibrium chemistry, the CO_2 absorption feature at 4.5 μm is the clearer tracer of metallicity, as the abundance of CO_2 increases more steeply with metallicity than other dominant species like H_2O.

5.3 Addendum

5.3.1 Description of the dynamical formation simulations

The first simulation considers 2 planets of 40 Earth masses around a solar-mass star. Their initial orbital elements are:
a_1=0.02000 au, e_1=0.006, i_1=1.27 deg., Ω_1=54.8 deg., Ω_1=297.5 deg, M_1=76.3 deg.
a_2=0.02121 au, e_2=0.002, i_2=1.02 deg., Ω_2=112.6 deg., Ω_2=227.2 deg, M_2=110.9 deg.
The two planets merged into a single one with orbital elements:
a=0.02065 au, e=0.007, i_2=0.76 deg.
The second simulation considers 4 planets of 20 Earth masses. Their initial orbital elements are:
a_1=0.02000 au, e_1=0.006, i_1=1.27 deg., Ω_1=54.8 deg., Ω_1=297.5 deg, M_1=76.3 deg.
a_2=0.02096 au, e_2=0.002, i_2=1.02 deg., Ω_2=112.6 deg., Ω_2=227.2deg, M_2=110.9 deg
a_3=0.02185 au, e_3=0.044, i_3=0.31 deg., Ω_3= 4.9 deg., Ω_3=18.3 deg, M_3=307.8 deg.

a_4=0.02258 au, e_4=0.004, i_4=1.07 deg., Ω_4=51.5 deg., Ω_4=322.0 deg, M_4=253.0 deg.
The planets merged into a single one with orbital elements: a=0.02121 au, e=0.012, i_2=0.81 deg.
In the third simulation we considered 8 planets of 10 Earth masses. Their initial orbital elements are:
a_1=0.02000 au, e_1=0.006, i_1=1.27 deg., Ω_1=54.8 deg., Ω_1=297.5 deg, M_1=76.3 deg.
a_2=0.02076 au, e_2=0.002, i_2=1.02 deg., Ω_2=112.6 deg., Ω_2=227.2deg, M_2=110.9 deg.
a_3=0.02146 au, e_3=0.044, i_3=0.31 deg., Ω_3= 4.9 deg., Ω_3=18.3 deg, M_3=307.8 deg.
a_4=0.02203 au, e_4=0.004, i_4=1.07 deg., Ω_4=51.5 deg., Ω_4=322.0 deg, M_4=253.0 deg.
a_5=0.02283 au, e_5=0.037, i_5=0.13 deg., Ω_5=247.6 deg., Ω_5=271.0 deg, M_5=216.5 deg.
a_6=0.02344 au, e_6=0.042, i_6=0.84 deg., Ω_6=245.6 deg., Ω_6=121.8 deg, M_6=203.5 deg.
a_7=0.02431 au, e_7=0.044, i_7=0.67 deg., Ω_7=183.5 deg., Ω_7= 99.4 deg, M_7=259.5 deg.
a_8=0.02521 au, e_8=0.031, i_8=0.28 deg., Ω_8=9.3 deg., Ω_8=268.3 deg, M_8=37.9 deg.
This system results into two planets of 50 and 30 Earth masses with, respectively, orbital elements:
a_1=0.02026 au, e_1=0.043, i_1=0.46 deg.
a_2=0.02642 au, e_2=0.081, i_2=0.63 deg.
The second simulation depicts a Jupiter-mass planet on an orbit with a 1 au, e=0.98 (so that its perihelion distance is 0.02 au) and i=10 deg. We simulated the effect of this planet on a disk of 1000 test particles (representing planetesimals or planets of smaller mass with respect ot the giant planet) with 0.02 au $<$ a $<$ 0.06 au, e$<$0.1 and i$<$2.5 degrees. We simulated the system for 150'000 years, at the end of which only 2 particles survive. 309 (31%) have been accreted by the giant planet. We then repeated the simulation with a disk of 1000 test particles with 0.1 au $<$ a $<$ 0.3 au and then with 0.5 au $<$ a $<$ 1.5 au, both still with e$<$0.1 and i$<$ 2.5 deg.. Only 65 and 20 particles from disk disks have been accreted by the giant planet, namely 6.5 and 2 of the total. This shows that the efficiency of accretion of particles by the eccentric giant planets falls rapidly with the distance of the particles from the star. All these simulations have been performed using the simplectic swift symba5 integrator (properly referenced in the main text), with a timestep of 5x10^{-5} years.

5.3.2 TTV

The observed transit times of TOI-1853b were evaluated by fitting its light curves with the orbital period fixed at its best-fitting value and leaving each time of transit as free to vary (see Figure 5.4). Then the observed times were compared with the calculated (expected) times from the orbital period. We found no evidence of Transit Time Variations (TTV) as all the observed transit times are compatible with their expected value within ≈1-sigma. The periodogram of O-C does not result in any relevant peaks either. Indeed, considering the mass and orbital period of TOI-1853b, the shallow transit depth, and also the lack of clear massive planets nearby (see Sect. 5.2.9), we did not expect to detect TTVs unless the planet was being rapidly engulfed by the host star (which is unlikely according to Sect. 5.2.10).

Data availability

TESS photometric time series can be freely obtained from the Mikulski Archive for Space Telescopes (MAST) archive at https://exo.mast.stsci.edu/. All follow-up light curve data are available on the `ExoFOP-TESS` website (https://exofop.ipac.caltech.edu/tess/ + target.php?id=73540072). Radial

velocities are presented in Table 5.1. The simulation dataset of Sect. 2.13 is available on Zenodo (10.5281/zenodo.8033965).

Code availability

The `juliet` python code is open and available at https://github.com/nespinoza/juliet. The `Pyrat Bay` modelling framework is open-source and available at https://github.com/pcubillos/pyratbay. `astropy` is a common core package for astronomy in Python, and `EXOFASTV2` is a well known public exoplanet fitting software. `swift` `symba5` is available on https://github.com/silburt/swifter. `SWIFT` is available on www.swiftsim.com. `WoMa` is available on https://github.com/srbonilla/WoMa. The `repack` package is available on https://github.com/pcubillos/repack. `PandExo` is available on https://github.com/natashabatalha/PandExo.

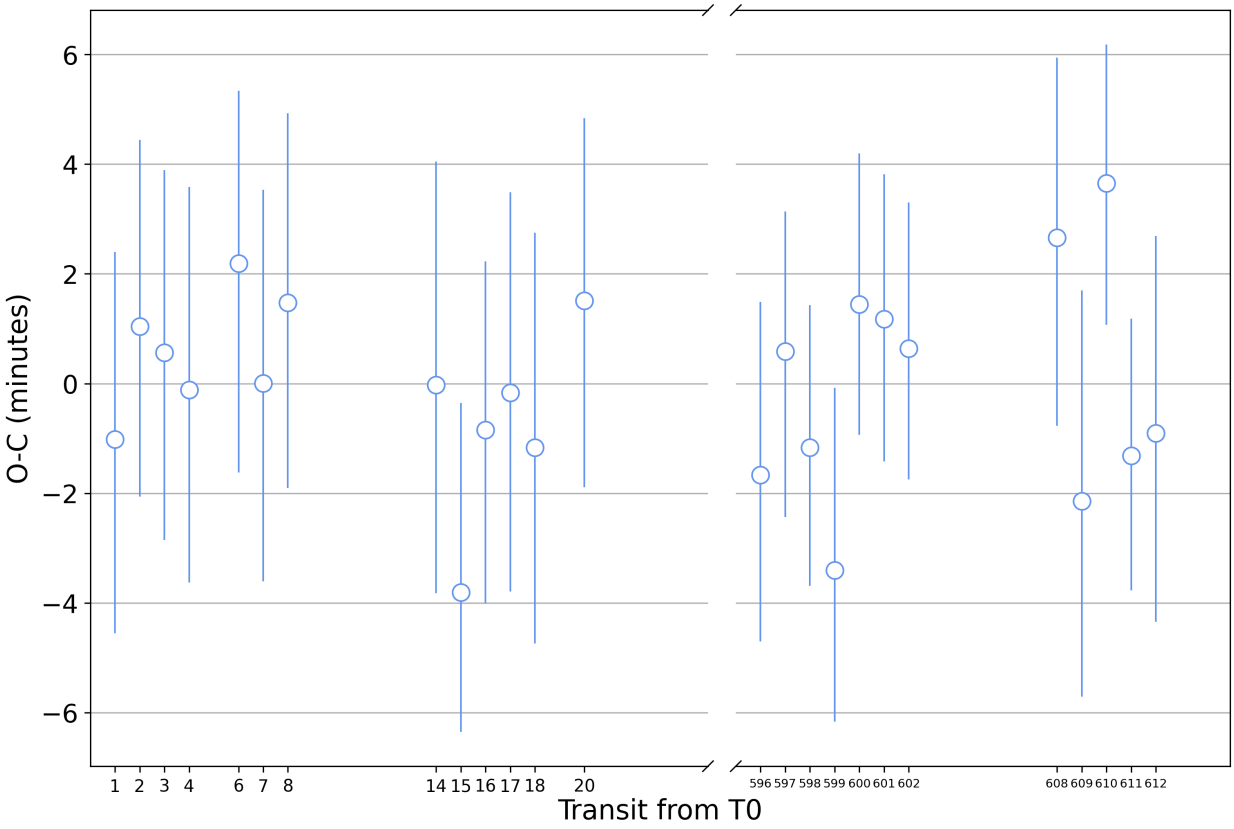

Figure 5.4: Observed - Calculated (O-C) time of transits for TOI-1853 b.

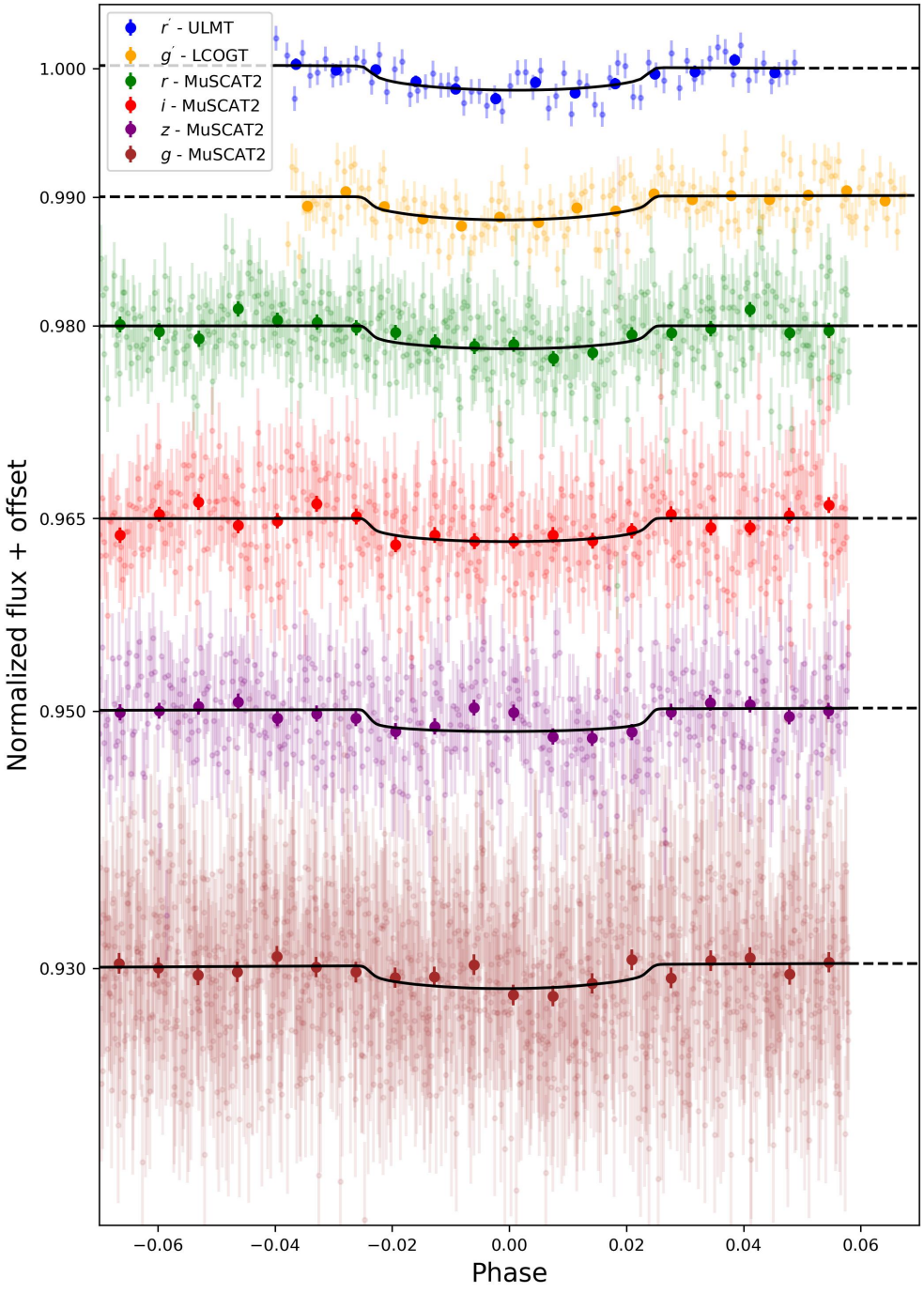

Figure 5.5: Global fit result for the ground-based transits. The light curves of MuSCAT2, LCOGT and ULMT have been shifted on the Y-axis for clarity, and their respective filter band has been indicated in the legend. The superimposed points represent ≈ 10-minute bins, while the error bars represent one standard deviation. The global fit from this work is depicted in black.

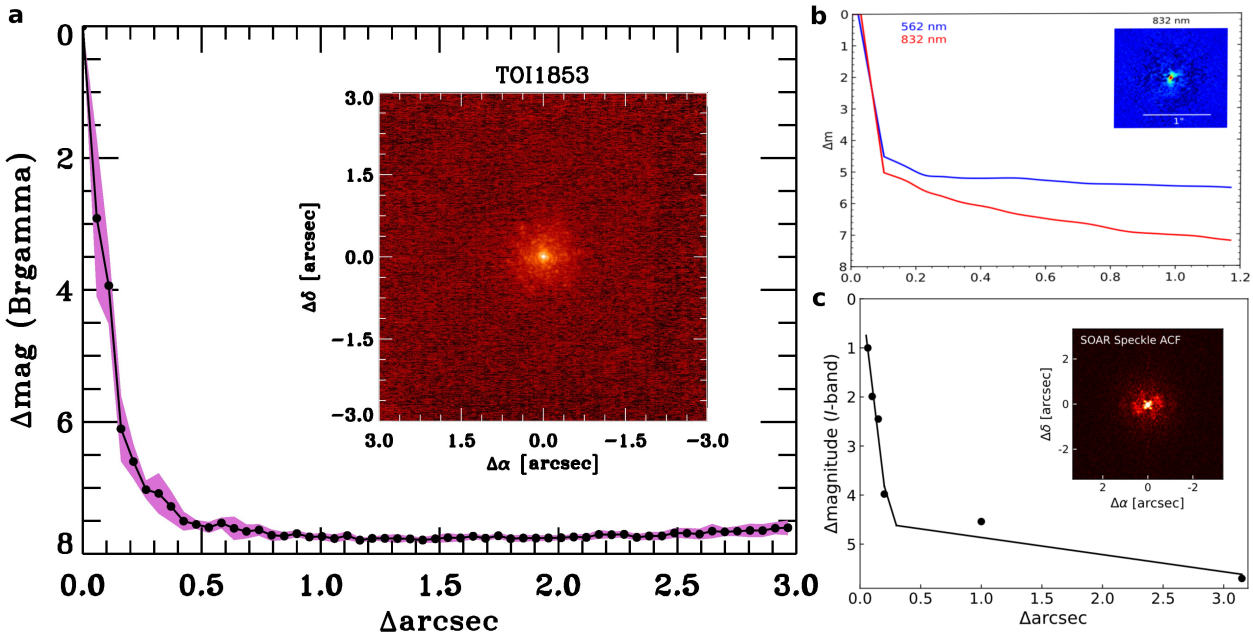

Figure 5.6: High-resolution sensitivity curves. Final sensitivity of (a) Keck, (b) Gemini and (c) SOAR, plotted as a function of angular separation from the host star. The images reach a contrast of (a) ~ 7.6, (b) ~ 5.2, ~ 6.3 and (c) ~ 4.7 magnitudes fainter than TOI-1853 within $0.5''$ in each respective band. Images of the central portion of the data are presented as insets in the relative panels.

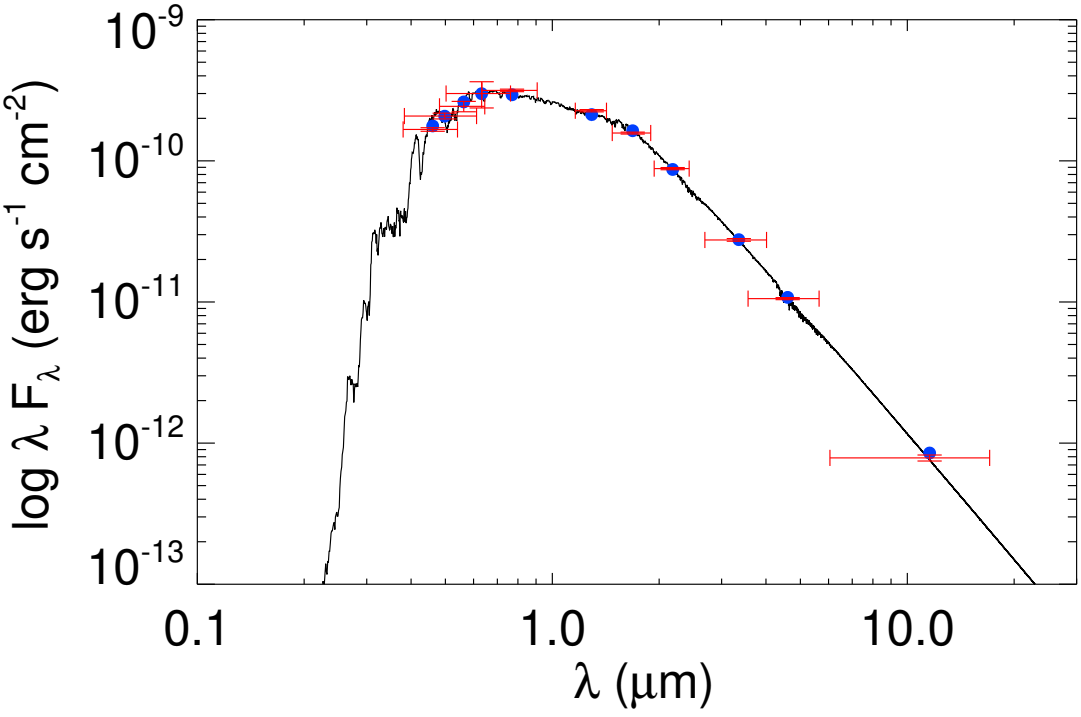

Figure 5.7: TOI-1853 Spectral Energy Distribution. The error bars represent one standard deviation. The best-fit model is displayed as a solid black line.

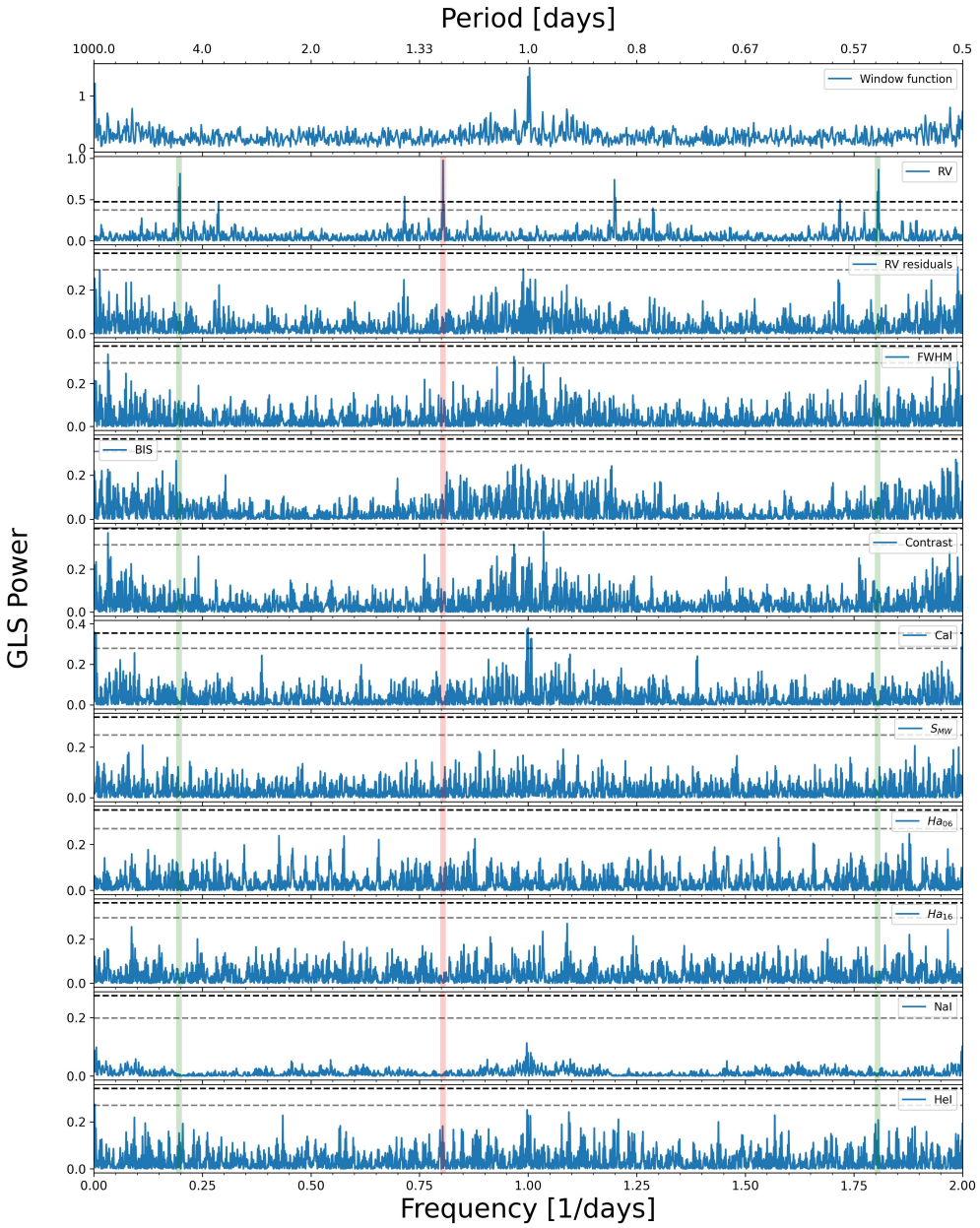

Figure 5.8: GLS periodograms. The periodograms of the RVs, its residuals from the global fit and several activity indexes are plotted consecutively, while the window function is on top as reference. The main peak of the RV GLS periodogram, at 1.24 days, and his 1-day aliases are highlighted by a red and green vertical bar, respectively. The horizontal dashed lines remark the 10% and 1% confidence levels (evaluated with the bootstrap method), respectively.

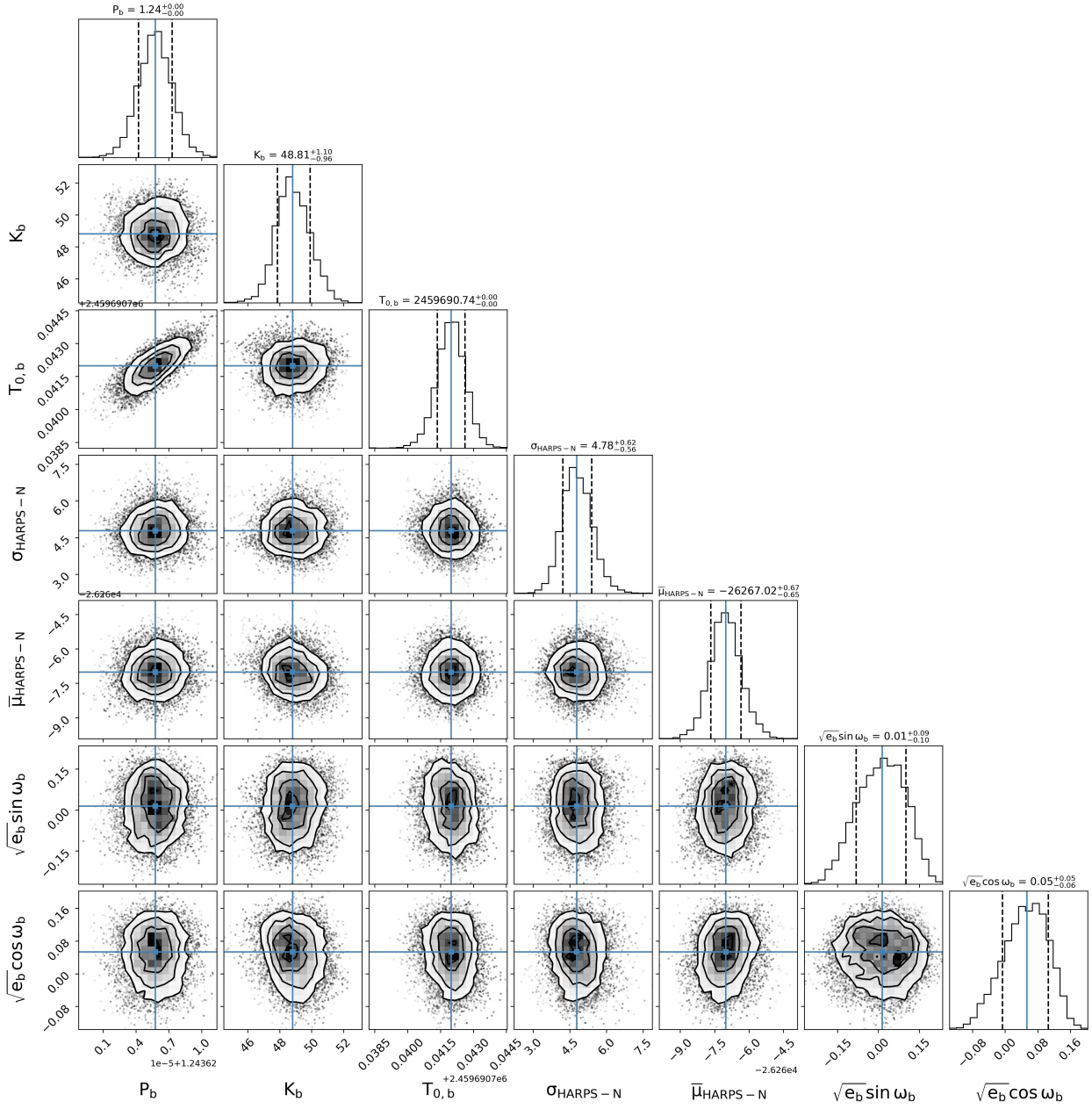

Figure 5.9: Corner plot for the posterior distributions of the global joint fit. The blue lines indicate the average value of every parameter, while the dashed vertical lines are indicate the confidence levels at one standard deviation.

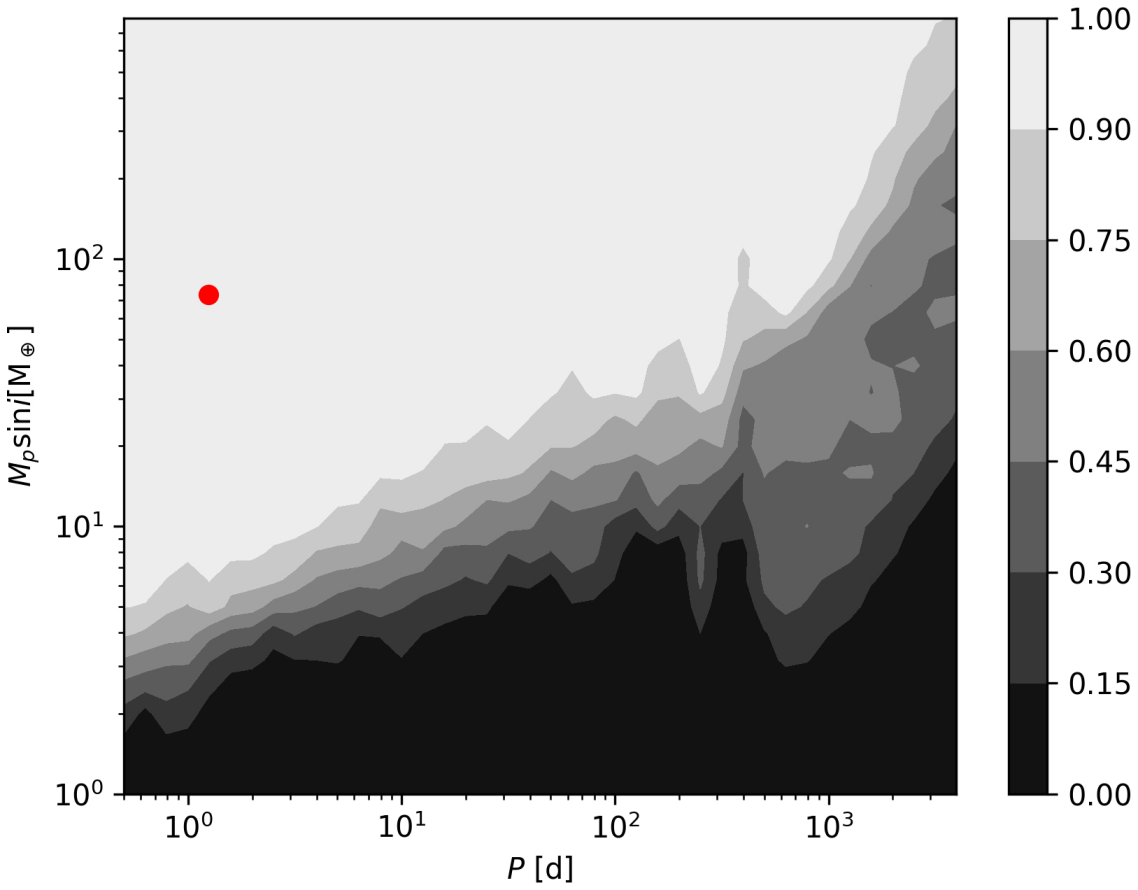

Figure 5.10: HARPS-N RV detection map. The color scale expresses the detection function (e.g. the detection probability), and the red circle marks the position of TOI-1853 b.

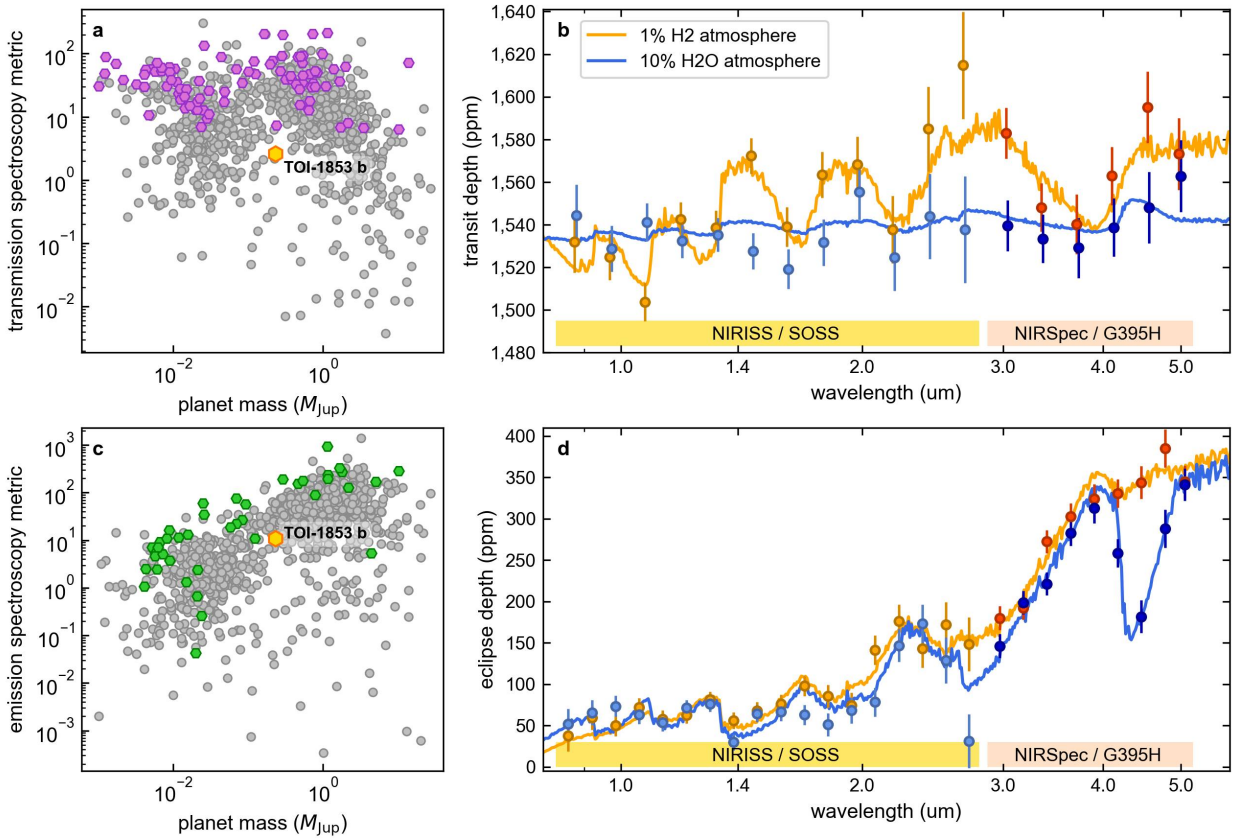

Figure 5.11: TSM, ESM and simulated spectra for JWST. Panels **a** and **c** show the transit and emission spectroscopic metrics for TOI-1853b (golden hexagon marker) in comparison to the population of transiting exoplanets (gray markers) and those selected for JWST cycles 1 and 2 observations (purple and green markers). TOI-1853b has a TSM of 2.6 and an ESM of 10.9. Panel **b** show synthetic transmission spectra for an H_2-dominated atmosphere (orange solid line) and an H_2O-dominated atmosphere (blue solid line). The markers with 1σ error bars show simulated JWST observations for selected detectors when combining 3 transits each. Panel **d**, same as panel **b** but for synthetic emission spectra.

Table 5.2: HARPS-N radial velocities. FWHM is the Full Width Half Maximum of the CCF profile, BIS is the Bisector Inverse Slope span, Contrast is referred to stellar line measurement of the spectral lines and S_{MW} is the Mount Wilson index

BJD_{TDB} (2 459 000 +)	RV ($m\,s^{-1}$)	σ_{RV} ($m\,s^{-1}$)	FWHM	BIS	Contrast	S_{MW}	$\sigma_{S_{MW}}$
277.591475	-26 222.45	3.76	6696	-24	66.70484	0.3101	0.0059
286.743959	-26 310.46	5.20	6658	-37	67.19193	0.2436	0.0096
288.667942	-26 227.52	3.32	6656	-37	66.92455	0.2719	0.0048
289.698557	-26 266.06	3.31	6646	-53	66.86836	0.2740	0.0046
297.604184	-26 219.74	6.08	6795	-7	65.98741	0.1466	0.0102
298.627811	-26 221.87	7.09	6720	-28	66.3382	0.4311	0.0126
299.645873	-26 263.84	5.51	6748	-42	66.35285	0.3371	0.0086
305.749103	-26 289.87	4.58	6697	-22	66.60946	0.323	0.0078
307.671216	-26 251.72	3.43	6743	-39	66.21211	0.3493	0.0041
325.603943	-26 298.31	7.99	6667	-68	66.49581	0.338	0.0158
327.671492	-26 280.93	3.56	6757	-32	66.08518	0.2944	0.0045
360.503076	-26 275.25	5.29	6789	-10	65.92973	0.3035	0.0072
365.572246	-26 251.83	4.71	6723	-37	66.24472	0.3000	0.0075
366.609855	-26 304.42	4.00	6734	-47	66.30966	0.2581	0.0064
367.546558	-26 299.77	3.13	6695	-34	66.79568	0.2893	0.0046
377.551116	-26 298.75	2.90	6712	-39	66.35716	0.3009	0.0037
378.532182	-26 245.57	3.57	6735	-41	66.01514	0.2932	0.0047
379.507227	-26 214.08	4.59	6748	-29	66.11978	0.3012	0.007
387.495223	-26 295.22	3.68	6705	-36	66.52209	0.2931	0.0058
391.502386	-26 294.81	4.65	6721	-24	66.32581	0.3742	0.0076
416.441714	-26 288.82	4.19	6683	-37	66.62051	0.2863	0.0069
565.753307	-26 264.28	3.97	6711	-46	66.64815	0.3154	0.0082
615.721992	-26 215.50	4.33	6621	-38	67.06423	0.2632	0.0093
617.727567	-26 316.77	7.21	6700	-65	66.12045	0.2601	0.0156
618.719631	-26 291.42	6.31	6703	-48	66.26545	0.2636	0.0138
624.713851	-26 245.94	2.79	6638	-39	67.17890	0.2693	0.005
625.734802	-26 228.39	3.67	6642	-48	66.95316	0.3119	0.0075
627.729205	-26 321.39	3.55	6675	-44	66.86213	0.3163	0.0069
642.724298	-26 306.52	5.95	6692	-61	66.50986	0.328	0.0139
646.687152	-26 247.78	2.34	6697	-45	66.83894	0.3069	0.0035
648.731285	-26 318.18	2.81	6682	-47	66.86892	0.2862	0.0049
649.716835	-26 275.88	3.58	6695	-41	66.83616	0.2651	0.007
650.721339	-26 223.28	2.49	6665	-35	67.0299	0.3126	0.0042
656.721298	-26 235.09	6.12	6685	-43	66.52727	0.2212	0.0139
663.759353	-26 316.48	3.21	6697	-53	66.54938	0.3136	0.0057
678.681216	-26 308.79	5.58	6664	-14	66.59712	0.2085	0.0131
681.703784	-26 224.39	3.36	6710	-43	66.56025	0.3083	0.0063
682.627666	-26 274.79	2.72	6673	-31	66.80372	0.3234	0.0047
690.693058	-26 256.22	4.57	6734	-40	66.21964	0.3055	0.0085
705.597822	-26 243.26	3.76	6706	-38	66.47439	0.3220	0.0069
706.532481	-26 220.40	3.70	6691	-41	66.80752	0.3202	0.0074
708.602432	-26 312.25	6.49	6705	-84	66.49706	0.3678	0.0151
717.556786	-26 253.85	2.14	6692	-37	66.83179	0.3263	0.0029
718.552650	-26 312.72	2.73	6707	-46	66.61027	0.3156	0.0041
735.582824	-26 292.60	9.38	6701	-81	66.50634	0.3421	0.0226
737.473873	-26 245.33	22.37	6692	24	65.65718	0.0604	0.0619
738.528763	-26 284.60	6.08	6694	-37	66.51006	0.3167	0.0134
748.535890	-26 263.99	6.92	6700	-51	66.38869	0.2286	0.0155
750.506612	-26 280.71	4.30	6717	-33	66.28337	0.2809	0.0075
751.517693	-26 226.76	3.34	6731	-39	66.26938	0.2608	0.0052
752.506892	-26 224.75	3.67	6685	-40	66.58633	0.2531	0.007
773.458642	-26 265.04	2.74	6693	-48	66.6854	0.3202	0.0042
774.449876	-26 319.92	2.21	6662	-56	66.99418	0.3100	0.0033
775.457294	-26 302.74	3.73	6689	-42	66.72325	0.3196	0.0072
803.398361	-26 236.87	2.73	6656	-32	66.94536	0.2849	0.0047
807.396243	-26 223.01	4.48	6705	-38	66.42269	0.2925	0.0095

Table 5.3: Global joint fit priors and posteriors. The best-fitting values and uncertainties are extracted from the posterior probability distributions. $\mathcal{U}(a, b)$ indicates a uniform distribution between a and b; $\mathcal{L}(a, b)$ a log-normal distribution, and $\mathcal{N}(a, b)$ a normal distribution with mean a and standard deviation b. The Limb-darkening coefficients are intended for a quadratic limb-darkening law.

Parameters	Unit	Prior distribution	Posterior Value ($\pm1\sigma$)
RV Parameters			
K_p	$\mathrm{m\,s^{-1}}$	$\mathcal{U}(0.0,\ 100.0)$	$48.8^{+1.1}_{-1.0}$
$\overline{\gamma}_{\mathsf{HARPS\text{-}N}}$	$\mathrm{m\,s^{-1}}$	$\mathcal{U}(-26280,\ -26250)$	$-26267.0^{+0.7}_{-0.6}$
$\sigma_{\mathsf{HARPS\text{-}N}}$	$\mathrm{m\,s^{-1}}$	$\mathcal{U}(0,\ 10)$	4.8 ± 0.6
Keplerian Parameters			
P	days	$\mathcal{N}(1.24,\ 0.01)$	1.2436258 ± 0.0000015
T_0	$\mathrm{BJD_{TDB}}$	$\mathcal{N}(2459690.7,\ 0.1)$	$2\,459\,690.7420 \pm 0.0006$
$\sqrt{e}\sin\omega$		$\mathcal{U}(-1.0,\ 1.0)$	$0.014^{+0.087}_{-0.095}$
$\sqrt{e}\cos\omega$		$\mathcal{U}(-1.0,\ 1.0)$	$0.053^{+0.053}_{-0.060}$
$\rho_\star$	$\mathrm{kg\,m^{-3}}$	$\mathcal{N}(2240,\ 150)$	2236^{+120}_{-114}
Transit Parameters			
r_1		$\mathcal{U}(0.0,\ 1.0)$	$0.681\pm^{+0.027}_{-0.027}$
r_2		$\mathcal{U}(0.0,\ 1.0)$	$0.0392\pm^{+0.0007}_{-0.0007}$
Limb-darkening coefficients			
q_1, TESS		$\mathcal{N}(0.40,\ 0.25)$	$0.36^{+0.13}_{-0.12}$
q_2, TESS		$\mathcal{N}(0.34,\ 0.30)$	$0.38^{+0.23}_{-0.21}$
q_1, LCOGT		$\mathcal{U}(0,\ 1)$	$0.57^{+0.23}_{-0.25}$
q_2, LCOGT		$\mathcal{U}(0,\ 1)$	$0.67^{+0.21}_{-0.25}$
q_1, ULMT		$\mathcal{U}(0,\ 1)$	$0.66^{+0.22}_{-0.26}$
q_2, ULMT		$\mathcal{U}(0,\ 1)$	$0.47^{+0.28}_{-0.29}$
q_1, MuSCAT2-g		$\mathcal{U}(0,\ 1)$	$0.59^{+0.24}_{-0.29}$
q_2, MuSCAT2-g		$\mathcal{U}(0,\ 1)$	$0.58^{+0.26}_{-0.28}$
q_1, MuSCAT2-r		$\mathcal{U}(0,\ 1)$	$0.52^{+0.27}_{-0.26}$
q_2, MuSCAT2-r		$\mathcal{U}(0,\ 1)$	$0.51^{+0.26}_{-0.28}$
q_1, MuSCAT2-i		$\mathcal{U}(0,\ 1)$	$0.57^{+0.21}_{-0.24}$
q_2, MuSCAT2-i		$\mathcal{U}(0,\ 1)$	$0.42^{+0.29}_{-0.25}$
q_1, MuSCAT2-z		$\mathcal{U}(0,\ 1)$	$0.31^{+0.33}_{-0.22}$
q_2, MuSCAT2-z		$\mathcal{U}(0,\ 1)$	$0.36^{+0.29}_{-0.23}$
Offset			
off, TESS (Sect. 23)		$\mathcal{N}(0,\ 0.01)$	$0.00009^{+0.00039}_{-0.00033}$
off, TESS (Sect. 50)		$\mathcal{N}(0,\ 0.01)$	0.0003 ± 0.0003
off, LCOGT		$\mathcal{N}(0,\ 0.1)$	$0.005^{+0.030}_{-0.017}$
off, ULMT		$\mathcal{N}(0,\ 0.1)$	$0.006^{+0.033}_{-0.012}$
off, MuSCAT2-g		$\mathcal{N}(0,\ 0.1)$	$0.0006^{+0.019}_{-0.012}$
off, MuSCAT2-r		$\mathcal{N}(0,\ 0.1)$	$0.002^{+0.019}_{-0.005}$
off, MuSCAT2-i		$\mathcal{N}(0,\ 0.1)$	$0.002^{+0.006}_{-0.015}$
off, MuSCAT2-z		$\mathcal{N}(0,\ 0.1)$	$-0.005^{+0.012}_{-0.029}$
Jitter			
jitt, TESS (Sect. 23)	ppm	$\mathcal{L}(10^{-1},\ 10^{5})$	$0.09^{+4.20}_{-0.09}$
jitt, TESS (Sect. 50)	ppm	$\mathcal{L}(10^{-1},\ 10^{5})$	$0.02^{+1.7}_{-0.02}$
jitt, LCOGT	ppm	$\mathcal{L}(10^{-1},\ 10^{5})$	55^{+640}_{-55}
jitt, ULMT	ppm	$\mathcal{L}(10^{-1},\ 10^{5})$	1^{+39}_{-1}
jitt, MuSCAT2-g	ppm	$\mathcal{L}(10^{-1},\ 10^{5})$	3^{+190}_{-3}
jitt, MuSCAT2-r	ppm	$\mathcal{L}(10^{-1},\ 10^{5})$	$0.3^{+4.6}_{-0.2}$
jitt, MuSCAT2-i	ppm	$\mathcal{L}(10^{-1},\ 10^{5})$	14^{+169}_{-13}
jitt, MuSCAT2-z	ppm	$\mathcal{L}(10^{-1},\ 10^{5})$	39^{+261}_{-37}
Hyper-parameters of the Matern GP model			
σ_{GP}, TESS		$\mathcal{L}(10^{-6},\ 0.1)$	$0.00069^{+0.00028}_{-0.00016}$
ρ_{GP}, TESS	days	$\mathcal{L}(0.1,\ 100)$	$3.9^{+1.4}_{-0.9}$

Table 5.4: Impact simulation results. Parameters and results for selected impact simulations. I:R represents the mass ratio of ice versus rock in a pre-impact planet – I:R = 3:1 refers to water-rich planets, I:R = 1:1 refers to equal water and rock planets, and I:R = 1:3 refers to rock-rich planets. The targets and impactors in each simulation have the same I:R ratio. V_{esc} is the mutual escape velocity in the corresponding impact simulation. $M_{\rm lr}$ is the mass of the largest post-collision remnant. f shows the mass ratio of each material in the largest post-collision remnant. X_{loss}^{atmos} shows the total mass fraction of the atmosphere that is lost. b is the impact parameter which is related to the impact angle (b=0.0 stands for a head-on impact, b=0.4 and 0.7 stands for an oblique impact with an impact angle of around 23.6° and 45° respectively).

id	I:R	$M_{\rm targ}/M_\oplus$	$M_{\rm imp}/M_\oplus$	$V_{\rm imp}$ [km s^{-1}]	$V_{\rm imp}/V_{esc}$	b	$M_{\rm lr}/M_\oplus$	f_{si}	f_{H2O}	$f_{H\&He}$	X_{loss}^{atmos}
1	3:1	25	25	32.6	1.0	0.0	49.4	22.65%	68.15%	9.20%	9.7%
2	3:1	25	25	32.6	1.0	0.4	49.79	22.49%	67.69%	9.82%	2.9%
3	3:1	25	25	32.6	1.0	0.7	49.9	22.43%	67.51%	10.06%	0.3%
4	3:1	25	25	48.9	1.5	0.4	47.8	23.24%	70.25%	6.31%	40.2%
5	1:1	25	25	33.8	1.0	0.0	49.51	45.21%	45.40%	9.39%	7.3%
6	1:1	25	25	33.8	1.0	0.4	49.68	45.06%	45.25%	9.69%	4.2%
7	1:1	25	25	33.8	1.0	0.7	49.86	44.89%	45.08%	10.03%	4.0%
8	1:1	25	25	50.7	1.5	0.4	47.53	47.10%	46.60%	6.30%	40.3%
9	1:3	25	25	34.2	1.0	0.0	49.27	69.29%	22.78%	8.93%	12.1%
10	1:3	25	25	34.2	1.0	0.4	49.61	67.82%	22.61%	9.57%	5.2%
11	1:3	25	25	34.2	1.0	0.7	49.86	67.49%	22.52%	9.99%	0.5%
12	1:3	25	25	51.3	1.5	0.4	47.56	70.74%	22.76%	6.50%	38.25%
13	3:1	60	30	63.0	1.5	0	85.0	23.74%	71.24%	5.02%	52.7%
14	1:1	60	30	64.8	1.5	0	82.8	48.65%	46.65%	4.70%	56.7%
15	1:3	60	30	73.5	1.5	0	82.3	73.63%	20.89%	5.48%	49.8%
16	3:1	60	30	75.5	1.8	0	74.2	27.20%	71.67%	1.13%	90.7%
17	1:1	60	30	77.7	1.8	0	72.8	55.30%	42.92%	1.78%	85.6%
18	1:3	60	30	80.2	1.8	0	73.5	81.11%	16.13%	2.76%	77.4%

Chapter 6

Conclusions and perspectives

The characterization of exoplanets, along with the architectures of the systems they inhabit, are continuously expanding and evolving through the acquisition of increasingly precise photometric and spectroscopic measurements. During this three-year PhD research, I actively participated in the GAPS project (Chapter 1), aiming in particular to characterize Neptunian TOIs. I first identified the ideal candidates for spectroscopic follow-up (Section 3.1) and then, for the selected targets, my collaborators collected RVs with HARPS-N at the TNG (Section 1.5.2), with the intent of deriving the stellar and planetary parameters through comprehensive joint analyses (Section 1.3, 2.6, and Chapter 3). This extensive effort employed state-of-the-art Bayesian techniques (Chapter 2), and resulted in novel findings which have contributed particularly to enlarging the population of well-characterized Neptune-type planets, as illustrated in Figure 6.1. While the observations and/or analysis of some targets are still ongoing, as of today my collaborators and I have validated and characterized two sub-Neptunes (TOI-5076 b – Section 3.4, TOI-2443 b – Section 3.5),

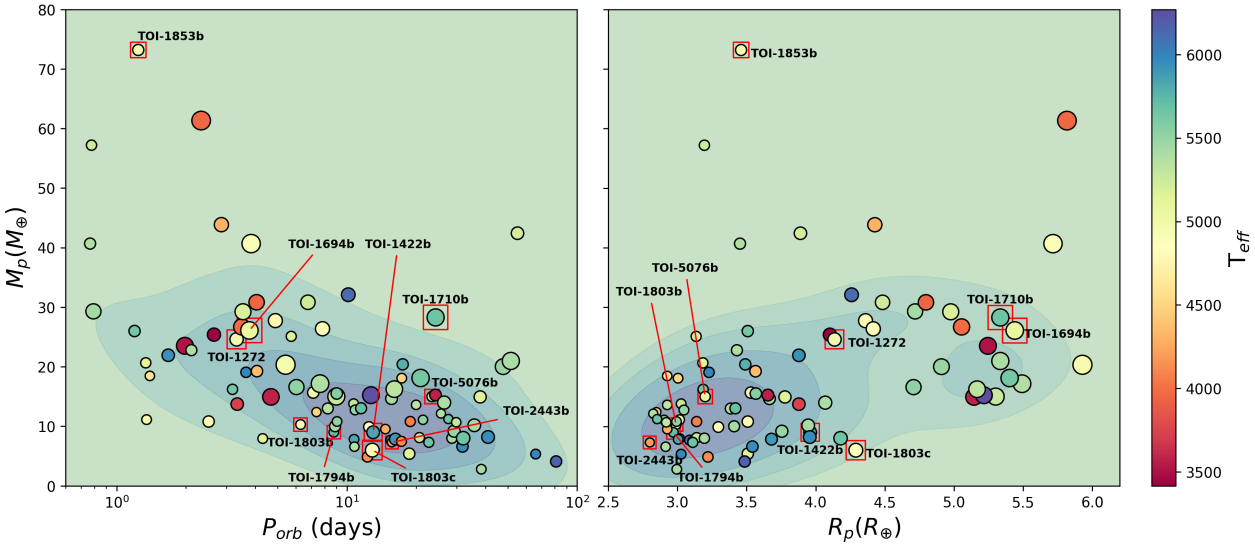

Figure 6.1: Diagrams of planetary mass vs. orbital period (left-hand panel) and planetary radius (right-hand panel) for all the exo-Neptunes known to date, with at least a $3\,\sigma$ precision on their estimated density. The sizes of the circles are proportional to the radius of the planets, while their colors indicate the effective temperature of their parent stars. The color intensity in the background is proportional to the number of planets occupying that area. The targets observed during this thesis work are highlighted in red; the error bars have been suppressed for clarity.

two super-Neptunes (TOI-1710 b – Section 3.2, TOI-1694 b – Section 3.3) and three Neptune-sized planets (TOI-1272 b – Section 3.3, TOI-1422 b – Chapter 4, TOI-1853 b – Chapter 5). We have further discovered three non-transiting Neptune-mass planets (TOI-1272 c and candidates TOI-1272 d, TOI-1422 c) and one Jovian (TOI-1694 c) on outer orbits.

Among them, an especially noteworthy discovery is that of TOI-1853 b (Naponiello et al. 2023, Nature), which boasts a radius of $3.46 \pm 0.08\,R_\oplus$, a mass of $73.2 \pm 2.7\,M_\oplus$, and an extraordinarily high bulk density of 9.7 ± 0.8 g cm^{-3}, which is approximately six times that of Neptune and nearly twice that of Earth (Chapter 5). The physical properties of this planet cannot be explained with the core accretion formation model alone (refer to Section 1.6.1), as they necessitate the exploration of alternative migration/evolution models in order to explain the assembly of its exceptionally heavy core (i.e. a catastrophic origin which may result from either multiple planetary impacts or HEM followed by severe tidal dissipation). The discovery of this super-massive planet highlights the imperative need to further investigate the parameter space occupied by Neptune-type worlds, as each new discovery has the potential to yield remarkable surprises and insights. In addition, TOI-1853 b is located in the hot-Neptune desert, as it orbits around its parent star every 1.24 days. In contrast, TOI-1710 b and TOI-1422 b both have longer orbital periods and eccentricities compatible with zero, hence their current separations from the parent star can be explained by disc migration, a process that should have damped their original eccentricities. TOI-1422 b, in particular, likely has a close-by Neptune-mass companion, which should have been scattered away if the inner planet migrated through planet-planet scattering instead, after the dissipation of the disc.

Similarly, the search for companion planets would prove especially crucial in the case of TOI-1853 b, where the presence of at least one nearby planet (within ≈ 1 au) could hold pivotal clues regarding the ultra-dense planet's formation history. In fact, the existence of a companion may help discern whether TOI-1853 b migrated within the protoplanetary disk and collided with multiple super-Earths, or if HEM destabilized the orbits of potential neighbouring companions, as postulated in Naponiello et al. (2023) (refer also to Section 1.6.2). While a thorough statistical analysis with a large sample of Neptunian planets is beyond the scope of this thesis, exploring the relationship between eccentricity and planet multiplicity will thus be key to assessing their prevailing formation and migration mechanisms. As an example, for planets discovered by *Kepler*, Van Eylen and Albrecht (2015) and subsequent studies (e.g., Zhu and Dong 2021 and reference therein) found that the eccentricities of mostly small planets in multi-planet systems exhibit different characteristics compared to those in single-planet systems. In particular, they found that multi-planet systems tend to show smaller eccentricity dispersion, suggesting that systems with more planets tend to have more circular orbits. Two studies by Van Eylen et al. (2019) and Mills et al. (2019) further confirmed that single transiting planets have a higher mean eccentricity (as anticipated in Section 1.3.4). The large eccentricities and mutual inclinations observed in low-multiplicity *Kepler* planetary systems imply significant dynamical interactions among the inner planets, and that alternative mechanisms may be at play in exciting these orbital parameters beyond what self-scatterings can achieve, potentially involving interactions with outer massive planets.

Nevertheless, an intriguing trend emerges from the sample depicted in Figure 6.2: as the orbital

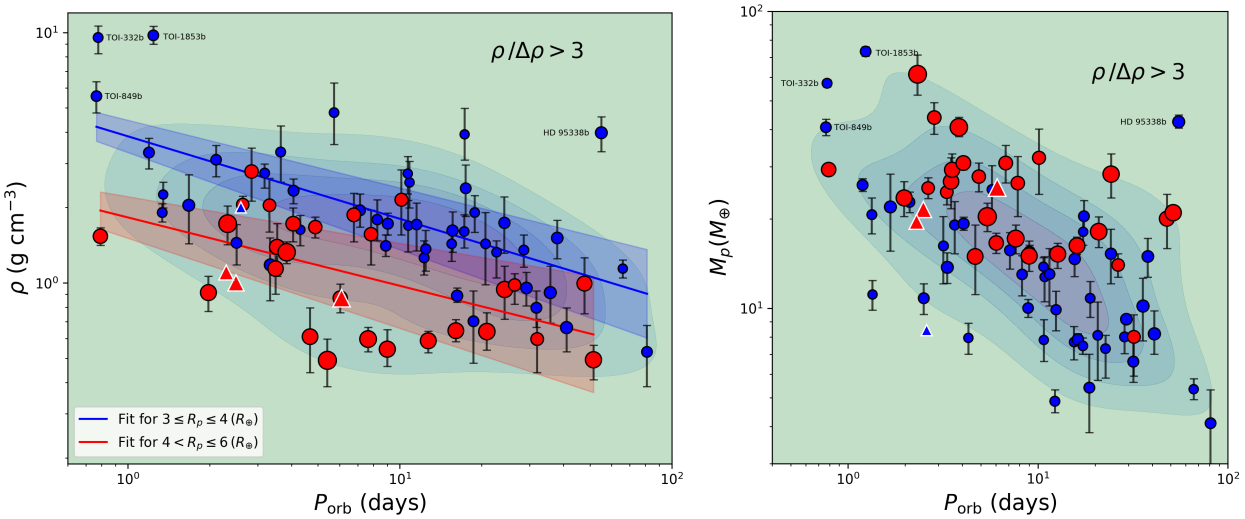

Figure 6.2: *Left-hand panel*: plot of the bulk density vs. orbital period for Neptune-sized exoplanets with precise density estimations ($\rho/\Delta\rho > 3$). The planets are plotted as circles, whose radius is represented both by their size and their color (blue and red for planets smaller and larger than Neptune, or $4R_\oplus$, respectively). The fits for the two populations are shown by lines of the same color, along with one standard deviation shades. Four examples of new planetary candidates that we have proposed for future observation runs are represented by triangles (three reds, one blue; the values of their mass have been deduced from the empirical law of Otegi et al. 2020). *Right-hand panel*: plot of the planetary mass vs. orbital period for the same planet sample.

period increases, the bulk density of Neptune-sized planets exhibits a linear decrease in log-log space. This trend is evident even for planets larger than Neptune ($R_p \gtrsim 4R_\oplus$), which exhibit lower densities on average, as one would anticipate. The escalating photo-evaporation effect could provide a possible explanation for most of these objects, since planets on shorter orbital periods receive elevated levels of X-UV radiation, which results in greater atmospheric loss, leading in turn to a reduced radius and increased density. However, the most dense exo-Neptunes, which are progressively occupying the previously desolate region known as the hot-Neptune desert, cannot be explained using photo-evaporation models (see e.g., Naponiello et al. 2023). The nearly-simultaneous discovery of TOI-332 b (Osborn et al., 2023) with properties similar to TOI-1853 b ($\rho_\mathrm{p} = 9.6^{+1.1}_{-1.3}$ g cm^{-3}, $R_\mathrm{p} = 3.20^{+0.16}_{-0.11}\,R_\oplus$, $M_\mathrm{p} = 57.2 \pm 1.6\,M_\oplus$), further suggests that the latter might not be an isolated anomaly, but rather a rare consequence of planet formation. Therefore, finding and characterizing more planets of this kind, starting from the candidates in the highly irradiated hot-Neptune desert ($P_\mathrm{orb} \lesssim 5$ days), with future observational campaigns, will be crucial to quantify how prevalent ultra-dense objects really are, and to study them in detail.

At the same time, the detection of signals associated with companions in outer orbits further enriches our understanding of these systems. As a matter of fact, there's currently a shortage of long-period transiting Neptunes orbiting around bright stars. For this reason, in this work I have also tried to select, for RV follow-up, a few transiting candidates on wider orbits ($P_\mathrm{orb} \approx 10 - 100$ days – see Table 3.1). While still relatively close to their parent stars, these planets have lower temperatures ($540 \lesssim T_{eq} \lesssim 870$ K) and represent an opportunity to determine the true mass fraction of Neptune-type planetary cores, owing to reduced irradiation (and photo-evaporation). Therefore, a comprehensive statistical analysis in the near future will hopefully be able not only to narrow

down the parameter space of exo-Neptunes (including radius, mass, separation and eccentricity) but also their multiplicity (along with the characterization of the planetary companions). This, in turn, will help to distinguish between different migration scenarios, elucidating the formation and evolution of these planets, and better discerning the differences from the processes that govern gas giants. For instance, Bonomo et al. (2017) focused on a large sample of 231 giant transiting planets in non-compact systems with accurate mass determinations through HARPS-N RV measurements. Their homogeneous analysis highlighted that the most eccentric giants indeed have larger orbital separations (see the left-hand panel of Figure 6.3) and/or high mass ratios, while for well-determined circular orbits the semi-major axes peak at $2.5\,a_R$ (see Eq. 1.23), as HEM would predict. However, they ultimately conclude that other migration scenarios might still contribute to the eccentricity distribution of giant planets, in view especially of the fact that some giants on circular orbits, with $\alpha = a/a_R > 5$, may have migrated through disc-planet interactions instead of HEM (similarly to TOI-1710 b and TOI-1422 b). This is hinted by the modified tidal diagram (right-hand panel of Figure 6.3 – see however Bonomo et al. 2017 for the details), which shows different circularization times (τ_e) in relation to the mass and separation of the transiting giants ($\tau_e \propto (M_p/M_s)(\alpha/R_p)^5$, refer e.g. to Goldreich and Soter 1966), independently of the orbital period, i.e. using $P \cdot M_p/M_s$ instead of M_p/M_s (hence why *modified*). In fact, the region where tidal circularization is not expected to occur within 7-14 Gyr is almost exclusively populated by eccentric planets, with the exception of four giants on circular orbits (with $\alpha > 5$) which have likely undergone disc migration instead of HEM. For the same reason, we would expect Neptunians with $P_{orb} > 10$ days to have significant eccentricities if they have migrated via HEM, due to low tidal interactions with the star. In this sense, comparing the tidal diagrams of the Jovian and Neptunian populations will also be useful in the future to better constrain their formation history.

Thanks to the resolute commitment to long-term observations of the ambitious *PLATO* space

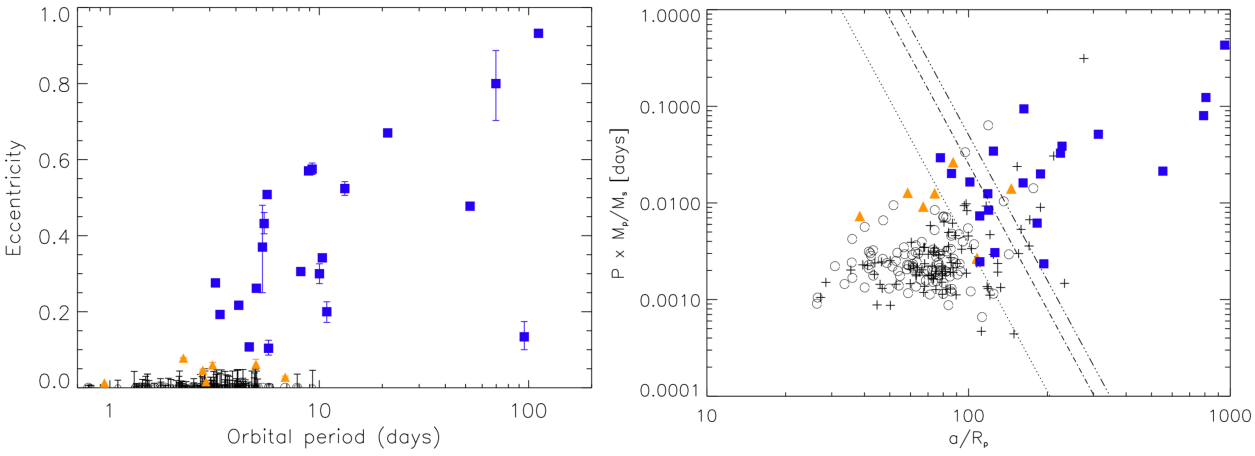

Figure 6.3: *Left-hand panel*: The well-determined eccentricity of 123 transiting giant planets is plotted over their orbital period. The giants on circular orbits, with small or large eccentricities ($e < 0.1$, $e \geq 0.1$) are depicted respectively with empty black circles, orange triangles and blue squares. *Right-hand panel*: Modified tidal diagram of the same population. The dotted, dash-dotted, and dash-three dotted lines display the 1, 7 and 14 Gyr circularisation timescales for $e = 0$ and tidal quality factor $\mathcal{Q}_p^{'} = 10^6$, i.e. a parametrization of the planet's interior response to tidal perturbations (the lower the dissipation rate of the tidal kinetic energy inside the planet, the higher is $\mathcal{Q}^{'}$). Figures courtesy of Bonomo et al. 2017.

mission (Rauer et al., 2014), led by the European Space Agency (ESA), many Warm Neptune-sized exoplanets, and hopefully a few Cold ones (with P_{orb} up to 1 year), will likely be revealed in the coming years (before the launch of *Ariel*). Although estimating the mass of these distant objects will present a formidable challenge, this quest falls within the reach of new RV instruments capable of achieving precision levels of $\lesssim 0.3$ m/s (Fischer et al., 2016). The expanding Neptunian data-set will not only enhance our knowledge of individual exoplanets but also refine our understanding of their density-orbital period relationship, facilitate the exploration of potential correlations between planetary and stellar parameters (such as host metallicity, mass and age), and contribute to our broader comprehension of the formation and migration of these intriguing worlds. Furthermore, the advent of *PLATO* is poised to provide valuable insights into exoplanets and their stellar counterparts by offering more accurate estimations of the stellar physical parameters. In fact, the asteroseismology technique (refer to Section 1.3.1) is at the core of this mission. By allowing for precise asteroseismic analyses, *PLATO* will in particular achieve accurate and precise age determinations, which have historically been plagued by large uncertainties, therefore allowing for an augmented comprehension of exoplanetary systems development.

Ultimately, such investigations will both benefit and pave the way for future transmission/emission spectroscopy endeavours with instruments like *JWST* and *Ariel*. On one hand, revealing the true nature of individual Neptunian planets such as TOI-1853 b is, in fact, a degenerate problem (see the discussion at the end of Section 1.3.2), and mass–radius measurements alone are not sufficient. As a case in point, there are multiple interior and atmospheric combinations that can be consistent with the observed bulk properties of TOI-1853 b. The super-massive planet could be described as having a rocky core (50% by mass) surrounded by an outer layer constituted by high-pressure water ice (also 50% by mass), or possibly supercritical liquid (Zeng et al., 2021), with negligible or no envelope. In contrast, TOI-1853 b could also have an Earth-like rocky composition (99% by mass) with a H/He envelope on top (1% by mass). Precise time-series spectroscopy (already within the reach of *JWST*) could break this degeneracy by directly probing the atmospheric molecular spectral features. Constraining TOI-1853 b atmospheric composition (likely through emission spectroscopy, rather than transmission, as suggested in Naponiello et al. 2023) will tell us whether the planet has entirely lost its atmosphere, if it has been able to preserve an atmosphere rich in hydrogen (like a smaller version of a Neptune planet), or instead if it now possesses a secondary atmosphere characterized by heavier molecules (such as H_2O and CO_2, like a super-Earth). As a result, this will allow us to discern between its different formation and migration models theorized (Naponiello et al., 2023), unravelling the history of the most massive Neptune-sized planet ever found.

On the flip side, precise mass determinations are fundamental for atmospheric characterization. As a case in point, Batalha et al. (2019) conducted a study to determine the level of planetary mass precision required for robust atmospheric characterization, and they ultimately recommended a precision of at least $\pm 20\%$ for any detailed atmospheric characterization (so that the atmospheric constraints are only limited by the spectroscopy data quality and not by the mass uncertainties themselves). Atmospheric characterisation is bound to provide further constraints on the mechanisms of planetary formation and evolution; for instance higher atmospheric metallicities suggest metal-rich protostellar disc formation environments or enrichment through processes like planetary

collisions (see Section 1.6.3) and, above all, ingestion of ice-rich planetesimals via migration. Constraining the Carbon-to-Oxygen (C/O) ratio (derived from the abundances of molecules seen in the near-infrared) is further valuable, as C/O is a tracer of both the formation site and the migration mechanism (Madhusudhan, 2019). Indeed, the field of precise exoplanet transmission spectroscopy (see Section 1.3.3) has already made significant progress in the past decade (see e.g., Borsa et al. 2021, Brogi et al. 2018, Diamond-Lowe et al. 2018, Knutson et al. 2014, Lustig-Yaeger et al. 2023). One of the most intriguing and unequivocal revelations stemming from this endeavour is the prevalence of atmospheric aerosols in exoplanetary atmospheres (Gao et al., 2023), i.e. tiny particles that act as a barrier and hinder our ability to probe the chemical compositions of these distant worlds. Tentative patterns have also emerged, suggesting in particular a link between the clarity of planetary atmospheres and their equilibrium temperatures (Estrela et al., 2022). However, the number of exoplanets whose atmospheres have been studied remains relatively modest, especially when one considers the vast diversity of atmospheric physics and chemistry that could exist. Consequently, many research efforts have resorted to grouping dissimilar planets together in order to amplify the statistical power of their findings. Recently, Brande et al. 2023 undertook a re-examination of a more physically similar sample of 15 exo-Neptunes spanning a temperature range from 200 to 1000 K. They found that these exoplanets exhibit high metallicities ($\approx$ 100 times that of our own Sun) and, therefore, relatively strong absorption features. This is because the atmospheric mean molecular weight (μ, refer to Section 1.3.3) is linked to the atmospheric metallicity, and for higher levels of metallicity the absorption features are *stronger* (Brande et al., 2023).

Each observed atmosphere exhibited signs of attenuation, which can be primarily attributed to the presence of clouds or hazes consisting of tiny particles. Moreover, a substantial attenuation in the transmission spectra becomes evident particularly for planets between 500 and 800 K, reaffirming the correlation between temperatures and atmospheric clarity that had been previously suggested (though only two Neptunes in their sample have temperatures lower than 500 K). Still, the intrinsic astrophysical scatter of these measurements (Brande et al., 2023) raises questions about the formation processes of Neptunian planets, suggesting a level of unpredictability or stochasticity in their evolution. Fortunately, at the end of this decade, the *Ariel* space telescope (Tinetti et al., 2021) will significantly increase the sample of well-characterized atmospheres (mainly by the *JWST*), by analyzing the atmospheres of a wide range of exoplanets ($\approx$ 1000), including many exo-Neptunes, and hopefully it will bring clarity to the overall picture.

Bibliography

Eric Agol and Katherine Deck. TRANSIT TIMING TO FIRST ORDER IN ECCENTRICITY. *The Astrophysical Journal*, 818(2):177, feb 2016. doi: 10.3847/0004-637x/818/2/177. URL https://doi.org/10.3847%2F0004-637x%2F818%2F2%2F177.

Suzanne Aigrain and Daniel Foreman-Mackey. Gaussian Process Regression for Astronomical Time Series. , 61:329–371, August 2023. doi: 10.1146/annurev-astro-052920-103508.

H. Akaike. A New Look at the Statistical Model Identification. *IEEE Transactions on Automatic Control*, 19:716–723, January 1974.

Y. Alibert, C. Mordasini, W. Benz, and C. Winisdoerffer. Models of giant planet formation with migration and disc evolution. *Astronomy & Astrophysics*, 434(1):343–353, apr 2005. doi: 10.1051/0004-6361:20042032. URL https://doi.org/10.1051%2F0004-6361%3A20042032.

A. Aller, J. Lillo-Box, D. Jones, L. F. Miranda, and S. Barceló Forteza. Planetary nebulae seen with TESS: Discovery of new binary central star candidates from Cycle 1. *Astronomy and Astrophysics*, 635:A128, March 2020. doi: 10.1051/0004-6361/201937118.

Sivaram Ambikasaran, Daniel Foreman-Mackey, Leslie Greengard, David W. Hogg, and Michael O'Neil. Fast Direct Methods for Gaussian Processes. *IEEE Transactions on Pattern Analysis and Machine Intelligence*, 38:252, June 2015. doi: 10.1109/TPAMI.2015.2448083.

Guillem Anglada-Escudé and R. Paul Butler. THE HARPS-TERRA PROJECT. i. DESCRIPTION OF THE ALGORITHMS, PERFORMANCE, AND NEW MEASUREMENTS ON a FEW REMARKABLE STARS OBSERVED BY HARPS. *The Astrophysical Journal Supplement Series*, 200(2):15, may 2012. doi: 10.1088/0067-0049/200/2/15. URL https://doi.org/10.1088%2F0067-0049%2F200%2F2%2F15.

David J. Armstrong, Théo A. Lopez, Vardan, et al. A remnant planetary core in the hot-Neptune desert. *Nature*, 583(7814):39–42, July 2020. doi: 10.1038/s41586-020-2421-7.

C. A. L. Bailer-Jones, J. Rybizki, M. Fouesneau, M. Demleitner, and R. Andrae. VizieR Online Data Catalog: Distances to 1.47 billion stars in Gaia EDR3 (Bailer-Jones+, 2021). *VizieR Online Data Catalog*, art. I/352, February 2021.

Roman V. Baluev. Detecting multiple periodicities in observational data with the multifrequency periodogram—II. Frequency Decomposer, a parallelized time-series analysis algorithm. *Astronomy and Computing*, 3:50, November 2013. doi: 10.1016/j.ascom.2013.11.003.

A. Baranne, D. Queloz, M. Mayor, G. Adrianzyk, G. Knispel, D. Kohler, D. Lacroix, J. P. Meunier, G. Rimbaud, and A. Vin. ELODIE: A spectrograph for accurate radial velocity measurements. *Astronomy and Astrophysics, Supplement*, 119:373–390, October 1996.

A J Barker. Tidal dissipation in evolving low-mass and solar-type stars with predictions for planetary orbital decay. *Monthly Notices of the Royal Astronomical Society*, 498(2):2270–2294, sep 2020. doi: 10.1093/mnras/staa2405. URL `https://doi.org/10.1093%2Fmnras%2Fstaa2405`.

J. K. Barstow, S. Aigrain, P. G. J. Irwin, S. Kendrew, and L. N. Fletcher. Transit spectroscopy with james webb space telescope: systematics, starspots and stitching. *Monthly Notices of the Royal Astronomical Society*, 448, 4 2015. ISSN 1365-2966. doi: 10.1093/mnras/stv186.

Natasha E. Batalha, Avi Mandell, Klaus Pontoppidan, Kevin B. Stevenson, Nikole K. Lewis, et al. PandExo: A community tool for transiting exoplanet science. *Publications of the Astronomical Society of the Pacific*, 129(976):064501, apr 2017. doi: 10.1088/1538-3873/aa65b0. URL `https://doi.org/10.1088%2F1538-3873%2Faa65b0`.

Natasha E. Batalha, Taylor Lewis, Jonathan J. Fortney, et al. The Precision of Mass Measurements Required for Robust Atmospheric Characterization of Transiting Exoplanets. , 885(1): L25, November 2019. doi: 10.3847/2041-8213/ab4909.

C. Beaugé and D. Nesvorný. Multiple-planet Scattering and the Origin of Hot Jupiters. *Astrophys. J.*, 751(2):119, June 2012.

C. Beaugé and D. Nesvorný. Emerging Trends in a Period-Radius Distribution of Close-in Planets. *Astrophys. J.*, 763(1):12, January 2013.

Andreas Becker, Winfried Lorenzen, Jonathan J. Fortney, Nadine Nettelmann, Manuel Schöttler, and Ronald Redmer. AB INITIO EQUATIONS OF STATE FOR HYDROGEN (h-REOS.3) AND HELIUM (he-REOS.3) AND THEIR IMPLICATIONS FOR THE INTERIOR OF BROWN DWARFS. *The Astrophysical Journal Supplement Series*, 215(2):21, dec 2014. doi: 10.1088/0067-0049/215/2/21. URL `https://doi.org/10.1088/0067-0049/215/2/21`.

Waqas Bhatti, Luke Bouma, Joshua, John, and Adrian Price-Whelan. waqasbhatti/astrobase: astrobase v0.5.0, March 2020. URL `https://doi.org/10.5281/zenodo.3723832`.

K. Biazzo, R. Gratton, S. Desidera, et al. The GAPS programme with HARPS-N at TNG. X. Differential abundances in the XO-2 planet-hosting binary. *Astronomy and Astrophysics*, 583: A135, November 2015. doi: 10.1051/0004-6361/201526375.

K. Biazzo, V. Bozza, L. Mancini, and A. Sozzetti. The Demographics of Close-In Planets. In Katia Biazzo, Valerio Bozza, Luigi Mancini, and Alessandro Sozzetti, editors, *Demographics of Exoplanetary Systems, Lecture Notes of the 3rd Advanced School on Exoplanetary Science*, volume 466 of *Astrophysics and Space Science Library*, pages 143–234, January 2022. doi: 10.1007/978-3-030-88124-5_3.

K. Biazzo, V. D'Orazi, Desidera, et al. The GAPS programme at TNG. *Astronomy & Astrophysics*, 664:A161, aug 2022. doi: 10.1051/0004-6361/202243467. URL `https://doi.org/10.1051%2F0004-6361%2F202243467`.

John B. Biersteker and Hilke E. Schlichting. Atmospheric mass-loss due to giant impacts: the importance of the thermal component for hydrogen-helium envelopes. , 485(3):4454–4463, May 2019. doi: 10.1093/mnras/stz738.

James Binney and Scott Tremaine. *Galactic Dynamics: Second Edition*. 2008.

Bertram Bitsch, Sean N. Raymond, and Andre Izidoro. Rocky super-Earths or waterworlds: the interplay of planet migration, pebble accretion, and disc evolution. *Astronomy and Astrophysics*, 624:A109, April 2019. doi: 10.1051/0004-6361/201935007.

Peter Bodenheimer, David J. Stevenson, Jack J. Lissauer, and Gennaro D'Angelo. New Formation Models for the Kepler-36 System. *Astrophys. J.*, 868(2):138, December 2018.

A. S. Bonomo, A. Sozzetti, C. Lovis, L. Malavolta, K. Rice, et al. Characterization of the planetary system Kepler-101 with HARPS-N. A hot super-Neptune with an Earth-sized low-mass companion. *Astronomy and Astrophysics*, 572:A2, December 2014. doi: 10.1051/0004-6361/201424617.

A. S. Bonomo, A. Sozzetti, A. Santerne, M. Deleuil, J. M. Almenara, et al. Improved parameters of seven Kepler giant companions characterized with SOPHIE and HARPS-N. *Astronomy and Astrophysics*, 575:A85, March 2015. doi: 10.1051/0004-6361/201323042.

A. S. Bonomo, S. Desidera, S. Benatti, et al. The GAPS Programme with HARPS-N at TNG . XIV. Investigating giant planet migration history via improved eccentricity and mass determination for 231 transiting planets. , 602:A107, June 2017. doi: 10.1051/0004-6361/201629882.

F. Borsa, R. Allart, N. Casasayas-Barris, H. Tabernero, M. R. Zapatero Osorio, et al. Atmospheric Rossiter-McLaughlin effect and transmission spectroscopy of WASP-121b with ESPRESSO. *Astronomy and Astrophysics*, 645:A24, January 2021. doi: 10.1051/0004-6361/202039344.

William J. Borucki, David Koch, Basri, et al. Kepler planet-detection mission: Introduction and first results. *Science*, 327, 2 2010. ISSN 0036-8075. doi: 10.1126/science.1185402.

Aleksandra Borysow, Uffe G. Jorgensen, and Yi Fu. High-temperature (1000-7000 K) collision-induced absorption of H"2 pairs computed from the first principles, with application to cool and dense stellar atmospheres. *Journal of Quantitiative Spectroscopy and Radiative Transfer*, 68: 235–255, February 2001. doi: 10.1016/S0022-4073(00)00023-6.

Jacek Borysow, Lothar Frommhold, and George Birnbaum. Collision-induced Rototranslational Absorption Spectra of H 2-He Pairs at Temperatures from 40 to 3000 K. *Astrophysical Journal*, 326:509, March 1988. doi: 10.1086/166112.

F. Bouchy, F. Pepe, and D. Queloz. Fundamental photon noise limit to radial velocity measurements. , 374:733–739, August 2001. doi: 10.1051/0004-6361:20010730.

Bouchy, F., Díaz, R. F., Hébrard, G., Arnold, L., Boisse, I., Delfosse, X., Perruchot, S., and Santerne, A. Sophie+: First results of an octagonal-section fiber for high-precision radial velocity measurements. *A&A*, 549:A49, 2013. doi: 10.1051/0004-6361/201219979. URL `https://doi.org/10.1051/0004-6361/201219979`.

V. Bozza, L. Mancini, and A. Sozzetti. Methods of Detecting Exoplanets. In *Methods of Detecting Exoplanets: 1st Advanced School on Exoplanetary Science*, volume 428 of *Astrophysics and Space Science Library*, January 2016. doi: 10.1007/978-3-319-27458-4.

Jonathan Brande, Ian J. M. Crossfield, Laura Kreidberg, Antonija Oklopčić, et al. A Mirage or an Oasis? Water Vapor in the Atmosphere of the Warm Neptune TOI-674 b. *arXiv e-prints*, art. arXiv:2201.04197, January 2022.

Jonathan Brande, Ian J. M. Crossfield, Laura Kreidberg, Caroline V. Morley, Travis Barman, Björn Benneke, Jessie L. Christiansen, Diana Dragomir, Jonathan J. Fortney, Thomas P. Greene, Kevin K. Hardegree-Ullman, Andrew W. Howard, Heather A. Knutson, Joshua D. Lothringer, and Thomas Mikal-Evans. Clouds and Clarity: Revisiting Atmospheric Feature Trends in Neptune-size Exoplanets. *arXiv e-prints*, art. arXiv:2310.07714, October 2023. doi: 10.48550/arXiv.2310.07714.

John M. Brewer, Debra A. Fischer, Jeff A. Valenti, and Nikolai Piskunov. SPECTRAL PROPERTIES OF COOL STARS: EXTENDED ABUNDANCE ANALYSIS OF 1,617 PLANET-SEARCH STARS. *The Astrophysical Journal Supplement Series*, 225(2):32, aug 2016. doi: 10.3847/0067-0049/225/2/32. URL `https://doi.org/10.3847%2F0067-0049%2F225%2F2%2F32`.

C. Broeg, A. Fortier, D. Ehrenreich, Y. Alibert, W. Baumjohann, W. Benz, M. Deleuil, M. Gillon, A. Ivanov, R. Liseau, M. Meyer, G. Oloffson, I. Pagano, G. Piotto, D. Pollacco, D. Queloz, R. Ragazzoni, E. Renotte, M. Steller, and N. Thomas and. CHEOPS: A transit photometry mission for ESA's small mission programme. *EPJ Web of Conferences*, 47:03005, 2013. doi: 10.1051/epjconf/20134703005. URL `https://doi.org/10.1051%2Fepjconf%2F20134703005`.

M. Brogi, P. Giacobbe, G. Guilluy, R. J. de Kok, A. Sozzetti, L. Mancini, and A. S. Bonomo. Exoplanet atmospheres with GIANO. I. Water in the transmission spectrum of HD 189 733 b. *Astronomy and Astrophysics*, 615:A16, July 2018. doi: 10.1051/0004-6361/201732189.

A. G. A. Brown, A. Vallenari, Prusti, et al. gaia data release 2. *Astronomy and Astrophysics*, 616:A1, 8 2018. ISSN 0004-6361. doi: 10.1051/0004-6361/201833051.

T. M. Brown, N. Baliber, F. B. Bianco, et al. Las Cumbres Observatory Global Telescope Network. *Publications of the ASP*, 125(931):1031, September 2013. doi: 10.1086/673168.

Timothy M. Brown. Expected Detection and False Alarm Rates for Transiting Jovian Planets. , 593(2):L125–L128, August 2003. doi: 10.1086/378310.

Stephen T. Bryson, Jon M. Jenkins, Todd C. Klaus, Miles T. Cote, et al. Selecting pixels for Kepler downlink. In Nicole M. Radziwill and Alan Bridger, editors, *Software and Cyberinfrastructure for Astronomy*, volume 7740 of *Society of Photo-Optical Instrumentation Engineers (SPIE) Conference Series*, page 77401D, July 2010. doi: 10.1117/12.857625.

Stephen T. Bryson, Jon M. Jenkins, Todd C. Klaus, Miles T. Cote, et al. Kepler Data Processing Handbook: Target and Aperture Definitions: Selecting Pixels for Kepler Downlink. Kepler Science Document KSCI-19081-003, March 2020.

Lars A. Buchhave, Martin Bizzarro, David W. Latham, Dimitar Sasselov, William D. Cochran, Michael Endl, Howard Isaacson, Diana Juncher, and Geoffrey W. Marcy. Three regimes of extrasolar planet radius inferred from host star metallicities. *Nature*, 509(7502):593–595, May 2014. doi: 10.1038/nature13254.

Douglas A. Caldwell, Peter Tenenbaum, Joseph D. Twicken, Jon M. Jenkins, Eric Ting, Jeffrey C. Smith, Christina L. Hedges, Michael M. Fausnaugh, Mark Rose, and Christopher J. Burke. Tess science processing operations center ffi target list products, 2020.

Andrew Collier Cameron and Moira Jardine. Hierarchical bayesian calibration of tidal orbit decay rates among hot jupiters. *Monthly Notices of the Royal Astronomical Society*, 476(2):2542–2555, feb 2018. doi: 10.1093/mnras/sty292. URL `https://doi.org/10.1093%2Fmnras%2Fsty292`.

I. Carleo, S. Desidera, D. Nardiello, L. Malavolta, A. F. Lanza, et al. The GAPS Programme at TNG. XXVIII. A pair of hot-Neptunes orbiting the young star TOI-942. *Astronomy and Astrophysics*, 645:A71, January 2021. doi: 10.1051/0004-6361/202039042.

Philip J. Carter, Zoë M. Leinhardt, Tim Elliott, Sarah T. Stewart, and Michael J. Walter. Collisional stripping of planetary crusts. *Earth and Planetary Science Letters*, 484:276–286, feb 2018. doi: 10.1016/j.epsl.2017.12.012. URL `https://doi.org/10.1016%2Fj.epsl.2017.12.012`.

N. Casasayas-Barris, E. Pallé, F. Yan, G. Chen, S. Kohl, M. Stangret, H. Parviainen, Ch. Helling, N. Watanabe, S. Czesla, A. Fukui, P. Montañés-Rodríguez, E. Nagel, N. Narita, L. Nortmann, G. Nowak, J. H. M. M. Schmitt, and M. R. Zapatero Osorio. Atmospheric characterization of the ultra-hot Jupiter MASCARA-2b/KELT-20b. Detection of CaII, FeII, NaI, and the Balmer series of H (Hα, Hβ, and Hγ) with high-dispersion transit spectroscopy. *Astronomy and Astrophysics*, 628:A9, August 2019. doi: 10.1051/0004-6361/201935623.

F. Castelli and R. L. Kurucz. New Grids of ATLAS9 Model Atmospheres. In N. Piskunov, W. W. Weiss, and D. F. Gray, editors, *Modelling of Stellar Atmospheres*, volume 210, page A20, January 2003.

J. E. Chambers. Late-stage planetary accretion including hit-and-run collisions and fragmentation. *Icarus*, 224(1):43–56, May 2013. doi: 10.1016/j.icarus.2013.02.015.

W. J. Chaplin, H. M. Cegla, C. A. Watson, G. R. Davies, and W. H. Ball. Filtering Solar-Like Oscillations for Exoplanet Detection in Radial Velocity Observations. , 157(4):163, April 2019. doi: 10.3847/1538-3881/ab0c01.

Ashley Chontos and Joseph M. Akana Murphy. The TESS-Keck Survey: Science Goals and Target Selection. *Astronomical Journal*, 163(6):297, June 2022. doi: 10.3847/1538-3881/ac6266.

Ryan Chornock, Philip S. Cowperthwaite, Margutti, et al. Multi-messenger astronomy with extremely large telescopes, 2019.

David R. Ciardi, Charles A. Beichman, Elliott P. Horch, and Steve B. Howell. Understanding the Effects of Stellar Multiplicity on the Derived Planet Radii from Transit Surveys: Implications for Kepler, K2, and TESS. *Astrophys. J.*, 805(1):16, May 2015.

Claret, A. Limb and gravity-darkening coefficients for the tess satellite at several metallicities, surface gravities, and microturbulent velocities. *A&A*, 600:A30, 2017. doi: 10.1051/0004-6361/201629705. URL https://doi.org/10.1051/0004-6361/201629705.

Ryan Cloutier and Jason D. Eastman. A Pair of TESS Planets Spanning the Radius Valley around the Nearby Mid-M Dwarf LTT 3780. *Astronomical Journal*, 160(1):3, July 2020. doi: 10.3847/1538-3881/ab91c2.

Karen Collins. TESS Follow-up Observing Program Working Group (TFOP WG) Sub Group 1 (SG1): Ground-based Time-series Photometry. In *American Astronomical Society Meeting Abstracts #233*, volume 233 of *American Astronomical Society Meeting Abstracts*, page 140.05, January 2019.

Karen A. Collins, John F. Kielkopf, Keivan G. Stassun, and Frederic V. Hessman. ASTROIMAGEJ: IMAGE PROCESSING AND PHOTOMETRIC EXTRACTION FOR ULTRA-PRECISE ASTRONOMICAL LIGHT CURVES. *The Astronomical Journal*, 153(2):77, jan 2017. doi: 10.3847/1538-3881/153/2/77. URL https://doi.org/10.3847%2F1538-3881%2F153%2F2%2F77.

Rosario Cosentino, Christophe Lovis, Pepe, et al. *Harps-N: the new planet hunter at TNG*, volume 8446 of *Society of Photo-Optical Instrumentation Engineers (SPIE) Conference Series*, page 84461V. 2012. doi: 10.1117/12.925738.

Jean C. Costes, Christopher A. Watson, Ernst de Mooij, Steven H. Saar, et al. Long-term stellar activity variations and their effect on radial-velocity measurements. , 505(1):830–850, July 2021. doi: 10.1093/mnras/stab1183.

E. Covino, M. Esposito, Barbieri, et al. The GAPS programme with HARPS-N at TNG. I. Observations of the Rossiter-McLaughlin effect and characterisation of the transiting system Qatar-1. *Astronomy and Astrophysics*, 554:A28, Jun 2013. doi: 10.1051/0004-6361/201321298.

Patricio Cubillos, Nikolai V. Erkaev, et al. An overabundance of low-density Neptune-like planets. *Mon. Not. R. Astron. Soc.*, 466(2):1868–1879, April 2017.

Patricio E. Cubillos. An algorithm to compress line-transition data for radiative-transfer calculations. *The Astrophysical Journal*, 850(1):32, nov 2017. doi: 10.3847/1538-4357/aa9228. URL https://doi.org/10.3847%2F1538-4357%2Faa9228.

Patricio E Cubillos and Jasmina Blecic. The pyrat bay framework for exoplanet atmospheric modelling: a population study of hubble/WFC3 transmission spectra. *Monthly Notices of the Royal Astronomical Society*, 505(2):2675–2702, may 2021. doi: 10.1093/mnras/stab1405. URL https://doi.org/10.1093%2Fmnras%2Fstab1405.

Andrew Cumming, R. Paul Butler, Geoffrey W. Marcy, Steven S. Vogt, Jason T. Wright, and Debra A. Fischer. The Keck Planet Search: Detectability and the Minimum Mass and Orbital Period Distribution of Extrasolar Planets. *Publications of the ASP*, 120(867):531, May 2008. doi: 10.1086/588487.

R. M. Cutri, M. F. Skrutskie, S. van Dyk, C. A. Beichman, et al. *2MASS All Sky Catalog of point sources.* 2003.

R. M. Cutri, E. L. Wright, T. Conrow, J. W. Fowler, et al. VizieR Online Data Catalog: AllWISE Data Release (Cutri+ 2013). *VizieR Online Data Catalog*, art. II/328, February 2021.

Francesca D'Antona and Italo Mazzitelli. New Pre–Main-Sequence Tracks for M <=2.5 M_{sun} as Tests of Opacities and Convection Model. , 90:467, January 1994. doi: 10.1086/191867.

Rebekah I. Dawson and John Asher Johnson. Origins of Hot Jupiters. , 56:175–221, September 2018. doi: 10.1146/annurev-astro-081817-051853.

Laetitia Delrez, David Ehrenreich, and Yann Alibert. Transit detection of the long-period volatile-rich super-earth ν2 lupi d with CHEOPS. *Nature Astronomy*, 5(8):775–787, jun 2021. doi: 10.1038/s41550-021-01381-5. URL `https://doi.org/10.1038%2Fs41550-021-01381-5`.

Pierre Demarque, Jong-Hak Woo, Yong-Cheol Kim, and Sukyoung K. Yi. Y^2 Isochrones with an Improved Core Overshoot Treatment. *Astrophysical Journal, Supplement*, 155(2):667–674, December 2004. doi: 10.1086/424966.

Thomas R Denman, Zoe M Leinhardt, Philip J Carter, and Christoph Mordasini. Atmosphere loss in planet–planet collisions. *Monthly Notices of the Royal Astronomical Society*, 496(2):1166–1181, jun 2020. doi: 10.1093/mnras/staa1623. URL `https://doi.org/10.1093%2Fmnras%2Fstaa1623`.

Thomas R Denman, Zoë M Leinhardt, and Philip J Carter. Atmosphere loss in oblique super-earth collisions. *Monthly Notices of the Royal Astronomical Society*, 513(2):1680–1700, apr 2022. doi: 10.1093/mnras/stac923. URL `https://doi.org/10.1093%2Fmnras%2Fstac923`.

Hannah Diamond-Lowe, Zachory Berta-Thompson, David Charbonneau, and Eliza M. R. Kempton. Ground-based Optical Transmission Spectroscopy of the Small, Rocky Exoplanet GJ 1132b. *Astronomical Journal*, 156(2):42, August 2018. doi: 10.3847/1538-3881/aac6dd.

Matías R. Díaz, James S. Jenkins, Fabo Feng, R. Paul Butler, et al. The Magellan/PFS Exoplanet Search: a 55-d period dense Neptune transiting the bright (V = 8.6) star HD 95338. *Mon. Not. R. Astron. Soc.*, 496(4):4330–4341, August 2020.

Jean-François Donati, D. Kouach, M. Lacombe, S. Baratchart, R. Doyon, X. Delfosse, et al. SPIRou: A NIR Spectropolarimeter/High-Precision Velocimeter for the CFHT. In Hans J. Deeg and Juan Antonio Belmonte, editors, *Handbook of Exoplanets*, page 107. 2018. doi: 10.1007/978-3-319-55333-7_107.

C. Dorn, L. Noack, and A. B. Rozel. Outgassing on stagnant-lid super-Earths. , 614:A18, June 2018. doi: 10.1051/0004-6361/201731513.

Caroline Dorn, Julia Venturini, Amir Khan, Kevin Heng, et al. A generalized Bayesian inference method for constraining the interiors of super Earths and sub-Neptunes. *Astron. & Astrophys.*, 597:A37, January 2017.

Aaron Dotter. MESA Isochrones and Stellar Tracks (MIST) 0: Methods for the Construction of Stellar Isochrones. *Astrophysical Journal, Supplement*, 222(1):8, January 2016. doi: 10.3847/0067-0049/222/1/8.

Aaron Dotter, Brian Chaboyer, Darko Jevremović, Veselin Kostov, E. Baron, and Jason W. Ferguson. The Dartmouth Stellar Evolution Database. *Astrophysical Journal, Supplement*, 178(1): 89–101, September 2008. doi: 10.1086/589654.

A. P. Doyle, G. R. Davies, B. Smalley, W. J. Chaplin, and Y. Elsworth. Determining stellar macroturbulence using asteroseismic rotational velocities from Kepler. *Monthly Notices of the RAS*, 444:3592–3602, November 2014. doi: 10.1093/mnras/stu1692.

X. Dumusque. Extremely precise HARPS-N solar RV to overcome the challenge of stellar signal. In *Plato Mission Conference 2021. Presentations and posters of the online PLATO Mission Conference 2021*, page 106, October 2021. doi: 10.5281/zenodo.5596351.

X. Dumusque, S. Udry, C. Lovis, N. C. Santos, and M. J. P. F. G. Monteiro. Planetary detection limits taking into account stellar noise. *Astronomy & Astrophysics*, 525:A140, dec 2010. doi: 10.1051/0004-6361/201014097. URL `https://doi.org/10.1051%2F0004-6361%2F201014097`.

Martin J. Duncan, Harold F. Levison, and Man Hoi Lee. A Multiple Time Step Symplectic Algorithm for Integrating Close Encounters. *Astronomical Journal*, 116(4):2067–2077, October 1998. doi: 10.1086/300541.

Jason Eastman, B. Scott Gaudi, and Eric Agol. EXOFAST: A Fast Exoplanetary Fitting Suite in IDL. *Publications of the ASP*, 125(923):83, January 2013. doi: 10.1086/669497.

Jason Eastman, J E Rodriguez, Agol, et al. EXOFASTv2: Generalized publication-quality exoplanet modeling code, October 2017.

Jason D. Eastman, Joseph E. Rodriguez, et al. EXOFASTv2: A public, generalized, publication-quality exoplanet modeling code. *arXiv e-prints*, art. arXiv:1907.09480, July 2019.

Richard G. Edgar. Type II Migration: Varying Planet Mass and Disc Viscosity. *arXiv e-prints*, art. arXiv:0807.0625, July 2008. doi: 10.48550/arXiv.0807.0625.

P. P. Eggleton. Aproximations to the radii of Roche lobes. *Astrophysical Journal*, 268:368–369, May 1983. doi: 10.1086/160960.

Barbara Ercolano and Ilaria Pascucci. The dispersal of planet-forming discs: Theory confronts observations, 2017.

ESA. The HIPPARCOS and TYCHO catalogues. Astrometric and photometric star catalogues derived from the ESA HIPPARCOS Space Astrometry Mission. In *ESA Special Publication*, volume 1200 of *ESA Special Publication*, January 1997.

Néstor Espinoza. Efficient Joint Sampling of Impact Parameters and Transit Depths in Transiting Exoplanet Light Curves. *Research Notes of the American Astronomical Society*, 2(4):209, November 2018. doi: 10.3847/2515-5172/aaef38.

Né stor Espinoza, Rafael Brahm, Andrés Jordán, James S. Jenkins, Felipe Rojas, Paula Jofré, Thomas Mädler, Markus Rabus, Julio Chanamé, Blake Pantoja, Maritza G. Soto, Katie M. Morzinski, Jared R. Males, Kimberly Ward-Duong, and Laird M. Close. DISCOVERY AND

VALIDATION OF a HIGH-DENSITY SUB-NEPTUNE FROM THEk2MISSION. *The Astrophysical Journal*, 830(1):43, oct 2016. doi: 10.3847/0004-637x/830/1/43. URL https://doi.org/10.3847%2F0004-637x%2F830%2F1%2F43.

Né stor Espinoza, Diana Kossakowski, and Rafael Brahm. juliet: a versatile modelling tool for transiting and non-transiting exoplanetary systems. *Monthly Notices of the Royal Astronomical Society*, 490(2):2262–2283, oct 2019. doi: 10.1093/mnras/stz2688. URL https://doi.org/10.1093%2Fmnras%2Fstz2688.

Raissa Estrela, Mark R. Swain, and Gael M. Roudier. A Temperature Trend for Clouds and Hazes in Exoplanet Atmospheres. , 941(1):L5, December 2022. doi: 10.3847/2041-8213/aca2aa.

Joshua A. Faber, Frederic A. Rasio, and Bart Willems. Tidal interactions and disruptions of giant planets on highly eccentric orbits. , 175(1):248–262, May 2005. doi: 10.1016/j.icarus.2004.10.021.

Daniel C. Fabrycky, Jack J. Lissauer, Darin Ragozzine, et al. Architecture of Kepler's Multi-transiting Systems. II. New Investigations with Twice as Many Candidates. , 790(2):146, August 2014. doi: 10.1088/0004-637X/790/2/146.

Debra A. Fischer, Guillem Anglada-Escude, Pamela Arriagada, Baluev, et al. State of the Field: Extreme Precision Radial Velocities. , 128(964):066001, June 2016. doi: 10.1088/1538-3873/128/964/066001.

Eric B. Ford and Frederic A. Rasio. Origins of Eccentric Extrasolar Planets: Testing the Planet-Planet Scattering Model. , 686(1):621–636, October 2008. doi: 10.1086/590926.

Daniel Foreman-Mackey, David W. Hogg, Dustin Lang, and Jonathan Goodman. <tt>emcee</tt>: The MCMC hammer. *Publications of the Astronomical Society of the Pacific*, 125(925):306–312, mar 2013. doi: 10.1086/670067. URL https://doi.org/10.1086%2F670067.

Daniel Foreman-Mackey, Eric Agol, Sivaram Ambikasaran, and Ruth Angus. Fast and Scalable Gaussian Process Modeling with Applications to Astronomical Time Series. *Astronomical Journal*, 154(6):220, December 2017. doi: 10.3847/1538-3881/aa9332.

Jonathan J. Fortney. The effect of condensates on the characterization of transiting planet atmospheres with transmission spectroscopy. *Monthly Notices of the Royal Astronomical Society*, 364 (2):649–653, dec 2005. doi: 10.1111/j.1365-2966.2005.09587.x. URL https://doi.org/10.1111%2Fj.1365-2966.2005.09587.x.

L. Fossati, N. V. Erkaev, H. Lammer, P. E. Cubillos, et al. Aeronomical constraints to the minimum mass and maximum radius of hot low-mass planets. *Astronomy & Astrophysics*, 598:A90, feb 2017. doi: 10.1051/0004-6361/201629716. URL https://doi.org/10.1051%2F0004-6361%2F201629716.

Marylou Fournier-Tondreau, Ryan J. MacDonald, Michael Radica, Lafrenière, et al. Near-Infrared Transmission Spectroscopy of HAT-P-18 b with NIRISS: Disentangling Planetary and Stellar Features in the Era of JWST. *arXiv e-prints*, art. arXiv:2310.14950, October 2023. doi: 10.48550/arXiv.2310.14950.

David Freedman, Robert Pisani, and Roger Purves. Statistics (international student edition). *Pisani, R. Purves, 4th edn. WW Norton & Company, New York*, 2007.

François Fressin, Guillermo Torres, David Charbonneau, Stephen T. Bryson, Jessie Christiansen, Courtney D. Dressing, Jon M. Jenkins, Lucianne M. Walkowicz, and Natalie M. Batalha. The False Positive Rate of Kepler and the Occurrence of Planets. *Astrophysical Journal*, 766(2):81, April 2013. doi: 10.1088/0004-637X/766/2/81.

Benjamin J. Fulton and Erik A. Petigura. The California-Kepler Survey. VII. Precise Planet Radii Leveraging Gaia DR2 Reveal the Stellar Mass Dependence of the Planet Radius Gap. *Astronomical Journal*, 156(6):264, December 2018. doi: 10.3847/1538-3881/aae828.

Benjamin J. Fulton, Erik A. Petigura, Andrew W. Howard, Howard Isaacson, Geoffrey W. Marcy, Phillip A. Cargile, Leslie Hebb, Lauren M. Weiss, John Asher Johnson, Timothy D. Morton, Evan Sinukoff, Ian J. M. Crossfield, and Lea A. Hirsch. The california-keplersurvey. III. a gap in the radius distribution of small planets. *The Astronomical Journal*, 154(3):109, aug 2017. doi: 10.3847/1538-3881/aa80eb. URL `https://doi.org/10.3847%2F1538-3881%2Faa80eb`.

Benjamin J. Fulton, Erik A. Petigura, Sarah Blunt, and Evan Sinukoff. RadVel: The radial velocity modeling toolkit. *Publications of the Astronomical Society of the Pacific*, 130(986):044504, mar 2018. doi: 10.1088/1538-3873/aaaaa8. URL `https://doi.org/10.1088%2F1538-3873%2Faaaaa8`.

E. Furlan, D. R. Ciardi, M. E. Everett, M. Saylors, J. K. Teske, E. P. Horch, et al. THEKEPLERFOLLOW-UP OBSERVATION PROGRAM. i. a CATALOG OF COMPANIONS TOKEPLERSTARS FROM HIGH-RESOLUTION IMAGING. *The Astronomical Journal*, 153(2):71, jan 2017. doi: 10.3847/1538-3881/153/2/71. URL `https://doi.org/10.3847%2F1538-3881%2F153%2F2%2F71`.

Gaia Collaboration. Gaia Early Data Release 3. Summary of the contents and survey properties. *Astronomy and Astrophysics*, 649:A1, May 2021. doi: 10.1051/0004-6361/202039657.

Gaia Collaboration. Gaia data release 3: Summary of the content and survey properties, 2022.

D. Gandolfi, O. Barragán, J. H. Livingston, M. Fridlund, et al. TESS's first planet. A super-Earth transiting the naked-eye star π Mensae. *Astronomy and Astrophysics*, 619:L10, November 2018. doi: 10.1051/0004-6361/201834289.

Peter Gao, Anjali A. A. Piette, Maria E. Steinrueck, Nixon, et al. The Hazy and Metal-rich Atmosphere of GJ 1214 b Constrained by Near- and Mid-infrared Transmission Spectroscopy. , 951(2):96, July 2023. doi: 10.3847/1538-4357/acd16f.

Rafael A. García and Jérôme Ballot. Asteroseismology of solar-type stars. *Living Reviews in Solar Physics*, 16(1), sep 2019. doi: 10.1007/s41116-019-0020-1. URL `https://doi.org/10.1007%2Fs41116-019-0020-1`.

Andrew Gelman and Donald B. Rubin. Inference from Iterative Simulation Using Multiple Sequences. *Statistical Science*, 7:457–472, January 1992. doi: 10.1214/ss/1177011136.

Hidenori Genda and Yutaka Abe. Enhanced atmospheric loss on protoplanets at the giant impact phase in the presence of oceans. *Nature*, Feb 2005. doi: 10.1038/nature03360.

Sivan Ginzburg, Hilke E. Schlichting, and Re'em Sari. Core-powered mass-loss and the radius distribution of small exoplanets. , 476(1):759–765, May 2018. doi: 10.1093/mnras/sty290.

Léo Girardi, Mauro Barbieri, Martin A. T. Groenewegen, et al. TRILEGAL, a TRIdimensional modeL of thE GALaxy: Status and Future. *Astrophysics and Space Science Proceedings*, 26:165, January 2012. doi: 10.1007/978-3-642-18418-5_17.

Peter Goldreich and Steven Soter. Q in the Solar System. , 5(1):375–389, January 1966. doi: 10.1016/0019-1035(66)90051-0.

R. Gomes, H. F. Levison, K. Tsiganis, and A. Morbidelli. Origin of the cataclysmic Late Heavy Bombardment period of the terrestrial planets. *Nature*, 435(7041):466–469, May 2005. doi: 10.1038/nature03676.

João Gomes da Silva, Pedro Figueira, Nuno Santos, and João Faria. ACTIN: A tool to calculate stellar activity indices. *The Journal of Open Source Software*, 3(31):667, Nov 2018. doi: 10.21105/joss.00667.

Richard O. Gray and Christopher Corbally. *Stellar Spectral Classification*. Princeton University Press, 2009.

Simon L. Grimm, Brice-Olivier Demory, Michaël Gillon, Caroline Dorn, Eric Agol, et al. The nature of the TRAPPIST-1 exoplanets. *Astronomy & Astrophysics*, 613:A68, may 2018. doi: 10.1051/0004-6361/201732233. URL `https://doi.org/10.1051%2F0004-6361%2F201732233`.

Natalia M. Guerrero, S. Seager, Huang, et al. The TESS Objects of Interest Catalog from the TESS Prime Mission. *Astrophysical Journal, Supplement*, 254(2):39, June 2021. doi: 10.3847/1538-4365/abefe1.

Jonas Haldemann, Yann Alibert, Christoph Mordasini, and Willy Benz. AQUA: a collection of h₂o equations of state for planetary models. *Astronomy & Astrophysics*, 643:A105, nov 2020. doi: 10.1051/0004-6361/202038367. URL `https://doi.org/10.1051%2F0004-6361%2F202038367`.

Rasmus Handberg, Mikkel N. Lund, Timothy R. White, Oliver J. Hall, et al. TESS Data for Asteroseismology: Photometry. , 162(4):170, October 2021. doi: 10.3847/1538-3881/ac09f1.

Gerald Handler. Asteroseismology. In Terry D. Oswalt and Martin A. Barstow, editors, *Planets, Stars and Stellar Systems. Volume 4: Stellar Structure and Evolution*, volume 4, page 207. 2013. doi: 10.1007/978-94-007-5615-1_4.

Jochen Heidt. *Hardware for Near-Infrared Observations—Adaptive Optics, Instrumentation, and Detectors*, pages 61–129. Springer International Publishing, Cham, 2022. ISBN 978-3-030-98441-0. doi: 10.1007/978-3-030-98441-0_4. URL `https://doi.org/10.1007/978-3-030-98441-0_4`.

Ravit Helled and Alessandro Morbidelli. Planet formation. In *ExoFrontiers*. IOP Publishing, oct 2021. doi: 10.1088/2514-3433/abfa8fch12. URL https://doi.org/10.1088%2F2514-3433%2Fabfa8fch12.

A. A. Henden, M. Templeton, D. Terrell, T. C. Smith, S. Levine, and D. Welch. VizieR Online Data Catalog: AAVSO Photometric All Sky Survey (APASS) DR9 (Henden+, 2016). *VizieR Online Data Catalog*, art. II/336, January 2016.

Arne A. Henden, Stephen Levine, Dirk Terrell, and Douglas L. Welch. APASS - The Latest Data Release. In *American Astronomical Society Meeting Abstracts #225*, volume 225 of *American Astronomical Society Meeting Abstracts*, page 336.16, January 2015.

Michael Hippke and René Heller. Optimized transit detection algorithm to search for periodic transits of small planets. *Astronomy & Astrophysics*, 623:A39, feb 2019. doi: 10.1051/0004-6361/201834672. URL https://doi.org/10.1051%2F0004-6361%2F201834672.

E. Høg, C. Fabricius, V. V. Makarov, S. Urban, T. Corbin, et al. The Tycho-2 catalogue of the 2.5 million brightest stars. *Astronomy and Astrophysics*, 355:L27–L30, March 2000.

Wilfried B. Holzapfel. Coherent thermodynamic model for solid, liquid and gas phases of elements and simple compounds in wide ranges of pressure and temperature. *Solid State Sciences*, 80: 31–34, June 2018. doi: 10.1016/j.solidstatesciences.2018.03.023.

F. Hormuth, W. Brandner, S. Hippler, and T. Henning. AstraLux - the Calar Alto 2.2-m telescope Lucky Imaging Camera. *Journal of Physics Conference Series*, 131(1):012051, October 2008. doi: 10.1088/1742-6596/131/1/012051.

Andrew W. Howard, Geoffrey W. Marcy, John Asher Johnson, Debra A. Fischer, Jason T. Wright, Howard Isaacson, Jeff A. Valenti, Jay Anderson, Doug N. C. Lin, and Shigeru Ida. The Occurrence and Mass Distribution of Close-in Super-Earths, Neptunes, and Jupiters. *Science*, 330(6004):653, October 2010. doi: 10.1126/science.1194854.

Andrew W. Howard, Geoffrey W. Marcy, Bryson, et al. Planet Occurrence within 0.25 AU of Solar-type Stars from Kepler. *Astrophysical Journal, Supplement*, 201(2):15, August 2012. doi: 10.1088/0067-0049/201/2/15.

Andrew W. Howard, Roberto Sanchis-Ojeda, Geoffrey W. Marcy, John Asher Johnson, Joshua N. Winn, Howard Isaacson, Debra A. Fischer, Benjamin J. Fulton, Evan Sinukoff, and Jonathan J. Fortney. A rocky composition for an earth-sized exoplanet. *Nature*, 503(7476):381–384, oct 2013. doi: 10.1038/nature12767. URL https://doi.org/10.1038%2Fnature12767.

Steve B. Howell, Mark E. Everett, William Sherry, Elliott Horch, and David R. Ciardi. Speckle camera observations for the nasa kepler mission follow-up program. *The Astronomical Journal*, 142(1):19, jun 2011. doi: 10.1088/0004-6256/142/1/19. URL https://dx.doi.org/10.1088/0004-6256/142/1/19.

Steve B. Howell, Charlie Sobeck, Michael Haas, Martin Still, et al. The K2 Mission: Characterization and Early Results. *Publications of the ASP*, 126(938):398, April 2014. doi: 10.1086/676406.

Chelsea X. Huang and Andrew Vanderburg. Tess lightcurves from the mit quick-look pipeline ("qlp"), 2020. URL `http://archive.stsci.edu/doi/resolve/resolve.html?doi=10.17909/t9-r086-e880`.

W. B. Hubbard and J. J. Macfarlane. Structure and evolution of Uranus and Neptune. *Journal of Geophysics Research*, 85:225–234, January 1980. doi: 10.1029/JB085iB01p00225.

A. Hunter, A. B. Macgregor, T. Szabo, C. Wellington, and M. I. Bellgard. Yabi: An online research environment for grid, high performance and cloud computing. *Source Code for Biology and Medicine*, 7(1):1, 2012. doi: 10.1186/1751-0473-7-1. URL `https://researchrepository.murdoch.edu.au/id/eprint/7974/`.

Brian Jackson, Phil Arras, Kaloyan Penev, Sarah Peacock, and Pablo Marchant. A new model of roche lobe overflow for short-period gaseous planets and binary stars. *The Astrophysical Journal*, 835(2):145, jan 2017. doi: 10.3847/1538-4357/835/2/145. URL `https://doi.org/10.3847%2F1538-4357%2F835%2F2%2F145`.

Jon M. Jenkins. The Impact of Solar-like Variability on the Detectability of Transiting Terrestrial Planets. *Astrophysical Journal*, 575(1):493–505, August 2002. doi: 10.1086/341136.

Jon M. Jenkins, Hema Chandrasekaran, Sean D. McCauliff, Douglas A. Caldwell, Peter Tenenbaum, Jie Li, Todd C. Klaus, Miles T. Cote, and Christopher Middour. Transiting planet search in the Kepler pipeline. In Nicole M. Radziwill and Alan Bridger, editors, *Software and Cyberinfrastructure for Astronomy*, volume 7740 of *Society of Photo-Optical Instrumentation Engineers (SPIE) Conference Series*, page 77400D, July 2010. doi: 10.1117/12.856764.

Jon M. Jenkins, Joseph D. Twicken, Sean McCauliff, Jennifer Campbell, et al. The TESS science processing operations center. In Gianluca Chiozzi and Juan C. Guzman, editors, *Software and Cyberinfrastructure for Astronomy IV*, volume 9913 of *Society of Photo-Optical Instrumentation Engineers (SPIE) Conference Series*, page 99133E, August 2016. doi: 10.1117/12.2233418.

Jon M. Jenkins, Peter Tenenbaum, Shawn Seader, Christopher J. Burke, Sean D. McCauliff, Jeffrey C. Smith, Joseph D. Twicken, and Hema Chandrasekaran. Kepler Data Processing Handbook: Transiting Planet Search. Kepler Science Document KSCI-19081-003, id. 9. Edited by Jon M. Jenkins., March 2020.

John Asher Johnson, Kimberly M. Aller, Andrew W. Howard, and Justin R. Crepp. Giant Planet Occurrence in the Stellar Mass-Metallicity Plane. , 122(894):905, August 2010. doi: 10.1086/655775.

C. Jurgenson, D. Fischer, T. McCracken, D. Sawyer, A. Szymkowiak, A. Davis, G. Muller, and F. Santoro. EXPRES: a next generation RV spectrograph in the search for earth-like worlds. In Christopher J. Evans, Luc Simard, and Hideki Takami, editors, *Ground-based and Airborne Instrumentation for Astronomy VI*, volume 9908 of *Society of Photo-Optical Instrumentation Engineers (SPIE) Conference Series*, page 99086T, August 2016. doi: 10.1117/12.2233002.

Stephen R. Kane, Selçuk Yalçınkaya, Osborn, et al. Transits of known planets orbiting a naked-eye star. *The Astronomical Journal*, 160(3):129, aug 2020. doi: 10.3847/1538-3881/aba835. URL `https://doi.org/10.3847%2F1538-3881%2Faba835`.

Shubham Kanodia, Gudmundur Stefansson, et al. TOI-532b: The habitable-zone planet finder confirms a large super neptune in the neptune desert orbiting a metal-rich m-dwarf host. *The Astronomical Journal*, 162(4):135, sep 2021. doi: 10.3847/1538-3881/ac1940. URL `https://doi.org/10.3847%2F1538-3881%2Fac1940`.

Robert E. Kass and Adrian E. Raftery. Bayes factors. *Journal of the American Statistical Association*, 90:773–795, 6 1995. ISSN 0162-1459. doi: 10.1080/01621459.1995.10476572.

A. Kaufer, O. Stahl, S. Tubbesing, P. Nørregaard, G. Avila, P. Francois, L. Pasquini, and A. Pizzella. Commissioning FEROS, the new high-resolution spectrograph at La-Silla. *The Messenger*, 95: 8–12, March 1999.

Eliza M.-R. Kempton, Jacob L. Bean, Louie, et al. A framework for prioritizing the tess planetary candidates most amenable to atmospheric characterization. *Publications of the Astronomical Society of the Pacific*, 130(993):114401, Sep 2018. ISSN 1538-3873. doi: 10.1088/1538-3873/aadf6f. URL `http://dx.doi.org/10.1088/1538-3873/aadf6f`.

A. Kessler and Y. Alibert. The interplay between pebble and planetesimal accretion in population synthesis models and its role in giant planet formation. , 674:A144, June 2023. doi: 10.1051/0004-6361/202245641.

David M. Kipping. Binning is sinning: morphological light-curve distortions due to finite integration time. *Monthly Notices of the Royal Astronomical Society*, 408(3):1758–1769, aug 2010. doi: 10.1111/j.1365-2966.2010.17242.x. URL `https://doi.org/10.1111%2Fj.1365-2966.2010.17242.x`.

David M. Kipping. Efficient, uninformative sampling of limb darkening coefficients for two-parameter laws. *Monthly Notices of the Royal Astronomical Society*, 435(3):2152–2160, aug 2013. doi: 10.1093/mnras/stt1435. URL `https://doi.org/10.1093%2Fmnras%2Fstt1435`.

Heather A. Knutson, David Charbonneau, Robert W. Noyes, Timothy M. Brown, and Ronald L. Gilliland. Using Stellar Limb-Darkening to Refine the Properties of HD 209458b. , 655(1): 564–575, January 2007. doi: 10.1086/510111.

Heather A. Knutson, Björn Benneke, Drake Deming, and Derek Homeier. A featureless transmission spectrum for the Neptune-mass exoplanet GJ436b. *Nature*, 505(7481):66–68, January 2014. doi: 10.1038/nature12887.

P. C. König, M. Damasso, G. Hébrard, L. Naponiello, et al. A warm super-Neptune around the G-dwarf star TOI-1710 revealed with TESS, SOPHIE, and HARPS-N. *Astron. Astrophys.*, 666: A183, October 2022.

Tommi T. Koskinen, Panayotis Lavvas, Chenliang Huang, Galen Bergsten, Rachel B. Fernandes, and Mitchell E. Young. Mass loss by atmospheric escape from extremely close-in planets. *The Astrophysical Journal*, 929(1):52, apr 2022. doi: 10.3847/1538-4357/ac4f45. URL `https://doi.org/10.3847%2F1538-4357%2Fac4f45`.

Tanja Kovačević, Felipe González-Cataldo, Sarah T. Stewart, and Burkhard Militzer. Miscibility of rock and ice in the interiors of water worlds. *Scientific Reports*, 12:13055, July 2022.

G. Kovács, S. Zucker, and T. Mazeh. A box-fitting algorithm in the search for periodic transits. *Astronomy & Astrophysics*, 391(1):369–377, jul 2002. doi: 10.1051/0004-6361:20020802. URL https://doi.org/10.1051%2F0004-6361%3A20020802.

Laura Kreidberg. <tt>batman</tt>: BAsic transit model cAlculatioN in python. *Publications of the Astronomical Society of the Pacific*, 127(957):1161–1165, nov 2015. doi: 10.1086/683602. URL https://doi.org/10.1086%2F683602.

Laura Kreidberg. Exoplanet atmosphere measurements from transmission spectroscopy and other planet star combined light observations. In *Handbook of Exoplanets*, pages 2083–2105. Springer International Publishing, 2018. doi: 10.1007/978-3-319-55333-7_100. URL https://doi.org/10.1007%2F978-3-319-55333-7_100.

Laura Kreidberg, Jacob L. Bean, Jean-Michel Désert, Björn Benneke, Drake Deming, Kevin B. Stevenson, Sara Seager, Zachory Berta-Thompson, Andreas Seifahrt, and Derek Homeier. Clouds in the atmosphere of the super-earth exoplanet GJ 1214b. *Nature*, 505(7481):69–72, jan 2014. doi: 10.1038/nature12888. URL https://doi.org/10.1038%2Fnature12888.

D. Kubyshkina and L. Fossati. The mass-radius relation of intermediate-mass planets outlined by hydrodynamic escape and thermal evolution. *Astron. Astrophys.*, 668:A178, December 2022.

R. L. Kurucz. Atlas: a Computer Program for Calculating Model Stellar Atmospheres. *SAO Special Report*, 309, February 1970.

G Lacedelli, L Malavolta, L Borsato, G Piotto, et al. An unusually low density ultra-short period super-earth and three mini-neptunes around the old star TOI-561. *Monthly Notices of the Royal Astronomical Society*, 501(3):4148–4166, dec 2020. doi: 10.1093/mnras/staa3728. URL https://doi.org/10.1093%2Fmnras%2Fstaa3728.

G Lacedelli, T. G. Wilson, Malavolta, et al. Investigating the architecture and internal structure of the TOI-561 system planets with CHEOPS, HARPS-n, and TESS. *Monthly Notices of the Royal Astronomical Society*, 511(3):4551–4571, jan 2022. doi: 10.1093/mnras/stac199. URL https://doi.org/10.1093%2Fmnras%2Fstac199.

M. Lafarga, I. Ribas, C. Lovis, M. Perger, M. Zechmeister, F. F. Bauer, M. Kürster, M. Corté s-Contreras, J. C. Morales, E. Herrero, A. Rosich, D. Baroch, A. Reiners, J. A. Caballero, A. Quirrenbach, P. J. Amado, J. M. Alacid, V. J. S. Béjar, S. Dreizler, A. P. Hatzes, T. Henning, S. V. Jeffers, A. Kaminski, D. Montes, S. Pedraz, C. Rodríguez-López, and J. H. M. M. Schmitt. The CARMENES search for exoplanets around m dwarfs. *Astronomy & Astrophysics*, 636:A36, apr 2020. doi: 10.1051/0004-6361/201937222. URL https://doi.org/10.1051%2F0004-6361%2F201937222.

Dong Lai. Tidal dissipation in planet-hosting stars: damping of spin-orbit misalignment and survival of hot jupiters. *Monthly Notices of the Royal Astronomical Society*, 423(1):486–492, apr 2012. doi: 10.1111/j.1365-2966.2012.20893.x. URL https://doi.org/10.1111%2Fj.1365-2966.2012.20893.x.

M. Lambrechts and A. Johansen. Forming the cores of giant planets from the radial pebble flux in protoplanetary discs. *Astron. Astrophys.*, 572:A107, December 2014.

Jean-Pierre Lasota and Jean-Marie Hameury. Disk instability models. In Stephen S. Holt and Timothy R. Kallman, editors, *Accretion processes in Astrophysical Systems: Some like it hot! - eigth AstroPhysics Conference*, volume 431 of *American Institute of Physics Conference Series*, pages 351–360, April 1998. doi: 10.1063/1.55920.

J. Leconte, G. Chabrier, I. Baraffe, and B. Levrard. Is tidal heating sufficient to explain bloated exoplanets? consistent calculations accounting for finite initial eccentricity. *Astronomy and Astrophysics*, 516:A64, jun 2010. doi: 10.1051/0004-6361/201014337. URL `https://doi.org/10.1051%2F0004-6361%2F201014337`.

A. Leleu, J. B. Delisle, S. Udry, and R. others Mardling. Removing biases on the density of sub-Neptunes characterised via transit timing variations. Update on the mass-radius relationship of 34 Kepler planets. *Astron. Astrophys.*, 669:A117, January 2023.

Jie Li, Peter Tenenbaum, Joseph D. Twicken, Christopher J. Burke, Jon M. Jenkins, Elisa V. Quintana, Jason F. Rowe, and Shawn E. Seader. Kepler data validation ii–transit model fitting and multiple-planet search. *Publications of the Astronomical Society of the Pacific*, 131(996): 1–28, 2019. ISSN 00046280, 15383873. URL `https://www.jstor.org/stable/26660723`.

Lightkurve Collaboration, J. V. d. M. Cardoso, C. Hedges, et al. Lightkurve: Kepler and TESS time series analysis in Python. Astrophysics Source Code Library, December 2018.

J. Lillo-Box, D. Barrado, and H. Bouy. Multiplicity in transiting planet-host stars. A lucky imaging study of Kepler candidates. *Astronomy and Astrophysics*, 546:A10, October 2012. doi: 10.1051/0004-6361/201219631.

J. Lillo-Box, D. Barrado, and H. Bouy. High-resolution imaging of Kepler planet host candidates. A comprehensive comparison of different techniques. *Astronomy and Astrophysics*, 566:A103, June 2014. doi: 10.1051/0004-6361/201423497.

Min-Kai Lin and John C. B. Papaloizou. Type III migration in a low-viscosity disc. , 405(3): 1473–1490, July 2010. doi: 10.1111/j.1365-2966.2010.16560.x.

K. Lind, M. Asplund, and P. S. Barklem. Departures from LTE for neutral Li in late-type stars. *Astronomy and Astrophysics*, 503:541L, August 2009. doi: 10.1051/0004-6361/200912221.

J. J. Lissauer. Timescales for planetary accretion and the structure of the protoplanetary disk. *Icarus*, 69(2):249–265, February 1987.

Jack J. Lissauer, Daniel Jontof-Hutter, Jason F. Rowe, et al. ALL SIX PLANETS KNOWN TO ORBIT KEPLER-11 HAVE LOW DENSITIES. *The Astrophysical Journal*, 770(2):131, jun 2013. doi: 10.1088/0004-637x/770/2/131. URL `https://doi.org/10.1088/0004-637x/770/2/131`.

Shang-Fei Liu, Yasunori Hori, D. N. C. Lin, and Erik Asphaug. Giant Impact: An Efficient Mechanism for the Devolatilization of Super-Earths. , 812(2):164, October 2015. doi: 10.1088/0004-637X/812/2/164.

Daniele Locci, Cesare Cecchi-Pestellini, and Giuseppina Micela. Photo-evaporation of close-in gas giants orbiting around g and m stars. *Astronomy & Astrophysics*, 624:A101, apr 2019. doi: 10.1051/0004-6361/201834491. URL https://doi.org/10.1051%2F0004-6361%2F201834491.

Eric D. Lopez and Jonathan J. Fortney. The Role of Core Mass in Controlling Evaporation: The Kepler Radius Distribution and the Kepler-36 Density Dichotomy. , 776(1):2, October 2013. doi: 10.1088/0004-637X/776/1/2.

Christophe Lovis, Michel Mayor, Francesco Pepe, Yann Alibert, Willy Benz, et al. An extrasolar planetary system with three Neptune-mass planets. , 441(7091):305–309, May 2006. doi: 10.1038/nature04828.

M. Lozovsky, R. Helled, C. Dorn, and J. Venturini. Threshold Radii of Volatile-rich Planets. *Astrophysical Journal*, 866(1):49, October 2018. doi: 10.3847/1538-4357/aadd09.

Stephen H. Lubow and Gordon I. Ogilvie. Kozai-Lidov disc instability. , 469(4):4292–4305, August 2017. doi: 10.1093/mnras/stx990.

J. Lustig-Yaeger, G. Fu, E. M. May, K. N. Ortiz Ceballos, S. E. Moran, S. Peacock, K. B. Stevenson, M. López-Morales, R. J. MacDonald, L. C. Mayorga, D. K. Sing, K. S. Sotzen, J. A. Valenti, J. Adams, M. K. Alam, N. E. Batalha, K. A. Bennett, J. Gonzalez-Quiles, J. Kirk, E. Kruse, J. D. Lothringer, Z. Rustamkulov, and H. R. Wakeford. A jwst transmission spectrum of a nearby earth-sized exoplanet, 2023.

Mason G. MacDougall, Erik A. Petigura, Tara Fetherolf, et al. The TESS-Keck Survey. XIII. An Eccentric Hot Neptune with a Similar-mass Outer Companion around TOI-1272. , 164(3):97, September 2022. doi: 10.3847/1538-3881/ac7ce1.

Nikku Madhusudhan. Exoplanetary Atmospheres: Key Insights, Challenges, and Prospects. , 57:617–663, August 2019. doi: 10.1146/annurev-astro-081817-051846.

A. Maggio, D. Locci, I. Pillitteri, S. Benatti, R. Claudi, S. Desidera, G. Micela, M. Damasso, A. Sozzetti, and A. Suarez Mascareñ o. New constraints on the future evaporation of the young exoplanets in the v1298 tau system. *The Astrophysical Journal*, 925(2):172, feb 2022. doi: 10.3847/1538-4357/ac4040. URL https://doi.org/10.3847%2F1538-4357%2Fac4040.

Luca Malavolta, Luca Borsato, Valentina Granata, et al. The kepler-19 system: A thick-envelope super-earth with two neptune-mass companions characterized using radial velocities and transit timing variations. *The Astronomical Journal*, 153(5):224, apr 2017. doi: 10.3847/1538-3881/aa6897. URL https://doi.org/10.3847%2F1538-3881%2Faa6897.

Robert A. Marcus, Sarah T. Stewart, Dimitar Sasselov, and Lars Hernquist. COLLISIONAL STRIPPING AND DISRUPTION OF SUPER-EARTHS. *The Astrophysical Journal*, 700(2):L118–L122, jul 2009. doi: 10.1088/0004-637x/700/2/l118. URL https://doi.org/10.1088%2F0004-637x%2F700%2F2%2Fl118.

P. F. L. Maxted, D. R. Anderson, A. Collier Cameron, et al. WASP-41b: A Transiting Hot Jupiter Planet Orbiting a Magnetically Active G8V Star. *Publications of the ASP*, 123(903):547, May 2011. doi: 10.1086/660007.

Lucio Mayer, Thomas Quinn, James Wadsley, and Joachim Stadel. The evolution of gravitationally unstable protoplanetary disks: Fragmentation and possible giant planet formation. *The Astrophysical Journal*, 609(2):1045–1064, jul 2004. doi: 10.1086/421288. URL `https://doi.org/10.1086%2F421288`.

M. Mayor, M. Marmier, C. Lovis, S. Udry, D. Ségransan, F. Pepe, W. Benz, J. L. Bertaux, F. Bouchy, X. Dumusque, G. Lo Curto, C. Mordasini, D. Queloz, and N. C. Santos. The HARPS search for southern extra-solar planets XXXIV. Occurrence, mass distribution and orbital properties of super-Earths and Neptune-mass planets. *arXiv e-prints*, art. arXiv:1109.2497, September 2011.

Michel Mayor and Didier Queloz. A Jupiter-mass companion to a solar-type star. *Nature*, 378 (6555):355–359, November 1995. doi: 10.1038/378355a0.

T. Mazeh, T. Holczer, and S. Faigler. Dearth of short-period Neptunian exoplanets: A desert in period-mass and period-radius planes. *Astron. Astrophys.*, 589:A75, May 2016.

Michael W. McElwain, Lee D. Feinberg, Perrin, et al. The james webb space telescope mission: Optical telescope element design, development, and performance. *Publications of the Astronomical Society of the Pacific*, 135(1047):058001, may 2023. doi: 10.1088/1538-3873/acada0. URL `https://doi.org/10.1088%2F1538-3873%2Facada0`.

D. B. McLaughlin. Some results of a spectrographic study of the Algol system. , 60:22–31, July 1924. doi: 10.1086/142826.

Karen Meech and Sean N. Raymond. *Planetary Astrobiology*. University of Arizona Press, 2005. doi: 10.2458/azu_uapress_9780816540068. URL `https://doi.org/10.2458%2Fazu_uapress_9780816540068`.

B. D. Metzger, D. Giannios, and D. S. Spiegel. Optical and x-ray transients from planet-star mergers. *Monthly Notices of the Royal Astronomical Society*, 425(4):2778–2798, sep 2012. doi: 10.1111/j.1365-2966.2012.21444.x. URL `https://doi.org/10.1111%2Fj.1365-2966.2012.21444.x`.

N. Meunier and A. M. Lagrange. Unexpectedly strong effect of supergranulation on the detectability of Earth twins orbiting Sun-like stars with radial velocities. , 625:L6, May 2019. doi: 10.1051/0004-6361/201935099.

Eliza Miller-Ricci, Sara Seager, and Dimitar Sasselov. The Atmospheric Signatures of Super-Earths: How to Distinguish Between Hydrogen-Rich and Hydrogen-Poor Atmospheres. *Astrophysical Journal*, 690(2):1056–1067, January 2009. doi: 10.1088/0004-637X/690/2/1056.

Sean M. Mills, Andrew W. Howard, Erik A. Petigura, et al. The California-Kepler Survey. VIII. Eccentricities of Kepler Planets and Tentative Evidence of a High-metallicity Preference for Small Eccentric Planets. , 157(5):198, May 2019. doi: 10.3847/1538-3881/ab1009.

Darius Modirrousta-Galian, Daniele Locci, and Giuseppina Micela. The bimodal distribution in exoplanet radii: Considering varying core compositions and h₂ envelope's sizes. *The Astrophysical Journal*, 891(2):158, mar 2020. doi: 10.3847/1538-4357/ab7379. URL `https://doi.org/10.3847%2F1538-4357%2Fab7379`.

M. Mohler-Fischer, L. Mancini, J. D. Hartman, Bakos, et al. HATS-2b: A transiting extrasolar planet orbiting a K-type star showing starspot activity. , 558:A55, October 2013. doi: 10.1051/0004-6361/201321663.

Caroline V. Morley, Jonathan J. Fortney, et al. Thermal Emission and Reflected Light Spectra of Super Earths with Flat Transmission Spectra. *Astrophysical Journal*, 815(2):110, December 2015. doi: 10.1088/0004-637X/815/2/110.

Robert L. Morris, Joseph D. Twicken, et al. Kepler Data Processing Handbook: Photometric Analysis. Kepler Science Document KSCI-19081-003, id. 6. Edited by Jon M. Jenkins., March 2020.

Olivier Mousis, Magali Deleuil, Artyom Aguichine, Emmanuel Marcq, et al. Irradiated Ocean Planets Bridge Super-Earth and Sub-Neptune Populations. *Astrophys. J. Lett.*, 896(2):L22, June 2020.

C. D. Murray and S. F. Dermott. *Solar system dynamics*. 1999.

Alexander J. Mustill, Melvyn B. Davies, and Anders Johansen. The effects of external planets on inner systems: multiplicities, inclinations and pathways to eccentric warm Jupiters. , 468(3):3000–3023, July 2017. doi: 10.1093/mnras/stx693.

M. Nagasawa, S. Ida, and T. Bessho. Formation of Hot Planets by a Combination of Planet Scattering, Tidal Circularization, and the Kozai Mechanism. , 678(1):498–508, May 2008. doi: 10.1086/529369.

L. Naponiello, L. Mancini, M. Damasso, et al. The GAPS programme at TNG. XL. A puffy and warm Neptune-sized planet and an outer Neptune-mass candidate orbiting the solar-type star TOI-1422. *Astron. Astrophys.*, 667:A8, November 2022.

L. Naponiello, L. Mancini, A. Sozzetti, et al. *arXiv e-prints*, art. arXiv:2309.01464, September 2023. doi: 10.48550/arXiv.2309.01464.

D Nardiello, L Borsato, G Piotto, L S Colombo, et al. A psf-based approach to tess high quality data of stellar clusters (pathos) – i. search for exoplanets and variable stars in the field of 47 tuc. *Monthly Notices of the Royal Astronomical Society*, 490:3806–3823, 12 2019. ISSN 0035-8711. doi: 10.1093/mnras/stz2878.

Norio Narita, Akihiko Fukui, Nobuhiko Kusakabe, Noriharu Watanabe, et al. MuSCAT2: four-color simultaneous camera for the 1.52-m telescopio carlos sánchez. *Journal of Astronomical Telescopes, Instruments, and Systems*, 5(01):1, dec 2018. doi: 10.1117/1.jatis.5.1.015001. URL `https://doi.org/10.1117%2F1.jatis.5.1.015001`.

S. Nayakshin. Positive metallicity correlation for coreless giant planets. , 448:L25–L29, March 2015. doi: 10.1093/mnrasl/slu191.

David Nesvorný . Dynamical evolution of the early solar system. *Annual Review of Astronomy and Astrophysics*, 56(1):137–174, sep 2018. doi: 10.1146/annurev-astro-081817-052028. URL `https://doi.org/10.1146%2Fannurev-astro-081817-052028`.

B. A. Nicholson and S. Aigrain. Quasi-periodic Gaussian processes for stellar activity: From physical to kernel parameters. , 515(4):5251–5266, October 2022. doi: 10.1093/mnras/stac2097.

G. I. Ogilvie and D. N. C. Lin. Tidal Dissipation in Rotating Solar-Type Stars. *Astrophysical Journal*, 661(2):1180–1191, June 2007. doi: 10.1086/515435.

E. Oliva, L. Origlia, C. Baffa, C. Biliotti, P. Bruno, F. D'Amato, Del Vecchio, et al. The GIANO-TNG spectrometer. In Ian S. McLean and Masanori Iye, editors, *Society of Photo-Optical Instrumentation Engineers (SPIE) Conference Series*, volume 6269 of *Society of Photo-Optical Instrumentation Engineers (SPIE) Conference Series*, page 626919, June 2006. doi: 10.1117/12.670006.

Ares Osborn, David J. Armstrong, Jorge Fernández Fernández, et al. TOI-332 b: a super dense Neptune found deep within the Neptunian desert. , 526(1):548–566, November 2023. doi: 10.1093/mnras/stad2575.

M. Oshagh, S. Dreizler, N. C. Santos, P. Figueira, and A. Reiners. Can stellar activity make a planet seem misaligned? *Astronomy &amp Astrophysics*, 593:A25, aug 2016. doi: 10.1051/0004-6361/201628728. URL `https://doi.org/10.1051%2F0004-6361%2F201628728`.

M. Oshagh, N. C. Santos, P. Figueira, S. C. C. Barros, et al. Understanding stellar activity-induced radial velocity jitter using simultaneous K2 photometry and HARPS RV measurements. , 606:A107, October 2017. doi: 10.1051/0004-6361/201731139.

J. F. Otegi, F. Bouchy, and R. Helled. Revisited mass-radius relations for exoplanets below 120 im/isub⊕/sub. *Astronomy &amp Astrophysics*, 634:A43, feb 2020. doi: 10.1051/0004-6361/201936482. URL `https://doi.org/10.1051%2F0004-6361%2F201936482`.

James E. Owen. Atmospheric Escape and the Evolution of Close-In Exoplanets. *Annual Review of Earth and Planetary Sciences*, 47:67–90, May 2019.

James E. Owen and Dong Lai. Photoevaporation and high-eccentricity migration created the sub-Jovian desert. *Mon. Not. R. Astron. Soc.*, 479(4):5012–5021, October 2018.

James E. Owen and Yanqin Wu. The Evaporation Valley in the Kepler Planets. , 847(1):29, September 2017. doi: 10.3847/1538-4357/aa890a.

Hannu Parviainen. Bayesian Methods for Exoplanet Science. In Hans J. Deeg and Juan Antonio Belmonte, editors, *Handbook of Exoplanets*, page 149. 2018. doi: 10.1007/978-3-319-55333-7_149.

L. Pasquini, K. Biazzo, P. Bonifacio, S. Randich, and L. R. Bedin. Solar twins in M67. *Astronomy and Astrophysics*, 489:677, October 2009. doi: 10.1051/0004-6361:200809714.

Bill Paxton, Pablo Marchant, Josiah Schwab, Evan B. Bauer, et al. MODULES FOR EXPERIMENTS IN STELLAR ASTROPHYSICS (MESA): BINARIES, PULSATIONS, AND EXPLOSIONS. *The Astrophysical Journal Supplement Series*, 220(1):15, sep 2015. doi: 10.1088/0067-0049/220/1/15. URL `https://doi.org/10.1088%2F0067-0049%2F220%2F1%2F15`.

F. Pepe, S. Cristiani, R. Rebolo, N. C. Santos, H. Dekker, A. Cabral, et al. ESPRESSO at VLT. On-sky performance and first results. , 645:A96, January 2021. doi: 10.1051/0004-6361/202038306.

Perger, M., García-Piquer, A., Ribas, I., Morales, J. C., Affer, L., et al. Hades rv programme with harps-n at tng - ii. data treatment and simulations. *A&A*, 598:A26, 2017. doi: 10.1051/0004-6361/201628985. URL https://doi.org/10.1051/0004-6361/201628985.

S. Perruchot, D. Kohler, F. Bouchy, Y. Richaud, et al. The SOPHIE spectrograph: design and technical key-points for high throughput and high stability. In Ian S. McLean and Mark M. Casali, editors, *Ground-based and Airborne Instrumentation for Astronomy II*, volume 7014, pages 235 – 246. International Society for Optics and Photonics, SPIE, 2008. doi: 10.1117/12.787379. URL https://doi.org/10.1117/12.787379.

Michael Perryman. *The Exoplanet Handbook*. 2018.

Carina M. Persson, Iskra Y. Georgieva, and Davide Gandolfi. TOI-2196 b: Rare planet in the hot Neptune desert transiting a G-type star. *Astron. Astrophys.*, 666:A184, October 2022.

Erik A. Petigura, Geoffrey W. Marcy, and Andrew W. Howard. A Plateau in the Planet Population below Twice the Size of Earth. *Astrophysical Journal*, 770(1):69, June 2013. doi: 10.1088/0004-637X/770/1/69.

Erik A. Petigura, Andrew W. Howard, Geoffrey W. Marcy, John Asher Johnson, Howard Isaacson, et al. The California-Kepler Survey. I. High-resolution Spectroscopy of 1305 Stars Hosting Kepler Transiting Planets. *Astronomical Journal*, 154(3):107, September 2017. doi: 10.3847/1538-3881/aa80de.

Raymond T. Pierrehumbert. *Principles of Planetary Climate*. 2010.

Lorenzo Pino, J.M. Désert, Brogi, et al. Neutral Iron Emission Lines from the Dayside of KELT-9b: The GAPS Program with HARPS-N at TNG XX. *Astrophysical Journal, Letters*, 894(2):L27, May 2020. doi: 10.3847/2041-8213/ab8c44.

Jorge Pinochet and Michael Van Sint Jan. Einstein ring: weighing a star with light. *Physics Education*, 53(5):055003, jun 2018. doi: 10.1088/1361-6552/aac7b9. URL https://doi.org/10.1088%2F1361-6552%2Faac7b9.

D. L. Pollacco, I. Skillen, A. Collier Cameron, D. J. Christian, et al. The WASP Project and the SuperWASP Cameras. *Publications of the ASP*, 118:1407–1418, October 2006. doi: 10.1086/508556.

James B. Pollack, Olenka Hubickyj, Peter Bodenheimer, Jack J. Lissauer, Morris Podolak, and Yuval Greenzweig. Formation of the Giant Planets by Concurrent Accretion of Solids and Gas. *Icarus*, 124(1):62–85, November 1996. doi: 10.1006/icar.1996.0190.

Sanson T. S. Poon, Richard P. Nelson, and Gavin A. L. Coleman. In situ formation of hot Jupiters with companion super-Earths. , 505(2):2500–2516, August 2021. doi: 10.1093/mnras/stab1466.

E. Poretti, C. Boccato, R. Claudi, R. Cosentino, E. Covino, S. Desidera, R. Gratton, A. F. Lanza, A. Maggio, G. Micela, E. Molinari, I. Pagano, G. Piotto, R. Smareglia, A. Sozzetti, and GAPS Collaboration. Global Architecture of Planetary Systems (GAPS), a project for the whole Italian Community. *Mem. Societa Astronomica Italiana*, 87:141, January 2016.

A.M. Price-Whelan and The Astropy Collaboration. The astropy project: Building an open-science project and status of the v2.0 core package. *The Astronomical Journal*, 156:123, 8 2018. ISSN 1538-3881. doi: 10.3847/1538-3881/aabc4f.

T. Prusti, J. H. J. de Bruijne, Brown, et al. The gaia mission. *Astronomy and Astrophysics*, 595:A1, 11 2016. ISSN 0004-6361. doi: 10.1051/0004-6361/201629272.

Elisa V. Quintana, Thomas Barclay, William J. Borucki, Jason F. Rowe, and John E. Chambers. THE FREQUENCY OF GIANT IMPACTS ON EARTH-LIKE WORLDS. *The Astrophysical Journal*, 821(2):126, apr 2016. doi: 10.3847/0004-637x/821/2/126. URL `https://doi.org/10.3847%2F0004-637x%2F821%2F2%2F126`.

A. Quirrenbach. CARMENES: high-resolution spectra and precise radial velocities in the red and infrared. In Christopher J. Evans, Luc Simard, and Hideki Takami, editors, *Ground-based and Airborne Instrumentation for Astronomy VII*, volume 10702 of *Society of Photo-Optical Instrumentation Engineers (SPIE) Conference Series*, page 107020W, July 2018. doi: 10.1117/12.2313689.

S. Ramsay, M. Cirasuolo, P. Amico, N. N. Bezawada, P. Caillier, et al. Instrumentation for ESO's Extremely Large Telescope. *The Messenger*, 182:3–6, March 2021. doi: 10.18727/0722-6691/5214.

Saul Rappaport, Roberto Sanchis-Ojeda, Leslie A. Rogers, Alan Levine, and Joshua N. Winn. THE ROCHE LIMIT FOR CLOSE-ORBITING PLANETS: MINIMUM DENSITY, COMPOSITION CONSTRAINTS, AND APPLICATION TO THE 4.2 hr PLANET KOI 1843.03. *The Astrophysical Journal*, 773(1):L15, jul 2013. doi: 10.1088/2041-8205/773/1/l15. URL `https://doi.org/10.1088%2F2041-8205%2F773%2F1%2Fl15`.

Carl Edward Rasmussen and Christopher K. I. Williams. *Gaussian Processes for Machine Learning*. 2006.

H. Rauer, C. Catala, C. Aerts, et al. The PLATO 2.0 mission. *Experimental Astronomy*, 38 (1-2):249–330, sep 2014. doi: 10.1007/s10686-014-9383-4. URL `https://doi.org/10.1007%2Fs10686-014-9383-4`.

George R. Ricker, Joshua N. Winn, Vanderspek, et al. Transiting exoplanet survey satellite. *Journal of Astronomical Telescopes, Instruments, and Systems*, 1(1):014003, oct 2014. doi: 10.1117/1.jatis.1.1.014003. URL `https://doi.org/10.1117%2F1.jatis.1.1.014003`.

Christian P. Robert. The Metropolis-Hastings algorithm. *arXiv e-prints*, art. arXiv:1504.01896, April 2015. doi: 10.48550/arXiv.1504.01896.

R. A. Rossiter. On the detection of an effect of rotation during eclipse in the velocity of the brigher component of beta Lyrae, and on the constancy of velocity of this system. , 60:15–21, July 1924. doi: 10.1086/142825.

L. S. Rothman, I. E. Gordon, R. J. Barber, H. Dothe, R. R. Gamache, et al. HITEMP, the high-temperature molecular spectroscopic database. *Journal of Quantitiative Spectroscopy and Radiative Transfer*, 111:2139–2150, October 2010. doi: 10.1016/j.jqsrt.2010.05.001.

S Ruiz-Bonilla, V R Eke, J A Kegerreis, R J Massey, and L F A Teodoro. The effect of pre-impact spin on the moon-forming collision. *Monthly Notices of the Royal Astronomical Society*, 500(3): 2861–2870, dec 2020. doi: 10.1093/mnras/staa3385. URL https://doi.org/10.1093%2Fmnras%2Fstaa3385.

V. S. Safronov. *Evolution of the protoplanetary cloud and formation of the earth and planets.* 1972.

Nicholas Scarsdale, Joseph M. Akana Murphy41, and Natalie M. Batalha. TESS-keck survey. v. twin sub-neptunes transiting the nearby g star HD 63935. *The Astronomical Journal*, 162(5): 215, oct 2021. doi: 10.3847/1538-3881/ac18cb. URL https://doi.org/10.3847%2F1538-3881%2Fac18cb.

Matthieu Schaller, Pedro Gonnet, Aidan B. G. Chalk, and Peter W. Draper. SWIFT. In *Proceedings of the Platform for Advanced Scientific Computing Conference*. ACM, jun 2016. doi: 10.1145/2929908.2929916. URL https://doi.org/10.1145%2F2929908.2929916.

N. Schanche, A. Collier Cameron, G. Hébrard, L. Nielsen, A. H. M. J. Triaud, J. M. Almenara, K. A. Alsubai, D. R. Anderson, D. J. Armstrong, S. C. C. Barros, F. Bouchy, P. Boumis, D. J. A. Brown, F. Faedi, K. Hay, L. Hebb, F. Kiefer, L. Mancini, P. F. L. Maxted, E. Palle, D. L. Pollacco, D. Queloz, B. Smalley, S. Udry, R. West, and P. J. Wheatley. Machine-learning approaches to exoplanet transit detection and candidate validation in wide-field ground-based surveys. , 483(4): 5534–5547, March 2019. doi: 10.1093/mnras/sty3146.

Edward F. Schlafly and Douglas P. Finkbeiner. Measuring Reddening with Sloan Digital Sky Survey Stellar Spectra and Recalibrating SFD. *Astrophysical Journal*, 737(2):103, August 2011. doi: 10.1088/0004-637X/737/2/103.

Kevin C. Schlaufman. Evidence of an upper bound on the masses of planets and its implications for giant planet formation. *The Astrophysical Journal*, 853(1):37, jan 2018. doi: 10.3847/1538-4357/aa961c. URL https://doi.org/10.3847%2F1538-4357%2Faa961c.

David J. Schlegel, Douglas P. Finkbeiner, and Marc Davis. Maps of Dust Infrared Emission for Use in Estimation of Reddening and Cosmic Microwave Background Radiation Foregrounds. *Astrophysical Journal*, 500(2):525–553, June 1998. doi: 10.1086/305772.

J. Schneider, C. Dedieu, P. Le Sidaner, R. Savalle, and I. Zolotukhin. Defining and cataloging exoplanets: the exoplanet.eu database. *Astronomy & Astrophysics*, 532:A79, jul 2011. doi: 10.1051/0004-6361/201116713. URL https://doi.org/10.1051%2F0004-6361%2F201116713.

C. Schwab, A. Rakich, Q. Gong, S. Mahadevan, S. P. Halverson, A. Roy, R. C. Terrien, P. M. Robertson, F. R. Hearty, E. I. Levi, A. J. Monson, J. T. Wright, M. W. McElwain, C. F. Bender, C. H. Blake, J. Stürmer, Y. V. Gurevich, A. Chakraborty, and L. W. Ramsey. Design of NEID, an extreme precision Doppler spectrograph for WIYN. In Christopher J. Evans, Luc Simard, and Hideki Takami, editors, *Ground-based and Airborne Instrumentation for Astronomy VI*, volume 9908 of *Society of Photo-Optical Instrumentation Engineers (SPIE) Conference Series*, page 99087H, August 2016. doi: 10.1117/12.2234411.

Gideon Schwarz. Estimating the Dimension of a Model. *Annals of Statistics*, 6(2):461–464, July 1978.

Nicholas J. Scott, Steve B. Howell, Crystal L. Gnilka, Andrew W. Stephens, Ricardo Salinas, et al. Twin High-resolution, High-speed Imagers for the Gemini Telescopes: Instrument description and science verification results. *Frontiers in Astronomy and Space Sciences*, 8:138, September 2021. doi: 10.3389/fspas.2021.716560.

Ivan I. Shevchenko. *The Lidov-Kozai Effect - Applications in Exoplanet Research and Dynamical Astronomy*, volume 441. 2017. doi: 10.1007/978-3-319-43522-0.

David K. Sing, Jonathan J. Fortney, Nikolay Nikolov, Hannah R. Wakeford, Tiffany Kataria, Thomas M. Evans, Suzanne Aigrain, Gilda E. Ballester, Adam S. Burrows, Drake Deming, Jean-Michel Désert, Neale P. Gibson, Gregory W. Henry, Catherine M. Huitson, Heather A. Knutson, Alain Lecavelier des Etangs, Frederic Pont, Adam P. Showman, Alfred Vidal-Madjar, Michael H. Williamson, and Paul A. Wilson. A continuum from clear to cloudy hot-jupiter exoplanets without primordial water depletion. *Nature*, 529(7584):59–62, dec 2015. doi: 10.1038/nature16068. URL `https://doi.org/10.1038%2Fnature16068`.

Warren Skidmore, TMT International Science Development Teams, and TMT Science Advisory Committee. Thirty Meter Telescope Detailed Science Case: 2015. *Research in Astronomy and Astrophysics*, 15(12):1945, December 2015. doi: 10.1088/1674-4527/15/12/001.

John Skilling. Nested Sampling. In Rainer Fischer, Roland Preuss, and Udo Von Toussaint, editors, *Bayesian Inference and Maximum Entropy Methods in Science and Engineering: 24th International Workshop on Bayesian Inference and Maximum Entropy Methods in Science and Engineering*, volume 735 of *American Institute of Physics Conference Series*, pages 395–405, November 2004. doi: 10.1063/1.1835238.

M. F. Skrutskie, R. M. Cutri, R. Stiening, M. D. Weinberg, et al. The two micron all sky survey (2mass). *The Astronomical Journal*, 131, 2 2006. ISSN 0004-6256. doi: 10.1086/498708.

Jeffrey C. Smith, Martin C. Stumpe, Jeffrey E. Van Cleve, et al. Kepler presearch data conditioning ii - a bayesian approach to systematic error correction. 3 2012. doi: 10.1086/667697.

C. Sneden. The nitrogen abundance of the very metal-poor star HD 122563. *Astronomical Journal*, 184:839, Sep 1973. doi: 10.1086/152374.

Ignas A. G. Snellen, Remco J. de Kok, Ernst J. W. de Mooij, and Simon Albrecht. The orbital motion, absolute mass and high-altitude winds of exoplanet HD209458b. *Nature*, 465(7301): 1049–1051, June 2010. doi: 10.1038/nature09111.

John Southworth. Homogeneous studies of transiting extrasolar planets - iii. additional planets and stellar models. *Monthly Notices of the Royal Astronomical Society*, 408:1689–1713, 11 2010. ISSN 00358711. doi: 10.1111/j.1365-2966.2010.17231.x.

John Southworth. Homogeneous studies of transiting extrasolar planets - IV. Thirty systems with space-based light curves. *Monthly Notices of the RAS*, 417(3):2166–2196, November 2011. doi: 10.1111/j.1365-2966.2011.19399.x.

Alessandro Sozzetti, Guillermo Torres, David Charbonneau, David W. Latham, Matthew J. Holman, Joshua N. Winn, John B. Laird, and Francis T. O'Donovan. Improving stellar and planetary parameters of transiting planet systems: The case of TrES-2. *The Astrophysical Journal*, 664(2): 1190–1198, aug 2007. doi: 10.1086/519214. URL https://doi.org/10.1086%2F519214.

Joshua S. Speagle. A Conceptual Introduction to Markov Chain Monte Carlo Methods. *arXiv e-prints*, art. arXiv:1909.12313, September 2019. doi: 10.48550/arXiv.1909.12313.

Joshua S Speagle. dynesty: a dynamic nested sampling package for estimating bayesian posteriors and evidences. *Monthly Notices of the Royal Astronomical Society*, 493(3):3132–3158, feb 2020. doi: 10.1093/mnras/staa278. URL https://doi.org/10.1093%2Fmnras%2Fstaa278.

C. Spearman. The proof and measurement of association between two things. *The American Journal of Psychology*, 15(1):72–101, 1904. ISSN 00029556. URL http://www.jstor.org/stable/1412159.

David S. Spiegel, Adam Burrows, and John A. Milsom. THE DEUTERIUM-BURNING MASS LIMIT FOR BROWN DWARFS AND GIANT PLANETS. *The Astrophysical Journal*, 727(1): 57, jan 2011. doi: 10.1088/0004-637x/727/1/57. URL https://doi.org/10.1088%2F0004-637x%2F727%2F1%2F57.

Keivan G. Stassun. The revised tess input catalog and candidate target list. *Astronomical Journal*, 158(4):138, oct 2019. doi: 10.3847/1538-3881/ab3467.

Keivan G. Stassun, Ryan J. Oelkers, et al. The TESS Input Catalog and Candidate Target List. *Astronomical Journal*, 156(3):102, September 2018. doi: 10.3847/1538-3881/aad050.

David J. Stevenson, Peter Bodenheimer, Jack J. Lissauer, and Gennaro D'Angelo. Mixing of Condensable Constituents with H-He during the Formation and Evolution of Jupiter. *Planetary Science Journal*, 3(4):74, April 2022.

Sarah Stewart, Erik Davies, Megan Duncan, Simon Lock, et al. The shock physics of giant impacts: Key requirements for the equations of state. In *SHOCK COMPRESSION OF CONDENSED MATTER - 2019: Proceedings of the Conference of the American Physical Society Topical Group on Shock Compression of Condensed Matter*. AIP Publishing, 2020. doi: 10.1063/12.0000946. URL https://doi.org/10.1063%2F12.0000946.

Sarah T. Stewart, Erik J. Davies, Megan S. Duncan, Simon J. Lock, Seth Root, Joshua P. Townsend, Richard G. Kraus, Razvan Caracas, and Stein B. Jacobsen. Equation of State Model Forsterite-ANEOS- SLVTv1.0G1: Documentation and Comparisons, October 2019. URL https://doi.org/10.5281/zenodo.3478631.

K. Strehl. Über die Bildschärfe der Fernrohre. *Astronomische Nachrichten*, 158:89, March 1902. doi: 10.1002/asna.19021580604.

Martin C. Stumpe, Jeffrey C. Smith, Jeffrey E. Van Cleve, Joseph D. Twicken, Thomas S. Barclay, et al. Kepler Presearch Data Conditioning I—Architecture and Algorithms for Error Correction in Kepler Light Curves. *Publications of the ASP*, 124(919):985, September 2012. doi: 10.1086/667698.

Martin C. Stumpe, Jeffrey C. Smith, Joseph H. Catanzarite, et al. Multiscale Systematic Error Correction via Wavelet-Based Bandsplitting in Kepler Data. *Publications of the ASP*, 126(935): 100, January 2014. doi: 10.1086/674989.

Sophia Sulis, David Mary, and Lionel Bigot. A Bootstrap Method for Sinusoid Detection in Colored Noise and Uneven Sampling. Application to Exoplanet Detection. *arXiv e-prints*, art. arXiv:1706.06657, June 2017. doi: 10.48550/arXiv.1706.06657.

L. Sun, P. Ioannidis, S. Gu, J. H. M. M. Schmitt, X. Wang, and M. B. N. Kouwenhoven. Kepler-411: a four-planet system with an active host star. *Astron. Astrophys.*, 624:A15, April 2019.

Jamie Tayar, Zachary R. Claytor, Daniel Huber, and Jennifer van Saders. A Guide to Realistic Uncertainties on the Fundamental Properties of Solar-type Exoplanet Host Stars. , 927(1):31, March 2022. doi: 10.3847/1538-4357/ac4bbc.

Jonathan Tennyson, Sergei N. Yurchenko, Ahmed F. Al-Refaie, Victoria H.J. Clark, et al. The 2020 release of the ExoMol database: Molecular line lists for exoplanet and other hot atmospheres. *Journal of Quantitative Spectroscopy and Radiative Transfer*, 255:107228, nov 2020. doi: 10.1016/j.jqsrt.2020.107228. URL `https://doi.org/10.1016%2Fj.jqsrt.2020.107228`.

Cajo J. F. Ter Braak. A Markov Chain Monte Carlo version of the genetic algorithm Differential Evolution: easy Bayesian computing for real parameter spaces. *Statistics and Computing*, 16(3): 239–249, September 2006a. doi: 10.1007/s11222-006-8769-1.

Cajo J. F. Ter Braak. A Markov Chain Monte Carlo version of the genetic algorithm Differential Evolution: easy Bayesian computing for real parameter spaces. *Statistics and Computing*, 16(3): 239–249, September 2006b. doi: 10.1007/s11222-006-8769-1.

Giovanna Tinetti, Paul Eccleston, Haswell, et al. Ariel: Enabling planetary science across light-years, 2021.

Andrei Tokovinin. Ten Years of Speckle Interferometry at SOAR. *Publications of the ASP*, 130 (985):035002, March 2018. doi: 10.1088/1538-3873/aaa7d9.

G. Torres, J. Andersen, and A. Giménez. Accurate masses and radii of normal stars: modern results and applications. , 18(1-2):67–126, February 2010. doi: 10.1007/s00159-009-0025-1.

Amaury H. M. J. Triaud. The rossiter–McLaughlin effect in exoplanet research. In *Handbook of Exoplanets*, pages 1375–1401. Springer International Publishing, 2018. doi: 10.1007/978-3-319-55333-7_2. URL `https://doi.org/10.1007%2F978-3-319-55333-7_2`.

Trifon Trifonov. The Exo-Striker: Transit and radial velocity interactive fitting tool for orbital analysis and N-body simulations. Astrophysics Source Code Library, record ascl:1906.004, June 2019.

Roberto Trotta. Bayes in the sky: Bayesian inference and model selection in cosmology. *Contemporary Physics*, 49(2):71–104, mar 2008. doi: 10.1080/00107510802066753. URL `https://doi.org/10.1080%2F00107510802066753`.

Martin Turbet, Emeline Bolmont, David Ehrenreich, Pierre Gratier, et al. Revised mass-radius relationships for water-rich rocky planets more irradiated than the runaway greenhouse limit. *Astronomy and Astrophysics*, 638:A41, June 2020. doi: 10.1051/0004-6361/201937151.

Joseph D. Twicken, Bruce D. Clarke, Stephen T. Bryson, et al. Photometric analysis in the Kepler Science Operations Center pipeline. In Nicole M. Radziwill and Alan Bridger, editors, *Software and Cyberinfrastructure for Astronomy*, volume 7740, pages 749 – 760. International Society for Optics and Photonics, SPIE, 2010. doi: 10.1117/12.856790. URL `https://doi.org/10.1117/12.856790`.

Joseph D. Twicken, Joseph H. Catanzarite, Bruce D. Clarke, et al. Kepler Data Validation I—Architecture, Diagnostic Tests, and Data Products for Vetting Transiting Planet Candidates. *Publications of the ASP*, 130(988):064502, June 2018. doi: 10.1088/1538-3873/aab694.

Nienke van der Marel, Ruobing Dong, Ralph Pudritz, James Wadsley, Aaron Boley, Eve Lee, Mohamad Ali-Dib, Brenda Matthews, Christian Marois, and Henry Ngo. Signposts of planet formation in protoplanetary disks. 2019. doi: 10.5281/ZENODO.3755917. URL `https://zenodo.org/record/3755917`.

V. Van Eylen, Camilla Agentoft, M. S. Lundkvist, H. Kjeldsen, J. E. Owen, B. J. Fulton, E. Petigura, and I. Snellen. An asteroseismic view of the radius valley: stripped cores, not born rocky. *Monthly Notices of the RAS*, 479(4):4786–4795, October 2018. doi: 10.1093/mnras/sty1783.

Vincent Van Eylen and Simon Albrecht. Eccentricity from Transit Photometry: Small Planets in Kepler Multi-planet Systems Have Low Eccentricities. , 808(2):126, August 2015. doi: 10.1088/0004-637X/808/2/126.

Vincent Van Eylen, Simon Albrecht, Xu Huang, Mariah G. MacDonald, Rebekah I. Dawson, Maxwell X. Cai, Daniel Foreman-Mackey, Mia S. Lundkvist, Victor Silva Aguirre, Ignas Snellen, and Joshua N. Winn. The Orbital Eccentricity of Small Planet Systems. , 157(2):61, February 2019. doi: 10.3847/1538-3881/aaf22f.

Judah Van Zandt, Erik A. Petigura, Mason MacDougall, et al. TESS-Keck Survey. XIV. Two Giant Exoplanets from the Distant Giants Survey. , 165(2):60, February 2023. doi: 10.3847/1538-3881/aca6ef.

Jacob T. VanderPlas. Understanding the lomb–scargle periodogram. *The Astrophysical Journal Supplement Series*, 236(1):16, may 2018. doi: 10.3847/1538-4365/aab766. URL `https://doi.org/10.3847%2F1538-4365%2Faab766`.

Harry Varvoglis. Solar System dynamics, beyond the two-body-problem approach. In Nikolaos Solomos, editor, *Recent Advances in Astronomy and Astrophysics*, volume 848 of *American Institute of Physics Conference Series*, pages 613–626, August 2006. doi: 10.1063/1.2348039.

Allona Vazan, Re'em Sari, and Ronit Kessel. A New Perspective on the Interiors of Ice-rich Planets: Ice-Rock Mixture Instead of Ice on Top of Rock. *Astrophys. J.*, 926(2):150, February 2022.

Dimitri Veras and Eric B. Ford. Secular Orbital Dynamics of Hierarchical Two-planet Systems. , 715(2):803–822, June 2010. doi: 10.1088/0004-637X/715/2/803.

Shreyas Vissapragada, Daniel Jontof-Hutter, Avi Shporer, Heather A. Knutson, Leo Liu, Daniel Thorngren, Eve J. Lee, Yayaati Chachan, Dimitri Mawet, Maxwell A. Millar-Blanchaer, Ricky Nilsson, Samaporn Tinyanont, Gautam Vasisht, and Jason T. Wright. Diffuser-assisted infrared transit photometry for four dynamically interacting kepler systems. *The Astronomical Journal*, 159(3):108, Feb 2020. ISSN 1538-3881. doi: 10.3847/1538-3881/ab65c8. URL `http://dx.doi.org/10.3847/1538-3881/ab65c8`.

S. S. Vogt, S. L. Allen, B. C. Bigelow, L. Bresee, et al. HIRES: the high-resolution echelle spectrometer on the Keck 10-m Telescope. In David L. Crawford and Eric R. Craine, editors, *Instrumentation in Astronomy VIII*, volume 2198 of *Society of Photo-Optical Instrumentation Engineers (SPIE) Conference Series*, page 362, June 1994. doi: 10.1117/12.176725.

Steven S. Vogt, Matthew Radovan, Robert Kibrick, Butler, et al. APF—The Lick Observatory Automated Planet Finder. , 126(938):359, April 2014. doi: 10.1086/676120.

H. R. Wakeford and P. A. Dalba. The exoplanet perspective on future ice giant exploration. *Philosophical Transactions of the Royal Society A: Mathematical, Physical and Engineering Sciences*, 378(2187):20200054, nov 2020. doi: 10.1098/rsta.2020.0054. URL `https://doi.org/10.1098%2Frsta.2020.0054`.

K. J. Walsh and A. Morbidelli. The effect of an early planetesimal-driven migration of the giant planets on terrestrial planet formation. , 526:A126, February 2011. doi: 10.1051/0004-6361/201015277.

Kevin J. Walsh, Alessandro Morbidelli, Sean N. Raymond, David P. O'Brien, and Avi M. Mandell. A low mass for mars from jupiter's early gas-driven migration. *Nature*, 475(7355):206–209, jun 2011. doi: 10.1038/nature10201. URL `https://doi.org/10.1038%2Fnature10201`.

Lauren M. Weiss and Geoffrey W. Marcy. The Mass-Radius Relation for 65 Exoplanets Smaller than 4 Earth Radii. *Astrophysical Journal, Letters*, 783(1):L6, March 2014. doi: 10.1088/2041-8205/783/1/L6.

J. N. Winn. Exoplanet Transits and Occultations. In S. Seager, editor, *Exoplanets*, pages 55–77. 2010. doi: 10.48550/arXiv.1001.2010.

Joshua N. Winn. Transits and occultations, 2014.

Joshua N. Winn and Daniel C. Fabrycky. The occurrence and architecture of exoplanetary systems. *Annual Review of Astronomy and Astrophysics*, 53(1):409–447, aug 2015. doi: 10.1146/annurev-astro-082214-122246. URL `https://doi.org/10.1146%2Fannurev-astro-082214-122246`.

P. Wizinowich, D. S. Acton, C. Shelton, P. Stomski, J. Gathright, et al. First Light Adaptive Optics Images from the Keck II Telescope: A New Era of High Angular Resolution Imagery. *Publications of the ASP*, 112(769):315–319, March 2000. doi: 10.1086/316543.

A. Wolszczan and D. A. Frail. A planetary system around the millisecond pulsar PSR1257 + 12. *Nature*, 355(6356):145–147, January 1992. doi: 10.1038/355145a0.

A. Wootten and A.R. Thompson. The atacama large millimeter/submillimeter array. *Proceedings of the IEEE*, 97(8):1463–1471, aug 2009. doi: 10.1109/jproc.2009.2020572. URL `https://doi.org/10.1109%2Fjproc.2009.2020572`.

J. T. Wright, Dimitri Veras, Eric B. Ford, et al. The California Planet Survey. III. A Possible 2:1 Resonance in the Exoplanetary Triple System HD 37124. , 730(2):93, April 2011. doi: 10.1088/0004-637X/730/2/93.

J. T. Wright, G. W. Marcy, A. W. Howard, John Asher Johnson, T. D. Morton, and D. A. Fischer. The Frequency of Hot Jupiters Orbiting nearby Solar-type Stars. *Astrophysical Journal*, 753(2): 160, July 2012. doi: 10.1088/0004-637X/753/2/160.

Jason T. Wright and B. Scott Gaudi. Exoplanet Detection Methods. In Terry D. Oswalt, Linda M. French, and Paul Kalas, editors, *Planets, Stars and Stellar Systems. Volume 3: Solar and Stellar Planetary Systems*, page 489. 2013. doi: 10.1007/978-94-007-5606-9_10.

Yanqin Wu and Yoram Lithwick. Secular Chaos and the Production of Hot Jupiters. , 735(2):109, July 2011. doi: 10.1088/0004-637X/735/2/109.

A. Wyttenbach, D. Ehrenreich, C. Lovis, S. Udry, and F. Pepe. Spectrally resolved detection of sodium in the atmosphere of HD 189733b with the HARPS spectrograph. *Astronomy and Astrophysics*, 577:A62, May 2015. doi: 10.1051/0004-6361/201525729.

Ji-Wei Xie, Subo Dong, Zhaohuan Zhu, et al. Exoplanet orbital eccentricities derived from LAMOST-Kepler analysis. *Proceedings of the National Academy of Science*, 113(41):11431–11435, October 2016. doi: 10.1073/pnas.1604692113.

Andrew N. Youdin and Jeremy Goodman. Streaming instabilities in protoplanetary disks. *The Astrophysical Journal*, 620(1):459–469, feb 2005. doi: 10.1086/426895. URL `https://doi.org/10.1086%2F426895`.

Jie Yu, Daniel Huber, Timothy R. Bedding, Dennis Stello, Marc Hon, Simon J. Murphy, and Shourya Khanna. Asteroseismology of 16,000 ikepler/i red giants: Global oscillation parameters, masses, and radii. *The Astrophysical Journal Supplement Series*, 236(2):42, jun 2018. doi: 10.3847/1538-4365/aaaf74. URL `https://doi.org/10.3847%2F1538-4365%2Faaaf74`.

M. Zechmeister and M. Kürster. The generalised lomb-scargle periodogram. *Astronomy & Astrophysics*, 496(2):577–584, jan 2009. doi: 10.1051/0004-6361:200811296. URL `https://doi.org/10.1051%2F0004-6361%3A200811296`.

Li Zeng, Stein B. Jacobsen, Dimitar D. Sasselov, Michail I. Petaev, Andrew Vanderburg, Mercedes Lopez-Morales, Juan Perez-Mercader, Thomas R. Mattsson, Gongjie Li, Matthew Z. Heising, Aldo S. Bonomo, Mario Damasso, Travis A. Berger, Hao Cao, Amit Levi, and Robin D. Wordsworth. Growth model interpretation of planet size distribution. *Proceedings of the National Academy of Science*, 116(20):9723–9728, May 2019. doi: 10.1073/pnas.1812905116.

Li Zeng, Stein B. Jacobsen, Eugenia Hyung, et al. New Perspectives on the Exoplanet Radius Gap from a Mathematica Tool and Visualized Water Equation of State. *Astrophys. J.*, 923(2):247, December 2021.

Wei Zhu and Subo Dong. Exoplanet Statistics and Theoretical Implications. , 59:291–336, September 2021. doi: 10.1146/annurev-astro-112420-020055.

Carl Ziegler, Andrei Tokovinin, Cé sar Briceño, James Mang, Nicholas Law, and Andrew W. Mann. SOAR TESS survey. i. sculpting of TESS planetary systems by stellar companions. *The Astronomical Journal*, 159(1):19, dec 2019. doi: 10.3847/1538-3881/ab55e9. URL `https://doi.org/10.3847%2F1538-3881%2Fab55e9`.